frontiers | Research Topics

Imaging the developing connectome of perinatal brain

Edited by
Dan Wu, Weihao Zheng, Patricia Ellen Grant and Hao Huang

Published in
Frontiers in Neuroscience

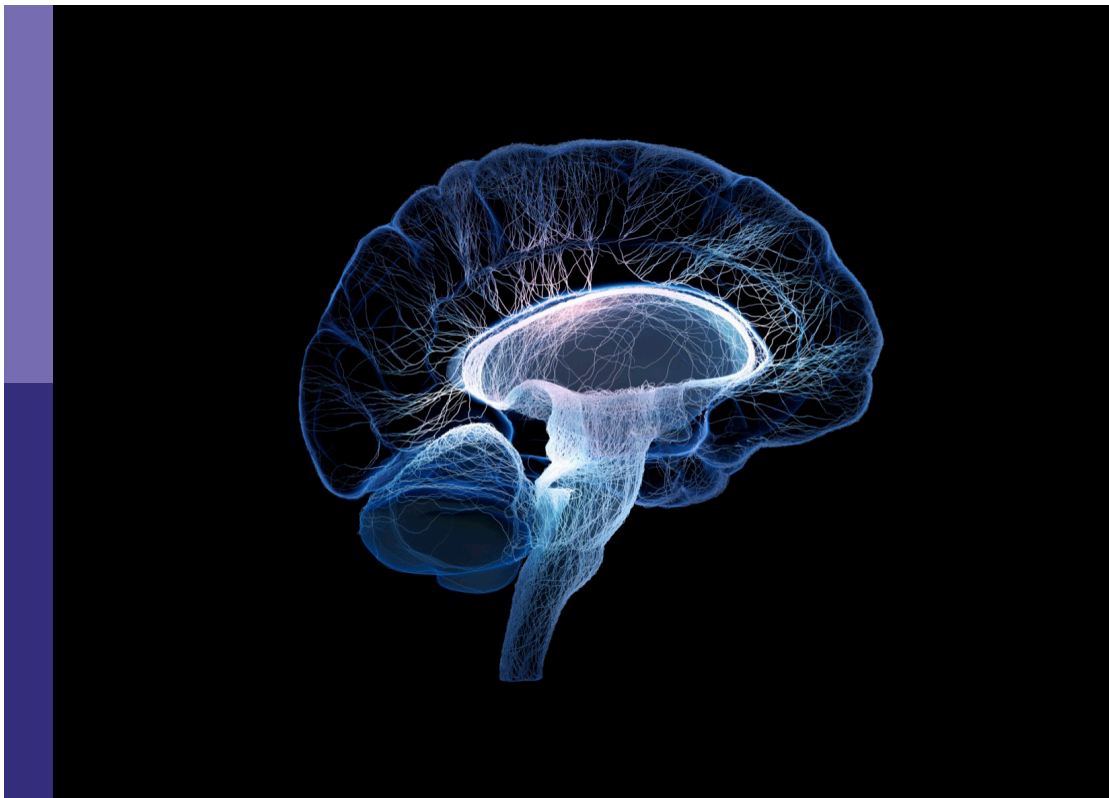

ISSN 1664-8714
ISBN 978-2-83251-712-3
DOI 10.3389/978-2-83251-712-3

About Frontiers

Frontiers is more than just an open access publisher of scholarly articles: it is a pioneering approach to the world of academia, radically improving the way scholarly research is managed. The grand vision of Frontiers is a world where all people have an equal opportunity to seek, share and generate knowledge. Frontiers provides immediate and permanent online open access to all its publications, but this alone is not enough to realize our grand goals.

Frontiers journal series

The Frontiers journal series is a multi-tier and interdisciplinary set of open-access, online journals, promising a paradigm shift from the current review, selection and dissemination processes in academic publishing. All Frontiers journals are driven by researchers for researchers; therefore, they constitute a service to the scholarly community. At the same time, the *Frontiers journal series* operates on a revolutionary invention, the tiered publishing system, initially addressing specific communities of scholars, and gradually climbing up to broader public understanding, thus serving the interests of the lay society, too.

Dedication to quality

Each Frontiers article is a landmark of the highest quality, thanks to genuinely collaborative interactions between authors and review editors, who include some of the world's best academicians. Research must be certified by peers before entering a stream of knowledge that may eventually reach the public - and shape society; therefore, Frontiers only applies the most rigorous and unbiased reviews. Frontiers revolutionizes research publishing by freely delivering the most outstanding research, evaluated with no bias from both the academic and social point of view. By applying the most advanced information technologies, Frontiers is catapulting scholarly publishing into a new generation.

What are Frontiers Research Topics?

Frontiers Research Topics are very popular trademarks of the *Frontiers journals series*: they are collections of at least ten articles, all centered on a particular subject. With their unique mix of varied contributions from Original Research to Review Articles, Frontiers Research Topics unify the most influential researchers, the latest key findings and historical advances in a hot research area.

Find out more on how to host your own Frontiers Research Topic or contribute to one as an author by contacting the Frontiers editorial office: frontiersin.org/about/contact

Imaging the developing connectome of perinatal brain

Topic editors

Dan Wu — Zhejiang University, China

Weihao Zheng — Lanzhou University, China

Patricia Ellen Grant — Boston Children's Hospital, Harvard Medical School, United States

Hao Huang — University of Pennsylvania, United States

Citation

Wu, D., Zheng, W., Grant, P. E., Huang, H., eds. (2023). *Imaging the developing connectome of perinatal brain*. Lausanne: Frontiers Media SA.

doi: 10.3389/978-2-83251-712-3

Table of contents

frontiers | Frontiers in Neuroscience

TYPE Editorial
PUBLISHED 06 February 2023
DOI 10.3389/fnins.2023.1122829

OPEN ACCESS

EDITED AND REVIEWED BY
Dustin Scheinost,
Yale University, United States

*CORRESPONDENCE
Dan Wu
✉ danwu.bme@zju.edu.cn
Weihao Zheng
✉ zhengweihao@lzu.edu.cn

SPECIALTY SECTION
This article was submitted to Neurodevelopment, a section of the journal Frontiers in Neuroscience

RECEIVED 13 December 2022
ACCEPTED 25 January 2023
PUBLISHED 06 February 2023

CITATION
Wu D, Zheng W, Grant PE and Huang H (2023) Editorial: Imaging the developing connectome of perinatal brain. *Front. Neurosci.* 17:1122829. doi: 10.3389/fnins.2023.1122829

Editorial: Imaging the developing connectome of perinatal brain

Dan Wu[1]*, Weihao Zheng[2]*, Patricia Ellen Grant[3,4,5,6] and Hao Huang[7,8]

[1]Key Laboratory for Biomedical Engineering of Ministry of Education, College of Biomedical Engineering and Instrument Science, Zhejiang University, Hangzhou, China, [2]Gansu Provincial Key Laboratory for Wearable Computing, School of Information Science and Engineering, Lanzhou University, Lanzhou, China, [3]Fetal Neonatal Neuroimaging and Developmental Science Center, Boston Children's Hospital, Boston, MA, United States, [4]Division of Newborn Medicine, Boston Children's Hospital, Boston, MA, United States, [5]Department of Radiology, Boston Children's Hospital, Boston, MA, United States, [6]Department of Pediatrics, Harvard Medical School, Boston, MA, United States, [7]Department of Radiology, Children's Hospital of Philadelphia, Philadelphia, PA, United States, [8]Department of Radiology, Perelman School of Medicine, University of Pennsylvania, Philadelphia, PA, United States

KEYWORDS

magnetic resonance imaging (MRI), perinatal brain, connectome, imaging biomarkers, development, analytic methods

Editorial on the Research Topic
Imaging the developing connectome of perinatal brain

Brain maturation during the perinatal period in the fetus and infant is a rapid and complex process. Neurodevelopment during this period is critical for supporting later cognitive, emotional, and behavioral abilities. Increasing evidence for the perinatal origins of various neurodevelopmental disorders underscores the importance of identifying features of early brain development (Dehaene-Lambertz and Spelke, 2015). Understanding the developing brain connectome will open new insights into the fundamental processes of brain circuit formation and maturation in early life and reveal the etiology of intractable neurodevelopmental disorders. Advances in magnetic resonance imaging (MRI), such as rapid imaging and motion correction techniques, have overcome significant challenges in fetal and infant brain MRI and enabled non-invasive *in vivo* assessment of functional and structural connectivity between separate brain regions (Kaiser, 2017; Dubois et al., 2021), offering great opportunities to capture the connectome of the fetal and postnatal brain with unprecedented accuracy. Thus, the purpose of this Research Topic focuses on neuroimaging studies of the early development of the brain connectome.

This Research Topic includes 8 original research paper and 1 data descriptor. Main research contents concentrate on atypical connectome pattern and novel imaging biomarkers for prematurity, hypoxic ischemic encephalopathy (HIE), etc. and machine learning algorithms for fetal brain analysis. Neumane et al. explored the impact of prematurity on the development and integrity of the sensorimotor connectivity and their relationship to later motor impairments. They found that prematurity affected early microstructural development of the primary sensorimotor network and these effects differed according to the level of prematurity. They also highlighted the microstructural development of specific tracts predicted fine motor and cognitive outcomes at 18 months. Li et al. investigated the effects of daily iron supplementation on motor development and brain structural connectivity of preterm infants. They found that iron status at early postnatal period was related to both motor development and connectivity decreases, and the delayed motor development can be reversed by supplying 2 mg/kg of iron per day for 6 months. Vishnubhotla et al. studied the influence of prenatal opioid exposure on brain structural connectivity, and identified two connectivity pathways that were significantly differed

between opioid exposure infants and unexposed controls. Votava-Smith et al. reported that clinical risk factors and brain dysplasia score were associated with distinct brain dysmaturation patterns in term neonates with congenital heart disease (CHD). Specifically, clinical factors were most predictive to postnatal microstructural dysmaturation, whereas subcortical dysplasia predicted connectome-based measures, suggesting the complementary effects of connectome and microstructure in deciphering risk factors related to poor neurodevelopment in CHD. Based on the least absolute shrinkage and selection operator (LASSO) regression model, Onda et al. developed a novel biomarker named composite diffusion tensor imaging (cDTI) score to assess the severity of short-term neurological functions of HIE neonates. They demonstrated high cDTI scores were related to the intensity of the early inflammatory response and the severity of neuronal impairment after therapeutic hypothermia.

Characterizing fetal brain development *in utero* is still challenging due to the difficulties in acquiring high-quality MRI data and lack of effective analytic methods. Based on 188 brain MRI of normal fetuses ranging from 19 to 37 gestational weeks, Ren et al. establish a reference of intracranial structure volumes during this period by manual segmentation from two experienced experts. Wang et al. developed a MRI-based semi-automatic pipeline to segment the cortex and subcortical structures of fetal brains, reducing the costs of manual segmentation. De Asis-Cruz et al. proposed a full automatic and computationally efficient generative adversarial neural network for segmenting the fetal brain based on functional MRI, which yielded whole brain masks that closely approximated the manually labeled ground truth. This study is of great significance in facilitating *in utero* investigations of emerging functional connectivity.

Lack of available and reliable data is one of dominating factors that limits the exploration of brain maturational trajectories early in life. Edwards et al. introduced the neonatal data release of the Developing Human Connectome Project, which includes 887 multimodal high-quality MR images from 783 preterm-born and term-born infants and essential metadata. This open dataset allows researchers to design the experiment as they wish, making great contribution to uncover the typical and atypical brain development across the perinatal period.

In conclusion, these nine papers included in this Research Topic summary the recent progression of normal brain maturation and markers of neurodevelopmental disorders during the perinatal period, as well as important technical advances in fetal and infantile brain MRI.

Author contributions

All authors listed have made a substantial, direct, and intellectual contribution to the work and approved it for publication.

Conflict of interest

The authors declare that the research was conducted in the absence of any commercial or financial relationships that could be construed as a potential conflict of interest.

Publisher's note

References

Dehaene-Lambertz, G., and Spelke, E. S. (2015). The infancy of the human brain. *Neuron* 88, 93–109. doi: 10.1016/j.neuron.2015.09.026

Dubois, J., Alison, M., Counsell, S. J., Hertz-Pannier, L., Hüppi, P. S., and Benders, M. (2021). MRI of the neonatal brain: a review of methodological challenges and neuroscientific advances. *J. Magn. Reson. Imag. JMRI* 53, 1318–1343. doi: 10.1002/jmri.27192

Kaiser, M. (2017). Mechanisms of connectome development. *Trends Cogn. Sci.* 21, 703–717. doi: 10.1016/j.tics.2017.05.010

frontiers in Neuroscience

ORIGINAL RESEARCH
published: 08 November 2021
doi: 10.3389/fnins.2021.769558

Effects of Daily Iron Supplementation on Motor Development and Brain Connectivity in Preterm Infants: A Diffusion Magnetic Resonance Study

Mingyan Li[1], Chai Ji[1], Weifeng Xuan[2], Weijun Chen[1], Ying Lv[1], Tingting Liu[3], Yuqing You[4], Fusheng Gao[4], Quan Zheng[1] and Jie Shao[1]*

[1] Department of Child Health Care, National Clinical Research Center for Child Health, The Children's Hospital, Zhejiang University School of Medicine, Hangzhou, China, [2] Shaoxing Maternal and Child Health Care Hospital, Shaoxing, China, [3] Key Laboratory for Biomedical Engineering of Ministry of Education, Department of Biomedical Engineering, College of Biomedical Engineering and Instrument Science, Zhejiang University, Hangzhou, China, [4] Department of Radiology, National Clinical Research Center for Child Health, Children's Hospital, Zhejiang University School of Medicine, Hangzhou, China

OPEN ACCESS

Edited by:
Hao Huang,
University of Pennsylvania,
United States

Reviewed by:
Zhijun Yao,
Lanzhou University, China
Xiaoqin Mai,
Renmin University of China, China

***Correspondence:**
Ying Lv
lvying@zju.edu.cn

Specialty section:
This article was submitted to Neurodevelopment, a section of the journal Frontiers in Neuroscience

Received: *02 September 2021*
Accepted: *12 October 2021*
Published: *08 November 2021*

Citation:
Li M, Ji C, Xuan W, Chen W, Lv Y, Liu T, You Y, Gao F, Zheng Q and Shao J (2021) Effects of Daily Iron Supplementation on Motor Development and Brain Connectivity in Preterm Infants: A Diffusion Magnetic Resonance Study. Front. Neurosci. 15:769558. doi: 10.3389/fnins.2021.769558

Objectives: The aim of the study is to demonstrate the characteristic of motor development and MRI changes of related brain regions in preterm infants with different iron statuses and to determine whether the daily iron supplementation can promote motor development for preterm in early infancy.

Methods: The 63 preterm infants were grouped into non-anemia with higher serum ferritin (NA-HF) group and anemia with lower serum ferritin (A-LF) group according to their lowest serum Hb level in the neonatal period as well as the sFer at 3 months old. Forty-nine participants underwent MRI scans and Infant Neurological International Battery (INFANIB) at their 3 months. At 6 months of corrected age, these infants received the assessment of Peabody Developmental Motor Scales (PDMS) after 2 mg/kg/day iron supplementation.

Results: In total, 19 preterm infants were assigned to the NA-HF group while 44 preterm infants to the A-LF groups. The serum ferritin (sFer) level of the infants in A-LF group was lower than that in NA-HF group (44.0 ± 2.8 mg/L vs. 65.1 ± 2.8 mg/L, $p < 0.05$) and was with poorer scores of INFANIB (66.8 ± 0.9 vs. 64.4 ± 0.6, $p < 0.05$) at 3 months old. The structural connectivity between cerebellum and ipsilateral thalamus in the NA-HF group was significantly stronger than that in the A-LF group ($n = 17$, 109.76 ± 23.8 vs. $n = 32$, 70.4 ± 6.6, $p < 0.05$). The decreased brain structural connectivity was positively associated with the scores of PDMS ($r = 0.347$, $p < 0.05$). After 6 months of routine iron supplementation, no difference in Hb, MCV, MCHC, RDW, and sFer was detected between A-LF and NA-HF groups as well as the motor scores of PDMS-2 assessments.

Conclusion: Iron status at early postnatal period of preterm infant is related to motor development and the enrichment of brain structural connectivity. The decrease in brain structural connectivity is related to the motor delay. After supplying 2 mg/kg of iron per day for 6 months, the differences in the iron status and motor ability between the A-LF and NA-HF groups were eliminated.

Keywords: preterm infant, iron supplementation, motor development, brain structural connectivity, diffusion MRI

INTRODUCTION

Iron deficiency (ID) continues to be the most prevalent nutrient deficiency in the world. As we know, preterm infants are more likely susceptible to be anemic than term infants, most of which were due to ID (Todorich et al., 2009). Iron is an essential mineral necessary for delivering oxygen to tissues throughout the body as well as serving important roles in metabolism, respiration, and immune functions (Todorich et al., 2009). It is also a cofactor in the central nervous system development processes (DellaValle, 2013). Our body carefully sustains a balance between iron loss, iron absorption, and iron storage. ID is a precursor to iron deficiency anemia (IDA). The first stage of ID is characterized by a decrease in serum ferritin (sFer), which is caused by the depletion of total body iron stores, while other iron indices and hemoglobin (Hb) remain normal. The IDA stage is not only symbolized by lower sFer and hemoglobin but also by lower mean corpuscular volume (MCV), lower mean hemoglobin concentration (MCHC), and higher red blood cell distribution width (RDW).

Brain ID occurs before IDA. It can alter the development of oligodendrocytes and result in hypomyelination of white matter, which is related to changes in startle response, auditory evoked potentials, and motor function in the infant (Beard, 2007; Todorich et al., 2009). Early ID also neurochemically alters the function of neurotransmitters. Animal models have shown that ID can alter the function of the frontal cortex, midline thalamus, and other brain regions by modifying the dopaminergic neurotransmission system (Beard and Connor, 2003).

Brain ID in fetuses or neonates is more detrimental than in toddler because of the rapidity of brain growth early in life. Obtaining adequate iron of the developing brain is necessary for behavioral and motor development (Felt and Lozoff, 1996). A number of studies have reported that term infants with IDA or chronic severe ID have lower motor development scores, compared with infants with normal iron status (Shafir et al., 2008). It is particularly concerning that the ID infants have poorer motor function because ID without anemia is more common than IDA, which cannot be detected by regular screening procedures (Shafir et al., 2008).

Compared with full-term infants, preterm infants are deprived of iron accretion that occurs in the third trimester of pregnancy, which results in a decrease in iron storage at birth, as reflected in the decrease in sFer (Lackmann et al., 1998; McCarthy et al., 2017). In addition, most studies have found that reduced brain iron concentration was accompanied with lower sFer (Georgieff, 2017). Therefore, sFer is a valuable index indicating the brain ID of these infants who are more susceptible to motor delay. As iron supplementation after birth could improve gross motor remarkably in term infants (Shafir et al., 2008), we speculate that early regular iron supplementation to these premature infants at high risk of ID can be beneficial to their motor development.

Clinical neuroimaging research on early motor abilities is still limited. Previous studies have found that structural connections between motor-related brain regions play an important role in movement development (Craig et al., 2020). Cranial magnetic resonance (MRI) is a common and valuable method to study the infant brain functions, and diffusion tensor imaging (DTI) is a non-invasive method to study the white matter of the brain. Great progress has also been made in the study of human brain architecture with ID or IDA by DTI and structural MRI (Hannah and D'Cruz, 2019). Probabilistic fiber tracking by DTI in ID adult has found that iron concentration is linked to structural connectivity of the subthalamic nucleus (Dimov et al., 2019). Therefore, MR tractography in premature infants with ID or IDA was a recommended method for exploring development delay.

To characterize the motor development and MRI changes of related brain regions in preterm infants with different iron status, we examined data from a follow-up study including brain imaging and behavior development of preterm infants with different levels of iron metabolism. The relationship between scores of gross and fine motor function of preterm infants and structural brain network based on DTI were analyzed. We hypothesized that preterm infants with neonatal anemia who have lower iron levels would present an altered brain network connectivity and motor ability. Routine iron supplementation can improve iron status as well as motor development.

MATERIALS AND METHODS

The present study was approved by the ethics committee of the Children's Hospital, Zhejiang University School of Medicine (Permit Number: 2019-IRB-027). Parents who accepted the participation provided written informed consent before enrolled on the study. All the data used in the present study were available to the community *via* a suitable open repository.

Participants

We conducted a follow up study of preterm infants who attended the High Risk Infant Clinic of the Children's Hospital, Zhejiang University School of Medicine, from January 2018 to December 2019. Participants included 63 preterm infants, with a gestational age (GA) of 28–36 weeks. All the enrolled infants were invited for regular follow-up every month since 40 weeks

GA. Information of medical records, including weight at birth, GA, neonatal complications, Hb during neonate period (the lowest Hb tested within the first month after birth), as well as anthropometric measurements were collected. The enrollment criteria included no chromosomal and genetic anomalies, no craniofacial anomalies, no neurological complications, no hematological disease, and no blood transfusions in the first 6 months (corrected age) of life.

Iron Status Detection and Iron Supplementation

Venous blood samples of enrolled participants have been tested for estimation Hb and ferritin at 3 months, and sFer, Hb, MCV, MCHC, and RDW were collected at 6 months (correct age). Anemia was defined as venous Hb $<$ 145 g/L within 28 days of age, Hb $<$ 90 g/L at 3 months old, and $<$ 110 g/L at 6 months old (Domellof, 2017). According to the lowest Hb level during the neonatal period as well as the sFer at 3 months, preterm infants were divided into two groups: anemia with lower ferritin group (A-LF, with Hb $<$ 145 g/L) and non-anemia with higher ferritin group (NA-HF, with Hb $\geq$ 145 g/L). C-reactive protein (CRP) were all $<$ 8 mg/L both at 3- and 6-month of age, which stands for no inflammation.

All participants in this study had delayed cord clamping at birth and were given iron supplements with a dosage of 2 mg/kg per day from 40 weeks of corrected GA according to the post-discharge feeding recommendations for premature, low birth weight infants in China (preterm infants in this study cohort were not introduced to have complementary food, so the total daily iron intake was calculated as the sum of iron supplements and the iron from formula and/or breast milk fortifier) (Wang and Liu, 2016).

The Motor Ability Assessment

Early neurological function was evaluated according to the Infant Neurological International Battery (INFANIB) at 3 months of age. Results are expressed as raw scores for total motor ability. Peabody Developmental Motor Scales, second edition (PDMS-2), was conducted at 6 months of corrected age. The scales contain sub-tests of the following six parameters: (a) reflexes, (b) stationary (body control and equilibrium), (c) locomotion, (d) object manipulation, and (e) grasping. Raw scores are converted into age-equivalent scores for each sub-test; motor quotient is calculated from the standard scores of five sub-tests of PDMS-2. The assessment of PDMS-2 was performed by two pediatricians who had no knowledge of the medical history of the infants.

Image Acquisition

Infants were scanned after receiving 50 mg/kg of enema or oral chloral hydrate within 3 months old. The scans were performed on a Philips 3.0T Achieva system with standard eight-channel head coils. Two sequences were used in this study: (1) 3-D sagittal T2-weighted sequence echo time [(TE) = 278 ms, repetition time (TR) = 2,200 ms, acquisition matrix = 224 $\times$ 204, voxel size = 0.8 $\times$ 0.8 $\times$ 0.8 mm^3, field of view (FOV) = 180 $\times$ 161 $\times$ 140 mm^3]; (2) DTI images were collected using an echo-planar image (EPI) sequence with 32 non-colinear diffusion encoding directions for b value = 800 and 1,500 s/mm^2 each, in addition with one non-weighted image (TE = 115 ms, TR = 9,652 ms, voxel size = 1.5 $\times$ 1.5 $\times$ 2 mm^3, flip angle = 90°, FOV = 180 $\times$ 180 $\times$ 120 mm^3, acquisition matrix = 120 $\times$ 118, bandwidth = 1,341 Hz/pixel, number of volumes = 60, 60 slices).

Brain Region Segmentation and Volume Calculation Using T2-Weighted Imaging

The T2-weighted images were preprocessed including brain extraction (Smith, 2002), creation of brain mask, and bias correction (Tustison et al., 2010). Then the whole brain of each subject was segmented into 83 brain regions using Draw-EM (Developing brain Region Annotation With Expectation-Maximization) (Makropoulos et al., 2014, 2018), and the volume of each region was extracted.

Diffusion Tensor Imaging Preprocessing

All DTI data were performed intra-subject registration using a linear image registration tool FLIRT (Jenkinson and Smith, 2001; Jenkinson et al., 2002), followed by eddy current correction using "topup" and "eddy" in FSL (Andersson and Sotiropoulos, 2016). Fractional anisotropy (FA) and mean/axial/radial diffusivity (MD/AD/RD) maps were generated from the diffusion tensor using the weighted linear least squares method (Basser et al., 1994). The individual images were transformed to the JHU-neonate single brain DWI atlas using a non-linear transformation of the multi-channel large deformation diffeomorphic metric mapping (LDDMM) (Miller et al., 1993; Djamanakova et al., 2013). Then the JHU-neonate parcellation map, which included 126 regions of interest (ROIs), was transformed to the individual native space. Registration of all subjects was checked.

Diffusion Tensor Imaging-Based Connectivity Analysis

Tractography was performed using a fiber orientation distribution-based probabilistic fiber tracking algorithm in MRtrix3,[1] with the whole-brain mask as the seed, and the following parameters were used: a cutoff of 0.05 min/max length of 10/250 mm, step size of 0.5 mm. An asymmetric connection matrix was generated for each subject from the whole brain tractography based on the JHU-neonate parcellation map, and the number of connection fibers between ipsilateral and contralateral motor-related regions, including frontal cortex, striatum, cerebellum, and thalamus, which were implicated in supporting early motor development (Todorich et al., 2009), was extracted.

Statistical Analysis

All analyses were performed using SPSS software, version 16.0 (IBM Corporation, Armonk, NY, United States).

An independent sample *t*-test was performed on the iron metabolism parameters, age and birth weight. A Chi-square test was performed on gender and maternal education background.

[1] www.mrtrix.org

ROIs were paired to compare the connectivity between A-LF and NA-HF groups. As all the data form a normal distribution and homogeneity, covariance analyses of the volume and connectivity of the brain regions, as well as the motor scores of PDMS-2, were performed by controlling GA and physical age before homogeneity test of variance. Multiple linear regression was used to test the relationship between INFANIB scores and the number of connection fibers/brain region volumes. Multiple comparison correction was conducted, and adjusted $p < 0.05$ was considered as statistically significant.

RESULTS

Demographic and Clinical Information

A total of 63 infants were enrolled in the present study. Demographic and clinical information are shown in **Table 1**. GA and birth weight were lower in the A-LF group than in the NA-HF group. No difference was detected in gender, maternal age at delivery, and maternal education background between the two groups. The neonatal Hb level of the A-LF group was significantly lower than that of the NA-HF group ($n = 44$, Hb:114.9 ± 6.3 g/L vs. $n = 19$, Hb:174.1 ± 2.8 g/L, $p < 0.05$). Although there was no significant difference of Hb between the A-LF and NA-HF groups at 3 months old ($n = 44$, Hb: 102.1 ± 1.3 mg/L vs. $n = 19$, Hb: 97.6 ± 2.7 g/L, $p = 0.127$), sFer of the A-LF group was lower than that of the NA-HF group ($n = 44$, sFer: 44.0 ± 2.8 mg/L vs. $n = 19$, sFer: 65.1 ± 2.8 mg/L, $p < 0.05$) (**Table 2**).

All preterm infants were tested with INFANIB at 3 months old. We found that the overall INFANIB scores were lower in the A-LF group. The discrepancy has statistical significance after controlling by GA and corrected age ($n = 44$, 64.4 ± 0.6 vs. $n = 19$, 66.8 ± 0.9, $p < 0.05$, **Figure 1**).

Structural Changes of Neuroimaging in Anemia Preterm Infant With Lower Serum Ferritin

Previous studies have found that structural connections between motor-related brain regions play an important role in movement development (Craig et al., 2020). Only 32 of A-LF infants and 17 of NA-HF infants had qualified MRI examination. MRI quality control was performed as follows: (1) without acquired punctate or focal lesions, marked dilation of the cerebral ventricles on MRI scans; (2) without visible artifacts on MRI scans. The ROI registration files of all the subjects were checked, and the registration effect was good. According to previous studies, a total of 12 connections were examined in the present study, including ipsilateral and contralateral precentral gyrus, cerebellum, thalamus, and striatum. The results showed that there was obvious fiber connection between the ipsilateral and contralateral precentral gyrus–cerebellum, precentral gyrus–striatum, cerebellum–thalamus, and cerebellum–striatum which had significance (**Table 3**) in both A-LF and NA-HF groups.

Then, we compared the above eight connections between the two groups. After controlling GA and physical age, only the connectivity between cerebellum and ipsilateral thalamus in the A-LF group was lower than that in the NA-HF group (109.76 ± 23.8 vs. 70.4 ± 6.6, $p < 0.05$). No statistical difference of the structural connectivity between other ROIs was detected in the two groups (**Figure 2**).

According to the reported decreased volume of brain regions in IDA infants, the volume of brain region was calculated in the present study. Based on the results of connectivity analysis, we calculated the volume of cerebellum and thalamus. It was found that the overall volume of the left and right thalamus was significantly lower in the A-LF group than that in the NA-HF group (8,369.3 ± 353.2 mm^3 vs. 6,926.2 ± 552.3 mm^3, $p < 0.05$), but no significant difference in the cerebellum volume was found between the two groups (**Figure 3**).

Iron Status and Scores of Peabody Developmental Motor Scales After Iron Supplementation at 6 Months of Corrected Age in Preterm Infant

To identify the effect of oral iron supplementation, iron metabolism parameters were compared between the two groups at 6 months of corrected age. No difference was detected in Hb (116.6 ± 2.8 g/L, $n = 19$ in the NA-HF group, and 117.2 ± 2.5 g/L, $n = 44$ in the A-LF group) and sFer (39.3 ± 15.0 μg/L, $n = 19$ in the NA-HF group, and 30.8 ± 3.6 μg/L, $n = 44$ in the A-LF group) between the two groups (**Table 2**).

As shown in **Figure 4**, although the mean of the total motor quotient, gross motor quotient, and fine motor quotient by PDMS-2 assessment was slightly higher in the NA-HF group at 6 months of correct age after 6 months supplementation, there was no significant difference between the two groups (**Figure 4**).

Brain Structure–Movement Relationship in Anemia Preterm Infant With Lower Serum Ferritin

After controlling GA and the age of MRI scan, the structural connection strength between the cerebellum and ipsilateral thalamus was positively correlated with motor scores of INFANIB at 3 months old ($r = 0.347$, $p < 0.05$), while

TABLE 1 | The baseline characteristics of the NA-HF and A-LF groups.

	NA-HF	A-LF	*p*-Value
Gestational age (week)	35.5 [3.2]	32.1 [3.6]	<0.05*
Birth weight (kg)	2,009.0 [373.2]	1,597.0 [447.3]	<0.05*
Sex [n (%)]			0.589
Male	11 (57.9%)	27 (61.4%)	
Female	8 (42.1%)	17 (38.6%)	
Maternal age (year)	30.5 (0.41%)	30.0 (0.36%)	0.669
Maternal education background [n (%)] ≤ senior middle school	6 (31.6%)	11 (25.0%)	0.292

*Values are means ± SEM, n = 19 in NA-HF group/44 in the A-LF group. *p < 0.05 indicates means with significant difference. NA-HF, non-anemia with higher serum ferritin; A-LF, anemia with lower serum ferritin.*

TABLE 2 | Iron status in the NA-HF and A-LF groups.

	NA-HF	A-LF	*p*-Value
Newborn			
Hb (g/L)	174.1 [2.8]	114.9 [6.3]	<0.05*
3 months			
Hb (g/L)	97.6 [2.7]	102.1 [1.3]	0.127
MCV (fl)	82.1 [1.4]	85.5 [0.9]	0.628
MCHC (g/L)	330.8 [2.8]	330.9 [1.9]	0.550
RDW (%)	13.7 [0.5]	14.5 [0.3]	0.790
SF (μg/L)	65.1 [2.8]	44.0 [2.8]	< 0.05*
6 months			
Hb (g/L)	116.6 [2.8]	117.2 [2.5]	0.881
MCV (fL)	79.1 [1.0]	75.5 [2.2]	0.336
MCHC (g/L)	327.1 [3.1]	328.4 [2.4]	0.753
RDW (%)	13.3 [0.4]	13.5 [0.3]	0.655
SF (μg/L)	39.3 [15.0]	30.8 [3.6]	0.460

*Values are means ± SEM, n = 19 in the NA-HF group/44 in the A-LF group. *p < 0.05 indicates means with significant difference. Hb, hemoglobin; MCV, mean corpuscular volume; MCHC, mean hemoglobin concentration; RDW, red blood cell distribution width.*

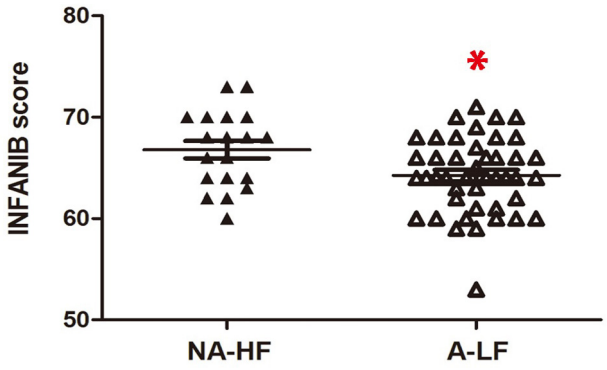

FIGURE 1 | The scores of Infant Neurological International Battery (INFANIB) display a lower value in anemia in the lower ferritin (A-LF) group than non-anemia in the higher ferritin (NA-HF) group at 3 months old. *$p < 0.05$.

there was no significant correlation between the volumes of cerebellum/thalamus and the motor scores ($r = 0.056$, $p = 0.930/r = 0.047$, = 0.951). In addition, we also found that the connection strength was significantly higher in the A-LF group than that in the NA-HF group controlling for the volume of thalamus and cerebellum ($p < 0.05$) (**Figure 5**).

DISCUSSION

This study together provides the following evidence: (1) Anemia with lower iron levels during the neonatal period was related to the poor motor performance during early postnatal life among preterm infants. (2) The volume of the thalamus and the structural connection between the cerebellum and ipsilateral thalamus was lower in A-LF than that in NA-HF preterm infants, but only the decreased connectivity between the cerebellum and ipsilateral thalamus in the A-LF group was related with the motor delay. (3) After 6 months of daily iron supplementation, no difference in iron status was detected between the A-LF and NA-HF groups, as well as the motor scores of PDMS-2 assessment.

As premature infants are susceptible to ID than term infants (Moreno-Fernandez et al., 2019), iron detection is necessary at early age of preterm infants. However, considering the limitation of venous blood sampling for iron detection in neonates, as well as the finding that preterm infants with neonatal anemia probably had a lower level of iron than those without neonatal anemia in the previous studies, we analyzed the serum Hb and sFer at 3 months of age. The findings demonstrated that infants with neonatal anemia had lower sFer levels at 3 months old, which may indicate lower iron levels early after birth. Furthermore, previous research found that brain ID occurs earlier than serum ID/IDA (Zamora et al., 2016), and we speculated that lower Hb at birth in the A-LF group might increase the risk of brain ID in our sample.

Many studies have shown that brain iron status is related to neurodevelopment of infants, which is involved in myelination, dopamine neurotransmission, and neuronal metabolism (Beard and Connor, 2003). Most researches focused on ID with cognitive development, but little is known about the motor development of premature infants with ID (Berglund et al., 2013, 2018). In our study, at the same time when blood sampling was tested at 3 months old, we conducted the INFANIB and found that the motor development of A-LF infants obviously lagged behind than that of NA-HF infants. This was consistent with the previous study on term infants that there is poorer motor function in ID group with or without anemia (Shafir et al., 2008).

Currently, most findings showed that brain ID is mainly related to the decrease in the volume of the brain regions (Mudd et al., 2018). Brain regions involved in our study, such as the frontal cortex, striatum, cerebellum, and thalamus, are associated with early motor development (Niendam et al., 2012). As Mudd reported in the pig model, pigs with ID demonstrated reduced iron content in the cerebellum and left cortex as well as decreased gray and white matter compared with the controlled group using the QSM and voxel-based morphometric analysis (Mudd et al., 2018). Another research also indicated that lower iron concentrations in 30-day-old pigs had smaller volume in cortical gray matter in the ID group compared with the control group (Leyshon et al., 2016). In our preterm cohort, the volumes of thalamus were different between the A-LF and NA-HF groups. After further analysis, there is no significant correlation between the volume of thalamus and motor development. It may be related to the limitation of our sample size. Further study with an expanding sample size will be needed to address this issue in more detail.

Despite the volume of brain regions, recent animal studies demonstrated that perinatal ID affected cortical neurons, and both apical and basal dendrites displayed a uniform decrease in branching (Felt et al., 2006; Greminger et al., 2014), which may lead to decreased neuron connection between cortex and other brain regions. Iron is important as it is involved in the production of myelin basic protein (MBP) and maintenance of myelination of neurons in brain gray matter, such as the thalamus (Mills et al., 2010; Huber et al., 2020). Other studies reported that the cerebellum and thalamus are susceptible to ID, which may lead to changes in monoamine metabolism,

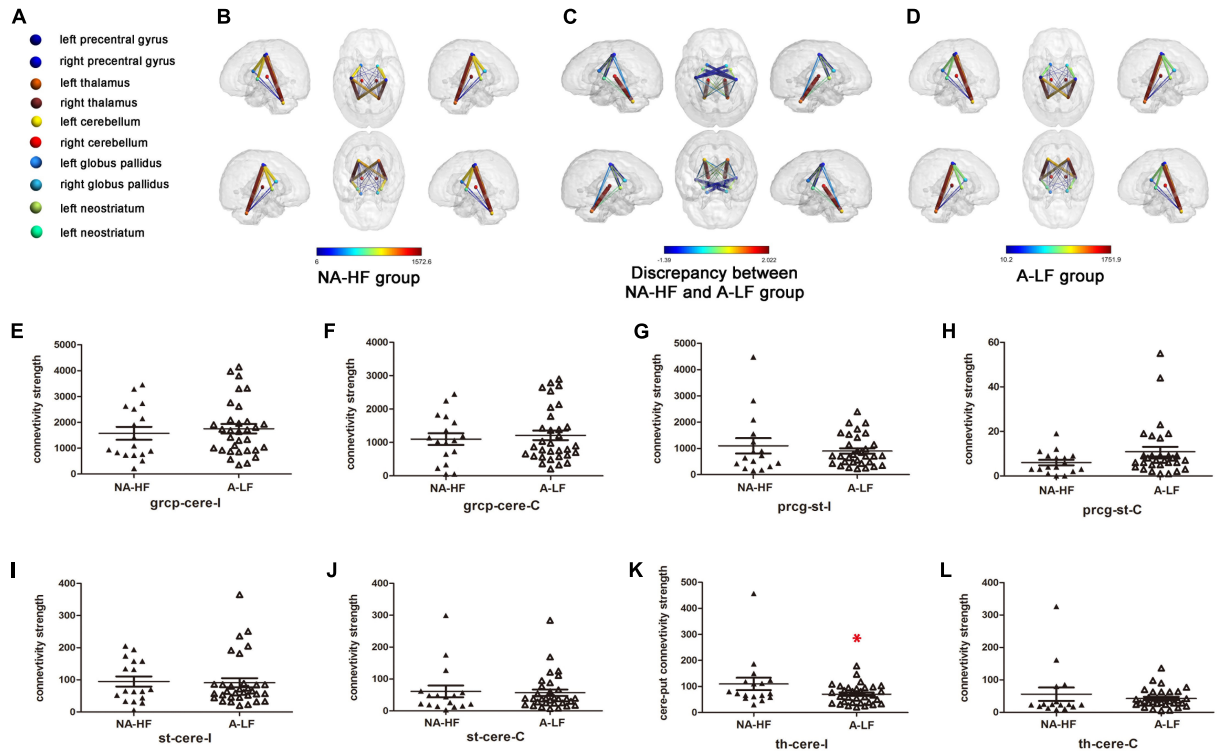

FIGURE 2 | Comparisons of clusters with significant connectivity between motor regions in the A-LF and NA-HF groups with multiple corrections by diffusion tensor imaging (DTI) at 3 months old. **(A)** Color-coded spheres present motor-related ROIs. **(B–D)** Locations and signs of brain structural connectivity between motor-related regions are illustrated. Spheres represent regions of interest (ROIs). Neostriatum and globus pallidus stand for striatum. Sticks with colors from blue to red represent probabilistic brain structural connectivity for an ROI pair. Color bars in **(B,D)** indicate the connectivity enrichment. Color bars in **(C)** indicate the discrepancy between the A-LF group and NA-HF group, respectively. **(E–L)** Comparisons of structural connectivity showed lower enrichment between cerebellum and ipsilateral thalamus in the A-LF group compared with the NA-HF group, and no significant difference was detected between other ROIs. grcp, precentralgyrus; cere, cerebellum; th, thalamus; st, striatum (include caudate nucleus, Cau/globus pallidus, GP); I, ipsilateral; C, contralateral; $^{*}p < 0.05$.

resulting in functional connection disorder (Felt et al., 2006). Our study has shown that the structural connections between the cerebellum and thalamus were lower in the A-LF than that in the NA-HF groups at 3 months old. The results of regression analysis demonstrated that the level of motor development of infants of the same age was positively correlated with the structural connection between the cerebellum and thalamus. Our study showed that the structural connections between the cerebellum and thalamus in A-LF were obviously lower than that in the NA-HF groups at 3 months old. Moreover, consistent with Andreasen's findings, the result of our regression analysis demonstrated that the level of motor development of infants at 3 months old was positively correlated with the number of nerve structural connections between the cerebellum and thalamus. ID may lead to the reduction in motor-related neural connections, thus, affecting the level of motor development of premature infants in our cohort. The findings of both studies, one based on probabilistic fiber tracking and another by Andreasen's team, suggested that anemic infants with lower iron levels had reduced structural connection between the cerebellum and thalamus. This evidence helps us to explain why A-LF preterm infants have poorer motor performance compared with the NA-HF group. Although the locus coeruleus drives disinhibiting in the midline thalamus *via* a dopaminergic mechanism (Beas et al., 2018), the relationship between structural and functional connection remains controversial. Most studies believed that the decrement in structural connectivity is prior to the reduction in functional connectivity, as structural connectivity is the basis of functional connectivity (Hampton et al., 2017), while Betzel et al. (2014) and Bernard et al. (2016) found an increase in functional connection followed by a secondary alteration of structural connection. As previous researches indicated, the findings by Bernard may be related to the reconstruction of synapsis at young age and the compensation of monoamine metabolism (Paolicelli et al., 2011). The findings above support the importance of the detection with DTI to evaluate the network level of structural connection.

To improve the motor development of preterm infants affected by ID, many guidelines for daily iron supplementation were proposed. Although there were discrepancies of the recommended dosage and initiation time of routine iron supplementation on preterm infants among the following consultations, the overall consensus is reached that early iron supplementation can be beneficial to preterm infants. The American Academy of Pediatrics recommends that breast-fed and formula-fed premature infants should receive 2 and 1 mg/kg/day element iron, respectively, from the age

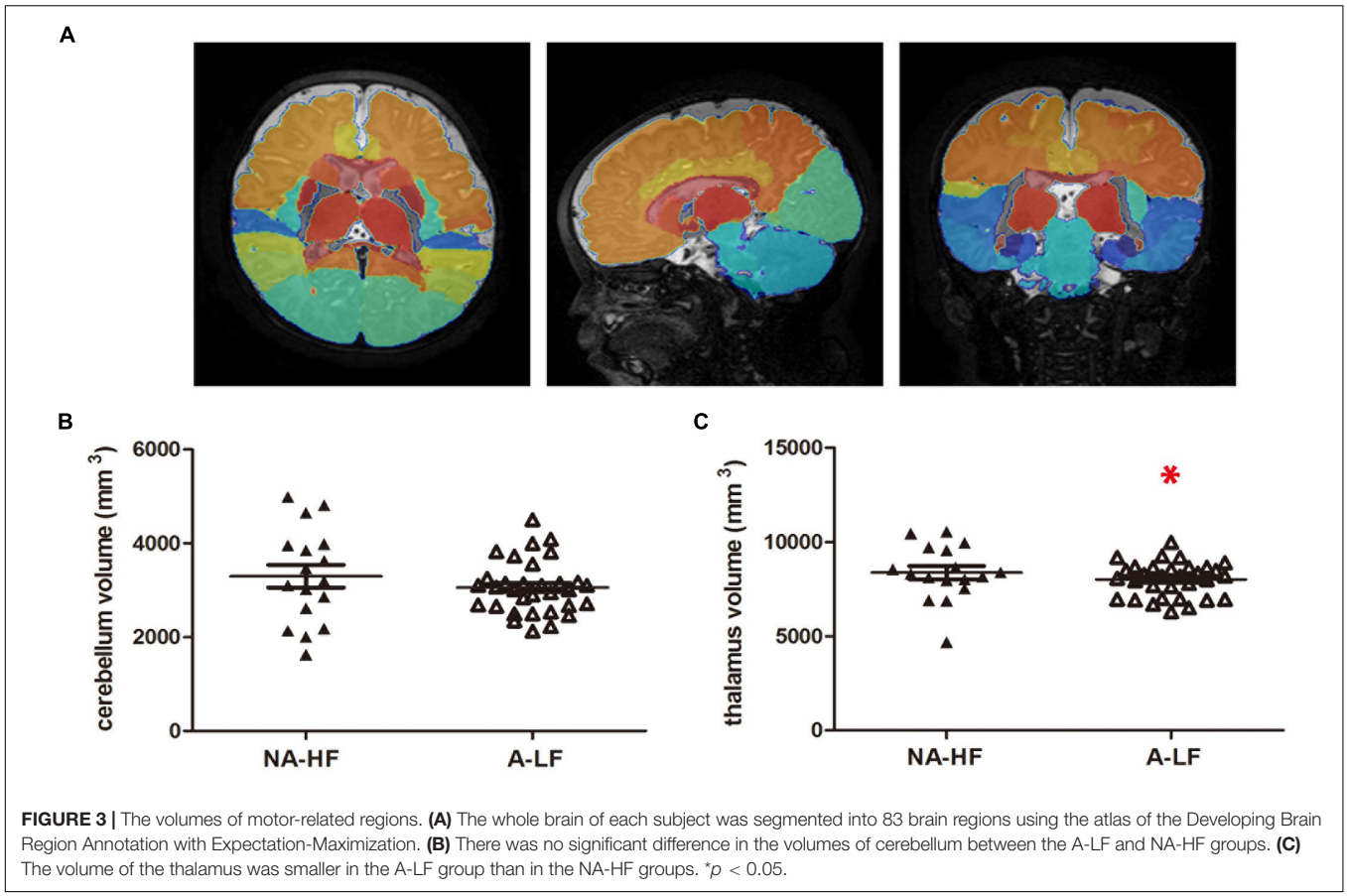

FIGURE 3 | The volumes of motor-related regions. **(A)** The whole brain of each subject was segmented into 83 brain regions using the atlas of the Developing Brain Region Annotation with Expectation-Maximization. **(B)** There was no significant difference in the volumes of cerebellum between the A-LF and NA-HF groups. **(C)** The volume of the thalamus was smaller in the A-LF group than in the NA-HF groups. *$p < 0.05$.

TABLE 3 | The number of fiber connectivity between motor related brain regions.

	NA-HF	A-LF	*p*-value
Precentral gyrus–cerebellum (ipsilateral)	1,572.6 [250.0]	1,751.9 [184.6]	0.568
Precentral gyrus–cerebellum (contralateral)	1,098.7 [175.1]	1,210.4 [143.3]	0.636
Precentral gyrus–striatum (ipsilateral)	1,032.2 [281.4]	900.0 [103.2]	0.664
Precentral gyrus–striatum (contralateral)	6 [1.2]	10.2 [2.1]	0.171
Cerebellum–thalamus (ipsilateral)	109.7 [23.8]	70.4 [6.6]	<0.05*
Cerebellum–thalamus (contralateral)	52.5 [19.6]	42.6 [5.1]	0.628
Cerebellum–striatum (ipsilateral)	94.8 [15.7]	91.1 [14.0]	0.869
Cerebellum–striatum (contralateral)	61.2 [18.3]	56.8 [10.0]	0.821

*Values are means ± SEM, n = 17 in NA-HF group/32 in A-LF group. *$p < 0.05$ indicates means with significant difference.*

of 1–12 months, and the European Society of Pediatric Gastroenterology and Nutrition and the Canadian Pediatric Society recommended a larger dose (Nutrition Committee, Canadian Paediatric Society, 1995; Rao and Georgieff, 2009). ID/IDA during pregnancy was associated with poorer motor development of the offspring, but iron supplementation during pregnancy has little effect on the impairment of motor function (Hernandez-Martinez et al., 2011; Tran et al., 2014). The optional time window of iron supplementation on neurodevelopment remains controversial. A longitudinal study from Costa Rica demonstrated that despite iron therapy in infancy, the motor development of infants with chronic ID was not improved over time (Shafir et al., 2006). However, a randomized controlled trial from Hebei of China demonstrated that iron supplementation during early infancy reduced the proportion of children in the lowest quartile of the locomotor subscale in the child, regardless of whether their mothers were receiving iron supplementation or not during pregnancy (Angulo-Barroso et al., 2016). Similar findings were also reported in another Chinese RCT cohort that iron supplementation from 6 weeks to 9 months had a positive effect on overall gross motor development at 9 months in term infants. These studies indicated the importance of iron supplementation in early infancy (Zhang et al., 2019). However, all of these studies only focused on term infants. Our study added the evidence of the significance of iron supplementation for premature infants that, similar to term infants, daily iron supplementation from early infancy can reverse the delayed motor development of preterm infants. However, whether we can maintain a more desirable iron level of preterm infants and improve their motor ability by long-term regular iron supplementation needs to be evaluated in the future.

Our study had some limitations and are as follows: First, the study was limited by a relatively small sample size, and there is a sample bias between the NA-HF and A-LF groups. It may

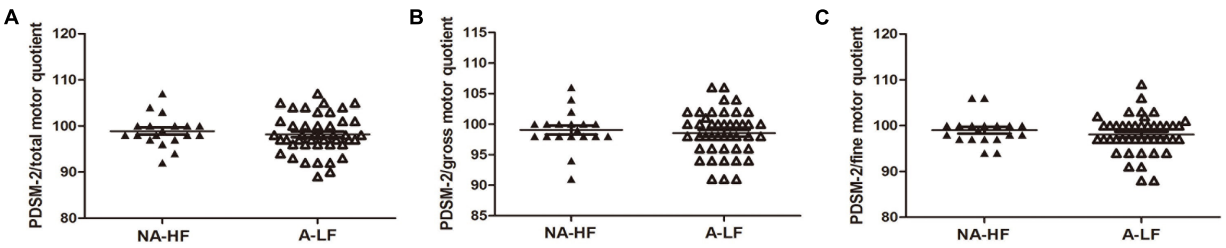

FIGURE 4 | The motor scores accessed by Peabody Developmental Motor Scales, second edition (PDMS-2) after iron supplementation at corrected age of 6 months old. **(A–C)** Although the mean of total motor quotient was slightly lower in A-LF group rather than NA-HF group, there was no significant difference in total motor quotients, gross motor quotients, and fine motor quotients between A-LF and NA-HF groups at this age.

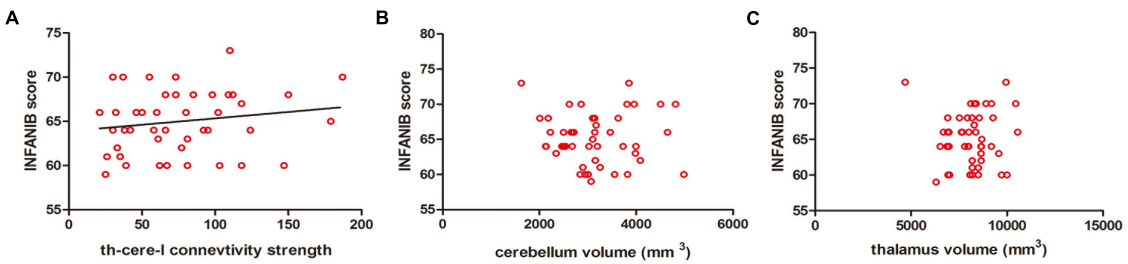

FIGURE 5 | Correlations between the motor scores of INFANIB and brain structural connectivity at 3 months old. **(A)** The structural connectivity between the cerebellum and ipsilateral thalamus was positively correlated with the scores of INFANIB at 3 months old. $r = 0.347$, $p < 0.05$. **(B,C)** The volume of the cerebellum and thalamus were not linearly related with the scores of INFANIB at this age. $r = 0.056$, $p = 0.930$/$r = 0.047$, $p = 0.951$. cere, cerebellum; th, thalamus; l, ipsilateral.

lead to a statistical bias. The sample size should be enlarged and balanced in future research. Second, considering ethical issues, we did not set up sub-groups without routine iron supplementation. A further well-designed study will help to better monitor the long-term effect of routine iron supplementation among preterm infants and to determine if our results can be generalized. Third, MRI scan including sequence for quantitative susceptibility mapping (QSM) as an indirect quantitative marker of brain iron and one more DTI detection at 6 months old of correct age will be needed to confirm the mechanism that the iron status of preterm infants is related to motor development *via* the decreased brain structural connectivity.

As a conclusion, in this study, we demonstrated that iron status of preterm infants is related to motor development, which is also related with the decreased connectivity between the cerebellum and ipsilateral thalamus. These neuroimaging outcomes together with the infantile iron status and motor abilities in our study provided evidence that structural connectivity assessed by diffusion MRI may serve as a biomarker to predict the motor development in ID preterm infants. Daily iron supplementation at an early age can reverse the delayed motor development in preterm infants with lower iron status.

DATA AVAILABILITY STATEMENT

The raw data supporting the conclusions of this article will be made available by the authors, without undue reservation.

ETHICS STATEMENT

The studies involving human participants were reviewed and approved by the Ethics Committee of the Children's Hospital, Zhejiang University School of Medicine. Written informed consent to participate in this study was provided by the participants' legal guardian/next of kin, for the publication of any potentially identifiable images or data included in this article.

AUTHOR CONTRIBUTIONS

ML: conceptualization and methodology. WX, WC, YL, and QZ: investigation and data curation. YL: writing and original draft preparation. TL, FG, and YY: visualization. CJ and JS: supervision, reviewing, and editing the manuscript. All authors contributed to the article and approved the submitted version.

FUNDING

This study was funded by the Natural Science Foundation of Zhejiang Province, China (LQ 19H260003), the Fundamental Research Funds for the Central Universities (2019FZA7010), the Medical Science and Technology Project of Zhejiang Province (2020385296 and 2021ky185), the National Natural Science Foundation of China (81273085 and 61801424), and the National Key Research and Development Program of China (2019YFC0840702).

ACKNOWLEDGMENTS

We would like to express our gratitude to the children whose ongoing participation made this follow-up possible. We also thank the team of the Key Laboratory for Biomedical Engineering of Ministry of Education, Zhejiang University, and the technicians from the Children's Hospital, Zhejiang University School of Medicine, for providing facilities to perform diffusion MRI studies during the course of this research.

REFERENCES

Andersson, J. L. R., and Sotiropoulos, S. N. (2016). An integrated approach to correction for off-resonance effects and subject movement in diffusion MR imaging. *Neuroimage* 125, 1063–1078. doi: 10.1016/j.neuroimage.2015.10.019

Angulo-Barroso, R. M., Li, M., Santos, D. C., Bian, Y., Sturza, J., Jiang, Y., et al. (2016). Iron supplementation in pregnancy or infancy and motor development: a randomized controlled trial. *Pediatrics* 137:e20153547. doi: 10.1542/peds.2015-3547

Basser, P. J., Mattiello, J., and LeBihan, D. (1994). MR diffusion tensor spectroscopy and imaging. *Biophys. J.* 66, 259–267. doi: 10.1016/S0006-3495(94)80775-1

Beard, J. (2007). Recent evidence from human and animal studies regarding iron status and infant development. *J. Nutr.* 137, 524S–530S. doi: 10.1093/jn/137.2.524S

Beard, J. L., and Connor, J. R. (2003). Iron status and neural functioning. *Annu. Rev. Nutr.* 23, 41–58. doi: 10.1146/annurev.nutr.23.020102.075739

Beas, B. S., Wright, B. J., Skirzewski, M., Leng, Y., Hyun, J. H., Koita, O., et al. (2018). The locus coeruleus drives disinhibition in the midline thalamus *via* a dopaminergic mechanism. *Nat. Neurosci.* 21, 963–973. doi: 10.1038/s41593-018-0167-4

Berglund, S. K., Chmielewska, A., Starnberg, J., Westrup, B., Hagglof, B., Norman, M., et al. (2018). Effects of iron supplementation of low-birth-weight infants on cognition and behavior at 7 years: a randomized controlled trial. *Pediatr. Res.* 83, 111–118. doi: 10.1038/pr.2017.235

Berglund, S. K., Westrup, B., Hagglof, B., Hernell, O., and Domellof, M. (2013). Effects of iron supplementation of LBW infants on cognition and behavior at 3 years. *Pediatrics* 131, 47–55. doi: 10.1542/peds.2012-0989

Bernard, J. A., Orr, J. M., and Mittal, V. A. (2016). Differential motor and prefrontal cerebello-cortical network development: evidence from multimodal neuroimaging. *Neuroimage* 124(Pt A), 591–601. doi: 10.1016/j.neuroimage.2015.09.022

Betzel, R. F., Byrge, L., He, Y., Goni, J., Zuo, X. N., and Sporns, O. (2014). Changes in structural and functional connectivity among resting-state networks across the human lifespan. *Neuroimage* 102(Pt 2), 345–357. doi: 10.1016/j.neuroimage.2014.07.067

Craig, B. T., Hilderley, A., Kinney-Lang, E., Long, X., Carlson, H. L., and Kirton, A. (2020). Developmental neuroplasticity of the white matter connectome in children with perinatal stroke. *Neurology* 95, e2476–e2486. doi: 10.1212/WNL.0000000000010669

DellaValle, D. M. (2013). Iron supplementation for female athletes: effects on iron status and performance outcomes. *Curr. Sports Med. Rep.* 12, 234–239. doi: 10.1249/JSR.0b013e31829a6f6b

Dimov, A., Patel, W., Yao, Y., Wang, Y., O'Halloran, R., and Kopell, B. H. (2019). Iron concentration linked to structural connectivity in the subthalamicnucleus: implications for deep brain stimulation. *J. Neurosurg.* 132, 197–204. doi: 10.3171/2018.8.JNS18531

Djamanakova, A., Faria, A. V., Hsu, J., Ceritoglu, C., Oishi, K., Miller, M. I., et al. (2013). Diffeomorphic brain mapping based on T1-weighted images: improvement of registration accuracy by multichannel mapping. *J. Magn. Reson. Imaging* 37, 76–84. doi: 10.1002/jmri.23790

Domellof, M. (2017). Meeting the iron needs of low and very low birth weight infants. *Ann. Nutr. Metab.* 71(Suppl. 3), 16–23. doi: 10.1159/000480741

Felt, B. T., and Lozoff, B. (1996). Brain iron and behavior of rats are not normalized by treatment of iron deficiency anemia during early development. *J. Nutr.* 126, 693–701. doi: 10.1093/jn/126.3.693

Felt, B. T., Beard, J. L., Schallert, T., Shao, J., Aldridge, J. W., Connor, J. R., et al. (2006). Persistent neurochemical and behavioral abnormalities in adulthood despite early iron supplementation for perinatal iron deficiency anemia in rats. *Behav. Brain Res.* 171, 261–270. doi: 10.1016/j.bbr.2006.04.001

Georgieff, M. K. (2017). Iron assessment to protect the developing brain. *Am. J. Clin. Nutr.* 106(Suppl. 6), 1588S–1593S. doi: 10.3945/ajcn.117.155846

Greminger, A. R., Lee, D. L., Shrager, P., and Mayer-Proschel, M. (2014). Gestational iron deficiency differentially alters the structure and function of white and gray matter brain regions of developing rats. *J. Nutr.* 144, 1058–1066. doi: 10.3945/jn.113.187732

Hampton, W. H., Alm, K. H., Venkatraman, V., Nugiel, T., and Olson, I. R. (2017). Dissociable frontostriatal white matter connectivity underlies reward and motor impulsivity. *Neuroimage* 150, 336–343. doi: 10.1016/j.neuroimage.2017.02.021

Hannah, J. R., and D'Cruz, D. P. (2019). Pulmonary complications of systemic lupus erythematosus. *Semin. Respir. Crit. Care Med.* 40, 227–234. doi: 10.1055/s-0039-1685537

Hernandez-Martinez, C., Canals, J., Aranda, N., Ribot, B., Escribano, J., and Arija, V. (2011). Effects of iron deficiency on neonatal behavior at different stages of pregnancy. *Early Hum. Dev.* 87, 165–169. doi: 10.1016/j.earlhumdev.2010.12.006

Huber, E., Patel, R., Hupp, M., Weiskopf, N., Chakravarty, M. M., and Freund, P. (2020). Extrapyramidal plasticity predicts recovery after spinal cord injury. *Sci. Rep.* 10:14102. doi: 10.1038/s41598-020-70805-5

Jenkinson, M., and Smith, S. (2001). A global optimisation method for robust affine registration of brain images. *Med. Image Anal.* 5, 143–156. doi: 10.1016/S1361-8415(01)00036-6

Jenkinson, M., Bannister, P., Brady, M., and Smith, S. (2002). Improved optimization for the robust and accurate linear registration and motion correction of brain images. *Neuroimage* 17, 825–841. doi: 10.1006/nimg.2002.1132

Lackmann, G. M., Schnieder, C., and Bohner, J. (1998). Gestational age-dependent reference values for iron and selected proteins of iron metabolism in serum of premature human neonates. *Biol. Neonate* 74, 208–213. doi: 10.1159/000014026

Leyshon, B. J., Radlowski, E. C., Mudd, A. T., Steelman, A. J., and Johnson, R. W. (2016). Postnatal iron deficiency alters brain development in piglets. *J. Nutr.* 146, 1420–1427. doi: 10.3945/jn.115.223636

Makropoulos, A., Gousias, I. S., Ledig, C., Aljabar, P., Serag, A., Hajnal, J. V., et al. (2014). Automatic whole brain MRI segmentation of the developing neonatal brain. *IEEE Trans. Med. Imaging* 33, 1818–1831. doi: 10.1109/TMI.2014.2322280

Makropoulos, A., Robinson, E. C., Schuh, A., Wright, R., Fitzgibbon, S., Bozek, J., et al. (2018). The developing human connectome project: a minimal processing pipeline for neonatal cortical surface reconstruction. *Neuroimage* 173, 88–112. doi: 10.1016/j.neuroimage.2018.01.054

McCarthy, E. K., Kenny, L. C., Hourihane, J. O. B., Irvine, A. D., Murray, D. M., and Kiely, M. E. (2017). Impact of maternal, antenatal and birth-associated factors on iron stores at birth: data from a prospective maternal-infant birth cohort. *Eur. J. Clin. Nutr.* 71, 782–787. doi: 10.1038/ejcn.2016.255

Miller, M. I., Christensen, G. E., Amit, Y., and Grenander, U. (1993). Mathematical textbook of deformable neuroanatomies. *Proc. Natl. Acad. Sci. U.S.A.* 90, 11944–11948. doi: 10.1073/pnas.90.24.11944

Mills, E., Dong, X. P., Wang, F., and Xu, H. (2010). Mechanisms of brain iron transport: insight into neurodegeneration and CNS disorders. *Future Med. Chem.* 2, 51–64. doi: 10.4155/fmc.09.140

Moreno-Fernandez, J., Ochoa, J. J., Latunde-Dada, G. O., and Diaz-Castro, J. (2019). Iron deficiency and iron homeostasis in low birth weight preterm infants: a systematic review. *Nutrients* 11:1090. doi: 10.3390/nu11051090

Mudd, A. T., Fil, J. E., Knight, L. C., Lam, F., Liang, Z. P., and Dilger, R. N. (2018). Early-life iron deficiency reduces brain iron content and alters brain tissue composition despite iron repletion: a neuroimaging assessment. *Nutrients* 10:135. doi: 10.3390/nu10020135

Niendam, T. A., Laird, A. R., Ray, K. L., Dean, Y. M., Glahn, D. C., and Carter, C. S. (2012). Meta-analytic evidence for a superordinate cognitive control network subserving diverse executive functions. *Cogn. Affect. Behav. Neurosci.* 12, 241–268. doi: 10.3758/s13415-011-0083-5

Nutrition Committee, Canadian Paediatric Society. (1995). Nutrient needs and feeding of premature infants. *CMAJ* 152, 1765–1785.

Paolicelli, R. C., Bolasco, G., Pagani, F., Maggi, L., Scianni, M., Panzanelli, P., et al. (2011). Synaptic pruning by microglia is necessary for normal brain development. *Science* 333, 1456–1458. doi: 10.1126/science.1202529

Rao, R., and Georgieff, M. K. (2009). Iron therapy for preterm infants. *Clin. Perinatol.* 36, 27–42. doi: 10.1016/j.clp.2008.09.013

Shafir, T., Angulo-Barroso, R., Calatroni, A., Jimenez, E., and Lozoff, B. (2006). Effects of iron deficiency in infancy on patterns of motor development over time. *Hum. Mov. Sci.* 25, 821–838. doi: 10.1016/j.humov.2006.06.006

Shafir, T., Angulo-Barroso, R., Jing, Y., Angelilli, M. L., Jacobson, S. W., and Lozoff, B. (2008). Iron deficiency and infant motor development. *Early Hum. Dev.* 84, 479–485. doi: 10.1016/j.earlhumdev.2007.12.009

Smith, S. M. (2002). Fast robust automated brain extraction. *Hum. Brain Mapp.* 17, 143–155. doi: 10.1002/hbm.10062

Todorich, B., Pasquini, J. M., Garcia, C. I., Paez, P. M., and Connor, J. R. (2009). Oligodendrocytes and myelination: the role of iron. *Glia* 57, 467–478. doi: 10.1002/glia.20784

Tran, T. D., Tran, T., Simpson, J. A., Tran, H. T., Nguyen, T. T., Hanieh, S., et al. (2014). Infant motor development in rural Vietnam and intrauterine exposures to anaemia, iron deficiency and common mental disorders: a prospective community-based study. *BMC Pregnancy Childbirth* 14:8. doi: 10.1186/1471-2393-14-8

Tustison, N. J., Avants, B. B., Cook, P. A., Zheng, Y., Egan, A., Yushkevich, P. A., et al. (2010). N4ITK: improved N3 bias correction. *IEEE Trans. Med. Imaging* 29, 1310–1320. doi: 10.1109/TMI.2010.2046908

Wang, D., and Liu, X. (2016). [Recommendations for feeding preterm or low birth weight infants after hospital discharge]. *Zhonghua Er Ke Za Zhi* 54, 6–12.

Zamora, T. G., Guiang, S. F. III, Widness, J. A., and Georgieff, M. K. (2016). Iron is prioritized to red blood cells over the brain in phlebotomized anemic newborn lambs. *Pediatr. Res.* 79, 922–928. doi: 10.1038/pr.2016.20

Zhang, Y. L., Zheng, S. S., Zhu, L. Y., Ji, C., Angulo-Barroso, R. M., Lozoff, B., et al. (2019). [Impact of iron deficiency in early life stages on children's motor development: a longitudinal follow-up]. *Zhonghua Er Ke Za Zhi* 57, 194–199.

Conflict of Interest: The authors declare that the research was conducted in the absence of any commercial or financial relationships that could be construed as a potential conflict of interest.

Publisher's Note: All claims expressed in this article are solely those of the authors and do not necessarily represent those of their affiliated organizations, or those of the publisher, the editors and the reviewers. Any product that may be evaluated in this article, or claim that may be made by its manufacturer, is not guaranteed or endorsed by the publisher.

frontiers | Frontiers in Neuroscience

ORIGINAL RESEARCH
published: 12 May 2022
doi: 10.3389/fnins.2022.886083

Quantification of Intracranial Structures Volume in Fetuses Using 3-D Volumetric MRI: Normal Values at 19 to 37 Weeks' Gestation

Jing-Ya Ren[1], *Ming Zhu*[1], *Guanghai Wang*[2,3,4,5], *Yiding Gui*[2,3,4,5], *Fan Jiang*[2,3,4,5] *and Su-Zhen Dong*[1]*

[1] Department of Radiology, Shanghai Children's Medical Center, School of Medicine, Shanghai Jiao Tong University, Shanghai, China, [2] Pediatric Translational Medicine Institution, Shanghai Children's Medical Center, School of Medicine, Shanghai Jiao Tong University, Shanghai, China, [3] Department of Developmental and Behavioral Pediatrics, Shanghai Children's Medical Center, School of Medicine, Shanghai Jiao Tong University, Shanghai, China, [4] MOE-Shanghai Key Laboratory of Children's Environmental Health, School of Medicine, Xinhua Hospital, Shanghai Jiao Tong University, Shanghai, China, [5] Shanghai Center for Brain Science and Brain-Inspired Technology, Shanghai, China

OPEN ACCESS

Edited by:
Dan Wu,
Zhejiang University, China

Reviewed by:
Yao Wu,
Children's National Hospital, United States
Guangbin Wang,
Shandong Provincial Hospital Affiliated to Shandong First Medical Hospital, China

***Correspondence:**
Su-Zhen Dong
dongsuzhen@126.com

Specialty section:
This article was submitted to Neurodevelopment, a section of the journal Frontiers in Neuroscience

Received: 28 February 2022
Accepted: 11 April 2022
Published: 12 May 2022

Citation:
Ren J-Y, Zhu M, Wang G-H, Gui Y-D, Jiang F and Dong S-Z (2022) Quantification of Intracranial Structures Volume in Fetuses Using 3-D Volumetric MRI: Normal Values at 19 to 37 Weeks' Gestation. Front. Neurosci. 16:886083. doi: 10.3389/fnins.2022.886083

Objective: The purpose of this study is to establish a reference of intracranial structure volumes in normal fetuses ranging from 19 to 37 weeks' gestation (mean 27 weeks).

Materials and Methods: A retrospective analysis of 188 MRI examinations (1.5 T) of fetuses with a normal brain appearance (19–37 gestational weeks) from January 2018 to December 2021 was included in this study. Three dimensional (3-D) volumetric parameters from slice-to-volume reconstructed (SVR) images, such as total brain volume (TBV), cortical gray matter volume (GMV), subcortical brain tissue volume (SBV), intracranial cavity volume (ICV), lateral ventricles volume (VV), cerebellum volume (CBV), brainstem volume (BM), and extra-cerebrospinal fluid volume (e-CSFV), were quantified by manual segmentation from two experts. The mean, SD, minimum, maximum, median, and 25th and 75th quartiles for intracranial structures volume were calculated per gestational week. A linear regression analysis was used to determine the gestational weekly age-related change adjusted for sex. A *t*-test was used to compare the mean TBV and ICV values to previously reported values at each gestational week. The formulas to calculate intracranial structures volume derived from our data were created using a regression model. In addition, we compared the predicted mean TBV values derived by our formula with the expected mean TBV predicted by the previously reported Jarvis' formula at each time point. For intracranial volumes, the intraclass correlation coefficient (ICC) was calculated to convey association within and between observers.

Results: The intracranial volume data are shown in graphs and tabular summaries. The male fetuses had significantly larger VV compared with female fetuses ($p = 0.01$). Measured mean ICV values at 19 weeks are significantly different from those published in the literature ($p < 0.05$). Means were compared with the expected TBV generated by the previously reported formula, showing statistically differences at 22, 26, 29, and 30 weeks' gestational age (GA) (all $p < 0.05$). A comparison between our data-derived formula and the previously reported formula for TBV showed very similar values at every GA. The

predicted TBV means derived from the previously reported formula were all within the 95% confidence interval (*CI*) of the predicted means of this study. Intra- and inter-observer agreement was high, with an intraclass correlation coefficient larger than 0.98.

Conclusion: We have shown that the intracranial structural volume of the fetal brain can be reliably quantified using 3-D volumetric MRI with a high degree of reproducibility and reinforces the existing data with more robust data in the earlier second and third stages of pregnancy.

Keywords: fetal brain development, magnetic resonance imaging, three dimensional volumetric, prenatal diagnosis, image processing

INTRODUCTION

Currently, ultrasound (US) biometry is the reference standard for assessing fetal brain development (Griffiths et al., 2017). With regard to the central nervous system (CNS), indirect indicators of fetal brain development are used routinely by measurement of two-dimensional (2-D) parameters (De Oliveira Júnior et al., 2021), such as biparietal diameter (BPD) and head circumference (HC) (Ruiz et al., 2017; Kline-Fath, 2019; Sibbald et al., 2021). However, BPD and HC can only be compared with the size of the head, including the skull, and the sizes of the brain and detailed study of different intracranial structures cannot be performed (Fried et al., 2021).

Although US has been the primary imaging method for prenatal screening for fetal brain anomalies, fetal MRI has become a useful supplemental imaging tool. Fetal MRI has been useful in evaluating abnormalities of fetal structures which are difficult to thoroughly evaluate by prenatal US alone, with obvious advantages over US in displaying neurological maturation and abnormalities (Grossman et al., 2006; Ruiz et al., 2017). The use of three-dimensional (3-D) volumetric *in utero* MRI is a relatively newer modality and allows more accurate measurement of intracranial structure volumes, which can more accurately reflect the growth of the fetal brain than 2-D parameters (Blondiaux and Garel, 2013; Jarvis and Griffiths, 2017; Kyriakopoulou et al., 2017; Takakuwa et al., 2021).

Although several existing studies (Clouchoux et al., 2012; Griffiths et al., 2019) have attempted to establish the normative MR data for intracranial compartment volume at varying gestational ages (GAs) as measured by fetal MRI, however, these have some limitations. Most studies had a relatively small GA range (Corbett-Detig et al., 2011; Clouchoux et al., 2012), as well as limited measurements of regional brain structures (Andescavage et al., 2017), thicker slice thickness of MRI scans (Gholipour et al., 2011). In our study, we aim to provide reference values for normal fetal intracranial structure volumes to reinforce existing data with more reliable normative data in the second and third stages of pregnancy. This is essential to understand the progression and timing of aberrant brain development and early detection of deviations from normal growth during this period.

Abbreviations: GA, Gestational age; 2D, Two-dimensional; 3D, Three-dimensional; ICV, Intracranial cavity volume; TBV, Total brain volume; VV, Lateral ventricles volume; CBV, Cerebellar volume; GMV, gray matter volume; SBV, subcortical brain volume; BM, Brainstem volume; E-CSFV, Extra-cerebrospinal fluid.

MATERIALS AND METHODS

Subjects

A retrospective study at our institution was performed. Fetal brain MRI databases spanning the years 2018–2021 in our medical center were searched for examinations performed between 18 and 38 weeks of gestation (median GA: 27 weeks). These data were from pregnant women who had been acquainted with the procedure and possible risks of fetal MRI and had given written informed consent to conduct prenatal studies before the examination. This study protocol was authorized by the review board of our medical hospital. All methods of the study were performed in accordance with the relevant guidelines and regulations.

We created a normative database by scanning low-risk pregnant women who were enrolled in our control cohort group. Inclusion criteria: women who had a previous child with a confirmed abnormality or US query of non-CNS mild abnormalities without brain abnormalities seen on fetal MRI. Fetal age was based on the first day of the last normal menstrual period and confirmed by a first-trimester US scan.

Exclusion criteria: twin or multiple pregnancies, fetal malformation or chromosomal abnormalities, associated arrhythmias, perinatal infections, fetal anemia, and maternal conditions that may affect fetal hemodynamics, such as thyroid disease, pregestational diabetes, and pre-eclampsia. The malformation of non-CNS that may be affect CNS development can also be excluded. Excessive fetal motion artifact prevents the acquisition of three orthogonal planes for reconstruction and measurement.

MRI Protocol and Analysis

All fetal MRI scans were performed using a Philips Achieva 1.5 T MRI scanner and a 16-channel sense-xl-torso coil (Philips Healthcare). Pregnant women were in the supine or the left-sided position. No maternal or fetal sedation was used during the MR imaging examinations. First, localizer images were acquired to determine the location of the fetal head. The following parameters were used for the single-shot fast spin-echo (SSFSE) sequence: TR/TE: 12,000/80 ms, matrix: 236 × 220, flip angle: 90 degrees, field of view: 260–355 mm^2, and slice thickness: 2 mm

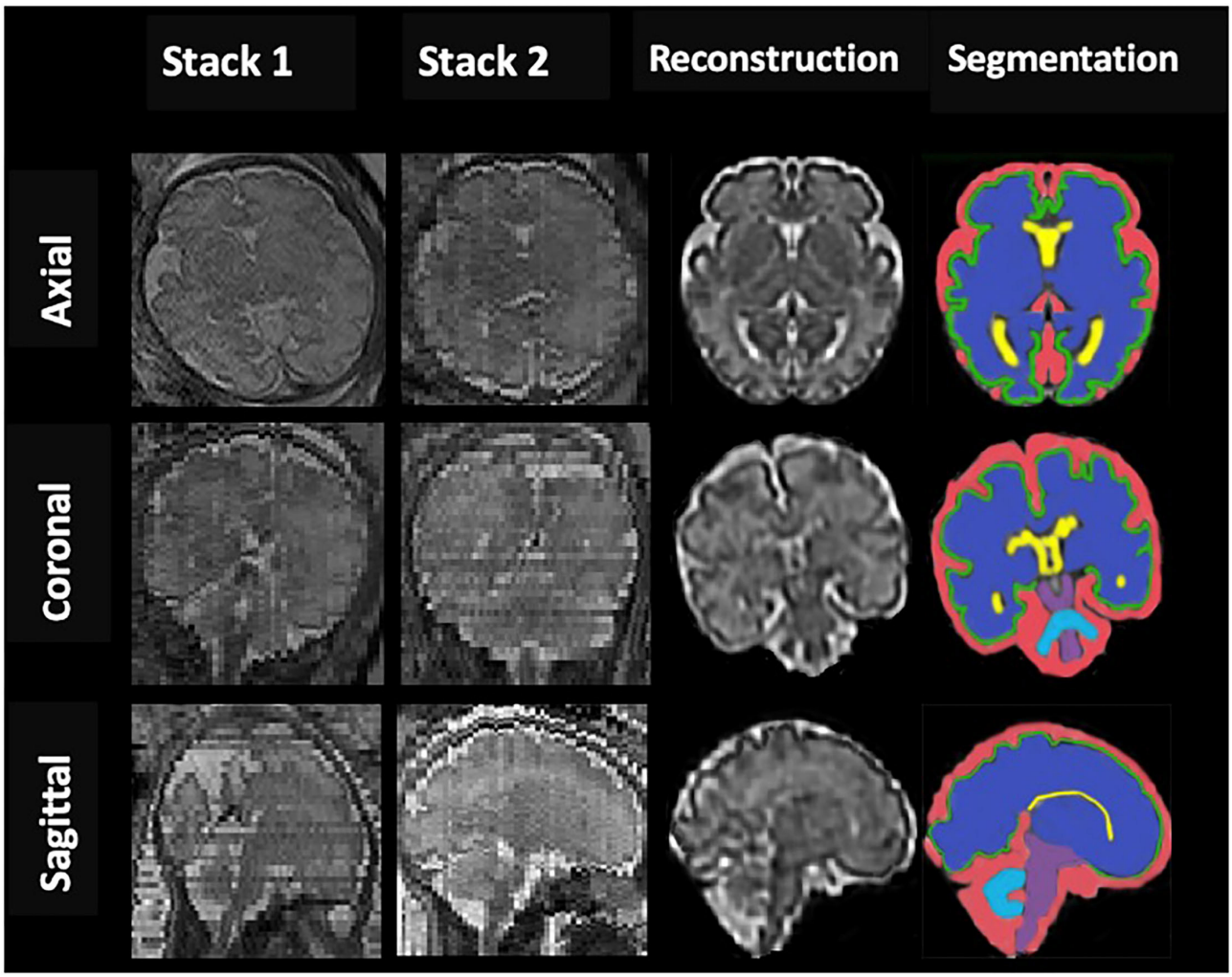

FIGURE 1 | An example of fetal brain reconstruction from two dimensional (2D) single-shot fast spin-echo (SSFSE) MRI slices of axial, sagittal, and coronal planes (Stack1; 2) to a single three dimensional (3D) reconstruction volumetric image (reconstruction column); 3D reconstructed brain of a normal control fetus at 32 gestational weeks with manual 3D segmentations of supratentorial brain tissue, lateral ventricles, cortex, cerebellum, brainstem (BM), and extra-cerebrospinal fluid volume (eCSF) (segmentation column).

with 0-mm spacing. The scan time of SSFSE sequence was 15–45 s. The repeat data acquisition or breath-holding of pregnant women at the end of expiration or both was used to reduce motion artifacts to improve the success of the SSTSE sequence.

MRI Processing and Segmentation

The post-acquisition processing was performed using the Linux workstation. The acquired data were converted from DICOM (Digital Imaging and Communications in Medicine) to NIfTI (Neuroimaging Informatics Technology Initiative) format with MATLAB (The MathWorks Inc, Natik, MA) and DCM2NII software (version 12.12.2012). For each subject, a single 3D motion-corrected high-resolution brain volume was reconstructed from the 2D SSTSE imaging stacks using a slice-to-volume reconstruction (SVR) method (Jiang et al., 2007; Gholipour et al., 2011). First, we used an atlas-based method to extract a mask of the brain by defining a region of interest (ROI) from surrounding fetal and maternal tissue in each of the 3 principal planes, namely, sagittal, coronal, and axial. Second, images were processed using the non-parametric non-uniform intensity normalization algorithm to correct for intensity inhomogeneity to get a consistent, spatially invariant, signal intensity distribution for each brain tissue. After that, the high-resolution isotropic reconstructed 3D volumetric images with the resolution of $0.5 \times 0.5 \times 0.5$ mm were reconstructed from the registered low resolution and motion-corrupted 2D slices by using the Gauss–Seidel and super-resolution reconstruction method (Gholipour et al., 2010; Askin Incebacak et al., 2022) (**Figure 1**).

Coronal slices were segmented manually by editing using ITK-SNAP software (version3.8, http://www.itksnap.org/) to volumetric measure in intracranial cavity volume (ICV), total

brain volume (TBV), lateral ventricles volume (VV), and extra-cerebrospinal fluid (e-CSFV). Besides, based on the created label-maps, gray matter (GMV), subcortical brain (SBV), cerebellar (CBV), and brainstem (BM) volumes were determined, and total brain (TBV = GMV + SBV+CBV+BM) and intracranial cavity (ICV=TBV+VV+ e-CSFV) volumes were calculated. All intracranial CSF spaces surrounding the supratentorial brain structures and infratentorial regions were included in E-CSF but not any ventricular tissue. Lateral ventricles volume represented the volume of left and right lateral ventricles. Volumes were determined by multiplying the voxel count by the number of voxels in the segmentation and converting to cubic centimeters (**Figure 1**). Raters were blinded to the patient's identity and gestation for all subjects.

The relative growth rate represents the percentage volume gain relative to the average volume for each intracranial structure and was calculated using the formula (Hoffmann and Poorter, 2002): $[(\ln V2 - \ln V1)/(GA2 - GA1)] \times 100$, where ln is the natural logarithm, GA1and GA2 are the gestational weeks at a given GA range, and V1 and V2 are the average volumes of different intracranial structures corresponding to GA1 and GA2 at the time point, respectively.

Statistical Analysis

Statistical analysis was performed using SPSS 22.0 software. The mean, SD, minimum, maximum, median, and 25th and 75th quartiles were calculated for the measured volumes of TBV, GMV, SBV, ICV, e-CSFV, VV, CBV, and BM at each GA and presented in tabulated form. A *t*-test was used to compare our mean TBV and ICV to previously reported values (Jarvis et al., 2016, 2019). Scatter plots were drawn according to the segmented volumes against GA and adjusted for sex, then a quadratic line showed the best fit for TBV, GMV, SBV, ICV, e-CSFV, VV, CBV, and BM with 95% confidence intervals (*CI*s). Then, the new formulas to calculate intracranial structures derived from our data were created. Jarvis' formula for calculating fetal TBV was derived from a fitting standard curve ($TBV = 0.53\ GA^2 - 13.33\ GA + 89.69$ [$R^2 = 0.97$]). Subsequently, student's *t*-tests analysis was performed to compare the predicted mean TBV values at each GA derived by our formula with the expected mean TBV predicted by the Jarvis' formula. About 30% of scans were randomly selected and were corrected by the same observer and another observer. For intracranial volumes, the intraclass correlation coefficient (ICC) was calculated to convey association within and between observers. The values of p were considered statistically significant when <0.05.

RESULTS

Fetal brain MRI data were collected from 700 singleton pregnancy fetuses at a GA between 18 and 38 weeks. After excluding 512 normal fetal brain data with noticeable motion artifacts that resulted in low-quality data and gross errors in segmentation, a total of 188 normal fetal brains (97 female

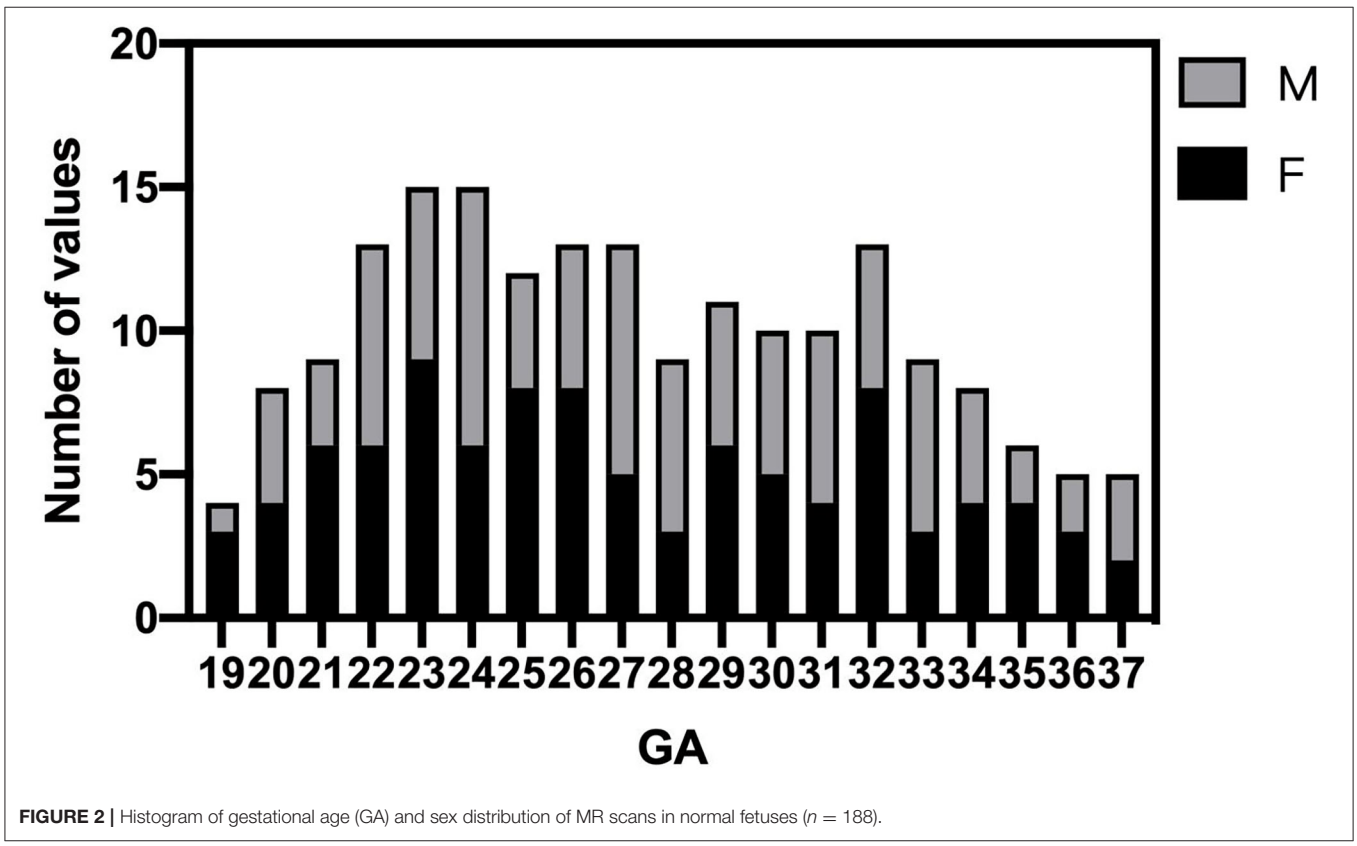

FIGURE 2 | Histogram of gestational age (GA) and sex distribution of MR scans in normal fetuses ($n = 188$).

TABLE 1 | The tabular summaries of min, max, mean, 25th, 50th, and 75th centiles of **(A)** TBV, **(B)** ICV, **(C)** GMV, **(D)** SBV, **(E)** e-CSFV, **(F)** VV, **(G)** CBV, and **(H)** BM.

			A:TBV(ml)				
GA	**Min**	**25th**	**50th**	**75th**	**Max**	**Mean**	**SD**
37	305.00	307.50	318.00	325.80	331.60	316.90	10.20
36	280.80	285.10	293.00	303.40	306.80	294.00	9.97
35	244.10	249.30	260.60	269.70	278.80	260.30	12.11
34	228.50	229.10	234.00	245.10	250.80	236.90	8.87
33	196.50	202.40	210.50	220.10	231.90	212.10	11.10
32	180.90	190.80	196.70	200.70	208.60	197.80	6.43
31	165.20	175.40	184.30	189.40	192.40	182.00	8.92
30	166.50	170.00	176.70	180.80	184.90	175.60	6.09
29	140.00	156.90	166.90	175.60	178.70	164.10	11.55
28	122.30	131.90	138.00	152.20	157.10	140.80	11.65
27	107.00	114.6	124.30	130.50	140.80	122.30	10.18
26	82.42	88.75	92.00	93.92	97.00	91.10	4.04
25	76.00	80.38	83.69	86.42	88.00	83.17	3.80
24	64.82	68.42	74.46	80.10	88.90	74.98	6.60
23	58.58	61.48	65.81	67.21	72.80	64.98	3.78
22	51.42	53.32	55.90	58.59	61.62	56.08	3.66
21	40.11	42.05	47.00	51.35	57.41	47.28	5.63
20	33.10	35.33	37.95	39.75	41.90	37.63	2.87
19	26.80	27.25	29.00	31.73	32.50	29.33	2.38
			B:ICV (ml)				
GA	**Min**	**25th**	**50th**	**75th**	**Max**	**Mean**	**SD**
37	480.00	480.20	493.30	502.80	505.50	491.80	11.47
36	448.80	449.60	463.60	468.50	470.00	460.00	9.74
35	384.50	410.40	432.40	443.30	451.10	426.70	23.28
34	367.50	376.40	387.50	398.30	402.70	386.60	12.09
33	330.60	333.70	345.50	354.20	358.00	344.50	10.24
32	308.90	321.50	330.20	336.30	340.40	328.80	9.25
31	283.60	296.00	308.50	312.30	324.00	304.70	12.19
30	278.90	287.70	306.50	317.00	319.60	302.50	15.51
29	256.00	266.70	274.40	289.00	301.00	277.50	13.94
28	225.60	234.10	246.10	260.60	269.70	246.80	15.27
27	187.50	196.90	212.80	235.50	253.40	215.50	21.33
26	157.60	167.50	176.00	183.00	189.00	175.40	9.45
25	143.70	149.60	158.30	167.00	173.10	158.50	9.53
24	122.20	128.70	139.50	147.50	160.10	141.50	12.11
23	112.50	118.70	123.50	135.60	140.60	125.70	9.34
22	94.00	98.64	106.90	119.60	128.40	109.30	11.90
21	79.26	80.78	86.00	91.36	95.60	86.40	5.65
20	73.50	74.99	76.89	78.23	80.00	76.74	2.13
19	65.70	66.53	69.75	72.38	73.00	69.55	3.05
			C:GMV (ml)				
GA	**Min**	**25th**	**50th**	**75th**	**Max**	**Mean**	**SD**
36	80.80	81.40	83.40	86.80	89.10	83.96	3.20
36	68.67	72.78	79.58	80.57	81.00	77.26	5.04

(Continued)

TABLE 1 | Continued

			C:GMV (ml)				
GA	**Min**	**25th**	**50th**	**75th**	**Max**	**Mean**	**SD**
35	60.00	61.56	64.79	69.39	70.89	65.24	4.23
34	52.35	55.10	58.77	61.29	63.49	58.23	3.70
33	42.86	44.64	47.50	50.18	54.79	47.84	3.68
32	39.87	41.74	45.67	49.61	52.38	45.78	4.14
31	37.65	39.13	40.34	42.42	46.33	40.95	2.53
30	34.23	36.49	39.00	43.26	45.69	39.71	3.76
29	27.00	29.60	32.06	37.72	40.00	33.44	4.44
28	26.22	28.19	29.00	32.49	34.09	29.98	2.66
27	20.18	23.46	24.60	25.75	26.91	24.31	1.81
26	16.69	17.90	18.00	19.40	20.68	18.47	1.18
25	15.45	16.09	17.00	17.50	18.66	16.96	0.96
24	13.46	14.78	15.59	16.09	17.03	15.42	0.97
23	12.24	13.00	13.54	14.35	15.01	13.63	0.88
22	10.77	11.52	12.03	12.74	13.02	12.05	0.68
21	8.14	9.23	10.00	10.66	11.89	9.99	1.08
20	6.55	6.99	7.23	7.70	8.00	7.28	0.48
19	6.00	6.12	6.63	6.95	7.00	6.57	0.43
			D:SBV (ml)				
GA	**Min**	**25th**	**50th**	**75th**	**Max**	**Mean**	**SD**
37	194.50	196.90	210.40	215.60	220.40	207.10	10.27
36	185.20	186.30	190.00	201.90	207.30	193.30	8.88
35	165.80	167.30	176.10	182.00	186.30	175.50	7.95
34	153.10	156.10	160.70	165.90	176.70	162.10	7.39
33	138.50	142.60	148.50	156.00	167.80	150.00	9.27
32	119.10	131.90	135.20	140.40	152.70	137.70	8.89
31	114.60	124.40	130.10	135.20	139.30	129.30	7.60
30	112.50	120.50	125.90	130.60	133.10	124.90	6.29
29	102.10	110.3	125.00	128.80	139.90	120.80	11.43
28	75.39	90.15	99.42	111.33	115.81	99.43	12.54
27	78.99	82.77	89.91	99.20	107.40	91.02	9.20
26	57.46	66.33	67.93	69.23	71.80	67.15	3.62
25	54.20	59.63	61.87	64.58	66.53	61.39	3.93
24	43.96	50.99	54.96	59.01	67.84	55.35	5.97
23	42.56	44.29	48.37	49.67	56.00	47.59	3.72
22	37.11	38.88	40.95	43.08	45.96	40.96	2.68
21	25.96	30.39	34.22	38.64	42.30	34.40	5.11
20	24.44	25.68	28.34	29.74	31.20	27.93	2.30
19	18.88	19.05	20.18	22.72	23.36	20.65	1.98
			E:e-CSFV (ml)				
GA	**Min**	**25th**	**50th**	**75th**	**Max**	**Mean**	**SD**
36	152.90	156.00	161.00	178.70	192.00	166.10	15.17
36	135.30	148.70	162.60	166.20	166.20	158.50	13.08
35	138.00	149.30	165.00	178.50	186.10	164.10	17.51
34	134.00	150.20	161.30	171.70	182.10	160.40	16.00
33	96.56	115.80	132.10	140.80	150.10	128.00	16.53
32	112.00	120.90	130.10	138.40	145.60	129.60	10.68

(Continued)

TABLE 1 | Continued

			E:e-CSFV (ml)				
GA	**Min**	**25th**	**50th**	**75th**	**Max**	**Mean**	**SD**
31	92.73	114.30	123.00	127.00	130.80	119.50	11.20
30	90.00	105.50	128.80	138.30	147.20	124.10	18.73
29	73.30	98.46	107.00	137.40	139.10	110.70	20.53
28	89.17	95.01	98.22	113.20	116.60	103.10	10.13
27	64.20	73.72	87.17	103.80	131.50	90.38	21.36
26	66.74	73.86	84.22	87.42	93.22	81.57	8.24
25	54.55	61.74	74.59	83.18	88.48	72.38	11.33
24	43.36	55.07	63.36	75.44	88.27	63.76	12.21
23	44.22	53.94	57.72	65.25	68.09	57.23	7.42
22	33.00	39.81	47.74	62.15	64.28	50.17	11.28
21	25.52	34.68	37.90	42.36	44.99	37.60	5.85
20	36.02	36.47	37.08	37.96	39.46	37.32	1.09
19	36.80	37.05	38.35	39.05	39.10	38.15	1.07
			F:VV (ml)				
GA	**Min**	**25th**	**50th**	**75th**	**Max**	**Mean**	**SD**
37	8.00	8.25	9.00	9.40	9.50	8.86	0.61
36	6.66	6.83	7.80	8.05	8.10	7.51	0.64
35	3.04	4.84	6.32	6.99	7.84	5.94	1.64
34	3.00	4.00	5.25	6.13	7.13	5.11	1.42
33	2.14	3.50	4.13	5.24	6.20	4.34	1.24
32	1.69	2.53	3.46	4.55	5.53	3.50	1.22
31	1.99	2.34	3.15	3.90	5.00	3.20	0.95
30	1.58	2.00	2.82	3.17	4.00	2.70	0.72
29	2.00	2.00	2.24	3.79	4.00	2.73	0.85
28	1.78	2.47	2.75	3.41	4.83	2.98	0.89
27	1.15	2.32	3.00	3.69	4.00	2.90	0.92
26	1.86	2.00	2.34	3.60	4.14	2.74	0.86
25	1.50	2.43	2.85	3.74	4.34	2.97	0.82
24	1.13	2.08	2.56	3.76	4.29	2.73	0.93
23	1.70	2.64	3.32	4.00	4.60	3.29	0.84
22	2.07	218	3.20	3.51	4.64	3.05	0.79
21	1.00	1.17	1.50	1.84	2.34	1.53	0.43
20	1.00	1.03	1.77	2.51	3.00	1.80	0.77
19	1.60	1.65	1.95	2.63	2.80	2.08	0.53
			G:CBV (ml)				
GA	**Min**	**25th**	**50th**	**75th**	**Max**	**Mean**	**SD**
37	17.96	18.23	18.78	19.45	19.45	18.83	0.64
36	16.98	17.35	17.82	18.13	18.26	17.76	0.48
35	11.95	13.59	15.00	17.07	17.72	15.14	2.00
34	11.28	11.31	12.69	14.11	14.25	12.71	1.32
33	8.45	9.48	10.20	10.94	15.10	10.49	1.91
32	9.11	9.57	10.00	11.21	12.44	10.43	0.99
31	6.63	7.39	8.34	9.18	10.00	8.32	1.09
30	6.45	6.94	7.58	8.02	9.00	7.54	0.76
29	6.00	6.30	6.72	7.00	7.77	6.75	0.54
28	4.45	4.99	5.84	5.98	6.75	5.63	0.70

(Continued)

TABLE 1 | Continued

			G:CBV (ml)				
GA	**Min**	**25th**	**50th**	**75th**	**Max**	**Mean**	**SD**
27	3.40	3.87	4.50	4.89	6.00	4.50	0.77
26	2.52	2.96	3.74	4.10	4.67	3.58	0.70
25	2.47	2.67	3.11	3.73	4.03	3.15	0.55
24	2.05	2.20	2.64	2.82	3.69	2.64	0.49
23	2.10	2.22	2.47	2.54	2.82	2.41	0.22
22	1.25	1.51	1.72	2.20	2.67	1.84	0.43
21	1.35	1.56	1.80	2.14	2.47	1.85	0.36
20	1.25	1.36	1.49	1.69	2.00	1.54	0.24
19	1.16	1.18	1.34	1.45	1.45	1.32	0.15
			H:BM (ml)				
GA	**Min**	**25th**	**50th**	**75th**	**Max**	**Mean**	**SD**
37	6.60	6.70	7.00	7.48	7.66	7.07	0.42
36	4.40	5.04	5.98	6.22	6.27	5.70	0.76
35	4.30	4.45	4.89	5.29	5.57	4.89	0.46
34	3.37	3.55	3.95	4.12	4.15	3.87	0.30
33	2.91	3.51	3.76	4.23	4.71	3.83	0.53
32	3.00	3.61	3.87	4.00	4.15	3.79	0.32
31	2.79	3.16	3.54	3.98	4.00	3.54	0.42
30	2.70	3.14	3.62	3.73	4.05	3.49	0.41
29	2.50	2.88	3.00	3.36	3.70	3.09	0.35
28	2.14	2.50	3.12	3.75	4.00	3.14	0.67
27	1.76	1.94	2.40	2.85	3.40	2.42	0.52
26	1.35	1.62	1.86	2.06	2.60	1.90	0.39
25	1.15	1.52	1.64	1.80	2.45	1.67	0.34
24	1.01	1.30	1.45	1.88	2.23	1.57	0.37
23	1.10	1.14	1.28	1.49	1.88	1.36	0.24
22	0.93	1.08	1.24	1.39	1.64	1.23	0.21
21	0.71	0.80	1.10	1.24	1.33	1.05	0.23
20	0.61	0.73	0.89	1.00	1.05	0.87	0.16
19	0.60	0.64	0.82	0.90	0.91	0.79	0.14

(A): TBV, total brain volume; (B): ICV, intracranial cavity volume; (C): GMV, gray matter volume; (D): SBV, subcortical brain volume; VV, and (E): e-CSFV, extra-cerebrospinal fluid; (F) VV, lateral ventricles volume; (G): CBV, cerebellar volume; (H): BM, brainstem volume.

fetuses/91 male fetuses) were analyzed between 19 and 37 GA. The GA of the fetuses ranged from 19 to 37 weeks (mean, 27.4 ± 4.8 weeks) is shown in **Figure 2**. Intra- and inter-observer agreement for supratentorial brain structures and infratentorial regions was high, with ICCs all larger than 0.98.

The tabular summaries of mean, SD, minimum, maximum, median, and 25th and 75th quartiles from the base data of TBV, GMV, SBV, ICV, e-CSFV, VV, CBV, and BM for fetuses between 19 and 37 GA are shown in **Tables 1A–H**. All volumetric measurements had significant positive correlations with GA and the quadratic lines for *CI*'s for each GA determined by the best regression fit for each structure are shown in **Figure 3**. Our measured volumes data were used to derive a best-fit formula, TBV = $0.45GA^2$-9.57GA + 47.41(R^2 = 0.98); ICV = $0.46GA^2$ – 2.10GA – 69.30 (R^2 = 0.98); GMV = $0.21GA^2$ –

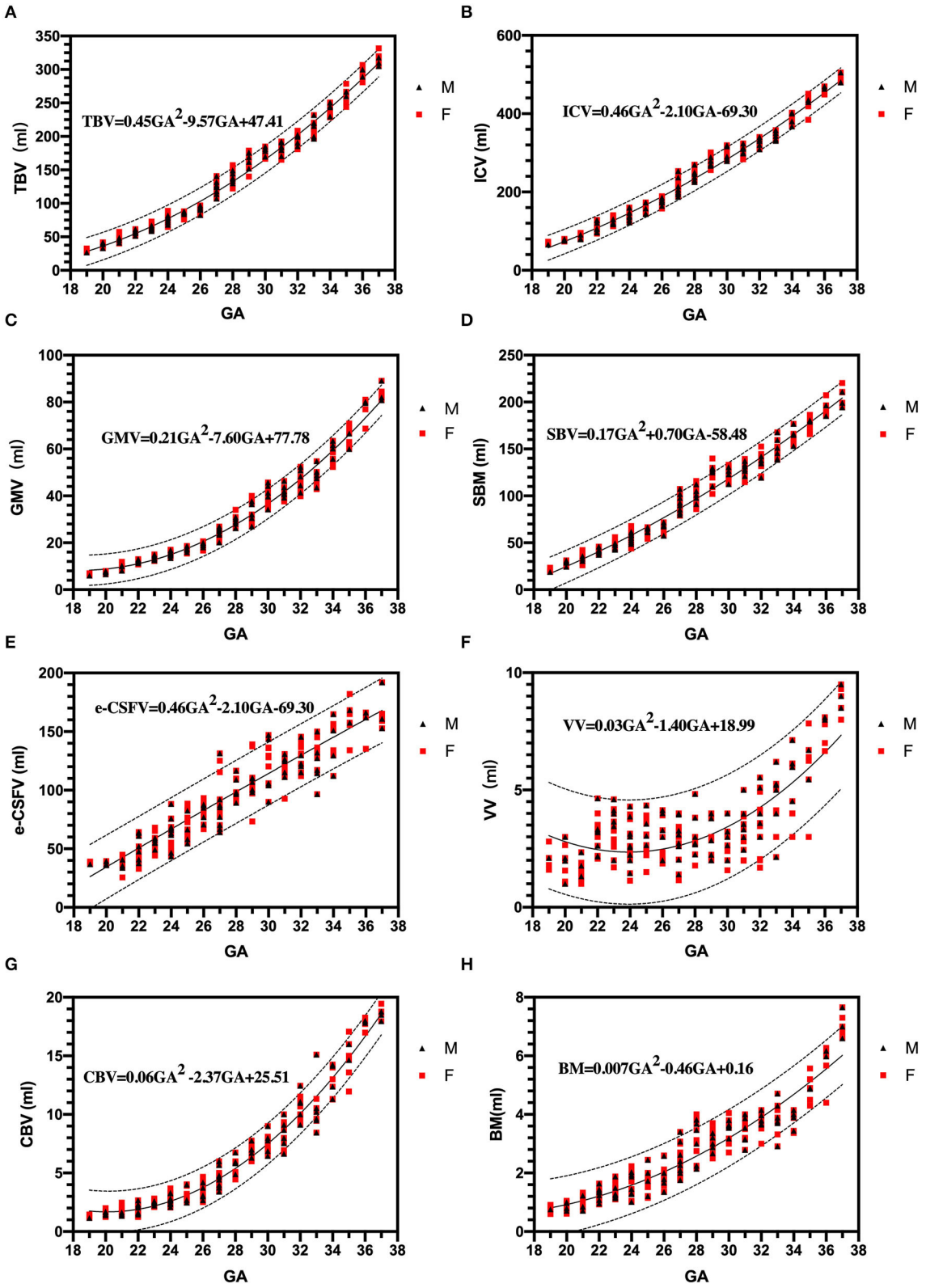

FIGURE 3 | Three dimensional measurements: growth trajectories and centiles. Best fit models for normal control 3D growth trajectories of an intracranial brain tissue, **(A)**: brain volume (TBV), **(B)**: intracranial cavity volume (ICV), **(C)**: gray matter volume (GMV), **(D)**: subcortical brain volume (SBV), **(E)**: extra-cerebrospinal fluid (e-CSFV), **(F)**: lateral ventricles volume (VV), **(G)**: cerebellar (CBV), **(H)**: brainstem (BM). Solid lines depict the 50th centile, and dotted lines the 5th and 95th centiles. Red square (F): female fetuses; black triangle (M): male fetuses.

TABLE 2 | Total brain volume and ICV analysis compared with values reported by Jarvis' study.

	TBV Analysis			ICV Analysis		
GA	**Mean**	**Mean difference (95% confidence)**	***P***	**Mean**	**Mean difference (95% confidence)**	***P***
36 ($n = 5$)	−3.81	(−20.12, 12.49)	0.59	−8.02	(−59.24, 43.20)	0.73
35 ($n = 6$)	5.90	(−11.95, 23.75)	0.46	−2.30	(−52.94, 48.33)	0.92
34 ($n = 8$)	6.40	(−6.01, 41.42)	0.23	10.21	(−28.68, 49.09)	0.58
33 ($n = 9$)	9.36	(−5.58, 18.81)	0.27	24.62	(−10.70, 59.94)	0.15
32 ($n = 12$)	5.00	(−4.63, 14.63)	0.28	12.59	(−15.21, 40.40)	0.35
31 ($n = 11$)	−1.10	(−12.90, 10.71)	0.84	8.86	(−23.45, 41.17)	0.56
30 ($n = 10$)	−13.41	(−21.56, −5.25)	0.004*	−16.73	(−49.30, 15.84)	0.29
29 ($n = 11$)	−19.45	(−34.50, −4.41)	0.02*	−19.30	(−48.38, 9.78)	0.18
28 ($n = 9$)	−12.77	(−28.37, 2.84)	0.10	−15.69	(−46.94, 15.55)	0.30
27 ($n = 13$)	−9.82	(−22.85, 3.21	0.13	−10.63	(−39.43, 18.17)	0.45
26 ($n = 13$)	6.87	(1.52, 12.22)	0.02*	4.03	(−16.48, 24.55)	0.68
25 ($n = 12$)	1.36	(−3.74, 6.46)	0.57	−3.28	(−22.97, 16.41)	0.73
24 ($n = 15$)	−2.88	(−11.25, 5.49)	0.48	−8.73	(−26.51, 9.06)	0.32
23 ($n = 15$)	−4.18	(−9.08, 0.71)	0.09	−13.74	(−13.00, 40.48)	0.27
22 ($n = 13$)	−5.62	(−9.90, −1.33)	0.01*	−14.70	(−30.81, 1.40)	0.07
21 ($n = 9$)	−6.05	(−13.89, 1.79)	0.12	−7.18	(−20.69, 6.33)	0.27
20 ($n = 8$)	−4.63	(−9.67, 0.42)	0.07	−11.04	(−22.61, −0.52)	0.06
19 ($n = 4$)	−3.43	(−11.37, 4.52)	0.32	−16.47	(−31.83, −1.11)	0.04*

*Denotes statistical significance.

7.60GA + 77.78 ($R^2 = 0.97$); SBV = $0.17GA^2$ + 0.70GA – 58.48 ($R^2 = 0.97$); e-CSFV = $0.46GA^2$ – 2.10GA – 69.30 ($R^2 = 0.98$); VV = $0.03GA^2$ – 1.40GA + 18.99 ($R^2 = 0.57$); CBV = $0.06GA^2$ – 2.37GA + 25.51 ($R^2 = 0.97$); BM = $0.007GA^2$ – 0.46GA + 0.16 ($R^2 = 0.89$). Measured mean ICV values at 19 weeks are significantly different from those previously reported ($p < 0.05$). When comparing the mean TBV values for each GA week as generated by the Jarvis' formula, our data were found to approximate the prediction at every GA week except weeks 22, 26, 29, and 30 (all $p < 0.05$; **Table 2**). The predicted mean TBV value generated by our formula (TBV = $0.45GA^2$ - 9.57GA + 47.41) were very similar at every GA week to values predicted by the Jarvis' formula, and the predicted TBV means derived from the previously reported formula were all within the 95% *CI* of the predicted means of this study (**Table 3**).

The relative growth rate of the volume of different intracranial structures is as follows: ICV: 10.87%; TBV: 13.22%; GMV: 14.15%; SBV: 12.81%; e – CSFV: 8.12%; VV: 8.05%; CBV: 14.77%; and BM: 12.18%.

Effect of Sex

Male fetuses had slightly larger measurements compared with female fetuses in any intracranial structure of the 3D measurements expect for e-CSFV (male fetuses, 93.08; female fetuses, 93.31; $p = 0.97$), while the difference between sexes were not significant in ICV (male fetuses, 234.0; female fetuses, 226.0; $p = 0.63$), TBV (male fetuses, 137.2; female fetuses, 129.6; $p = 0.50$), GMV (male fetuses, 31.16; female fetuses, 29.11; $p = 0.48$), SBV (male fetuses, 96.95; female fetuses, 91.91; $p = 0.50$), CBV (male fetuses, 6.38; female fetuses, 6.01; $p = 0.60$), and BM (male fetuses, 2.72; female fetuses, 2.56; $p = 0.47$). The largest sex-related differences were significantly higher volumes in male fetuses for the lateral ventricles (male fetuses, 3.69; female fetuses, 3.08; $p = 0.01$).

DISCUSSION

Quantitative image analysis of the human brain *in utero* plays an important role in clinical decision-making and neuroscience investigation. With the advent of image post-processing technology and motion correction algorithms to obtain high-quality 3D images (Kim et al., 2010), it is now possible to improve the accuracy of manual segmentation of the fetal brain in the early and middle trimesters (Habas et al., 2010). We have presented normative data of the intracranial contents from a large cohort ($n = 188$) of control fetuses and individualized data on the regional fetal brain volumes (not all these structures were assessed by previous articles) between 19 and 37 GA. In addition, we found that the largest sex-related differences were significantly higher volumes in male fetuses for the VV.

In recent years, different studies have analyzed and reported changes in fetal brain volume (Jarvis et al., 2019; Cai et al., 2020; Dovjak et al., 2021), but the results are inconsistent and may depend on different measurement methods and whether or not fetal movement artifacts are processed. In addition, the number of fetuses in the cohorts studied varied widely in these studies, from the smaller cohort of 25 fetuses reported by Gholipour et al. (2017) to the largest cohort of 659 normal fetuses studied by Shi

TABLE 3 | Total brain volume derived by our formula compared with predictive inference values calculated with formula by Jarvis et al.

GA	Predicted Mean Value	Lower Predicted CI	Upper Predicted CI	Prediction by Jarvis' formula
37	309.82	288.93	330.71	–
36	286.52	265.85	307.19	290.20
35	264.12	243.60	284.63	266.20
34	242.62	222.19	263.04	243.30
33	222.02	201.64	242.40	221.50
32	202.32	181.96	222.68	200.70
31	183.52	163.17	203.88	180.90
30	165.62	145.27	185.98	162.20
29	148.63	128.27	168.99	144.60
28	132.53	112.17	152.89	128.00
27	117.33	96.98	137.69	112.40
26	103.04	82.69	123.39	98.00
25	89.64	69.30	109.98	84.50
24	77.15	56.81	97.48	72.10
23	65.55	45.20	85.90	60.80
22	54.86	34.47	75.24	50.50
21	45.06	24.61	65.52	41.20
20	36.17	15.58	56.76	33.00
19	28.18	7.39	48.96	25.90

et al. (2020), which proposed an automated fetal brain analysis method, such as brain extraction, 3D volumetric reconstruction, atlas generation, and quantification of brain development. This method reduces the time required for manual editing following automatic segmentation to achieve such a surprising amount. While the data in most studies with large sample sizes are acquired from multi-institutions with multi-sequences (SSFSE and steady-state free precession, SSFP) on different scanners (different field strength and manufacturers). We are looking forward to using a single device and a single sequence to get a large sample of normative data of fetal intracranial structures, which would be more meaningful and perfect. So the accurate manual segmentations as prior knowledge could be used for the design and verification of the automatic volumetric segmentation method.

We made a like-to-like comparison of our total fetal brain volumes with those predicted by Jarvis et al., which used a large cohort ($n = 200$) of control fetuses and individualized data on the intracranial volumes between 18 and 37 GA (Jarvis et al., 2016, 2019). While a major strength of Jarvis' study is the inclusion of 200 fetuses across a wide GA range, they limited their measurements to total and regional brain structures without different tissue types (e.g., cortical gray matter and white matter). In an earlier publication (Jarvis et al., 2016), they reported on the TBV (only) from 132 of the cases reported in this manuscript along with a prediction equation. By substituting GA into this model, the difference between the actual and theoretical mean values of TBV can be analyzed to obtain a more accurate assessment of fetal brain development. Jarvis' formula measured an average TBV of 25.9 ml at 19 weeks gestation and 290.6 ml at 36 GA. In our study, the mean TBV of 188 fetuses was 29.33 ml at 19 weeks and 294 ml at 36 weeks. When comparing the mean TBV with the expected values generated by the Jarvis' formula for each GA week, our data were found to approximate the prediction at every GA week except weeks 22, 26, 29, and 30 ($p < 0.05$).

A number of reasons could explain this difference. First, the thickness of their MRI acquisitions ranged from 2 to 2.6 mm, whereas ours was 2 mm thick. Another source of bias is that the reconstructed volumetric images allowed us to develop supervised image segmentation techniques to improve the accuracy and ease of obtaining precise fetal brain volumetry. These may have introduced large errors in volume measurements, especially for small intracranial structures. The results generated by our formula were very similar to values predicted by the Jarvis' formula at every GA week. Therefore, using the formula by Jarvis' to predict expected small intracranial structures is based on extrapolation by the formula, which introduces potential error. So, our study reinforces the formula by Jarvis et al. but provides more robust total fetal brain volume measurements in the earlier second and third stages of pregnancy as a result of our larger study population.

From our results, the GMV followed a quadratic growth pattern, indicating accelerated growth at this stage of development, as demonstrated by the progressing growth velocity in brain volume in the later middle and third trimesters. The GMV increased at a relative growth rate of 14.15% per week in our study. This is consistent with a previous study (Kyriakopoulou et al., 2017) performed on 127 normal fetuses at 21–38 gestational weeks (14.78%). Although the overall growth rate of GMV and SBV is not very different throughout pregnancy, the growth trajectory and proportion of cerebral volume of GMV and SBV between 18 and 37 weeks are different. We found that subcortical white matter is a major contributor to fetal brain volume development during the middle and later trimesters of pregnancy, reaching the peak between 29 and 30 weeks of gestation. Our results showed that the proportion of cerebral cortex to the fetal total brain volume in the late trimester increased significantly with the increase of gestation.

Our results indicated that the relative growth rates varied between structures with the CBV (14.77%), which showed the fastest growth per week followed by the cortex and the supratentorial brain tissue, while the growth of the lateral ventricles was the slowest (8.05%). During the second and third trimesters of pregnancy, the cerebellum undergoes extensive proliferation and migration of external granulosa cells, and the formation of the internal granulosa layer, which are the basis for significant increase in CBV (Griffiths et al., 2004; Bolduc et al., 2012). Reductions in total cerebellum and local volume in infants with microcephaly are associated with delays in cognition, motor function, and social-affective disorders.

The size of lateral ventricles can be used to predict fetal nervous system dysfunction (Carta et al., 2018; Fox et al., 2018). Therefore, the accurate measurement of bilateral ventricles volume is crucial to the diagnosis of lateral ventricle enlargement, and ventriculomegaly is an indicator of fetal brain development abnormalities. In our study, we found that male fetuses had significantly larger VV compared with female fetuses. This result is supported by extensive US data, which consistently report

that the standard 2-D indicators of ventricular diameter are larger in male fetuses (Salomon et al., 2007). This result is very critical, as ventriculomegaly is frequently encountered at fetal MRI. So the difference in the VV between fetuses of different sexes suggests that this variable should be considered in the assessment of ventriculomegaly.

There are some limitations to this study. First, the number of fetal brains in our cohort for 3D construction is still limited, because the poor imaging quality caused by motion artifacts, causing failures of fetal brain super-resolution reconstruction. We acknowledge that we did not have successful neurodevelopment outcomes for all of the children who had been studied as normal fetuses in our cohort. However, previous research (Griffiths et al., 2017) has shown that the false positive and negative rates for detecting abnormalities by prenatal MR are very low. In the future, we hope to optimize the reconstructed algorithm and segmental process with the eventual aim to provide accurate automatic segmentation.

The normative values of fetal intracranial structures across a broad range of gestations with associated prediction limits could potentially be used as a reference tool in prenatal counseling. Volumetric growth of the fetal brain follows a complex trajectory that is dependent on structure, GA, and sex. Therefore, we propose preferential use of these measured mean values over formula-derived predictions in clinical counseling for fetuses with GA in the early second and third stages of pregnancy.

DATA AVAILABILITY STATEMENT

The original contributions presented in the study are included in the article, further inquiries can be directed to the corresponding author.

ETHICS STATEMENT

The studies involving human participants were reviewed and approved by Shanghai Children's Medical Center. The patients/participants provided their written informed consent to participate in this study.

AUTHOR CONTRIBUTIONS

J-YR performed experiments, analyzed the data, and drafted the manuscript. S-ZD and MZ designed this study, analyzed the fetal MRI data, and revised the manuscript. G-HW, Y-DG, and FJ designed the cohort and following up. All authors read and approved the final manuscript.

FUNDING

This work was supported by the National Natural Science Foundation of China (nos. 81971582 and 81571628), the Natural Science Foundation of Shanghai (no. 19ZR1476700), the Shanghai Pujiang Program (no. 2019PJD030), the Collaborative Innovation Program of Shanghai Municipal Health Commission (no. 2020CXJQ01), the Shanghai Jiao Tong University School of Child Developing Brian Research Center Construction Funds, and the Shanghai Jiao Tong University School of Medicine (Innovation Team on Pediatric Research Funds).

ACKNOWLEDGMENTS

This article is dedicated to all who participated in and assisted in this study.

REFERENCES

Andescavage, N. N., Du Plessis, A., Mccarter, R., Serag, A., Evangelou, I., Vezina, G., et al. (2017). Complex trajectories of brain development in the healthy human fetus. *Cereb Cortex.* 27, 5274–5283. doi: 10.1093/cercor/bhw306

Askin Incebacak, N. C., Sui, Y., Gui Levy, L., Merlini, L., Sa De Almeida, J., Courvoisier, S., et al. (2022). Super-resolution reconstruction of T2-weighted thick-slice neonatal brain MRI scans. *J. Neuroimaging.* 32, 68–79. doi: 10.1111/jon.12929

Blondiaux, E., and Garel, C. (2013). Fetal cerebral imaging - ultrasound vs. MRI: an update. *Acta. Radiol.* 54, 1046–1054. doi: 10.1258/ar.2012.120428

Bolduc, M. E., Du Plessis, A. J., Sullivan, N., Guizard, N., Zhang, X., Robertson, R. L., et al. (2012). Regional cerebellar volumes predict functional outcome in children with cerebellar malformations. *Cerebellum.* 11, 531–542. doi: 10.1007/s12311-011-0312-z

Cai, S., Zhang, G., Zhang, H., and Wang, J. (2020). Normative linear and volumetric biometric measurements of fetal brain development in magnetic resonance imaging. *Childs Nerv. Syst.* 36, 2997–3005. doi: 10.1007/s00381-020-04633-3

Carta, S., Kaelin Agten, A., Belcaro, C., and Bhide, A. (2018). Outcome of fetuses with prenatal diagnosis of isolated severe bilateral ventriculomegaly: systematic review and meta-analysis. *Ultrasound Obstet. Gynecol.* 52, 165–173. doi: 10.1002/uog.19038

Clouchoux, C., Guizard, N., Evans, A. C., Du Plessis, A. J., and Limperopoulos, C. (2012). Normative fetal brain growth by quantitative in vivo magnetic resonance imaging. *Am. J. Obstet. Gynecol.* 206, 173.e171–178. doi: 10.1016/j.ajog.2011.10.002

Corbett-Detig, J., Habas, P. A., Scott, J. A., Kim, K., Rajagopalan, V., Mcquillen, P. S., et al. (2011). 3D global and regional patterns of human fetal subplate growth determined in utero. *Brain Struct. Funct.* 215, 255–263. doi: 10.1007/s00429-010-0286-5

De Oliveira Júnior, R. E., Teixeira, S. R., Santana, E. F. M., Elias Junior, J., Costa, F. D. S., Araujo Júnior, E., et al. (2021). Magnetic resonance imaging of skull and brain parameters in fetuses with intrauterine growth restriction. *Radiol. Bras.* 54, 141–147. doi: 10.1590/0100-3984.2020.0025

Dovjak, G. O., Schmidbauer, V., Brugger, P. C., Gruber, G. M., Diogo, M., Glatter, S., et al. (2021). Normal human brainstem development in vivo: a quantitative fetal MRI study. *Ultrasound Obstet. Gynecol.* 58, 254–263. doi: 10.1002/uog.22162

Fox, N. S., Monteagudo, A., Kuller, J. A., Craigo, S., and Norton, M. E. (2018). Mild fetal ventriculomegaly: diagnosis, evaluation, and management. *Am. J. Obstet. Gynecol.* 219, B2–b9. doi: 10.1016/j.ajog.2018.04.039

Fried, S., Gafner, M., Jeddah, D., Gosher, N., Hoffman, D., Ber, R., et al. (2021). Correlation between 2D and 3D Fetal Brain MRI biometry and neurodevelopmental outcomes in fetuses with suspected microcephaly and macrocephaly. *AJNR Am. J. Neuroradiol.* 42, 1878–1883. doi: 10.3174/ajnr.A7225

Gholipour, A., Estroff, J. A., Barnewolt, C. E., Connolly, S. A., and Warfield, S. K. (2011). Fetal brain volumetry through MRI volumetric reconstruction and segmentation. *Int. J. Comput. Assist. Radiol. Surg.* 6, 329–339. doi: 10.1007/s11548-010-0512-x

Gholipour, A., Estroff, J. A., and Warfield, S. K. (2010). Robust super-resolution volume reconstruction from slice acquisitions: application to fetal brain MRI. *IEEE Trans. Med. Imaging.* 29, 1739–1758. doi: 10.1109/TMI.2010.2051680

Gholipour, A., Rollins, C. K., Velasco-Annis, C., Ouaalam, A., Akhondi-Asl, A., Afacan, O., et al. (2017). A normative spatiotemporal MRI atlas of the fetal brain for automatic segmentation and analysis of early brain growth. *Sci. Rep.* 7, 476. doi: 10.1038/s41598-017-00525-w

Griffiths, P. D., Bradburn, M., Campbell, M. J., Cooper, C. L., Graham, R., Jarvis, D., et al. (2017). Use of MRI in the diagnosis of fetal brain abnormalities in utero (MERIDIAN): a multicentre, prospective cohort study. *Lancet.* 389, 538–546. doi: 10.1016/S0140-6736(16)31723-8

Griffiths, P. D., Mousa, H. A., Finney, C., Mooney, C., Mandefield, L., Chico, T. J. A., et al. (2019). An integrated in utero MR method for assessing structural brain abnormalities and measuring intracranial volumes in fetuses with congenital heart disease: results of a prospective case-control feasibility study. *Neuroradiology.* 61, 603–611. doi: 10.1007/s00234-019-02184-2

Griffiths, P. D., Wilkinson, I. D., Variend, S., Jones, A., Paley, M. N., and Whitby, E. (2004). Differential growth rates of the cerebellum and posterior fossa assessed by post mortem magnetic resonance imaging of the fetus: implications for the pathogenesis of the chiari 2 deformity. *Acta. Radiol.* 45, 236–242. doi: 10.1080/02841850410003572

Grossman, R., Hoffman, C., Mardor, Y., and Biegon, A. (2006). Quantitative MRI measurements of human fetal brain development in utero. *Neuroimage.* 33, 463–470. doi: 10.1016/j.neuroimage.2006.07.005

Habas, P. A., Kim, K., Corbett-Detig, J. M., Rousseau, F., Glenn, O. A., Barkovich, A. J., et al. (2010). A spatiotemporal atlas of MR intensity, tissue probability and shape of the fetal brain with application to segmentation. *Neuroimage.* 53, 460–470. doi: 10.1016/j.neuroimage.2010.06.054

Hoffmann, W. A., and Poorter, H. (2002). Avoiding bias in calculations of relative growth rate. *Ann. Bot.* 90, 37–42. doi: 10.1093/aob/mcf140

Jarvis, D., Akram, R., Mandefield, L., Paddock, M., Armitage, P., and Griffiths, P. D. (2016). Quantification of total fetal brain volume using 3D MR imaging data acquired in utero. *Prenat. Diagn.* 36, 1225–1232. doi: 10.1002/pd.4961

Jarvis, D., and Griffiths, P. D. (2017). Clinical applications of 3D volume MR imaging of the fetal brain in utero. *Prenat. Diagn.* 37, 556–565. doi: 10.1002/pd.5042

Jarvis, D. A., Finney, C. R., and Griffiths, P. D. (2019). Normative volume measurements of the fetal intra-cranial compartments using 3D volume in utero MR imaging. *Eur. Radiol.* 29, 3488–3495. doi: 10.1007/s00330-018-5938-5

Jiang, S., Xue, H., Glover, A., Rutherford, M., Rueckert, D., and Hajnal, J. V. (2007). MRI of moving subjects using multislice snapshot images with volume reconstruction (SVR): application to fetal, neonatal, and adult brain studies. *IEEE Trans Med. Imaging.* 26, 967–980. doi: 10.1109/TMI.2007.895456

Kim, K., Habas, P. A., Rousseau, F., Glenn, O. A., Barkovich, A. J., and Studholme, C. (2010). Intersection based motion correction of multislice MRI for 3-D in utero fetal brain image formation. *IEEE Trans. Med. Imaging.* 29, 146–158. doi: 10.1109/TMI.2009.2030679

Kline-Fath, B. M. (2019). Ultrasound and MR Imaging of the Normal Fetal Brain. *Neuroimaging Clin. N. Am.* 29, 339–356. doi: 10.1016/j.nic.2019.03.001

Kyriakopoulou, V., Vatansever, D., Davidson, A., Patkee, P., Elkommos, S., Chew, A., et al. (2017). Normative biometry of the fetal brain using magnetic resonance imaging. *Brain Struct. Funct.* 222, 2295–2307. doi: 10.1007/s00429-016-1342-6

Ruiz, A., Cruz-Lemini, M., Masoller, N., Sanz-Cortés, M., Ferrer, Q., Ribera, I., et al. (2017). Longitudinal changes in fetal biometry and cerebroplacental hemodynamics in fetuses with congenital heart disease. *Ultrasound Obstet Gynecol* 49, 379–386. doi: 10.1002/uog.15970

Salomon, L. J., Bernard, J. P., and Ville, Y. (2007). Reference ranges for fetal ventricular width: a non-normal approach. *Ultrasound Obstet. Gynecol.* 30, 61–66. doi: 10.1002/uog.4026

Shi, W., Yan, G., Li, Y., Li, H., Liu, T., Sun, C., et al. (2020). Fetal brain age estimation and anomaly detection using attention-based deep ensembles with uncertainty. *Neuroimage.* 223, 117316. doi: 10.1016/j.neuroimage.2020.117316

Sibbald, C. A., Nicholas, J. L., Chapnick, M., Ross, N., Gandor, P. L., Waters, W. F., et al. (2021). Fetal brain ultrasound measures and maternal nutrition: A feasibility study in Ecuador. *Am J Hum Biol* 33, e23467. doi: 10.1002/ajhb.23467

Takakuwa, T., Shiraishi, N., Terashima, M., Yamanaka, M., Okamoto, I., Imai, H., et al. (2021). Morphology and morphometry of the human early foetal brain: A three-dimensional analysis. *J. Anat.* 239, 498–516. doi: 10.1111/joa.13433

Conflict of Interest: The authors declare that the research was conducted in the absence of any commercial or financial relationships that could be construed as a potential conflict of interest.

Publisher's Note: All claims expressed in this article are solely those of the authors and do not necessarily represent those of their affiliated organizations, or those of the publisher, the editors and the reviewers. Any product that may be evaluated in this article, or claim that may be made by its manufacturer, is not guaranteed or endorsed by the publisher.

frontiers | Frontiers in Neuroscience

ORIGINAL RESEARCH
published: 23 May 2022
doi: 10.3389/fnins.2022.886772

The Developing Human Connectome Project Neonatal Data Release

A. David Edwards[1,2], Daniel Rueckert[3,4], Stephen M. Smith[5], Samy Abo Seada[6], Amir Alansary[3], Jennifer Almalbis[1], Joanna Allsop[1], Jesper Andersson[5], Tomoki Arichi[1,2], Sophie Arulkumaran[1], Matteo Bastiani[5,7], Dafnis Batalle[1,8], Luke Baxter[5], Jelena Bozek[5,9], Eleanor Braithwaite[10], Jacqueline Brandon[1], Olivia Carney[1], Andrew Chew[1], Daan Christiaens[1,11], Raymond Chung[12], Kathleen Colford[1], Lucilio Cordero-Grande[1,13], Serena J. Counsell[1], Harriet Cullen[1,14], John Cupitt[3], Charles Curtis[12], Alice Davidson[1], Maria Deprez[1,6], Louise Dillon[1], Konstantina Dimitrakopoulou[1,15], Ralica Dimitrova[1,8], Eugene Duff[5], Shona Falconer[1], Seyedeh-Rezvan Farahibozorg[5], Sean P. Fitzgibbon[5], Jianliang Gao[3], Andreia Gaspar[16], Nicholas Harper[1], Sam J. Harrison[5], Emer J. Hughes[1], Jana Hutter[1,6], Mark Jenkinson[5], Saad Jbabdi[5], Emily Jones[10], Vyacheslav Karolis[1,5], Vanessa Kyriakopoulou[1], Gregor Lenz[3], Antonios Makropoulos[1,3], Shaihan Malik[1,6], Luke Mason[10], Filippo Mortari[3], Chiara Nosarti[1,17], Rita G. Nunes[1,16], Camilla O'Keeffe[1], Jonathan O'Muircheartaigh[1,2,8], Hamel Patel[12], Jonathan Passerat-Palmbach[3], Maximillian Pietsch[1,8], Anthony N. Price[1,6], Emma C. Robinson[1,6], Mary A. Rutherford[1], Andreas Schuh[3], Stamatios Sotiropoulos[5,7], Johannes Steinweg[1], Rui Pedro Azeredo Gomes Teixeira[1,6], Tencho Tenev[3], Jacques-Donald Tournier[1,6], Nora Tusor[1], Alena Uus[1,6], Katy Vecchiato[1], Logan Z. J. Williams[1], Robert Wright[3], Julia Wurie[1] and Joseph V. Hajnal[1,6]*

[1] Centre for the Developing Brain, School of Biomedical Engineering and Imaging Sciences, King's College London, London, United Kingdom, [2] MRC Centre for Neurodevelopmental Disorders, King's College London, London, United Kingdom, [3] Biomedical Image Analysis Group, Department of Computing, Imperial College London, London, United Kingdom, [4] Institute for AI and Informatics in Medicine, Klinikum Rechts der Isar, Technical University of Munich, Munich, Germany, [5] Wellcome Centre for Integrative Neuroimaging, FMRIB, Nuffield Department of Clinical Neurosciences, University of Oxford, Oxford, United Kingdom, [6] Biomedical Engineering Department, School of Biomedical Engineering & Imaging Sciences, King's College London, London, United Kingdom, [7] Sir Peter Mansfield Imaging Centre, Mental Health and Clinical Neurosciences, School of Medicine, University of Nottingham, Nottingham, United Kingdom, [8] Department of Forensic and Neurodevelopmental Sciences, Institute of Psychiatry, Psychology & Neuroscience, King's College London, London, United Kingdom, [9] Faculty of Electrical Engineering and Computing, University of Zagreb, Zagreb, Croatia, [10] Centre for Brain and Cognitive Development, Department of Psychological Sciences, Birkbeck, University of London, London, United Kingdom, [11] Department of Electrical Engineering, ESAT/PSI, KU Leuven, Leuven, Belgium, [12] BioResource Centre, NIHR Biomedical Research Centre, South London and Maudsley NHS Trust, London, United Kingdom, [13] Biomedical Image Technologies, ETSI Telecomunicación, Universidad Politécnica de Madrid and CIBER-BBN, Madrid, Spain, [14] Department of Medical and Molecular Genetics, School of Basic and Medical Biosciences, King's College London, London, United Kingdom, [15] Translational Bioinformatics Platform, NIHR Biomedical Research Centre, Guy's and St. Thomas' NHS Foundation Trust and King's College London, London, United Kingdom, [16] Institute for Systems and Robotics (ISR-Lisboa)/LaRSyS, Department of Bioengineering, Instituto Superior Técnico, Universidade de Lisboa, Lisbon, Portugal, [17] Department of Child and Adolescent Psychiatry, Institute of Psychiatry, Psychology and Neuroscience, King's College London, London, United Kingdom

OPEN ACCESS

Edited by:
Hao Huang, University of Pennsylvania, United States

Reviewed by:
Olga Tymofiyeva, University of California, San Francisco, United States
Lana Vasung, Harvard Medical School, United States

***Correspondence:**
A. David Edwards
ad.edwards@kcl.ac.uk

Specialty section:
This article was submitted to Brain Imaging Methods, a section of the journal Frontiers in Neuroscience

Received: *28 February 2022*
Accepted: *19 April 2022*
Published: *23 May 2022*

The Developing Human Connectome Project has created a large open science resource which provides researchers with data for investigating typical and atypical brain development across the perinatal period. It has collected 1228 multimodal magnetic resonance imaging (MRI) brain datasets from 1173 fetal and/or neonatal participants, together with collateral demographic, clinical, family, neurocognitive and genomic data from 1173 participants, together with collateral demographic, clinical, family, neurocognitive and genomic data. All subjects were studied *in utero* and/or soon

after birth on a single MRI scanner using specially developed scanning sequences which included novel motion-tolerant imaging methods. Imaging data are complemented by rich demographic, clinical, neurodevelopmental, and genomic information. The project is now releasing a large set of neonatal data; fetal data will be described and released separately. This release includes scans from 783 infants of whom: 583 were healthy infants born at term; as well as preterm infants; and infants at high risk of atypical neurocognitive development. Many infants were imaged more than once to provide longitudinal data, and the total number of datasets being released is 887. We now describe the dHCP image acquisition and processing protocols, summarize the available imaging and collateral data, and provide information on how the data can be accessed.

Keywords: Developing Human Connectome Project, brain development, MRI, neonatal, connectome, perinatal

INTRODUCTION

Recent advances in MRI acquisition, image processing and analysis have made it possible to gain a non-invasive yet detailed multimodal characterization of the human brain's macroscopic connections (Craddock et al., 2013). Novel connectivity maps encompass not only the structural connections relating to white matter tracts, but the functional connections revealed by coordinated gray-matter activations, and connectivity related to coordinated development revealed in structural covariance (Alexander-Bloch et al., 2013) and multimodal similarity networks (Seidlitz et al., 2018). The value of these approaches has been highlighted in recent years by the Human Connectome Project (HCP), which has fostered growing interest in the science of connectomics and become a critical resource for research into the mature human brain (Van Essen et al., 2013).

Human brain development accelerates rapidly in late pregnancy to reach maximum global growth rate before 6 months (Bethlehem et al., 2022). This rapid growth is accompanied by equally dramatic changes in the brain's associated architecture of structural and functional connectivity, and therefore understanding these processes in both the healthy and pathological brain can provide marked new insights into fundamental neural processes and the possible changes that underlie intractable neuropsychiatric conditions. However, characterization of this process has previously been limited by the challenges inherent in safely and robustly studying the brain during this vulnerable phase of life. The Developing Human Connectome Project (dHCP) is an open science study, funded by the European Research Council to obtain and disseminate Magnetic Resonance Imaging (MRI) data which map the brain's structural and functional development across the period from 20 weeks gestational age to full term. By coupling advances in imaging with bespoke solutions developed for the fetal and neonatal population, principally but not exclusively solving the problems of subject motion, the dHCP captures the development of brain anatomy and connectivity at a systems level. This enables exploration of maturational trajectories, structure and function relationships, the neural substrates for behavior and cognition, and the influences of genetic and environmental factors. The dHCP includes both *in utero* imaging of fetal brain and postnatal imaging of preterm and term born infants, capturing typical and atypical brain development. It has created maps of the developing human brain and its connections as a resource for the neuroscience community and a platform for connectome research.

The dHCP dataset includes a large number of healthy, term-born infants which allow definition of typical development with previously unobtainable precision. It is increasingly appreciated that the perinatal period is crucial for lifelong brain health, and multiple lines of evidence show that early life influences have a critical effect on brain circuitry in later childhood and adult life (Batalle et al., 2018). This has key implications for understanding the pathophysiology of neurodevelopmental conditions, such as autism (Hisle-Gorman et al., 2018) or the difficulties associated with preterm birth (Montagna and Nosarti, 2016). Understanding these effects has important clinical implications, and to support relevant investigations clinical and demographic data were collected and saliva samples obtained for genetic and epigenetic analysis, with participating families invited back at 18 months of age for a developmental assessment using standard tests and questionnaires, including eye-tracking studies.

A key priority for the project was that the data be made available to the research community, and preliminary data releases[1] have been accessed and used by a number of research groups. We now describe the main neonatal data release, providing a summary of the participants, the MR imaging data acquisition and processing, the collateral data including sociodemographic and neuropsychological outcome data, and the genomic data. We also describe available data for each category and how to obtain it. Fetal data will be described and released separately.

PARTICIPANTS

Infants were recruited at St Thomas' Hospital, London and imaged at the Evelina Newborn Imaging Centre, Centre for the Developing Brain, King's College London, United Kingdom. The MR suite is sited within the neonatal intensive care unit which allows imaging of even the smallest and most vulnerable newborn

[1] www.developingconnectome.org

infants, as well as having proximity to the maternity unit to support fetal scanning.

The images of 783 newborn infants are being released. Infants were recruited with specified inclusion and exclusion criteria[2] across a spread of gestational ages at birth (range: 23 to 43 + 1 weeks + days) and post-menstrual ages at the time of study (range: 26 + 5 to 45 + 1). The distributions of gestational age at birth and post-menstrual age at scan are shown in **Figure 1**.

The study population includes 583 subjects born at term equivalent age (37–44 weeks post-menstrual age) without any known pregnancy or neonatal problems and are regarded as healthy. All the anatomical images were reviewed by an expert perinatal neuroradiologist and radiologic scores included in the released data. Incidental findings were noted in a proportion and a report on these have been published (Carney et al., 2021).

MAGNETIC RESONANCE IMAGING DATA

Overview

A summary schematic of the imaging data flow is shown in **Figure 2** with further detail about the steps in the following section. This incorporated optimized MR acquisition sequences, novel image reconstruction methods, transfer to an intermediate server (InstraDB) prior to processing using state-of-the-art pipelines, and packaging of the data for final public release.

The data release contains anatomical [T1 weighted (T1w) and T2 weighted (T2w)], resting state functional MRI (rsfMRI) and diffusion MRI (dMRI) images supplied as both original image data and after the processing pipelines described below have been applied.

The neonatal brain has significantly different tissue properties to the adult brain, including higher water content and incomplete myelination of white matter, and T1 and T2 relaxation times are generally longer than in the adult brain. Neonatal white matter in particular, has longer T1 and T2 times in comparison to gray matter, and brain anatomy is revealed more clearly on T2w images as there is greater contrast compared to T1w images. T2w images are thus treated as the primary data for anatomical segmentation and to provide the anatomical substrates for functional and diffusion analysis.

To ameliorate the effects of infants and fetuses moving during image acquisition novel neonatal patient handling and motion-tolerant acquisition approaches were developed (Hughes et al., 2017; Cordero-Grande et al., 2018, 2020; Hutter et al., 2018a). Participants were imaged in natural sleep, with six exceptions who were sedated with chloral hydrate. If a baby woke up, scanning was halted and the infant settled without taking them out of the imaging cradle. However, as many infants still move even when sleeping peacefully, all subjects were motion corrected.

A total of 887 sessions are being released. 886 had T2w images that passed quality control (QC). 818 had fMRI data that passed QC and 758 had dMRI data that passed QC. Detailed information about the QC process are described in the notes accompanying the data release.[3] The T1w images were not required by pre-processing pipelines and were placed at the end of the scanning protocol resulting in more variable quality than the T2w data; the release contains 711 sessions with T1w multi-slice fast spin-echo (FSE) images and 734 sessions with T1 3D magnetization-prepared rapid gradient-echo (MPRAGE) images.

Imaging Acquisition Methods and Parameters

Imaging was carried out on a 3T Philips Achieva scanner running modified Release 3.2.2 software, using a dedicated neonatal imaging system which included a neonatal 32 channel phased array head coil and customized patient handling system (Rapid Biomedical GmbH, Rimpar, Germany) (Hughes et al., 2017). Infants were imaged following feeding and swaddling in a vacuum-evacuated blanket. Infants were provided with hearing protection in the form of: molded dental putty placed in the external auditory meatus (President Putty, Coltene Whaledent, Mahwah, NJ, United States); Minimuffs (Natus Medical Inc., San Carlos, CA, United States); and an acoustic hood. Monitoring throughout the scanning session (*In vivo* Expression, Philips, Best, NL), included pulse oximetry, respiration (using a small air cushion placed on the lower abdomen) and body temperature *via* a fiber optic probe placed in the axilla. The bespoke imaging cradle system (Hughes et al., 2017) placed subjects in a standardized pose and allowed a fixed imaging geometry to be deployed, with only the position in the head-foot direction adjusted at the start of the examination. The field of view was set after a biometric analysis of data from 91 previously studied term-born infants with dimensions sufficient to accommodate 95% of late-term neonates (Hughes et al., 2017).

To reduce the risk of waking infants due to startle responses at the start of new sequences, the scanner software was modified to ramp up the gradient waveforms gradually over 5 s as each acquisition commenced and prior to any radiofrequency (RF) pulses or data being acquired. Calibration scans, anatomical images (T1w and T2w), resting state functional (rs-fMRI) and diffusion (dMRI) acquisitions were acquired, with an average data rate of 27 slices/second including all preparation and calibration phases. The acquisition protocol was optimized for the properties of the neonatal brain and for efficiency and is summarized in **Table 1**.

Calibration Scans

Static magnetic field (B0) mapping was performed using an interleaved dual TE spoiled gradient echo sequence and localized image-based shimming performed for use with all EPI sequences (Gaspar et al., 2015). Following application of optimized 1st and 2nd order shim settings, B0 (shimmed) field maps were acquired after the fMRI and dMRI acquisitions, and later in the cohort were acquired between the two acquisitions. B1 mapping was performed using the dual refocusing echo acquisition mode (DREAM) method (Nehrke and Bornert, 2012), with STE first and STEAM flip angle of 60.

[2]http://www.developingconnectome.org/study-inclusion-and-exclusion-criteria/

[3]https://biomedia.github.io/dHCP-release-notes/

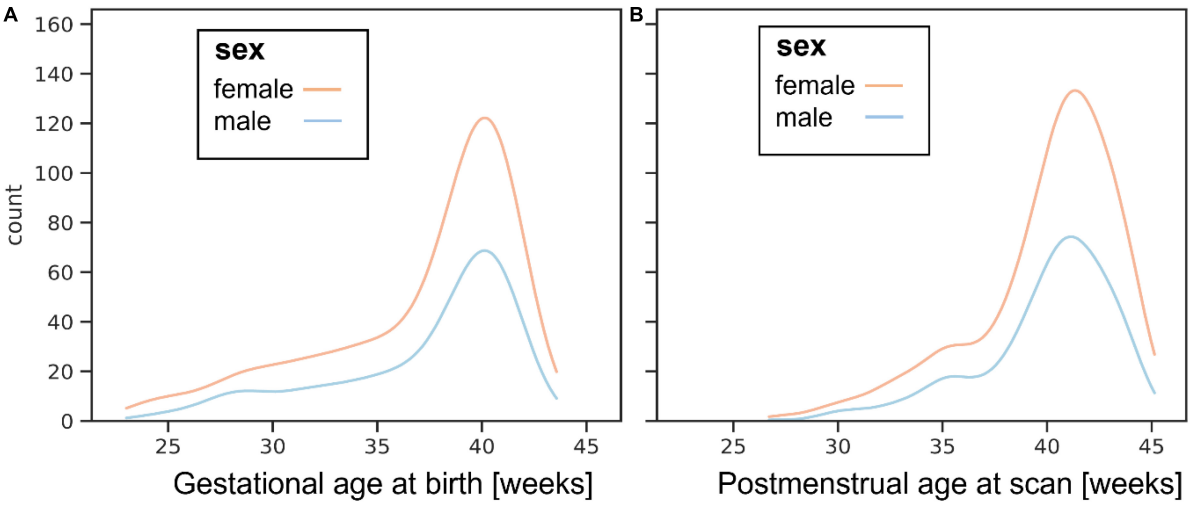

FIGURE 1 | Histograms showing ages for boys and girls at **(A)** birth and **(B)** postnatal MR imaging.

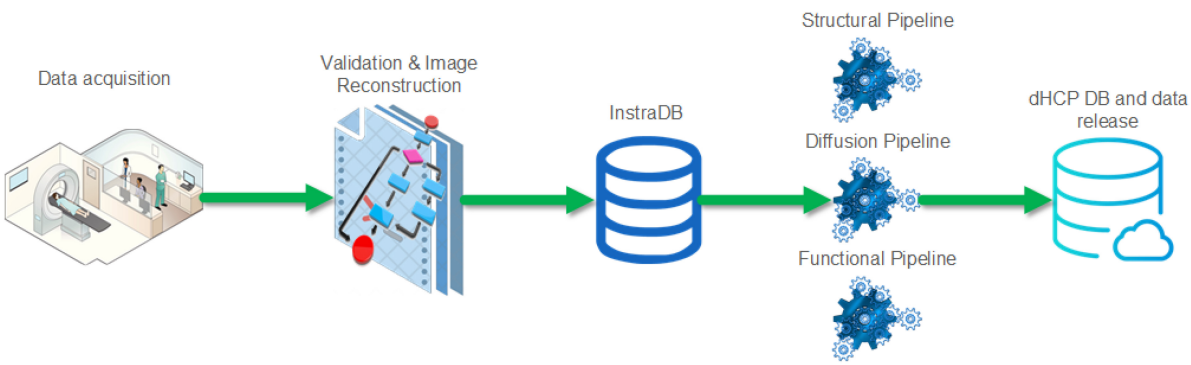

FIGURE 2 | Schematic of the Developing Human Connectome Project imaging data flow from acquisition to data release.

Anatomical Acquisition

Imaging parameters were optimized for contrast to noise ratio using a Cramer Rao Lower bound approach (Lankford and Does, 2013) with nominal relaxation parameter values for gray matter T1/T2: 1800/150 ms and white matter T1/T2: 2500/250 ms (Williams et al., 2005). T2w and inversion recovery T1w multi-slice FSE images were each acquired in sagittal and axial slice stacks with in-plane resolution 0.8 × 0.8 mm^2 and 1.6 mm slices overlapped by 0.8 mm (except in T1w Sagittal which used a slice overlap of 0.74 mm). Other parameters were–T2w: TR/TE = 12000/156 ms, SENSE factor 2.11 (axial) and 2.60 (sagittal); T1w: TR/TI/TE = 4795/1740/8.7 ms, SENSE factor 2.27 (axial) and 2.66 (sagittal). 3D MPRAGE images were acquired with 0.8 mm isotropic resolution and parameters: TR/TI/TE = 11/1400/4.6 ms, SENSE factor 1.2 RL (Right-Left). The FSE acquisitions were each reconstructed using a motion correction algorithm and then the transverse and sagittal images were fused into a single 3D volume for each modality using slice-to-volume methods (Cordero-Grande et al., 2016).

Resting State Functional Magnetic Resonance Imaging

A fMRI acquisition with high temporal resolution developed for neonates (Price et al., in preparation; Fitzgibbon et al., 2020) using multiband (MB) 9× accelerated echo-planar imaging was collected for 15 min, with parameters: TE/TR = 38/392 ms, 2300 volumes, with an acquired spatial resolution of 2.15 mm isotropic. No in-plane acceleration or partial Fourier was used. Single-band reference scans were also acquired with bandwidth matched readout, along with additional spin-echo acquisitions with both anterior-posterior/posterior-anterior (AP/PA) fold-over encoding directions. Physiological recordings of vectorcardiogram (VCG), photoplethysmogram (PPU) and respiratory traces during the fMRI data acquisition are provided unprocessed in the source data folder for optional physiological artifact removal. Alignment to rs-fMRI data can be achieved by means of locating the "end of scan" marker (scripts are available to aid loading and interpretation of this file) and knowledge of the frequency of the recordings (496 Hz) and TR × number of volumes acquired (0.392 s × 2300) can be used to identify

TABLE 1 | Neonatal imaging protocol, lasting a total of 1 h 3 min 11 s.

Sequence name	Duration	Acquisition reference publications	Processing pipeline reference publications
Pilot	00:00:10		
Coil reference	00:01:14		
B0 calibration map	00:00:20	Gaspar et al., 2015	
B1 map	00:00:05		
T2 Turbo Spin Echo (TSE) axial	00:03:12	Cordero-Grande et al., 2016; Hughes et al., 2017; Cordero-Grande et al., 2018	Schuh et al., 2017; Makropoulos et al., 2018
T1 MPRAGE	00:04:35		
T2 TSE sagittal	00:03:12		
Spin Echo (SE) fMRI ref.	00:01:53	Price et al., in preparation	Baxter et al., 2019; Fitzgibbon et al., 2020
Single-Band (SB) fMRI ref.	00:00:19		
Multi-Band (MB) fMRI	00:15:03		
SB fMRI ref. repeat	00:00:19		
SB diffusion MRI ref.	00:01:39	Cordero-Grande et al., 2018; Hutter et al., 2018a,b; Cordero-Grande et al., 2019; Tournier et al., 2020	Bastiani et al., 2019; Christiaens et al., 2019; Pietsch et al., 2019; Christiaens et al., 2021
MB diffusion MRI	00:19:20		
B0 shim map	00:00:20		
T1 TSE Inversion Recovery (IR) axial	00:05:45	Cordero-Grande et al., 2018	
T1 TSE IR sagittal	00:05:45		
Total	01:03:11		

the start of scan timepoint. Note, for improved accuracy on this cohort a small delay of ∼85 ms between the true end of data acquisition and "end of scan" marker has been identified. After accounting for this, the precision of identifying the true start of scan in the physiological file should be on the order of ±50 ms, for a complete scan of 15 min duration.

Diffusion Magnetic Resonance Imaging

The dMRI acquisition was optimized for the properties of the developing brain (Tournier et al., 2020) and implemented as a uniformly distributed set of directions on 4 shells (b = 0 s/mm^2: 20, b = 400 s/mm^2: 64, b = 1000 s/mm^2: 88, b = 2600 s/mm^2: 128), each of which was split into 4 optimal subsets acquired using AP, PA, RL, and LR phase encoding (Hutter et al., 2018b). As described in Hutter et al. (2018b), the diffusion gradient b-values and directions and the phase encoding directions were spread temporally taking the risk of infant motion and gradient duty cycle considerations into account in order to achieve maximal imaging efficiency. If the subject woke up during the diffusion scan, the acquisition could be halted and restarted (after resettling the subject) with a user defined overlap in acquired diffusion weightings. The EPI sequence uses MB factor 4, SENSE factor 1.2, partial Fourier factor 0.86, in-plane resolution 1.5 × 1.5 mm, 3 mm slices with 1.5 mm overlap, TE = 90 ms, TR = 3800 ms. Image reconstruction used a dedicated SENSE algorithm (Hennel et al., 2016; Zhu et al., 2016; Cordero-Grande et al., 2018).

Processing Pipelines

Standardized processing pipelines for all three MRI modalities (anatomical, diffusion, and functional imaging) have been developed specifically for the dHCP neonatal data. The outputs of these pipelines are supplied as part of the data release. Details of the individual pipelines have been published elsewhere including: anatomical segmentations into 9 tissues and 87 regions, and extracted cortical surfaces (Makropoulos et al., 2018) and cortical atlases (Bozek et al., 2018), resting state fMRI analysis (Fitzgibbon et al., 2020) and two diffusion analysis pipelines based on FSL EDDY (Bastiani et al., 2019) and based on SHARD slice-to-volume reconstruction (Christiaens et al., 2019, 2021). The SHARD pipeline also includes de-noised source diffusion data (Cordero-Grande et al., 2019) and inter-slice intensity correction (Pietsch et al., 2021). These offer natural entry points for those wishing to use image analysis software such as FSL[4] and MRtrix3[5] for further analysis. An atlas of diffusion properties has also been created based on a multi-shell multi-tissue constrained spherical deconvolution model (Pietsch et al., 2019). Whilst the majority of the processing pipelines are designed specifically for neonatal data given the inherent differences in tissue contrast and image properties, most analysis pipelines were also set up for comparison with adult data in mind. For instance, the cortical analysis pipeline was aligned with the young adult HCP FS_LR template space. However, we would urge caution about directly comparing adult and neonatal data given that much of the HCP dataset is aligned and parcellated using adult functional networks, and it is likely that the developing functional networks are not sufficiently developed to support this.

Exemplar Imaging Data

Figures 3–8 show examplar data for one participant to provide an indication of what is available. **Figure 3** shows anatomical T1w and T2w fast spin echo data from this infant with the native images for all the acquisitions and the final motion corrected reconstructions. Although the infant was asleep, there is still

[4]www.fmrib.ox.ac.uk/

[5]www.mrtrix.org

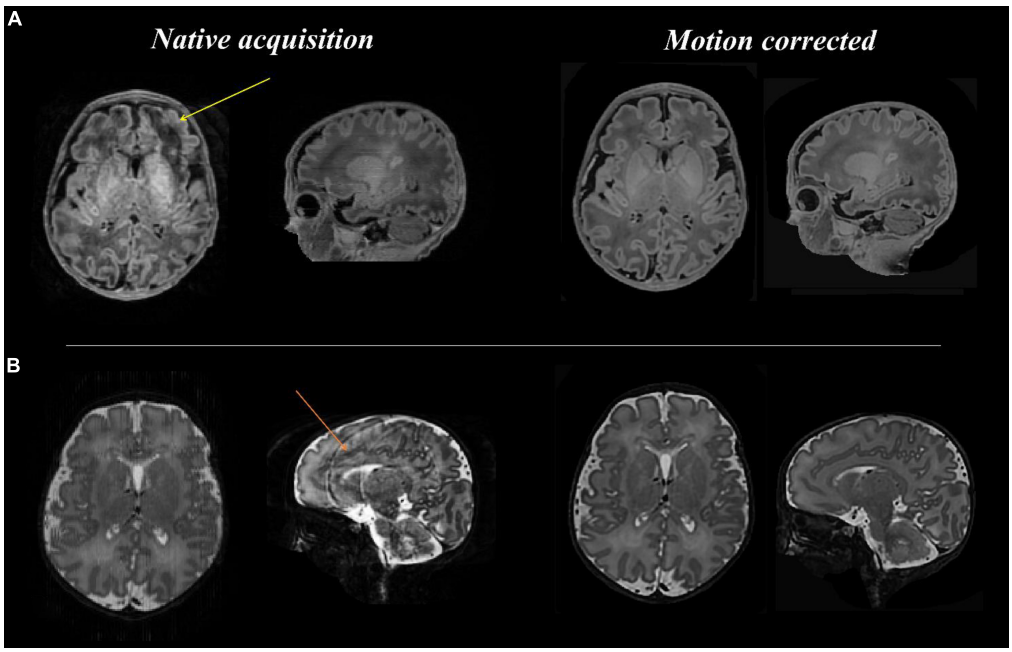

FIGURE 3 | Anatomical T1 and T2 weighted images before and after motion correction for one participant. (**A:** top row) T1 native acquisition (left) with motion artifact visible in the left frontal region in the transverse plane (yellow arrow), which is resolved in the motion corrected images (right) after slice to volume reconstruction. (**B:** bottom row) T2 native acquisition (left) with motion artifact visible in the sagittal plane (orange arrow), which is resolved in the motion corrected images (right).

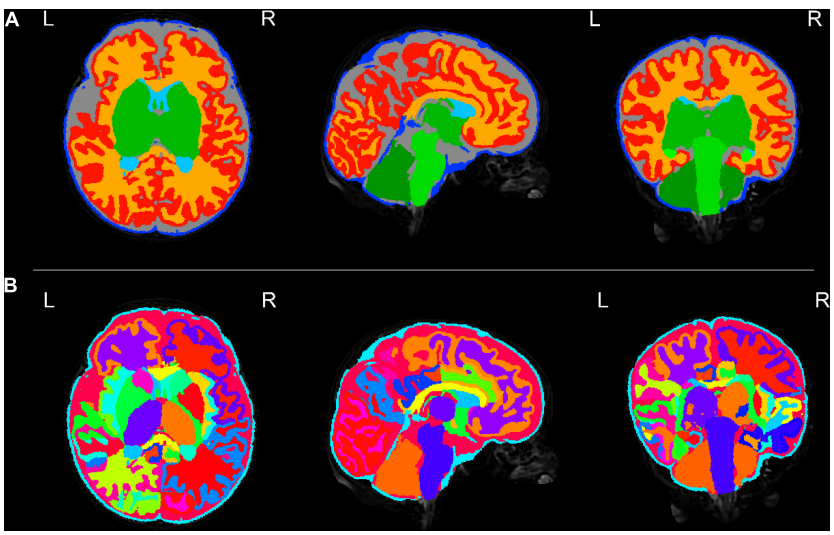

FIGURE 4 | Tissue segmentation and neonatal atlas parcelation for the same infant. Using the automated dHCP structural pipeline, the anatomical images can be segmented into nine tissue classes (**A:** top row) and parcellated into 87 brain regions (**B:** bottom row).

some residual motion artifact. However, the final reconstruction can be seen to be of high quality after motion correction. The MPRAGE data (not shown) is not motion corrected, so is more vulnerable to subject motion. The anatomical segmentation into tissue type and neonatal brain atlas regions are shown in **Figure 4**, and cortical surfaces with projection of the atlas and example derived measures for this subject are shown in **Figure 5**. Anatomical atlases at one week intervals are available for download[6] and will also be available from the NIMH database.[7] **Figure 6** shows one volume of the fMRI time series and a single subject network analysis from the pipeline. **Figures 7**, **8** show diffusion data. **Figure 7** shows selected images from all shells, before correction, after denoising, and after motion

[6]https://brain-development.org/brain-atlases/atlases-from-the-dhcp-project/
[7]https://nda.nih.gov/edit_collection.html?id=3955

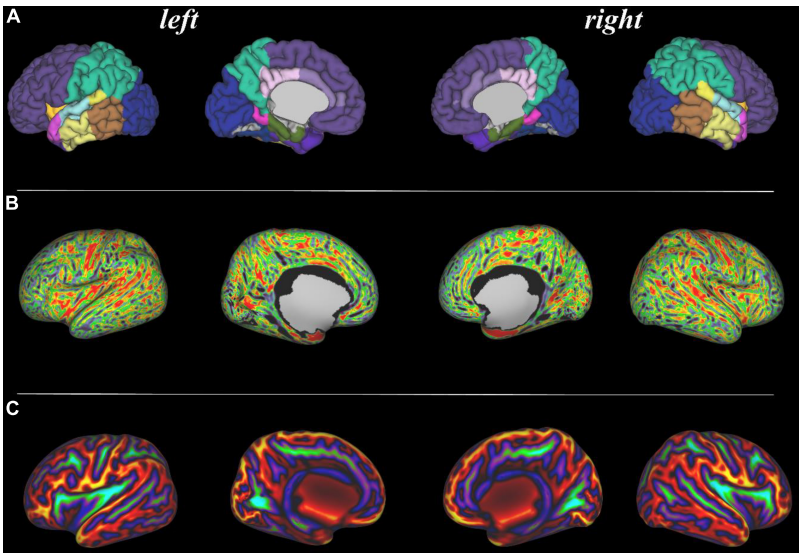

FIGURE 5 | Surface projections using the dHCP structural pipeline for the same infant. (**A:** top row) 87 region neonatal brain atlas projected onto the pial surface; (**B:** middle row) Cortical thickness projected onto the inflated cortical surface; and (**C:** bottom row) Sulcal depth projected onto the inflated cortical surface.

and distortion correction and destriping (Pietsch et al., 2021). **Figure 8** shows derived dMRI metrics in the same slice, including the mean diffusivity (8a) and fractional anisotropy (8b) of the diffusion tensor (Basser et al., 1994), fiber orientation distribution functions (8c) estimated using multi-component spherical deconvolution (Jeurissen et al., 2014; Pietsch et al., 2019) produced with MRtrix3 (Tournier et al., 2019), and (9d) whole brain probabilistic streamline tractography using all tissue components and using only the mature white matter like component from the neonatal multi-component model (Pietsch et al., 2019).

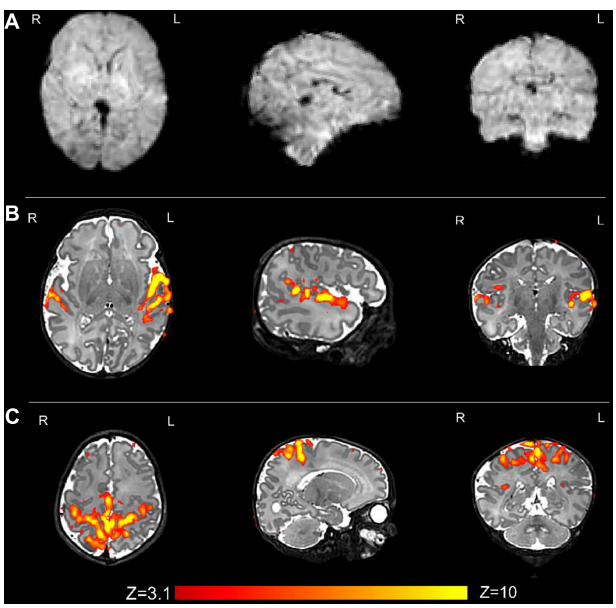

FIGURE 6 | Resting state functional MRI data from the same infant. **(A)** An example volume from the fMRI acquisition after image reconstruction and the preprocessing pipeline has been applied; and **(B)** the auditory and **(C)** sensorimotor resting state networks. Resting state networks were defined using independent component analysis (ICA) as implemented in FSL MELODIC and have been overlaid onto the native T2 image for ease of visualization.

COLLATERAL DATA

A broad spread of demographic and other data is available, although practical constraints, including the COVID-19 pandemic, have led to a certain amount of missing data. The data codebook can currently be accessed through the dHCP website (see text footnote 1) and NIMH database (see text footnote 7), providing a listing with descriptions of the variables. The data sets include the following categories of data.

Demographic, Family, and Clinical Data

Demographic Data for Parents

Age at conception; ethnicity according to United Kingdom census categories; highest age enrolled in full-time education; occupation. This data is collected at enrollment and again at the 18-month neurodevelopmental assessment.

Mother's Past Medical History

Height, weight, body mass index (BMI); blood group; history of medical conditions prior to the pregnancy; smoking, alcohol, and recreational drug use; injury during the pregnancy.

Mother's Obstetric History

Previous pregnancies; number of live births; number of miscarriages; previous premature birth; current pregnancy type,

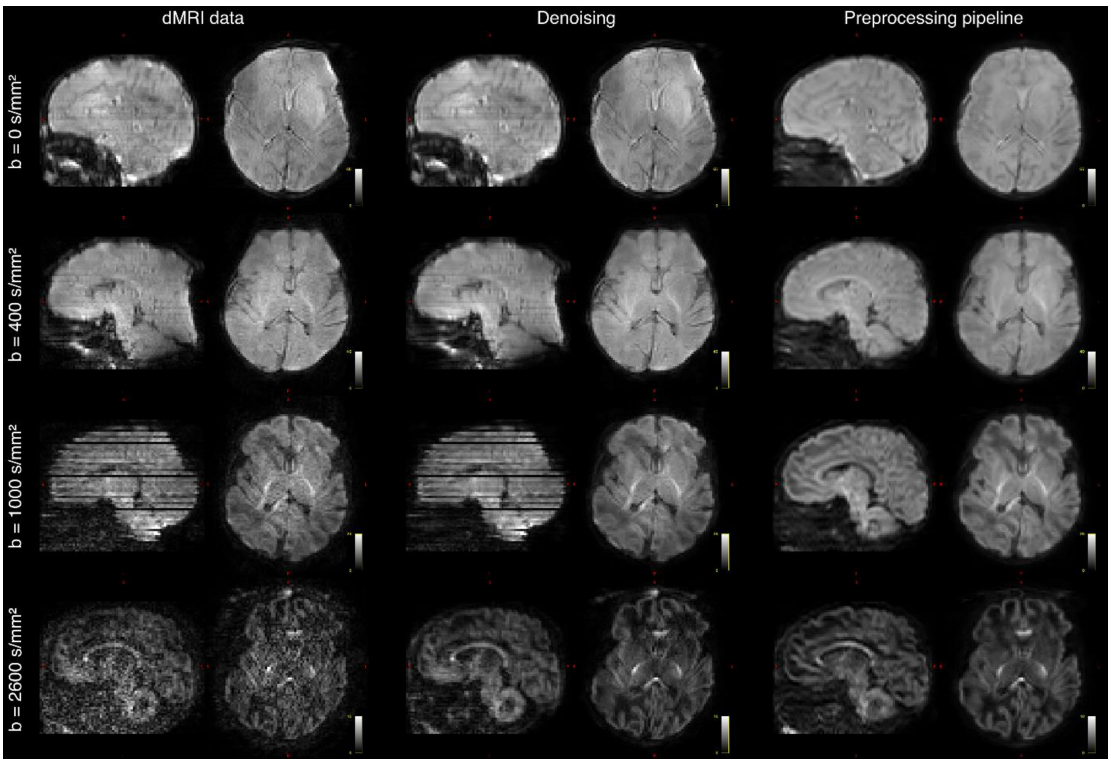

FIGURE 7 | Diffusion MRI (dMRI) data from the same infant. Shown are four selected volumes with different *b*-values and phase encoding directions. Left: input data after MB-SENSE reconstruction. Middle: images after denoising. Right: images after motion and distortion correction and destriping.

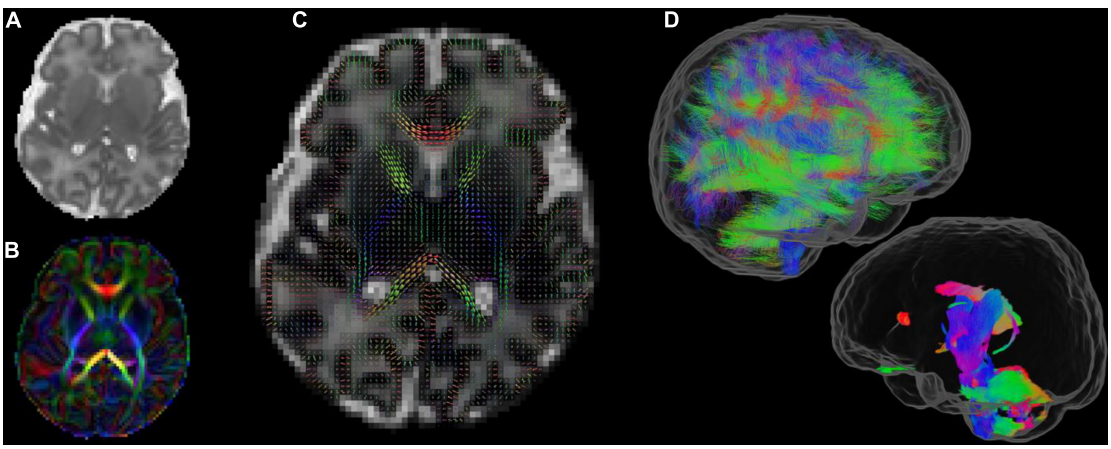

FIGURE 8 | Diffusion MRI metrics in a single subject from the same infant **(A)** Mean Diffusivity and **(B)** Color Fractional Anisotropy maps of the Diffusion Tensor Imaging (DTI) model. **(C)** Tissue Orientation Distribution Function (ODF) of the multi-component analysis in Pietsch et al. (2019). **(D)** Full brain probabilistic streamline tractography based on the tissue ODF (top image) and based on the mature appearing tissue component (bottom image).

mode of conception (natural or IVF); pregnancy number; late pregnancy and labor/delivery history for the pregnancy.

Mental Health History

Self-reported by mother at enrollment and self-reported by both parents at the 18-month assessment, including any history of parental psychiatric problems and how treated; parental history of attention deficit hyperactivity disorder (ADHD), bipolar disease, autistic spectrum disorder (ASD), or schizophrenia; ASD or ADHD in proband's siblings; close relatives with history of ASD, ADHD, bipolar disease, or schizophrenia.

Baby Medical Details at Birth

Gestational age at birth; birth weight, length, and occipito-frontal head circumference; presentation and mode of delivery; medication required at delivery, nutrition and feeding; Apgar scores at 1 and 5 min of age; arterial cord blood pH and base excess where available. The majority of dHCP participants were born in good health and were not admitted to the neonatal intensive care unit (NICU), for those who were, summary data for each day on the neonatal unit and an overall summary of the stay are recorded.

Neurodevelopmental and Neurocognitive Testing at 18 Months

A series of standardized age-appropriate child-centered assessments, parent-report questionnaires, and gaze-tracking tasks were used to provide a targeted overview of toddlers' development. These measures were chosen were chosen to be able to capture individual differences along a typical-to-atypical continuum, to probe associations between early imaging features and emerging behavioral outcomes and to provide normative reference data for future studies.

A total of 619 infants (79%) attended for follow-up assessment, planned for 18 months corrected age but affected by the COVID-19 pandemic, so that median (range) of assessment was 18 months + 12 days (range 17 + 8–34 + 15). Completion rates for broad components of this assessment are shown in **Tables 2**, **3**.

TABLE 2 | Completion rates for neurodevelopmental assessments and questionnaires.

Neurodevelopmental assessment/Questionnaire	Number (%)
Bayley III Cognitive, language, motor neurodevelopmental variables	602 (77%)
Neurological examination total score	594 (76%)
Early Childhood Behavioral Questionnaire (ECBQ)	592 (76%)
Child Behavioral Checklist (CBCL)	591 (76%)
Quantitative Checklist for Autism in Toddlers (Q-CHAT)	591 (76%)
Cognitively Stimulating Parenting Scale (CSPS)	583 (75%)
Parenting Scale: primary caregivers' laxness, over reactivity, verbosity	589 (75%)
Parenting Scale: secondary caregivers' laxness, over reactivity, verbosity	517 (66%)

TABLE 3 | Tests and completion rates for eye tracking assessments.

Eye-tracking task	*N* (%)
Gap-overlap	602 (77)
Non-social contingency	597 (76)
Visual search	597 (76)
Fishtanks	596 (76)
Cognitive control	585 (75)
Working memory	585 (75)
Emotions	576 (74)
Smooth pursuit fixation	568 (72)
Fixation	484 (64)
Scenes	483 (61)
Static images	481 (61)
Entire eye-tracking battery completed	453 (58)

The Bayley Scales of Infant and Toddler Development, Third Edition (Bayley-III)

Assessed toddlers' cognitive, language (receptive and expressive) and motor abilities (gross and fine) using age normed standardized scores (mean = 100, SD = 15) (Albers and Grieve, 2007). The age of assessment and distribution of Bayley III cognitive scores for boys and girls are shown in **Figure 9**.

The Neurological Examination of Infant/Child

Used 26 non-age dependent items to assess cranial nerve function, posture, movements, tone, and reflexes (Haataja et al., 1999).

Behavioral Questionnaires Completed by Primary Caregivers

Early Childhood Behavior Questionnaire

This measures dimensions of temperament, referring to individual differences in reactivity and self-regulation (Putnam and Rothbart, 2006). The Early Childhood Behavior Questionnaire (ECBQ) describes three broad scales: Surgency, characterized by impulsivity, intense pleasure seeking and high activity levels; Negative Affectivity, which refers to the disposition to experience aversive affective states, such as anger, fear, anxiety, shame, and disgust; Effortful Control, which refers to the capacity to inhibit/activate a behavioral response by focusing attention.

Child Behavioral Checklist for Ages 1.5–5

Which is a 100-item measure on the frequency of behavioral and emotional problems in young children (Achenbach and Ruffle, 2000). The Child Behavioral Checklist (CBCL) yields scores for seven problem behavior syndrome subscales: Emotionally Reactive, Anxious/Depressed, Somatic Complaints, Withdrawn, Sleep Problems, Attention Problems, and Aggressive Behavior. Scores are also derived for Externalizing Problems, Internalizing Problems, and Total Problems.

Quantitative Checklist for Autism in Toddlers

A 25-item questionnaire designed to assess potential autistic traits in children (Allison et al., 2008).

Cognitively Stimulating Parenting Scale

Adapted from Wolke et al. (2013), which assesses the availability and variety of experiences that promote cognitive stimulation in the home. This includes availability of educational toys, parental interactions such as teaching words or reading stories, and cognitively stimulating activities such as family excursions. The version of the Cognitively Stimulating Parenting Scale (CSPS) used here was updated to include four items now widely used by toddlers (i.e., iPhone and Apps) (Bonthrone et al., 2021). Scores from the 28 items included in the CSPS can be aggregated to provide an overall cognitively stimulating parenting score.

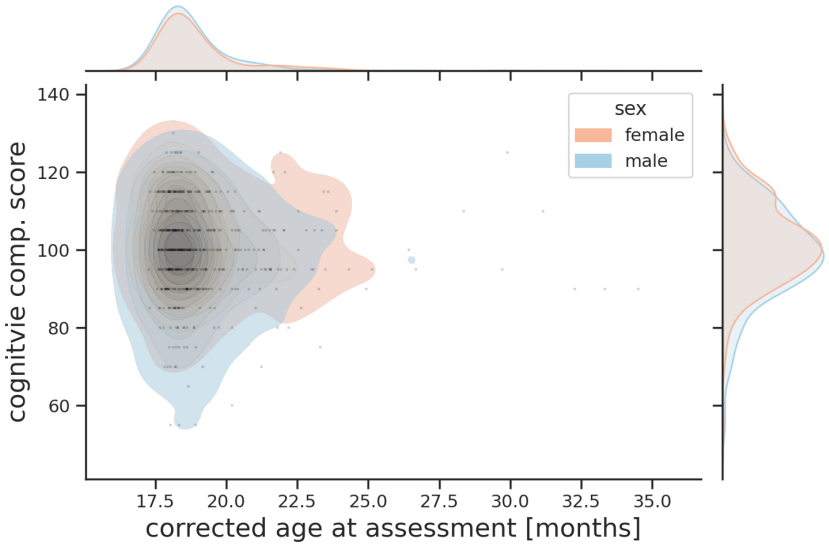

FIGURE 9 | Probability plot showing age of assessment and combined Bayley III cognitive score for boys and girls.

Parenting Scale

Is a 30-item rating scale that measures dysfunctional parenting in discipline situations (Arnold et al., 1993). Parents are asked to indicate their tendency to use specific discipline practices using a 7-point scale. The Parenting Scale identifies three different suboptimal parenting styles, as well as a total score providing a dysfunctional parenting index. Over-reactivity indicates authoritarian and coercive discipline practices; Laxness, in contrast, describes a permissive parent who is inconsistent in providing discipline; Verbosity refers to a parenting style characterized by lengthy and ineffective verbal reprimands. Primary careers were usually mothers and secondary careers usually fathers.

Eye-Tracking

Used to obtain data on a number of cognitive processes. The Tobii TX-300 (Tobii AB, Sweden) gaze tracking system was used to record the temporal and spatial features of the children's direction of gaze in 609 infants (78%) at a median age of 18 months + 12 days (range 17 + 8 − 34 + 15). The battery of tasks comprised a series of animated video clips designed to measure endogenous and exogenous visual attention (Elsabbagh et al., 2009, 2013; Gliga et al., 2009; Wass et al., 2011). Extracted metrics included visual engagement and disengagement, efficiency of attention shifting, social and non-social attention and memory guided choices and visual search. The list of tests and completion rates are shown in **Table 3**. A manuscript describing the tasks and the results in detail has been submitted for publication (Braithewaite et al., submitted). The project codebook details the variables to be released, while the rich meta-data from these tests may be available through discussion with the dHCP investigators.

Genomic Data

Genetic Data

Saliva samples were collected at the initial neonatal MRI data acquisition and 18-month old infant timepoints using Oragene DNA OG-250 kits (DNAGenotek Inc., Kanata, Canada). The genotyping was performed on only one sample (usually the first). There are no linked maternal or paternal samples. Samples were genotyped on the Illumina Infinium Omni5-4 array v1.2, which comprises a total of 4327108 single-nucleotide polymorphisms (SNPs), by NIHR BioResource Centre Maudsley Genomics & Biomarker Core Facility. Genotyping was undertaken in two batches. Basic quality control was performed by the Department of Biostatistics & Health Informatics, King's College London for the combined dHCP batches and a small additional independent study cohort. Raw Illumina microarray genotype image (IDAT) files were uploaded into GenomeStudio and processed according to the GenomeStudio quality control Standard Operating Procedure (Patel et al., 2022).[8] Data was then further processed according to a pipeline which identified and removed samples with call rates below 95% (Patel et al., 2022). It also identified gender mismatches and potential heterozygosity outliers which are flagged in the metadata files. SNP data are available for 731 infants.

Methylation Data

Saliva-derived DNA from each sample was treated with sodium bisulfite [Zymo Research EZ-96 DNA Methylation Kit (D5004)]. DNA methylation was quantified using the Illumina Infinium HumanMethylationEPIC BeadChip Kit. Methylation analysis for the dHCP samples was undertaken alongside two additional independent study cohorts. A randomized sample layout was generated using key study parameters including all study cohorts,

[8]https://khp-informatics.github.io/COPILOT/index.html

with Omixer R/Bioconductor package (Sinke et al., 2021).[9] Saliva samples have been processed for 739 infants, including a subset with samples taken at birth and repeated at the 18-month visit, but QC has yet to be carried out.

GOVERNANCE AND ACCESS

The study was approved by the United Kingdom Health Research Authority (Research Ethics Committee reference number: 14/LO/1169) and written parental consent was obtained in every case for imaging and open data release of the anonymized data. The main imaging data, essential metadata and the collateral data, will be available after accepting a data sharing agreement. Downloaded data should not be passed on to third parties outside the research group, and no attempt should be made to de-anonymize the data which have been face stripped to prevent attempts at facial recognition.

The preliminary data releases are currently available to download by academic torrent *via* the dHCP website (see text footnote 1). The primary long-term site for curation and access of the full data release will be the National Institute for Mental Health (NIMH) data repository portal at https://nda.nih.gov/edit_collection.html?id=3955.

Examples of Developing Human Connectome Project Data Use

The preliminary data releases of a proportion of the images have been available to scientists since 2019. There datasets have been accessed frequently and already a large number of studies have been published using dHCP data. These include studies of prenatal opioid exposure (Merhar et al., 2021), cerebral gene expression (Ball et al., 2020), the effects of preterm birth on brain structure and function (Dimitrova et al., 2020; Kline et al., 2020; Eyre et al., 2021), the development of specific cognitive functions (Li et al., 2020), and the neural response to noxious stimuli (Baxter et al., 2019), as well as a number of analyses of brain connectivity and growth (Eyre et al., 2021; Wang et al., 2021; Bethlehem et al., 2022). The data have been widely used to develop novel imaging analytic methods (Ding et al., 2020; Collins-Jones et al., 2021; Grigorescu et al., 2021) and to define new approaches to understanding brain development (Adamson et al., 2020; O'Muircheartaigh et al., 2020).

DISCUSSION

We describe here the main neonatal data release of the Developing Human Connectome Project which includes 887 datasets from 783 subjects. We are releasing data from all steps in the project, from the initial images through intermediate steps in processing, to results from running our processing pipelines. The aim is to allow researchers to work with the data as they wish, without pre-filtering the available selection. In the majority of cases high quality images across all modalities are available, and are linked to rich collateral data, although practical issues, notably the COVID-19 pandemic, led to some incomplete ascertainment.

Each image acquisition that contributes to the dHCP collection was individually optimized both to take account of the properties of the developing neonatal brain and to achieve the most efficient total examination. After the initial piloting in which the head-foot location of the imaging volume was set, the scanner operated without pause for the entire examination.

Virtually all subjects were examined during natural sleep, so available time for imaging was constrained. We took steps to reduce the risk that infants would awaken by minimizing preparation time after feeding was complete, improving the patient-handling equipment (see Hughes et al., 2017 for details) and modifying the scanner software to avoid sudden changes in acoustic conditions that might create a startle response. Despite these precautions some babies did wake up during the scanning session, but it was often possible to re-settle them and the protocol was designed to allow restart with minimal time penalty, particularly for the dMRI, which was the longest single acquisition. Although precise information about whether a baby woke up during image acquisition was not recorded, it would be of interest in future studies exploring the specific relationship between imaging measures and behavior.

However, even those babies that continued to sleep often moved sufficiently to impair the data quality of the advanced images being collected, so data were motion corrected, either as part of a motion corrected image reconstruction (Anatomical T2w and T1w FSE sequences, but not MPRAGE) or as part of the data processing pipelines, each of which had motion correction steps included. These pipelines were designed and optimized specifically for neonatal data, and software for pipelines is freely available.[10] Full details are available as part of the data download documentation.

The data from the dHCP naturally sits within a context of other connectome-oriented collections and will be curated alongside many similar resources by the National Institutes of Mental Health in the large multimodal neuroinformatic data repository. The dHCP neonatal data collection will prove valuable to a broad range of users and that it will complement and augment other available materials. Taken together with the dHCP fetal data release, this collection provides what is currently a unique observational resource that captures information on the developing human brain at a key stage of rapid growth and change. The companion genetic and follow-up behavioral resources, as well as atlases, which will be accessed from the same locations, can provide rich materials to address a range of scientific and clinical questions. The data are already being widely used.

[9]http://www.bioconductor.org/packages/release/bioc/html/Omixer.html

[10]https://biomedia.github.io/dHCP-release-notes/open-resources.html

DATA AVAILABILITY STATEMENT

The datasets presented in this study can be found in online repositories. The names of the repository/repositories and accession number(s) can be found below: http://www.developingconnectome.org/data-release/third-data-release/, 1; https://nda.nih.gov/edit_collection.html?id=3955, 3955.

ETHICS STATEMENT

The studies involving human participants were reviewed and approved by United Kingdom Health Research Authority (Research Ethics Committee reference number: 14/LO/1169). Written informed consent to participate in this study was provided by the participants' legal guardian/next of kin.

AUTHOR CONTRIBUTIONS

AE, DR, SMS, and JH obtained funding. SAS, LC-G, AG, EH, JH, SM, RN, AP, RT, J-DT, and JH developed acquisition methods. JAlm, JAll, TA, SA, AC, KC, RC, AD, LD, S-RF, NH, EH, CO'K, HP, JS, NT, KV, and JW collected data. DR, SMS, AA, JAn, TA, MB, LB, JBr, DC, JC, SC, MD, ED, S-RF, SPF, JG, SH, MJ, SJ, VKa, GL, AM, FM, JO'M, JP-P, MP, ER, AS, SS, TT, J-DT, AU, RW, JH, and JBo developed analysis methods. AE, SMS, TA, SA, DB, LB, EB, OC, DC, RD, ED, EJ, VKy, CN, JO'M, MP, MR, LW, and LM analyzed data. AE, DR, TA, DC, HC, KD, S-RF, NH, VKa, MP, AP, and JH prepared manuscript. All authors have reviewed the manuscript.

FUNDING

The Developing Human Connectome Project was funded by the European Research Council under the European Union Seventh Framework Programme (FP/20072013)/ERC Grant Agreement no. 319456. This work was supported by the NIHR Biomedical Research Centres at Guys and St Thomas NHS Trust and the South London and Maudsley NHS Trust; the ESPRC/Wellcome Centre for Medical Engineering; and the MRC Centre for Neurodevelopmental Disorders. TA was supported by a MRC Clinician Scientist Fellowship (MR/P008712/1) and MRC translation support award (MR/V036874/1). JO'M was supported by a Sir Henry Dale Fellowship jointly funded by the Wellcome Trust and the Royal Society (Grant Number 206675/Z/17/Z).

ACKNOWLEDGMENTS

We are grateful for all the families who kindly agreed to participate in the project and recognize their particular commitment in remaining engaged with the programme during the COVID-19 Pandemic. We also acknowledge the support of the Neonatal Intensive Care Unit and the Newborn Imaging Centre at Evelina London Children's Hospital. We also thank the external advisory board for their expert advice and contribution across the dHCP project: David van Essen, Arthur Toga, Richard Frackowiak, Dan Marcus, Petra Huppi, Essa Yacoub, and John Ashburner.

REFERENCES

Achenbach, T. M., and Ruffle, T. M. (2000). The child behavior checklist and related forms for assessing behavioral/emotional problems and competencies. *Pediatr. Rev.* 21, 265–271. doi: 10.1542/pir.21-8-265

Adamson, C. L., Alexander, B., Ball, G., Beare, R., Cheong, J. L. Y., Spittle, A. J., et al. (2020). Parcellation of the neonatal cortex using surface-based Melbourne children's regional infant brain atlases (M-CRIB-S). *Sci. Rep.* 10:4359. doi: 10.1038/s41598-020-61326-2

Albers, C. A., and Grieve, A. J. (2007). Test review: Bayley, N. (2006). Bayley scales of infant and toddler development-third edition. San Antonio, TX: Harcourt assessment. *J. Psychoeduc. Assess.* 25, 180–190. doi: 10.1177/073428290629 7199

Alexander-Bloch, A., Giedd, J. N., and Bullmore, E. (2013). Imaging structural co-variance between human brain regions. *Nat. Rev. Neurosci.* 14, 322–336. doi: 10.1038/nrn3465

Allison, C., Baron-Cohen, S., Wheelwright, S., Charman, T., Richler, J., Pasco, G., et al. (2008). The Q-CHAT (Quantitative CHecklist for Autism in Toddlers): a normally distributed quantitative measure of autistic traits at 18-24 months of age: preliminary report. *J. Autism Dev. Disord.* 38, 1414–1425. doi: 10.1007/s10803-007-0509-7

Arnold, D. S., O'leary, S. G., Wolff, L. S., and Acker, M. M. (1993). The parenting scale: a measure of dysfunctional parenting in discipline situations. *Psychol. Assess.* 5, 137–144. doi: 10.1037/1040-3590.5.2.137

Ball, G., Seidlitz, J., O'muircheartaigh, J., Dimitrova, R., Fenchel, D., Makropoulos, A., et al. (2020). Cortical morphology at birth reflects spatiotemporal patterns of gene expression in the fetal human brain. *PLoS Biol.* 18:e3000976. doi: 10.1371/journal.pbio.3000976

Bastiani, M., Andersson, J. L. R., Cordero-Grande, L., Murgasova, M., Hutter, J., Price, A. N., et al. (2019). Automated processing pipeline for neonatal diffusion MRI in the developing human connectome project. *Neuroimage* 185, 750–763. doi: 10.1016/j.neuroimage.2018.05.064

Basser, P. J., Mattiello, J., and LeBihan, D. (1994). MR diffusion tensor spectroscopy and imaging. *Biophys. J.* 66, 259–267.

Batalle, D., Edwards, A. D., and O'muircheartaigh, J. (2018). Annual research review: not just a small adult brain: understanding later neurodevelopment through imaging the neonatal brain. *J. Child. Psychol. Psychiatry* 59, 350–371. doi: 10.1111/jcpp.12838

Baxter, L., Fitzgibbon, S., Moultrie, F., Goksan, S., Jenkinson, M., Smith, S., et al. (2019). Optimising neonatal fMRI data analysis: design and validation of an extended dHCP preprocessing pipeline to characterise noxious-evoked brain activity in infants. *Neuroimage* 186, 286–300. doi: 10.1016/j.neuroimage.2018.11.006

Bethlehem, R. A. I., Seidlitz, J., White, S. R., Vogel, J. W., Anderson, K. M., Adamson, C., et al. (2022). Brain charts for the human lifespan. *Nature* [Online ahead of print]. doi: 10.1038/s41586-022-04554-y

Bonthrone, A. F., Chew, A., Kelly, C. J., Almedom, L., Simpson, J., Victor, S., et al. (2021). Cognitive function in toddlers with congenital heart disease: the impact of a stimulating home environment. *Infancy* 26, 184–199. doi: 10.1111/infa.12376

Bozek, J., Makropoulos, A., Schuh, A., Fitzgibbon, S., Wright, R., Glasser, M. F., et al. (2018). Construction of a neonatal cortical surface atlas using multimodal surface matching in the developing human connectome

project. *Neuroimage* 179, 11–29. doi: 10.1016/j.neuroimage.2018.06.018

Carney, O., Hughes, E., Tusor, N., Dimitrova, R., Arulkumaran, S., Baruteau, K. P., et al. (2021). Incidental findings on brain MR imaging of asymptomatic term neonates in the developing human connectome project. *EClinicalMedicine* 38:100984. doi: 10.1016/j.eclinm.2021.100984

Christiaens, D., Cordero-Grande, L., Hutter, J., Price, A. N., Deprez, M., Hajnal, J. V., et al. (2019). Learning compact q -space representations for multi-shell diffusion-weighted MRI. *IEEE Trans. Med. Imaging* 38, 834–843. doi: 10.1109/TMI.2018.2873736

Christiaens, D., Cordero-Grande, L., Pietsch, M., Hutter, J., Price, A. N., Hughes, E. J., et al. (2021). Scattered slice SHARD reconstruction for motion correction in multi-shell diffusion MRI. *Neuroimage* 225:117437. doi: 10.1016/j.neuroimage.2020.117437

Collins-Jones, L. H., Arichi, T., Poppe, T., Billing, A., Xiao, J., Fabrizi, L., et al. (2021). Construction and validation of a database of head models for functional imaging of the neonatal brain. *Hum. Brain Mapp.* 42, 567–586. doi: 10.1002/hbm.25242

Cordero-Grande, L., Christiaens, D., Hutter, J., Price, A. N., and Hajnal, J. V. (2019). Complex diffusion-weighted image estimation via matrix recovery under general noise models. *Neuroimage* 200, 391–404. doi: 10.1016/j.neuroimage.2019.06.039

Cordero-Grande, L., Ferrazzi, G., Teixeira, R., O'muircheartaigh, J., Price, A. N., and Hajnal, J. V. (2020). Motion-corrected MRI with DISORDER: distributed and incoherent sample orders for reconstruction deblurring using encoding redundancy. *Magn. Reson. Med.* 84, 713–726. doi: 10.1002/mrm.28157

Cordero-Grande, L., Hughes, E. J., Hutter, J., Price, A. N., and Hajnal, J. V. (2018). Three-dimensional motion corrected sensitivity encoding reconstruction for multi-shot multi-slice MRI: application to neonatal brain imaging. *Magn. Reson. Med.* 79, 1365–1376. doi: 10.1002/mrm.26796

Cordero-Grande, L., Teixeira, R. P. A. G., Hughes, E. J., Hutter, J., Price, A. N., and Hajnal, J. V. (2016). Sensitivity encoding for aligned multishot magnetic resonance reconstruction. *IEEE Trans. Comput. Imaging* 2, 266–280. doi: 10.1109/tci.2016.2557069

Craddock, R. C., Jbabdi, S., Yan, C. G., Vogelstein, J. T., Castellanos, F. X., Di Martino, A., et al. (2013). Imaging human connectomes at the macroscale. *Nat. Methods* 10, 524–539. doi: 10.1038/nmeth.2482

Dimitrova, R., Pietsch, M., Christiaens, D., Ciarrusta, J., Wolfers, T., Batalle, D., et al. (2020). Heterogeneity in brain microstructural development following preterm birth. *Cereb Cortex* 30, 4800–4810. doi: 10.1093/cercor/bhaa069

Ding, Y., Acosta, R., Enguix, V., Suffren, S., Ortmann, J., Luck, D., et al. (2020). Using deep convolutional neural networks for neonatal brain image segmentation. *Front. Neurosci.* 14:207. doi: 10.3389/fnins.2020.00207

Elsabbagh, M., Gliga, T., Pickles, A., Hudry, K., Charman, T., Johnson, M. H., et al. (2013). The development of face orienting mechanisms in infants at-risk for autism. *Behav. Brain Res.* 251, 147–154. doi: 10.1016/j.bbr.2012.07.030

Elsabbagh, M., Volein, A., Holmboe, K., Tucker, L., Csibra, G., Baron-Cohen, S., et al. (2009). Visual orienting in the early broader autism phenotype: disengagement and facilitation. *J. Child. Psychol. Psychiatry* 50, 637–642. doi: 10.1111/j.1469-7610.2008.02051.x

Eyre, M., Fitzgibbon, S. P., Ciarrusta, J., Cordero-Grande, L., Price, A. N., Poppe, T., et al. (2021). The developing human connectome project: typical and disrupted perinatal functional connectivity. *Brain* 144, 2199–2213. doi: 10.1093/brain/awab118

Fitzgibbon, S. P., Harrison, S. J., Jenkinson, M., Baxter, L., Robinson, E. C., Bastiani, M., et al. (2020). The developing human connectome project (dHCP) automated resting-state functional processing framework for newborn infants. *Neuroimage* 223:117303. doi: 10.1016/j.neuroimage.2020.117303

Gaspar, A. S., Price, A. N., and Nunes, R. G. (2015). *Improving Foetal and Neonatal Echo-Planar Imaging with Image-Based Shimming*. http://hdl.handle.net/10451/22886

Gliga, T., Elsabbagh, M., Andravizou, A., and Johnson, M. (2009). Faces attract infants' attention in complex displays. *Infancy* 14, 550–562. doi: 10.1080/15250000903144199

Grigorescu, I., Vanes, L., Uus, A., Batalle, D., Cordero-Grande, L., Nosarti, C., et al. (2021). Harmonized segmentation of neonatal brain MRI. *Front. Neurosci.* 15:662005. doi: 10.3389/fnins.2021.662005

Haataja, L., Mercuri, E., Regev, R., Cowan, F., Rutherford, M., Dubowitz, V., et al. (1999). Optimality score for the neurologic examination of the infant at 12 and 18 months of age. *J. Pediatr.* 135, 153–161. doi: 10.1016/s0022-3476(99)70016-8

Hennel, F., Buehrer, M., Von Deuster, C., Seuven, A., and Pruessmann, K. P. (2016). SENSE reconstruction for multiband EPI including slice-dependent N/2 ghost correction. *Magn. Reson. Med.* 76, 873–879. doi: 10.1002/mrm.25915

Hisle-Gorman, E., Susi, A., Stokes, T., Gorman, G., Erdie-Lalena, C., and Nylund, C. M. (2018). Prenatal, perinatal, and neonatal risk factors of autism spectrum disorder. *Pediatr. Res.* 84, 190–198. doi: 10.1038/pr.2018.23

Hughes, E. J., Winchman, T., Padormo, F., Teixeira, R., Wurie, J., Sharma, M., et al. (2017). A dedicated neonatal brain imaging system. *Magn. Reson. Med.* 78, 794–804. doi: 10.1002/mrm.26462

Hutter, J., Christiaens, D. J., Schneider, T., Cordero-Grande, L., Slator, P. J., Deprez, M., et al. (2018a). Slice-level diffusion encoding for motion and distortion correction. *Med. Image Anal.* 48, 214–229. doi: 10.1016/j.media.2018.06.008

Hutter, J., Tournier, J. D., Price, A. N., Cordero-Grande, L., Hughes, E. J., Malik, S., et al. (2018b). Time-efficient and flexible design of optimized multishell HARDI diffusion. *Magn. Reson. Med.* 79, 1276–1292. doi: 10.1002/mrm.26765

Jeurissen, B., Tournier, J. D., Dhollander, T., Connelly, A., and Sijbers, J. (2014). Multi-tissue constrained spherical deconvolution for improved analysis of multi-shell diffusion MRI data. *Neuroimage* 103, 411–426. doi: 10.1016/j.neuroimage.2014.07.061

Kline, J. E., Illapani, V. S. P., He, L., Altaye, M., Logan, J. W., and Parikh, N. A. (2020). Early cortical maturation predicts neurodevelopment in very preterm infants. *Arch. Dis. Child. Fetal Neonatal. Ed.* 105, 460–465. doi: 10.1136/archdischild-2019-317466

Lankford, C. L., and Does, M. D. (2013). On the inherent precision of mcDESPOT. *Magn. Reson. Med.* 69, 127–136. doi: 10.1002/mrm.24241

Li, J., Osher, D. E., Hansen, H. A., and Saygin, Z. M. (2020). Innate connectivity patterns drive the development of the visual word form area. *Sci. Rep.* 10:18039. doi: 10.1038/s41598-020-75015-7

Makropoulos, A., Robinson, E. C., Schuh, A., Wright, R., Fitzgibbon, S., Bozek, J., et al. (2018). The developing human connectome project: a minimal processing pipeline for neonatal cortical surface reconstruction. *Neuroimage* 173, 88–112. doi: 10.1016/j.neuroimage.2018.01.054

Merhar, S. L., Kline, J. E., Braimah, A., Kline-Fath, B. M., Tkach, J. A., Altaye, M., et al. (2021). Prenatal opioid exposure is associated with smaller brain volumes in multiple regions. *Pediatr. Res.* 90, 397–402. doi: 10.1038/s41390-020-01265-w

Montagna, A., and Nosarti, C. (2016). Socio-emotional development following very preterm birth: pathways to psychopathology. *Front. Psychol.* 7:80. doi: 10.3389/fpsyg.2016.00080

Nehrke, K., and Bornert, P. (2012). DREAM—a novel approach for robust, ultrafast, multislice B_1 mapping. *Magn. Reson. Med.* 68, 1517–1526. doi: 10.1002/mrm.24158

O'Muircheartaigh, J., Robinson, E., Pietsch, M., Wolfers, T., Aljabar, P., Grande, L. C., et al. (2020). Modelling brain development to detect white matter injury in term and preterm born neonates. *Brain* 143, 467–479. doi: 10.1093/brain/awz412

Patel, H., Lee, S.-H., Breen, G., Menzel, S., Ojewunmi, O., and Dobson, R. J. B. et al. (2022). The COPILOT raw Illumina genotyping QC protocol. *Curr. Protoc.* 2:e373. doi: 10.1002/cpz1.373

Pietsch, M., Christiaens, D., Hajnal, J. V., and Tournier, J. D. (2021). dStripe: slice artefact correction in diffusion MRI via constrained neural network. *Med. Image Anal.* 74:102255. doi: 10.1016/j.media.2021.102255

Pietsch, M., Christiaens, D., Hutter, J., Cordero-Grande, L., Price, A. N., Hughes, E., et al. (2019). A framework for multi-component analysis of diffusion MRI data over the neonatal period. *Neuroimage* 186, 321–337. doi: 10.1016/j.neuroimage.2018.10.060

Putnam, S. P., and Rothbart, M. K. (2006). Development of short and very short forms of the children's behavior questionnaire. *J. Pers. Assess.* 87, 102–112. doi: 10.1207/s15327752jpa8701_09

Schuh, A., Makropoulos, A., Wright, R., Robinson, E. C., Tusor, N., Steinweg, J., et al. (2017). "A deformable model for the reconstruction of the neonatal cortex," in *2017 IEEE 14th International Symposium on Biomedical Imaging (ISBI 2017)*, (Piscataway, NJ: IEEE), 800–803.

Seidlitz, J., Vasa, F., Shinn, M., Romero-Garcia, R., Whitaker, K. J., Vertes, P. E., et al. (2018). Morphometric similarity networks detect microscale cortical organization and predict inter-individual cognitive variation. *Neuron* 97, 231–247.e7. doi: 10.1016/j.neuron.2017.11.039

Sinke, L., Cats, D., and Heijmans, B. T. (2021). Omixer: multivariate and reproducible sample randomization to proactively counter batch effects in omics studies. Bioinformatics 37, 3051–3052.

Tournier, J. D., Smith, R., Raffelt, D., Tabbara, R., Dhollander, T., Pietsch, M., et al. (2019). MRtrix3: a fast, flexible and open software framework for medical image processing and visualisation. *Neuroimage* 202, 116–137.

Tournier, J. D., Christiaens, D., Hutter, J., Price, A. N., Cordero-Grande, L., Hughes, E., et al. (2020). A data-driven approach to optimising the encoding for multi-shell diffusion MRI with application to neonatal imaging. *NMR Biomed.* 33:e4348. doi: 10.1002/nbm.4348

Van Essen, D. C., Smith, S. M., Barch, D. M., Behrens, T. E., Yacoub, E., Ugurbil, K., et al. (2013). The WU-Minn human connectome project: an overview. *Neuroimage* 80, 62–79. doi: 10.1016/j.neuroimage.2013.05.041

Wang, Q., Xu, Y., Zhao, T., Xu, Z., He, Y., and Liao, X. (2021). Individual uniqueness in the neonatal functional connectome. *Cereb Cortex* 31, 3701–3712. doi: 10.1093/cercor/bhab041

Wass, S., Porayska-Pomsta, K., and Johnson, M. H. (2011). Training attentional control in infancy. *Curr. Biol.* 21, 1543–1547. doi: 10.1016/j.cub.2011.08.004

Williams, L. A., Gelman, N., Picot, P. A., Lee, D. S., Ewing, J. R., Han, V. K., et al. (2005). Neonatal brain: regional variability of in vivo MR imaging relaxation rates at 3.0 T–initial experience. *Radiology* 235, 595–603. doi: 10.1148/radiol.2352031769

Wolke, D., Jaekel, J., Hall, J., and Baumann, N. (2013). Effects of sensitive parenting on the academic resilience of very preterm and very low birth weight adolescents. *J. Adolesc. Health* 53, 642–647. doi: 10.1016/j.jadohealth.2013.06.014

Zhu, K., Dougherty, R. F., Wu, H., Middione, M. J., Takahashi, A. M., Zhang, T., et al. (2016). Hybrid-space SENSE reconstruction for simultaneous multi-slice MRI. *IEEE Trans. Med. Imaging* 35, 1824–1836. doi: 10.1109/TMI.2016.2531635

Conflict of Interest: The authors declare that the research was conducted in the absence of any commercial or financial relationships that could be construed as a potential conflict of interest.

Citation: Edwards AD, Rueckert D, Smith SM, Abo Seada S, Alansary A, Almalbis J, Allsop J, Andersson J, Arichi T, Arulkumaran S, Bastiani M, Batalle D, Baxter L, Bozek J, Braithwaite E, Brandon J, Carney O, Chew A, Christiaens D, Chung R, Colford K, Cordero-Grande L, Counsell SJ, Cullen H, Cupitt J, Curtis C, Davidson A, Deprez M, Dillon L, Dimitrakopoulou K, Dimitrova R, Duff E, Falconer S, Farahibozorg S-R, Fitzgibbon SP, Gao J, Gaspar A, Harper N, Harrison SJ, Hughes EJ, Hutter J, Jenkinson M, Jbabdi S, Jones E, Karolis V, Kyriakopoulou V, Lenz G, Makropoulos A, Malik S, Mason L, Mortari F, Nosarti C, Nunes RG, O'Keeffe C, O'Muircheartaigh J, Patel H, Passerat-Palmbach J, Pietsch M, Price AN, Robinson EC, Rutherford MA, Schuh A, Sotiropoulos S, Steinweg J, Teixeira RPAG, Tenev T, Tournier J-D, Tusor N, Uus A, Vecchiato K, Williams LZJ, Wright R, Wurie J and Hajnal JV (2022) The Developing Human Connectome Project Neonatal Data Release. Front. Neurosci. 16:886772. doi: 10.3389/fnins.2022.886772

frontiers | Frontiers in Neuroscience

ORIGINAL RESEARCH
published: 07 June 2022
doi: 10.3389/fnins.2022.887634

FetalGAN: Automated Segmentation of Fetal Functional Brain MRI Using Deep Generative Adversarial Learning and Multi-Scale 3D U-Net

*Josepheen De Asis-Cruz[1], Dhineshvikram Krishnamurthy[1], Chris Jose[2], Kevin M. Cook[1] and Catherine Limperopoulos[1]**

[1] Developing Brain Institute, Department of Diagnostic Radiology, Children's National Hospital, Washington, DC, United States, [2] Department of Computer Science, University of Maryland, College Park, MD, United States

An important step in the preprocessing of resting state functional magnetic resonance images (rs-fMRI) is the separation of brain from non-brain voxels. Widely used imaging tools such as FSL's BET2 and AFNI's 3dSkullStrip accomplish this task effectively in children and adults. In fetal functional brain imaging, however, the presence of maternal tissue around the brain coupled with the non-standard position of the fetal head limit the usefulness of these tools. Accurate brain masks are thus generated manually, a time-consuming and tedious process that slows down preprocessing of fetal rs-fMRI. Recently, deep learning-based segmentation models such as convolutional neural networks (CNNs) have been increasingly used for automated segmentation of medical images, including the fetal brain. Here, we propose a computationally efficient end-to-end generative adversarial neural network (GAN) for segmenting the fetal brain. This method, which we call FetalGAN, yielded whole brain masks that closely approximated the manually labeled ground truth. FetalGAN performed better than 3D U-Net model and BET2: FetalGAN, Dice score = 0.973 ± 0.013, precision = 0.977 ± 0.015; 3D U-Net, Dice score = 0.954 ± 0.054, precision = 0.967 ± 0.037; BET2, Dice score = 0.856 ± 0.084, precision = 0.758 ± 0.113. FetalGAN was also faster than 3D U-Net and the manual method (7.35 s vs. 10.25 s vs. ∼5 min/volume). To the best of our knowledge, this is the first successful implementation of 3D CNN with GAN on fetal fMRI brain images and represents a significant advance in fully automating processing of rs-MRI images.

Keywords: fetal rs-fMRI, resting state, segmentation, deep learning, generative adversarial networks (GANs), 3D U-Net, fetal brain

OPEN ACCESS

Edited by:
Weihao Zheng,
Lanzhou University, China

Reviewed by:
Jian Shen,
Beijing Institute of Technology, China
Shijie Zhao,
Northwestern Polytechnical University, China

***Correspondence:**
Catherine Limperopoulos
climpero@childrensnational.org

Specialty section:
This article was submitted to Brain Imaging Methods, a section of the journal Frontiers in Neuroscience

Received: *01 March 2022*
Accepted: *16 May 2022*
Published: *07 June 2022*

Citation:
De Asis-Cruz J, Krishnamurthy D, Jose C, Cook KM and Limperopoulos C (2022) FetalGAN: Automated Segmentation of Fetal Functional Brain MRI Using Deep Generative Adversarial Learning and Multi-Scale 3D U-Net. Front. Neurosci. 16:887634. doi: 10.3389/fnins.2022.887634

INTRODUCTION

Resting state functional MRI (rs-fMRI) is an emergent technique for interrogating *in-vivo* fetal brain function. A critical step in preparing rs-fMRI images for analyses is separating brain from non-brain voxels. In most cases, fetal brain masks are generated manually, as imaging tools that are effectively used for adult whole brain segmentation do not accurately extract the fetal brain.

This suboptimal performance likely arises from the presence of surrounding maternal tissue, non-standard orientation of the fetal head, and reduced gray/white matter contrast in the fetal brain. While manual segmentation of the fetal brain provides reasonable brain masks, the process is time consuming and operator dependent. Automated processes have the potential to increase efficiency of pipelines and reproducibility of results.

A growing body of literature has demonstrated that deep learning-based segmentation outperforms traditional approaches including multi-atlas registration techniques (Huo et al., 2019; Khalili et al., 2019; Dolz et al., 2020; Zhao et al., 2022). Deep convolutional neural networks (CNN) such as U-Net have achieved remarkable success for anatomical medical image segmentation and have been shown to be versatile and effective (Ronneberger et al., 2015; Yang et al., 2018; Zhao et al., 2018; Son et al., 2020). Recently, 2D U-Net has been successfully applied to fetal resting state functional MRI data (Rutherford et al., 2021), a crucial step in automating preprocessing of fetal rs-fMRI. However, there are several limitations in using CNN-based approaches for segmentation (Ronneberger et al., 2015; Xue et al., 2018; Li et al., 2019; Rutherford et al., 2021). Although U-Nets can use skip connections to combine both low- and high-level features, there is no guarantee of spatial consistency in the final segmentation map, especially at the boundaries (Isola et al., 2017; Yang et al., 2018; Zhao et al., 2018; Dhinagar et al., 2021). To address this limitation, methods that consider spatial correlations among neighboring pixels such as conditional random field and other graph cut techniques are used as post-processing refinement (Pereira et al., 2016b; Nancy, 2019; Son et al., 2020). Utilizing pair-wise potentials, however, may cause serious boundary leakage, especially in low-contrast regions (Vijayanarasimhan and Grauman, 2010). To prevent leakage and the lack of spatial consistency, methods such as patch-based networks for training CNNs and multi-scale, multi-path CNNs with different input resolutions/network architectures have been used (Pereira et al., 2016a; Havaei et al., 2017; Kamnitsas et al., 2017; Chattopadhay et al., 2018; Xiao et al., 2020; Ghimire et al., 2021; Zhang et al., 2021; Zhu et al., 2021). However, patch-based training is computationally costly. Moreover, finding the optimal patch size that achieves superior localization accuracy is challenging. Generally, traditional CNNs have a tradeoff between achieving good localization performance/higher level of semantics (i.e., correctly classifying each voxel's label) and crisper, more well-defined boundaries. This is a potential disadvantage specifically when applied to brain segmentation of fetal rs-fMRI, which often have low-contrast boundaries, varied voxel intensities, and features at different scales/orientations (Ronneberger et al., 2015; Xue et al., 2018; Dolz et al., 2020; Rutherford et al., 2021).

Recently, generative adversarial networks (GANs) have been shown to be a robust approach for automated medical image segmentation and to yield better, stable performance compared to state-of-the-art CNN-based models (Isola et al., 2017; Xue et al., 2018; Xun et al., 2021). Using two competing neural networks—a generator and a discriminator—GANs create exemplar images that are difficult to distinguish from real (i.e., training) images, effectively modeling any distribution of data (Gonog and Zhou, 2019). The generative network creates new examples of the data while the discriminator simultaneously evaluates these exemplars in a cyclic fashion effectively giving rise to a network that self-optimizes its error rate and converges on a model with high accuracy. Specifically, adversarial losses enforced by the discriminator network consider higher-order potentials, as opposed to the pairwise correlations utilized by voxel-wise loss functions, such as softmax. This adversarial loss serves as an adaptively learned similarity measure between the predicted segmentation label maps and the annotated ground truth that improves localization accuracy while enforcing spatial contiguity at low contrast regions, including image boundaries. Various end-to-end adversarial neural networks (e.g., SegAN) have been proposed as stable and effective frameworks for automatic segmentation (SegAN) of organs such as the brain, chest, and abdomen, among others (Frid-Adar et al., 2018; Giacomello et al., 2020; Xun et al., 2021; Zhu et al., 2021). Furthermore, a recent study by Chen et al. (2022) showed that a GAN-based paradigm improved the robustness and generalizability of deep learning models like graph neural networks (GNNs). Using their model on multi-modal MRI data, they identified autism spectrum disorders (ASD) with higher accuracy (74.7%) compared to other state-ot-the-art deep learning methods.

Motivated by SegAN, here, we propose FetalGAN, a GAN based end-to-end architecture for the automated segmentation of fetal rs-fMRI brain images. FetalGAN addresses the previously described drawbacks of deep CNNs and may be better suited for low-contrast fetal rs-fMRI. We hypothesized that FetalGAN will produce whole brain labels that closely approximate the manually created ground truth and will outperform deep CNN-based models (i.e., 3D U-Net) and the commonly used BET2 algorithm.

MATERIALS AND METHODS

Data

We initially evaluated 75 rs-fMRI scans. Out of the 75 datasets, four were excluded from further analyses: three had image dimensions (x, y, or z) that exceeded the chosen patch size of $32 \times 32 \times 32$, and one had incomplete demographic data. The final sample consisted of 71 datasets from 64 healthy fetuses.

Pregnant women were recruited as part of a larger study investigating brain development in healthy and high-risk fetuses. All participants had normal ultrasonograms/echocardiograms and structurally normal brains on MRI. Fetal exclusion criteria included: dysmorphic features by antenatal ultrasound, chromosomal abnormalities by amniocentesis, evidence of congenital infections, presentation after 28 weeks gestational age, and multiple gestation. Maternal exclusion criteria included: pregnant women with known psychiatric/metabolic/genetic disorders, complicated/multiple pregnancies, alcohol and/or tobacco use, maternal medications, and contraindications to MRI.

Data were collected using a 1.5T GE MRI scanner (GE Healthcare, Milwaukee, WI) with an 8-channel receiver

coil. Anatomical single-shot fast spin-echo anatomical T2-weighted images were collected with the following parameters: TR = 1,100 ms, TE = 160 ms, flip angle = 90°, and slice thickness = 2 mm. Resting-state echo planar images (EPI) images were collected with the following parameters: TR = 3,000 ms, TE = 60 ms, voxel size = 2.578 mm × 2.578 mm × 3 mm, flip angle = 90°, field of view = 33 cm, matrix size = 128 × 128, and scan duration = 7 min (140 volumes). On average, 5:21 min (107 volumes) of resting-state data was available after preprocessing.

Preprocessing

Fetal resting state data were preprocessed up to the point of brain segmentation using AFNI, unless specified otherwise (Cox, 1996). Briefly, as previously described here (De Asis-Cruz et al., 2021), fetal EPI images were slice time corrected, trimmed by removing the first four volumes to stabilize magnetic gradients, manually oriented to radiologic orientation using landmark based rigid registration (IRTK[1]), despiked, and then corrected for bias-field inhomogeneities (N4BiasFieldCorrection) (Tustison et al., 2010). At this point, the oriented EPI images were ready for motion correction. For this step, we used a two-pass registration approach optimized to correct for the high-motion typically observed in fetuses and newborns (Joshi et al., 2011; Scheinost et al., 2018). This method required two inputs: a reference volume and its mask. For each resting state (RS) dataset, a reference volume was defined using AFNI's 3dToutcount; this identifies the volume with the lowest fraction of outlier voxels based on signal intensity trend. A brain mask was then manually drawn (JDC) for each reference brain volume using ITK-SNAP (Yushkevich et al., 2006). The goal was to automatically create this whole brain mask and provide it as input to the motion correction algorithm. The selected reference volume and the manual brain mask were utilized as inputs for training the model. During testing, the reference image was segmented using three different approaches: FSL Brain Extraction Tool v2 (BET2) (Smith, 2002), 3D U-Net (Çiçek et al., 2016), and FetalGAN. Segmentation outputs were compared to the manually created mask using the following metrics: Dice index, Jaccard score, sensitivity, specificity, and precision. We also reported the computation time for each method.

SegAN Architecture

We used the GAN framework to automatically segment the fetal brain from rs-fMRI scans. The algorithm consisted of two neural networks: the generator (segmenter) based on 3D U-Net, and the discriminator (critic) based on a fully convolutional decoder network (Xue et al., 2018).

The generator network received a 3D patch as an input and consisted of eight residual convolutional blocks with the leaky rectified linear unit (ReLU) activation, batch normalization, and maxpooling layers (**Figure 1**, top; see 3D U-Net Architecture for details). In the encoding branch, the upsampling layers had a kernel size of 3 × 3 × 3 with stride 2 × 2 × 2; in the decoding branch, the downsampling layers resized by a factor of 2 and used a kernel size of 2 × 2 × 2. The discriminator network's structure was like the deconvolution block of the generator. Receiving both the ground truth and predicted label map, the discriminator extracted hierarchical features to quantify differences between these two input images. Please see **Supplementary Material** for a summary of generator and discriminator parameters.

SegAN learns a loss function that penalizes structural differences between the discriminator network output and target (Xue et al., 2018). Rather than computing discriminator loss for the entire network, we computed loss at each discriminator layer. The multi-scale loss function L was defined by Xue et al. (2018) as,

$$\min_{\theta_G} \max_{\theta_D} L\ (\theta_G, \theta_D) = \frac{1}{N} \sum_{n=1}^{N} l_{mae}\left(f_D\left(x_n \cdot G\left(x_n\right)\right),\ f_D(x_n \cdot y_n)\right) \tag{1}$$

where x is the training image; y its corresponding ground truth; N is the number of training images; l_{mae} is the mean absolute error (MAE) or $L1$ distance; $x_n \cdot G(x_n)$ is the probabilistic map generated by the generator network; $x_n \cdot y_n$ is the input image masked by its corresponding ground truth; and $f_D(x)$ represent the hierarchical features extracted from image x by the discriminator network. Using a multi-scale loss function to quantify training error, the network sequentially learned both global and local features and encoded long and short-range spatial relationships between voxels. As training progressed, the generator network was able to produce probabilistic predictions that more closely approximated the expert-annotated, ground truth.

3D U-Net Architecture

3D U-Net, patch-based architecture was also performed (**Figure 1**, top). The network consisted of both an expanding and contracting path. Here, the contracting path was supplemented with successive layers where the standard pooling operators were replaced with upsampling operators to enhance image resolution. The high-resolution feature from the contracting path was then concatenated with the upsampled features from the expanding path for localization of the fetal brain. The expanding and contracting paths had four convolutional blocks, each with two Conv3D layers, BatchNormalization, and the PReLU activation function. In each convolutional block, the number of feature maps was doubled per layer (96 initial feature maps and 364 feature maps generated after the last block); a kernel size of 3 and 2 was used for the expanding and contracting paths, respectively. At the junction of the contracting/expanding path, the layers were regularized using dropout with a rate of 15%. In the expanding path, a MaxPooling (downsampling) layer with stride 2 followed each convolution block to encode the input 3D patches into feature representations at different levels. Deconvolution layers (upsampling) were used intermittently throughout the contracting path to increase the density of the sparse feature maps of the expanding path using a transpose convolution with multiple trainable filters.

[1]https://github.com/BioMedIA/IRTK

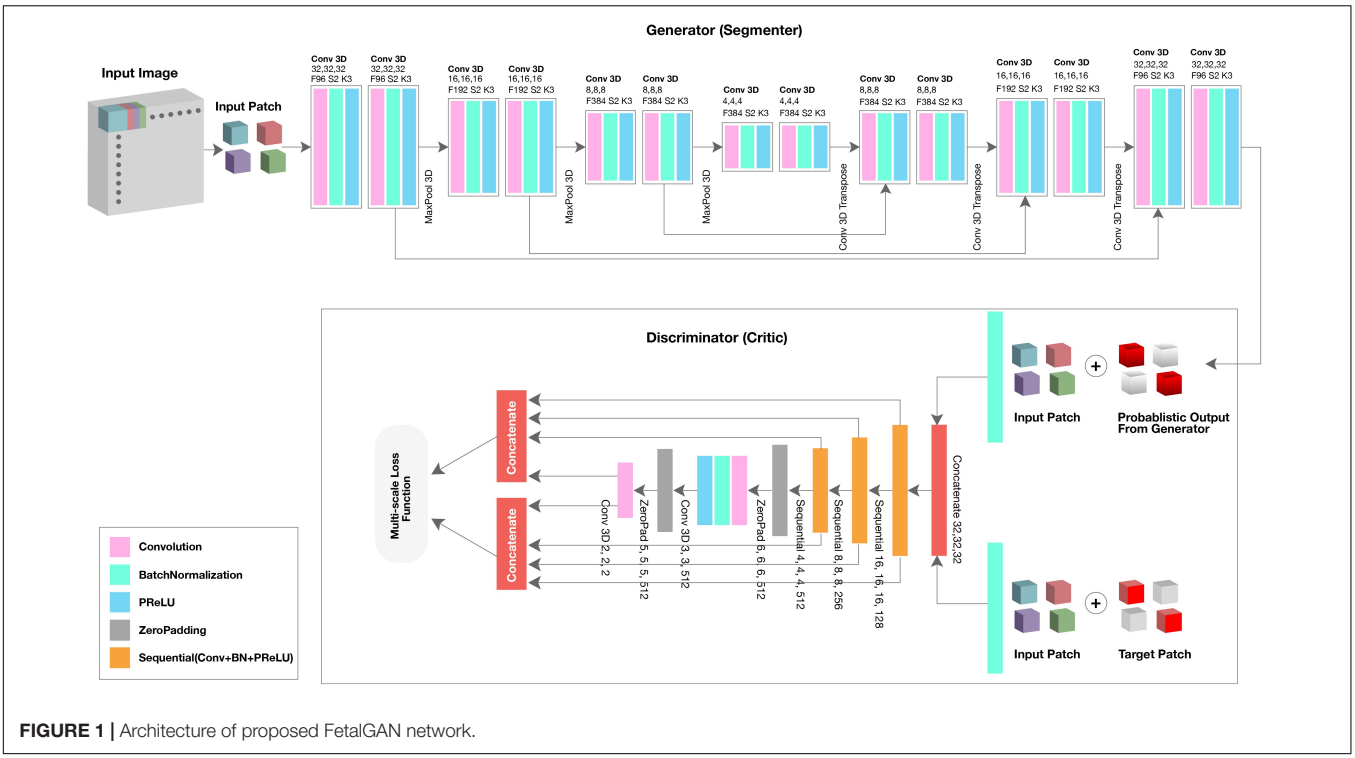

FIGURE 1 | Architecture of proposed FetalGAN network.

TABLE 1 | Comparison of FetalGAN, 3D U-Net, and BET2.

	FetalGAN	3D U-Net		BET2	
	Mean ± SD	**Mean ± SD**	***p****	**Mean ± SD**	***p****
Dice	0.973 ± 0.013	0.954 ± 0.054	9.260×10^{-4}	0.856 ± 0.084	1.124×10^{-18}
Jaccard	0.948 ± 0.024	0.916 ± 0.082	1.993×10^{-4}	0.756 ± 0.113	4.910×10^{-23}
Precision	0.977 ± 0.015	0.967 ± 0.037	0.043	0.758 ± 0.113	6.685×10^{-26}
Sensitivity	0.971 ± 0.021	0.945 ± 0.077	0.002	0.996 ± 0.011	$1.493 \times \times 10^{-17}$
Specificity	0.994 ± 0.005	0.992 ± 0.010	0.239	0.915 ± 0.051	3.703×10^{-21}
Time/patch (s)	0.05	0.08		-	
Time/vol (s)	7.35	10.25		4.40	

**FetalGAN compared to 3D U-Net and BET2, asterisk (*) indicates significant difference between method and FetalGAN using paired t-test.*

The successive downsampling and upsampling feature maps were concatenated to localize and learn representations after each convolution.

Training Specifications

The SegAN was trained using a multi-scale loss function, the U-Net model using binary cross-entropy loss. For both, weights were determined using an Adam optimizer (Kingma and Ba, 2014). The models were trained on 71 reference brain volumes and their corresponding manually drawn masks. We used k-fold cross validation, where $k = 5$, for evaluating the model's performance. Each 3D MR scan and its respective normalized mask was split into patches of size $32 \times 32 \times 32$ with stride $2 \times 2 \times 2$ and fed into the model for training. Given a test EPI image, we extracted the overlapped patches with size $32 \times 32 \times 32$, and fed them to the trained network to obtain the final probability label map.

The final segmentation results were derived by averaging together the probability maps of each overlapped patch. The model training and validation are performed on NVIDIA V100 multi-GPU. After prediction, isolated and/or misidentified voxels were corrected, and internal holes were filled using morphological operations available in the openCV library (Bradski, 2000).

RESULTS

We evaluated 71 datasets from 64 healthy fetuses between 25 and 39.43 gestational weeks (mean GA ± SD: 33.28 ± 3.79; see **Supplementary Material** for age distribution). The average scan interval for the seven fetuses with two scans is 7.63 ± 2.48 weeks.

The proposed SegAN method was more time efficient than 3D U-Net, requiring, on average, 7.35 s to segment a single volume

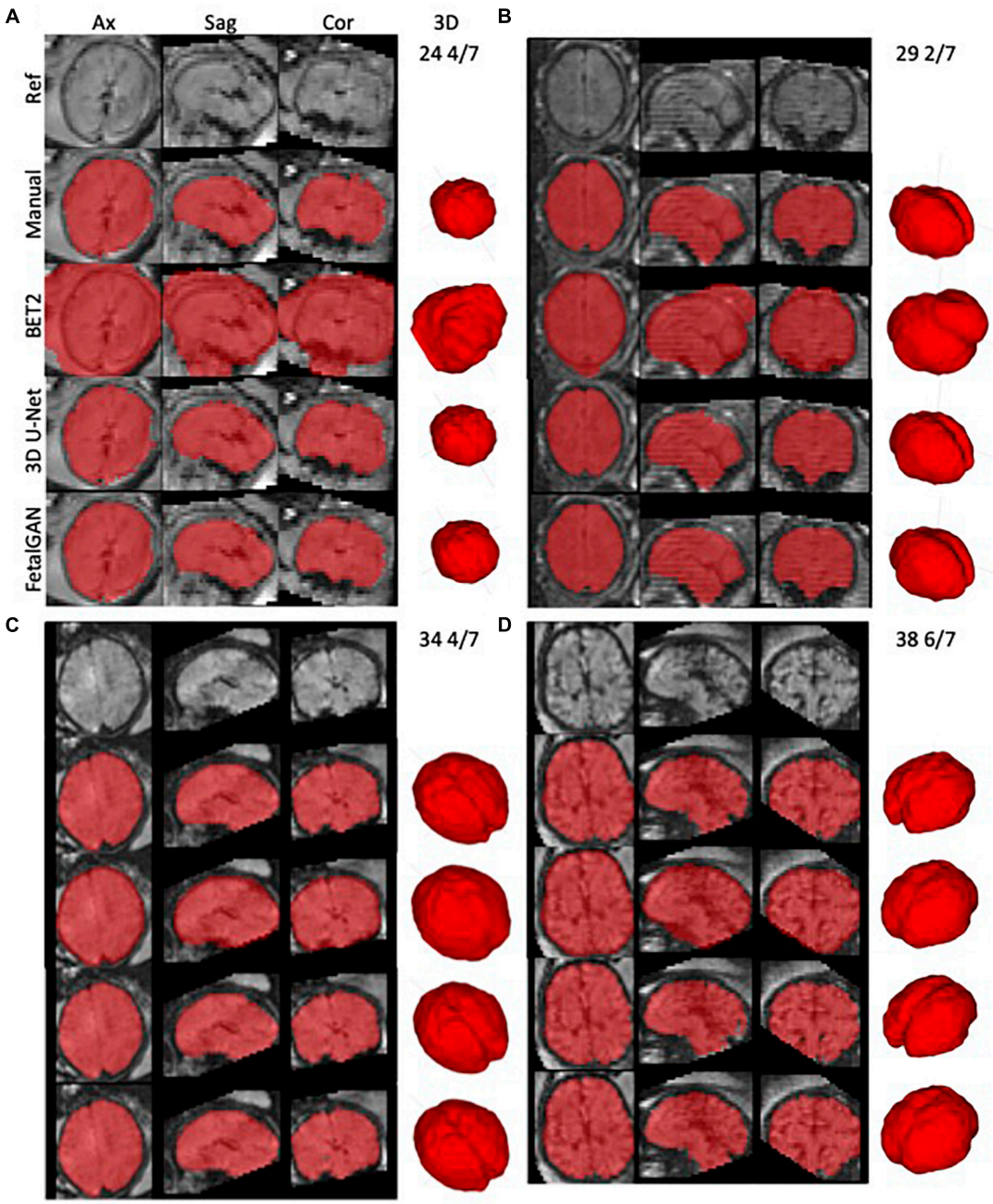

FIGURE 2 | Representative whole brain masks from manual segmentation, BET2, 3D U-Net, and FetalGAN. Manual corrections were done using ITK-SNAP. FetalGAN produced the most accurate segmentation relative to the ground truth with an average Dice score of 0.942 ± 0.095. **(A)** 25 4/7 weeks, **(B)** 29 2/7 weeks, **(C)** 34 4/7 weeks, and **(D)** 38 6/7 weeks.

compared to 10.25 s for the latter (**Table 1**). BET2 was the fastest algorithm, needing only 4.40 s to extract the brain.

Whole brain segmentation outputs of FetalGAN, FSL's BET2, and 3D U-Net were compared to the manually segmented brains. The proposed method's Dice score, Jaccard index, precision, and specificity were significantly higher than 3d U-Net and BET2 (paired t-test $p < 0.05$; see **Table 1**). FetalGAN's specificity was comparable to 3D U-Net and higher than BET2. Visual inspection of representative scans (**Figure 2**) showed FetalGAN outputs more closely resembled the ground truth. The 3D reconstructed surface of the segmentations by SegAN and U-Net is smoother when compared to the outputs of the manual and BET segmentation.

FetalGAN and 3D U-Net performance showed stability across GAs (**Figure 3**). The Dice and Jaccard scores for these

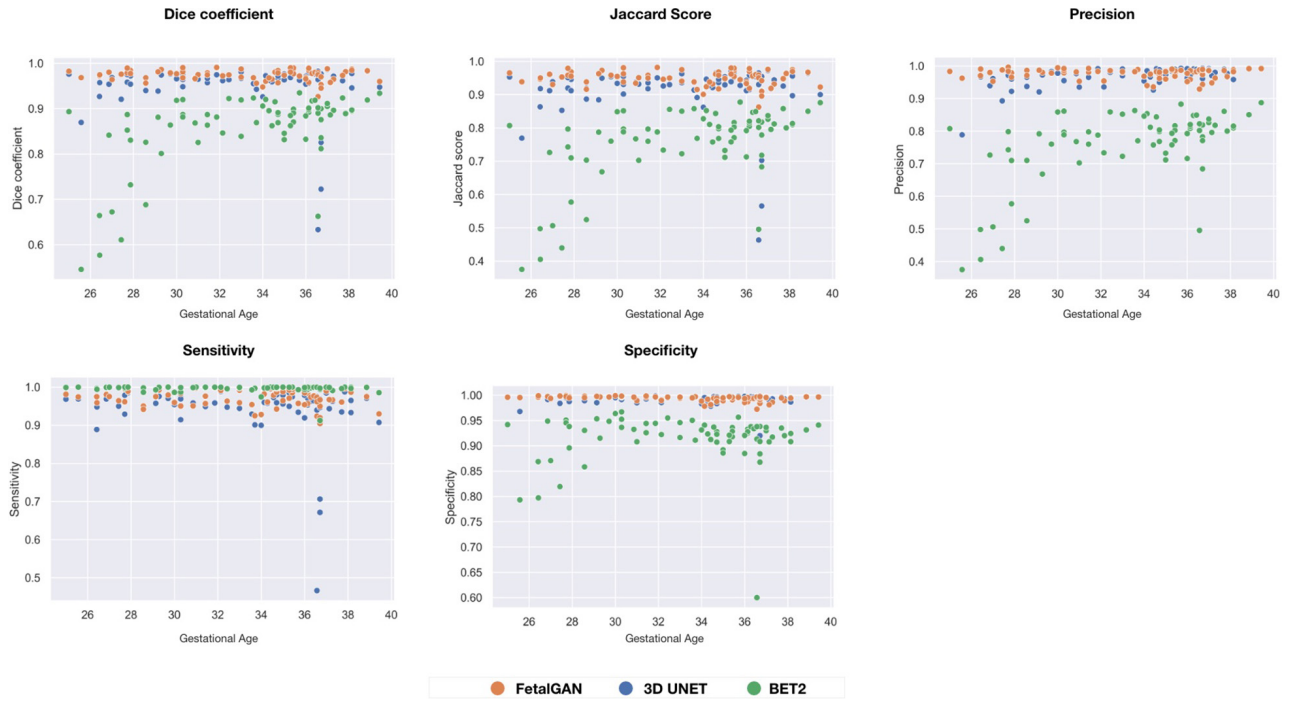

FIGURE 3 | Performance scores fo FetalGAN, 3D U-Net and BET2 methods across gestation ages: **(A)** Dice coefficient, **(B)** Jaccard Score, **(C)** Precision, **(D)** Sensitivity, and **(E)** Specificity.

two models were uncorrelated with age (Pearson r = –0.114, p = 0.230 and r = –0.1410, p = 0.241, FetalGAN and 3D U-Net, respectively; see **Supplementary Table 1**). FetalGAN specificity decreased with increasing GA. Despite this decrease, specificity remained high (range: 0.9723–0.9993) and was comparable to 3D U-Net and significantly better than BET2. Unlike the deep learning models, BET2 Dice coefficients and Jaccard indices were positively correlated with age (r = 0.558, p = 4.228 × 10^{-7} and r = 0.564, p = 2.985 × 10^{-7}, respectively). Precision also positively scaled with increasing GA for both BET2 (r = 0.568, p = 2.396 × 10^{-7}) and 3D U-Net (r = 0.317, p = 0.007).

DISCUSSION

We successfully implemented FetalGAN, a SegAN-based model, to accurately extract the fetal EPI brain from the maternal compartment in a sample of 71 normative fetal rs-fMRI datasets. The whole brain mask generated by FetalGAN closely approximated manually segmented images. The proposed model produced outputs superior to labels derived from 3D U-Net and FSL's BET2. FetalGAN masks were also generated at a faster rate than U-Net and with only a minimal increase in preprocessing time compared to BET2. In addition, the proposed method produced consistently accurate segmentation across gestational ages. These findings suggest that FetalGAN is a robust, fast, and reliable approach to segmenting fetal rs-fMRI images.

To the best of our knowledge, the proposed method is the first successful application of the SegAN framework for segmentation of the fetal EPI brain and only the second automated tool for accurately separating the fetal brain from surrounding maternal tissue (Rutherford et al., 2021). We speculate that the modifications applied to the conventional GAN framework accounted for the superior performance of FetalGAN over the 3D U-Net model. Previous, conventional GAN approaches have been reported to be unstable at times due to failures during training, such as vanishing gradients and non-convergence (Isola et al., 2017; Xue et al., 2018). In other words, the adversarial loss, which classifies the image based on a scalar output by the discriminator, was unable to propagate sufficient gradients to improve the performance of the generator network (i.e., insufficient information passed on to the generator). FetalGAN utilized a multi-scale, weighted feature loss function, which effectively quantified minute differences between the generated and ground truth segmentation across multiple layers of the network. This enabled both the generator and discriminator networks to learn hierarchical features that captured relationships between voxels, especially in low contrast regions around the boundary between the fetal brain and maternal tissue. Altogether, these permitted the training process of FetalGAN to be end-to-end and stable. Moreover, FetalGAN performed faster than the comparable 3D U-Net implementation because the number of trainable parameters in the generator network was less than a 3D U-Net model. FetalGAN also outperformed BET2, likely because the boundary between fetal brain and non-brain voxels was

low-contrast and BET2 relied on intensity differences between tissues to accurately estimate the boundary of the brain (Smith, 2002).

One recent study successfully implemented 2D U-Net to automatically segment the fetal EPI brain (Rutherford et al., 2021). Trained on 855 images from 129 subjects, their model yielded slightly lower performance metrics compared to FetalGAN (2D U-Net: Dice score = 0.94 ± 0.069, Jaccard index = 0.89 ± 0.069 vs. FetalGAN: Dice score = 0.973 ± 0.013, Jaccard index = 0.948 ± 0.024). In the 2D U-Net model, images were segmented in their original space; in contrast, FetalGAN was applied to oriented images. During development of our pipeline, we observed that orienting images prior to brain extraction allowed more options in subsequent preprocessing steps, thus we repositioned the brains prior to segmentation. Another critical difference between the two models is that FetalGAN was trained using 3D patches, thus it can leverage spatial information across three dimensions (i.e., interslice relationships) whereas 2D convolutional kernels obtain context only across the width and height of a slice. Moreover, with 3D U-Net, warping or normalization was not required. While we did not directly compare 2D and 3D U-Net models, previous studies have demonstrated the advantage of 3D over 2D CNNs (Nemoto et al., 2020; Woo and Lee, 2021).

FetalGAN aims to provide an automated alternative to manual segmentation of fetal rs-fMRI data. FetalGAN addresses drawbacks inherent to manual processes. First, since the process is automated, outputs are replicable. Second, the need for highly skilled operators is eliminated. Lastly, relative to manual segmentation, the time required to segment a brain volume is markedly reduced. Taken together, these three main areas of improvement are a critical step toward increasing rigor and reproducibility in fetal neuroimaging. While this is but one of the first steps in fetal rs-fMRI preprocessing, we believe that our proposed method will contribute to the field's broader and overarching goal of creating fully automated pipelines such as what's currently available for older children and adults with SPM,[2] AFNI (Cox, 1996), or FSL (Jenkinson et al., 2012) (or pipelines that combine these such as fMRIPrep[3] and CPAC,[4] among others). The widespread availability of these tools to the larger scientific community has been instrumental in advancing our understanding of human health and disease.

Our work has several limitations. First, we used fewer training data sets for fetal EPI brain segmentation compared to a previous study (Rutherford et al., 2021). With the smaller sample size, however, we achieved comparable performance. Moreover, it should be noted that our inputs are 3D rather than 2D, thus the information that is fed into the learning model is likely comparable. Second, we used data from a single site. Additional studies that test the model on data collected from other institutions would support the generalizability of FetalGAN. Lastly, the paper demonstrated FetalGAN's superior performance, but further studies that integrate brain extraction with other preprocessing steps to yield a fully automated pipeline are needed.

With mounting evidence supporting the fetal origins of many prevalent adult disorders including mental illness (Barker et al., 2009; Al-Haddad et al., 2019), there has been increased interest in investigating fetal functional brain development *in vivo* using MRI. FetalGAN, an implementation of SegAN for fetal rs-fMRI brain, offers a fast, automated, unbiased, and accurate alternative to currently available fetal EPI brain extraction techniques. Further improvements that focus on increasing computational efficiency, extracting the brain in the original space, and integrating FetalGAN into a fully automated fetal rs-fMRI pipeline, among others, are currently underway. It is our hope that this technique would help facilitate *in utero* investigations of emerging functional connectivity.

DATA AVAILABILITY STATEMENT

The datasets presented will be provided upon reasonable request to the corresponding author. Requests to access the datasets should be directed to CL, climpero@childrensnational.org.

ETHICS STATEMENT

The studies involving human participants were reviewed and approved by the Institutional Review Board at Children's National Hospital. The patients/participants provided their written informed consent to participate in this study.

AUTHOR CONTRIBUTIONS

JD-C: conceptualization, methodology, validation, formal analysis, investigation, data curation, writing—original draft, review, and editing, and supervision. DK and CJ: conceptualization, methodology, validation, formal analysis, investigation, data curation, writing—original draft, review, and editing, and visualization. KC: investigation and writing—original draft, review, and editing. CL: conceptualization, methodology, resources, writing—review and editing, supervision, and funding acquisition. All authors contributed to the article and approved the submitted version.

FUNDING

This study was funded by grant R01 HL116585–01 from the National Heart, Lung, and Blood Institute, National Institutes of Health (CL) and grant MOP-81116 from the Canadian Institute of Health Research (CL).

[2]https://www.fil.ion.ucl.ac.uk/spm/software/spm12/

[3]https://fmriprep.org/en/stable/index.html

[4]https://fcp-indi.github.io/docs/latest/user/quick

ACKNOWLEDGMENTS

We thank the pregnant women who participated in this study. We are grateful to our study team for supporting recruitment, enrollment, and for performing the fetal MRI studies.

SUPPLEMENTARY MATERIAL

The Supplementary Material for this article can be found online at: https://www.frontiersin.org/articles/10.3389/fnins.2022.887634/full#supplementary-material

REFERENCES

Al-Haddad, B. J. S., Jacobsson, B., Chabra, S., Modzelewska, D., Olson, E. M., Bernier, R., et al. (2019). Long-term risk of neuropsychiatric disease after exposure to infection in utero. *JAMA Psychiatry* 76, 594–602. doi: 10.1001/jamapsychiatry.2019.0029

Barker, D. J. P., Osmond, C., Kajantie, E., and Eriksson, J. G. (2009). Growth and chronic disease: findings in the helsinki birth cohort. *Ann. Hum. Biol.* 36, 445–458. doi: 10.1080/03014460902980295

Bradski, G. (2000). The openCV library. *Dr. Dobb's J. Soft. Tools Profess. Progr.* 25, 120–123.

Chattopadhay, A., Sarkar, A., Howlader, P., and Balasubramanian, V. N. (2018). "Grad-CAM++: generalized gradient-based visual explanations for deep convolutional networks," in *Proceeding of the 2018 IEEE Winter Conference on Applications of Computer Vision (WACV) (IEEE)*, doi: 10.1109/wacv.2018.00097

Chen, Y., Yan, J., Jiang, M., Zhang, T., Zhao, Z., Zhao, W., et al. (2022). Adversarial learning based node-edge graph attention networks for autism spectrum disorder identification. *Trans. Neural Netw. Learn. Syst.* 2022:4755. doi: 10.1109/TNNLS.2022.3154755

Çiçek, Ö, Abdulkadir, A., Lienkamp, S. S., Brox, T., and Ronneberger, O. (2016). "3D U-net: learning dense volumetric segmentation from sparse annotation," in *Medical Image Computing and Computer-Assisted Intervention – MICCAI 2016 Lecture Notes in Computer Science*, eds S. Ourselin, L. Joskowicz, M. R. Sabuncu, G. Unal, and W. Wells (Cham: Springer International Publishing), 424–432.

Cox, R. W. (1996). AFNI: software for analysis and visualization of functional magnetic resonance neuroimages. *Comput. Biomed. Res.* 29, 162–173. doi: 10.1006/cbmr.1996.0014

De Asis-Cruz, J., Andersen, N., Kapse, K., Khrisnamurthy, D., Quistorff, J., Lopez, C., et al. (2021). Global network organization of the fetal functional connectome. *Cereb. Cortex* 2021:410. doi: 10.1093/cercor/bhaa410

Dhinagar, N. J., Thomopoulos, S. I., Owens-Walton, C., Stripelis, D., Ambite, J. L., Ver Steeg, G., et al. (2021). 3D convolutional neural networks for classification of Alzheimer's and parkinson's disease with T1-weighted brain MRI. *bioRxiv* [Preprint] doi: 10.1101/2021.07.26.453903

Dolz, J., Desrosiers, C., Wang, L., Yuan, J., Shen, D., and Ben Ayed, I. (2020). Deep CNN ensembles and suggestive annotations for infant brain MRI segmentation. *Comput. Med. Imaging Graph.* 79:101660. doi: 10.1016/j.compmedimag.2019.101660

Frid-Adar, M., Diamant, I., Klang, E., Amitai, M., Goldberger, J., and Greenspan, H. (2018). GAN-based synthetic medical image augmentation for increased CNN performance in liver lesion classification. *Neurocomputing* 321, 321–331. doi: 10.1016/j.neucom.2018.09.013

Ghimire, K., Chen, Q., and Feng, X. (2021). "Patch-based 3D UNet for head and neck tumor segmentation with an ensemble of conventional and dilated convolutions," in *Head and Neck Tumor Segmentation Lecture Notes in Computer Science*, (Cham: Springer International Publishing), 78–84.doi: 10.1007/978-3-030-67194-5_9

Giacomello, E., Loiacono, D., and Mainardi, L. (2020). "Brain MRI tumor segmentation with adversarial networks," in *Proceeding of the 2020 International Joint Conference on Neural Networks (IJCNN) (IEEE)*, doi: 10.1109/ijcnn48605.2020.9207220

Gonog, L., and Zhou, Y. (2019). "A review: generative adversarial networks," in *Proceeding of the 2019 14th IEEE Conference on Industrial Electronics and Applications (ICIEA) (IEEE)*, doi: 10.1109/iciea.2019.8833686

Havaei, M., Davy, A., Warde-Farley, D., Biard, A., Courville, A., Bengio, Y., et al. (2017). Brain tumor segmentation with deep neural networks. *Med. Image Anal.* 35, 18–31. doi: 10.1016/j.media.2016.05.004

Huo, Y., Xu, Z., Xiong, Y., Aboud, K., Parvathaneni, P., Bao, S., et al. (2019). 3D whole brain segmentation using spatially localized atlas network tiles. *Neuroimage* 194, 105–119. doi: 10.1016/j.neuroimage.2019.03.041

Isola, P., Zhu, J.-Y., Zhou, T., and Efros, A. A. (2017). "Image-to-image translation with conditional adversarial networks," in *Proceeding of the 2017 IEEE Conference on Computer Vision and Pattern Recognition (CVPR) (IEEE)*, doi: 10.1109/cvpr.2017.632

Jenkinson, M., Beckmann, C. F., Behrens, T. E. J., Woolrich, M. W., and Smith, S. M. (2012). FSL. *Neuroimage* 62, 782–790. doi: 10.1016/j.neuroimage.2011.09.015

Joshi, A., Scheinost, D., Okuda, H., Belhachemi, D., Murphy, I., Staib, L. H., et al. (2011). Unified framework for development, deployment and robust testing of neuroimaging algorithms. *Neuroinformatics* 9, 69–84. doi: 10.1007/s12021-010-9092-8

Kamnitsas, K., Ledig, C., Newcombe, V. F. J., Simpson, J. P., Kane, A. D., Menon, D. K., et al. (2017). Efficient multi-scale 3D CNN with fully connected CRF for accurate brain lesion segmentation. *Med. Image Anal.* 36, 61–78. doi: 10.1016/j.media.2016.10.004

Khalili, N., Turk, E., Benders, M. J. N. L., Moeskops, P., Claessens, N. H. P., de Heus, R., et al. (2019). Automatic extraction of the intracranial volume in fetal and neonatal MR scans using convolutional neural networks. *NeuroImage Clin.* 24:102061. doi: 10.1016/j.nicl.2019.102061

Kingma, D. P., and Ba, J. (2014). Adam: a method for stochastic optimization. *arXiv* [preprint] doi: 10.48550/arXiv.1412.6980

Li, J., Gao, M., and D'Agostino, R. (2019). Evaluating classification accuracy for modern learning approaches. *Stat. Med.* 38, 2477–2503. doi: 10.1002/sim.8103

Nancy, W. A. (2019). Brain tumor segmentation using normalized graph cuts. *Int. J. Eng. Adv. Technol.* 8, 3159–3161. doi: 10.35940/ijeat.F9258.088619

Nemoto, T., Futakami, N., Yagi, M., Kumabe, A., Takeda, A., Kunieda, E., et al. (2020). Efficacy evaluation of 2D, 3D U-Net semantic segmentation and atlas-based segmentation of normal lungs excluding the trachea and main bronchi. *J. Radiat. Res.* 61, 257–264. doi: 10.1093/jrr/rrz086

Pereira, S., Pinto, A., Oliveira, J., Mendrik, A. M., Correia, J. H., and Silva, C. A. (2016b). Automatic brain tissue segmentation in MR images using random forests and conditional random fields. *J. Neurosci. Methods* 270, 111–123. doi: 10.1016/j.jneumeth.2016.06.017

Pereira, S., Pinto, A., Alves, V., and Silva, C. A. (2016a). Brain tumor segmentation using convolutional neural networks in MRI images. *IEEE Trans. Med. Imaging* 35, 1240–1251. doi: 10.1109/TMI.2016.2538465

Ronneberger, O., Fischer, P., and Brox, T. (2015). "U-net: convolutional networks for biomedical image segmentation," in *Medical Image Computing and Computer-Assisted Intervention – MICCAI 2015*, eds N. Navab, J. Hornegger, W. Wells, and A. Frangi (Cham: Springer International Publishing), 234–241.

Rutherford, S., Sturmfels, P., Angstadt, M., Hect, J., Wiens, J., van den Heuvel, M. I., et al. (2021). Automated brain masking of fetal functional MRI with open data. *Neuroinformatics* 2021:528. doi: 10.1007/s12021-021-09528-5

Scheinost, D., Onofrey, J. A., Kwon, S. H., Cross, S. N., Sze, G., Ment, L. R., et al. (2018). "A fetal fMRI specific motion correction algorithm using 2nd order edge features," in *Proceeding of the 2018 IEEE 15th International Symposium on Biomedical Imaging (ISBI 2018)*, (IEEE), doi: 10.1109/isbi.2018.8363807

Smith, S. M. (2002). Fast robust automated brain extraction. *Hum. Brain Mapp.* 17, 143–155. doi: 10.1002/hbm.10062

Son, H. H., Phuong, P. C., van Walsum, T., and Ha, L. M. (2020). Liver segmentation on a variety of computed tomography (CT) images based on convolutional neural networks combined with connected components. *VNU J. Sci. Comput. Sci. Commun. Eng.* 36:241. doi: 10.25073/2588-1086/vnucsce.241

Tustison, N. J., Avants, B. B., Cook, P. A., Zheng, Y., Egan, A., Yushkevich, P. A., et al. (2010). N4ITK: improved N3 bias correction. *IEEE Trans. Med. Imaging* 29, 1310–1320. doi: 10.1109/TMI.2010.2046908

Vijayanarasimhan, S., and Grauman, K. (2010). "Top-down pairwise potentials for piecing together multi-class segmentation puzzles," in *Proceeding of the 2010 IEEE Computer Society Conference on Computer Vision and Pattern Recognition - Workshops*, (IEEE), doi: 10.1109/cvprw.2010.5543728

Woo, B., and Lee, M. (2021). "Comparison of tissue segmentation performance between 2D U-Net and 3D U-net on brain MR images," in *Proceeding of the 2021 International Conference on Electronics, Information, and Communication (ICEIC)*, (IEEE), doi: 10.1109/iceic51217.2021.9369797

Xiao, Z., Liu, B., Geng, L., Zhang, F., and Liu, Y. (2020). Segmentation of lung nodules using improved 3D-UNet neural network. *Symmetry (Basel)* 12:1787. doi: 10.3390/sym12111787

Xue, Y., Xu, T., Zhang, H., Long, L. R., and Huang, X. (2018). SegAN: adversarial network with multi-scale L1 loss for medical image segmentation. *Neuroinformatics* 16, 383–392. doi: 10.1007/s12021-018-9377-x

Xun, S., Li, D., Zhu, H., Chen, M., Wang, J., Li, J., et al. (2021). Generative adversarial networks in medical image segmentation: a review. *Comput. Biol. Med.* 140, 105063. doi: 10.1016/j.compbiomed.2021.105063

Yang, C., Rangarajan, A., and Ranka, S. (2018). Visual explanations from deep 3D convolutional neural networks for Alzheimer's disease classification. *AMIA Ann. Symp. Proc.* 2018, 1571–1580.

Yushkevich, P. A., Piven, J., Hazlett, H. C., Smith, R. G., Ho, S., Gee, J. C., et al. (2006). User-guided 3D active contour segmentation of anatomical structures: significantly improved efficiency and reliability. *Neuroimage* 31, 1116–1128. doi: 10.1016/j.neuroimage.2006.01.015

Zhang, Y., Zhong, P., Jie, D., Wu, J., Zeng, S., Chu, J., et al. (2021). Brain tumor segmentation from multi-modal MR images via ensembling UNets. *Front. Radio* 1:704888. doi: 10.3389/fradi.2021.704888 doi: 10.3389/fradi.2021.704888

Zhao, L., De Asis-Cruz, J., Feng, X., Wu, Y., Kapse, K., Largent, A., et al. (2022). Automated 3D fetal brain segmentation using an optimized deep learning approach. *AJNR Am. J. Neuroradiol.* 2022:7419. doi: 10.3174/ajnr.A7419

Zhao, X., Wu, Y., Song, G., Li, Z., Zhang, Y., and Fan, Y. (2018). "3D brain tumor segmentation through integrating multiple 2D FCNNs," in *Brainlesion: Glioma, Multiple Sclerosis, Stroke and Traumatic Brain Injuries Lecture notes in computer science*, eds A. Crimi, S. Bakas, H. Kuijf, B. Menze, and M. Reyes (Cham: Springer International Publishing), 191–203.

Zhu, C., Mei, K., Peng, T., Luo, Y., Liu, J., Wang, Y., et al. (2021). Multi-level colonoscopy malignant tissue detection with adversarial CAC-UNet. *Neurocomputing* 438, 165–183. doi: 10.1016/j.neucom.2020.04.154

Conflict of Interest: The authors declare that the research was conducted in the absence of any commercial or financial relationships that could be construed as a potential conflict of interest.

The handling editor WZ declared a past co-authorship with CL.

frontiers | Frontiers in Neuroscience

TYPE Original Research
PUBLISHED 02 August 2022
DOI 10.3389/fnins.2022.931360

OPEN ACCESS

EDITED BY
Weihao Zheng,
Lanzhou University, China

REVIEWED BY
Masahiro Tsuji,
Kyoto Women's University, Japan
Joanne George,
The University of Queensland, Australia

*CORRESPONDENCE
Kenichi Oishi
koishi2@jhmi.edu

†These authors have contributed equally to this work

SPECIALTY SECTION
This article was submitted to Neurodevelopment, a section of the journal Frontiers in Neuroscience

RECEIVED 28 April 2022
ACCEPTED 08 July 2022
PUBLISHED 02 August 2022

CITATION
Onda K, Catenaccio E, Chotiyanonta J, Chavez-Valdez R, Meoded A, Soares BP, Tekes A, Spahic H, Miller SC, Parker S-J, Parkinson C, Vaidya DM, Graham EM, Stafstrom CE, Everett AD, Northington FJ and Oishi K (2022) Development of a composite diffusion tensor imaging score correlating with short-term neurological status in neonatal hypoxic–ischemic encephalopathy.
Front. Neurosci. 16:931360.
doi: 10.3389/fnins.2022.931360

Development of a composite diffusion tensor imaging score correlating with short-term neurological status in neonatal hypoxic–ischemic encephalopathy

Kengo Onda[1†], Eva Catenaccio[2†], Jill Chotiyanonta[1], Raul Chavez-Valdez[3,4], Avner Meoded[5], Bruno P. Soares[6], Aylin Tekes[3,7], Harisa Spahic[4], Sarah C. Miller[4], Sarah-Jane Parker[8], Charlamaine Parkinson[3,4], Dhananjay M. Vaidya[9], Ernest M. Graham[10], Carl E. Stafstrom[3,11], Allen D. Everett[12], Frances J. Northington[3,4] and Kenichi Oishi[1*]

[1]The Russell H. Morgan Department of Radiology and Radiological Science, The Johns Hopkins University School of Medicine, Baltimore, MD, United States, [2]Division of Pediatric Neurology, Department of Pediatrics, Children's Hospital of Philadelphia, Philadelphia, PA, United States, [3]Neuroscience Intensive Care Nursery Program, Division of Neonatology, The Johns Hopkins University School of Medicine, Baltimore, MD, United States, [4]Division of Neonatology, Department of Pediatrics, The Johns Hopkins University School of Medicine, Baltimore, MD, United States, [5]Edward B. Singleton Department of Radiology, Texas Children's Hospital, Baylor College of Medicine, Houston, TX, United States, [6]Division of Neuroradiology, Department of Radiology, Larner College of Medicine at the University of Vermont, Burlington, VT, United States, [7]Division of Pediatric Radiology and Pediatric Neuroradiology, Department of Radiology, The Johns Hopkins University School of Medicine, Baltimore, MD, United States, [8]St. George's University of London, London, United Kingdom, [9]Department of General Internal Medicine, The Johns Hopkins University School of Medicine, Baltimore, MD, United States, [10]Division of Maternal-Fetal Medicine, Department of Gynecology and Obstetrics, The Johns Hopkins University School of Medicine, Baltimore, MD, United States, [11]Division of Pediatric Neurology, Department of Neurology, The Johns Hopkins University School of Medicine, Baltimore, MD, United States, [12]Division of Pediatric Cardiology, Department of Pediatrics, The Johns Hopkins University School of Medicine, Baltimore, MD, United States

Hypoxic–ischemic encephalopathy (HIE) is the most common cause of neonatal acquired brain injury. Although conventional MRI may predict neurodevelopmental outcomes, accurate prognostication remains difficult. As diffusion tensor imaging (DTI) may provide an additional diagnostic and prognostic value over conventional MRI, we aimed to develop a composite DTI (cDTI) score to relate to short-term neurological function. Sixty prospective neonates treated with therapeutic hypothermia (TH) for HIE were evaluated with DTI, with a voxel size of 1 × 1 × 2 mm. Fractional anisotropy (FA) and mean diffusivity (MD) from 100 neuroanatomical regions (FA/MD *100 = 200 DTI parameters in total) were quantified using an atlas-based image parcellation technique. A least absolute shrinkage and selection operator (LASSO) regression was applied to the DTI parameters to generate

the cDTI score. Time to full oral nutrition [short-term oral feeding (STO) score] was used as a measure of short-term neurological function and was correlated with extracted DTI features. Seventeen DTI parameters were selected with LASSO and built into the final unbiased regression model. The selected factors included FA or MD values of the limbic structures, the corticospinal tract, and the frontotemporal cortices. While the cDTI score strongly correlated with the STO score (rho = 0.83, $p = 2.8 \times 10^{-16}$), it only weakly correlated with the Sarnat score (rho = 0.27, $p = 0.035$) and moderately with the NICHD-NRN neuroimaging score (rho = 0.43, $p = 6.6 \times 10^{-04}$). In contrast to the cDTI score, the NICHD-NRN score only moderately correlated with the STO score (rho = 0.37, $p = 0.0037$). Using a mixed-model analysis, interleukin-10 at admission to the NICU ($p = 1.5 \times 10^{-13}$) and tau protein at the end of TH/rewarming ($p = 0.036$) and after rewarming ($p = 0.0015$) were significantly associated with higher cDTI scores, suggesting that high cDTI scores were related to the intensity of the early inflammatory response and the severity of neuronal impairment after TH. In conclusion, a data-driven unbiased approach was applied to identify anatomical structures associated with some aspects of neurological function of HIE neonates after cooling and to build a cDTI score, which was correlated with the severity of short-term neurological functions.

KEYWORDS

hypoxic-ischemic encephalopathy, outcome prediction, diffusion tensor imaging, neonatal brain atlas, least absolute shrinkage and selection operator, short-term neurologic outcome, serum biomarkers

Introduction

Neonatal hypoxic–ischemic encephalopathy (HIE) is the most common neonatal acquired brain injury and is caused by the disruption of cerebral blood flow and oxygen supply near birth. HIE can lead to significant lifelong neurological morbidity (Douglas-Escobar and Weiss, 2015), and HIE represents about half of all cases of neonatal encephalopathy. Therapeutic hypothermia (TH) reduces by one-third the death and major disability in neonates with moderate-to-severe HIE (Gluckman et al., 2005; Shankaran et al., 2005; Tagin et al., 2012). Identifying which neonates are at the highest risk of poor neurological outcomes despite TH is still difficult, and accurate prognostic indicators are needed.

Assessment of injury by qualitative and quantitative analyses of magnetic resonance imaging (MRI) has been correlated with short- and long-term outcomes in HIE (van Laerhoven et al., 2013; Massaro, 2015; Shankaran et al., 2015). However, conventional MRI may under-estimate injury, and advanced techniques, including diffusion tensor imaging (DTI), provide an additional diagnostic and prognostic value (Thayyil et al., 2010; Alderliesten et al., 2011; Martinez-Biarge et al., 2011; van Laerhoven et al., 2013) by detecting mild neuronal injury that is difficult to evaluate with conventional MRI sequences. Prior research using DTI data has been limited by the need for the manual segmentation of regions of interest (ROIs), which are labor-intensive and require anatomical expertise, thus limiting both the number of patients and the number of regions that can be evaluated (Massaro et al., 2015; Lemmon et al., 2017; Seo et al., 2017; Jang and Kwon, 2018; Gerner et al., 2019; Salas et al., 2019; Longo et al., 2020). Moreover, many of the previously published studies have relied on the hypothesis-driven identification of brain regions known to be involved in HIE, including brainstem, basal ganglia, thalamus, posterior limb of the internal capsule, postcentral gyrus, and cortical white matter. Voxel-based analysis using tract-based spatial statistics (TBSS) is a data-driven approach, but is limited to white matter tracts (Tusor et al., 2012; Ly et al., 2015). Moreover, although previous studies have shown a relationship between anatomical impairment in specific brain regions and clinical severity, the prediction of prognosis has remained problematic, especially for mild cases (Zarifi et al., 2002; Rollins et al., 2014; Bano et al., 2017), suggesting the need to introduce a predictive model that combines DTI findings from multiple areas of the brain in an unbiased manner.

To overcome the limitations of previous studies, we used an atlas-based approach to parcellate whole-brain DTI into 122 anatomical regions covering the whole brain, including both gray and white matter structures (Oishi et al., 2011). The

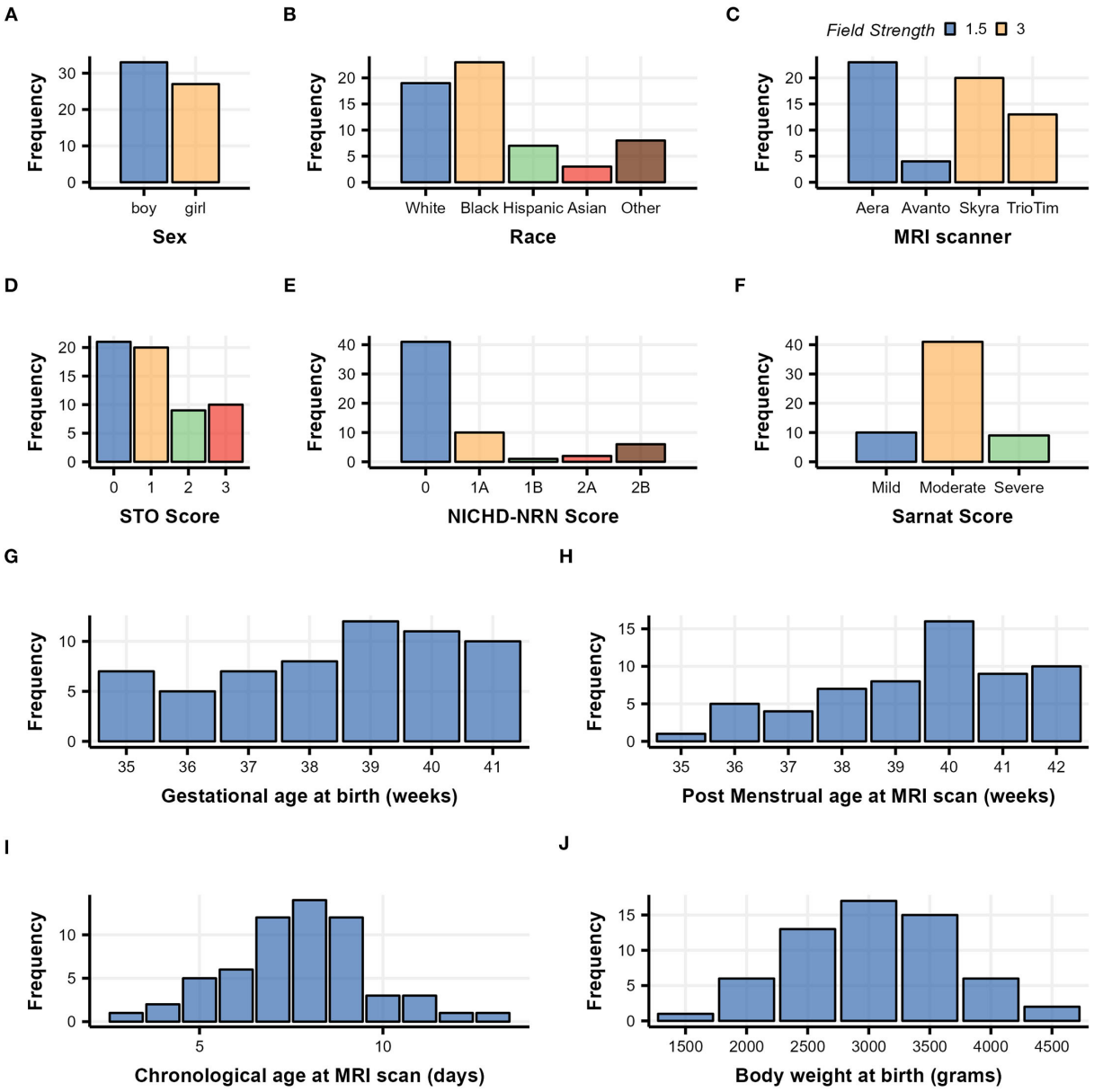

FIGURE 1
Demographic histograms of 60 subjects with neonatal HIE who underwent therapeutic hypothermia treatment. Categorical clinical variables are summarized in **(A–F)** with color scaled by variables, and continuous clinical variables are summarized in **(G–J)**.

DTI information in these regions was analyzed by the LASSO regression analysis to create a model that outputs a numerical value [composite DTI (cDTI) score] correlating with time to full oral feedings as a short-term neuro-functional measure [short-term oral feeding (STO) score]. Serum biomarkers previously reported in this cohort of HIE newborns (Dietrick et al., 2020; Chavez-Valdez et al., 2021b) were used to elucidate the longitudinal mechanistic origins related to the cDTI score.

Materials and methods

Participants

Data were obtained from a prospective cohort of neonates who underwent TH for neonatal encephalopathy at the Johns Hopkins Hospital, Baltimore, MD, USA. The study was approved by the institutional review board. A diagnosis of HIE was based on the National Institute of Child Health and Human

Development (NICHD) Neonatal Research Network criteria (Shankaran et al., 2005). Out of 659 cases in total, 535 cases were excluded due to a lack of brain MRI. In addition, neonates with arterial ischemic stroke or IVH or both ($n = 21$), neonates requiring extracorporeal membrane oxygenation (ECMO) ($n = 4$), non-perinatal events ($n = 3$), incomplete clinical data ($n = 3$), partial TH administration (<72 h) ($n = 2$), TH off-label use (<35-week gestation at birth) ($n = 1$), and non-HIE neonatal encephalopathy ($n = 1$) were also excluded; three of the 89 eligible neonates were excluded due to motion artifact from the baby's arousal during scanning. Additionally, DTIs that did not meet the voxel size criteria ($n = 22$) and neonates who were older than 14 days at the time of the MRI scan ($n = 4$) were excluded. A total of 60 patients were included in the final analysis.

Clinical variables

Clinical data were obtained from the medical record. The race was assigned based on maternal race. The sex and GA were assigned by the NICU team at admission to the NICU. The highest modified Sarnat score during the first 6 h of admission to the NICU was determined by the study team (RC-V, CP, and FJN) (Sarnat and Sarnat, 1976). The distributions of clinical categorical/numerical characteristics, such as sex, race, NICHD-NRN score, Sarnat score, GA at birth, and post-menstrual age (PMA) at MRI scan, chronological age at MRI scan, and birth weight (BW) are summarized in Figure 1 and Table 1.

Short-term oral-feeding (STO) score

The STO score was designed as a measure of short-term neurological function, with a focus on the attainment of oral feeding (Graham et al., 2008; Badran et al., 2020). This score ranged from 0 to 4. For all neonates undergoing TH, no feeds were offered until the day of life (DOL) 3, which corresponded to the end of the rewarming phase. Thus, a score of 0 was assigned if a patient achieved full oral feeds within 3 days after initiation ($\leq$ 7 days of life); a score of 1 was assigned if 3 extra days were needed (8–10 days of life), which corresponded to the standard weaning of parenteral fluids and transition to enteral feeds; a score of 2 was assigned if a patient achieved full oral feeding in $\leq$ 5 weeks; a score of 3 was assigned if $>$ 5 weeks was needed or a gastrostomy tube (G-tube) was placed for discharge; and a score of 4 was assigned if a patient died during the hospitalization due to withdrawal of care as a result of the severity of brain injury. Data were obtained by RC-V, HS, SM, and CP, and the data were revised and scored by RC-V.

TABLE 1 Clinical characteristics of 60 neonatal HIE patients who underwent therapeutic hypothermia treatment.

Categorical clinical variables, n / N (%)	***N* = 60**
Sex of patients	
Male	33 (55%)
Female	27 (45%)
Race	
White	19 (32%)
Black	23 (38%)
Hispanic	7 (12%)
Asian	3 (5.0%)
other	8 (13%)
STO score	
0	21 (35%)
1	20 (33%)
2	9 (15%)
3	10 (17%)
Sarnat score	
Mild	10 (17%)
Moderate	41 (68%)
Severe	9 (15%)
NICHD-NRN score	
0	41 (68%)
1A	10 (17%)
1B	1 (1.7%)
2A	2 (3.3%)
2B	6 (10%)
Scanner type	
Aera (1.5T)	23 (38%)
Avanto (1.5T)	4 (6.7%)
Skyra (3T)	20 (33%)
TrioTim (3T)	13 (22%)
Continuous clinical variables, Mean (SD)	***N* = 60**
Gestational age at birth (weeks)	38.81 (1.92)
Post-menstrual age at MRI scan (weeks)	39.91 (1.89)
Chronological age at MRI scan (days)	7.73 (1.96)
Body weight at birth (grams)	3,299 (621)

Serum biomarkers

Serum levels of central nervous system injury (glial fibrillary acidic protein [GFAP], neurogranin [NRGN], tau), inflammation (interleukin [IL]-6, IL-8, IL-10), and trophism (brain-derived neurotrophic factor [BDNF] and vascular endothelial growth factor [VEGF]) proteins were available for those patients included in the study. Serial samples at up to eight separate time periods (from DOL 0 to 7) were measured from stored laboratory samples using a custom, multiplex assay (Meso Scale Discovery [MSD], Rockville, MD, USA) as previously

described (Dietrick et al., 2020; Chavez-Valdez et al., 2021b). For each patient, the measurements were reorganized into four time points, namely, baseline [admission to NICU], during TH, end of TH/rewarming, and after rewarming, according to the DOL; the value sampled at DOL 0 was set as baseline; the larger value sampled at DOL 1 and 2 as during TH; the larger value sampled at DOL 3 and 4 as the end of TH/rewarming; and the largest value sampled at DOL 5, 6, and 7 as after rewarming.

MRI acquisition

The MR imaging studies were acquired at either 1.5 tesla or 3.0 tesla on four clinical types of MR scanners, namely, Aera, Avanto, Skyra, and TrioTim (Siemens, Erlangen, Germany), using a standard eight-channel head coil. The neonatal imaging protocols included a single-shot spin-echo, echo-planar axial DTI sequence with diffusion gradients along 20 noncollinear directions. For each of the 20 diffusion-encoding directions, a *b*-value of 800 s/mm^2 was used for four patients and 1,000 s/mm^2 was used for the rest of the patients. An additional measurement without diffusion weighting (b0 s/mm^2) was taken. The voxel size was $1 \times 1 \times 2$ mm. The distributions of field strength, field of view (FOV), and *b*-value among the four types of MR scanners are summarized in Figure 1C and Table 2.

Evaluation of the impact of differences in MR scanner, magnetic field strength, and *b*-value on DTI quantification

As the four different scanners, namely, Aera, Avanto, Skyra, and TrioTim, were used to obtain DTI for this population, we first investigated whether the neurological severity of the neonates was evenly distributed among the scanners used. We built a proportional odds model and performed a type II likelihood ratio test on the model to evaluate the difference in the STO score distribution among the four MR scanners. To compare the effect size of the MR scanners, the preference of the STO score was estimated based on the model for each MR scanner, and those estimations were analyzed through the type II likelihood ratio test. The Brant–Wald test was conducted to check whether there was a violation of the proportional odds model assumption. We used the MASS library version 7.3-54 for model building and the Brant library version 0.3-0 for testing, both of which run on R (version 4.1.2). The same analysis was performed for two field strength levels (1.5T/3.0T), and the results are summarized in Supplementary Table 1. Then, we examined the impact of the scanner used on the cDTI score, applying Spearman's rank pairwise correlation test to investigate the correlation between the cDTI score and the use of each scanner (not used = 0 and used = 1), as described in Section "Relationship between the cDTI score and the clinical variables." To determine the effect of including different *b*-values (four patients were scanned with $b = 800$ s/mm^2 and the rest of the patients were scanned with 1,000 s/mm^2) on the results, an additional analysis was performed on a group of 56 patients using a *b*-value of 1,000 s/mm^2.

Clinical scoring of the T1- and T2-weighted images and diffusion-weighted images

Two experienced pediatric neuroradiologists (BPS and AT) scored the neonatal brain MRIs using the National Institute of Child Health and Human Development (NICHD) Neonatal Research Network (NRN) score (Shankaran et al., 2015). In addition, the overall image quality of all sequences was reviewed to determine the quality of DTI data. Throughout the quality control, three MRIs that had significant artifacts were excluded from the subsequent quantitative DTI analysis, as described in Section "Participant."

Atlas-based image analysis

The diffusion-weighted images were first linearly registered to the b0 image, followed by voxel-wise tensor fitting using DtiStudio (www.mristudio.org) (Jiang et al., 2006). An automated outlier rejection function (Li et al., 2013) was applied to reject slices with a relative fitting error of more than 3%. The fractional anisotropy (FA) and the mean diffusivity (MD) maps were calculated from the tensor field. The JHU-neonate single-brain DTI atlas and the parcellation map that contains 122 anatomical areas as the regions of interest (ROIs) (Oishi et al., 2011) were transformed into each individual's FA and MD images through the dual-channel (FA and MD) large deformation diffeomorphic metric mapping (LDDMM), as described in Oishi et al. (2011), Akazawa et al. (2016), and Wu et al. (2017a,b). Among 122 ROIs defined on each neonate's brain, 100 ROIs with a minimum volume greater than 2 mm^3 were analyzed as reliable ROIs (Otsuka et al., 2019). The names of the 100 ROIs are provided in Supplementary Table 2. Two of the authors (KOn. and KOi) inspected the resultant parcellation maps and identified eight parcellation maps with minor errors in structural boundaries, which were manually corrected. For each ROI, an FA threshold of > 0.2 was applied to select white matter areas and fiber-rich components within the deep gray matter. The mean

TABLE 2 MRI scan parameters used in this study.

Scanner type, n/N (%)	Aera, $N = 23$	Avanto, $N = 4$	Skyra, $N = 20$	TrioTim, $N = 13$
FOV				
1,344 × 1,344	0 (0%)	0 (0%)	1 (5.0%)	0 (0%)
1,536 × 1,536	23 (100%)	4 (100%)	19 (95%)	9 (69%)
1,728 × 1,728	0 (0%)	0 (0%)	0 (0%)	4 (31%)
Field strength				
	1.5T	1.5T	3T	3T
***B*-value**				
800 s/mm^2	0 (0%)	0 (0%)	0 (0%)	4 (31%)
1,000 s/mm^2	23 (100%)	4 (100%)	20 (100%)	9 (69%)

FA and MD values were quantified for statistical analysis. Figure 2 shows the representative parcellation maps overlaid on FA maps.

LASSO regression model

The least absolute shrinkage and selection operator (LASSO) regression method with cross-validation was applied to extract important DTI features from 200 measures (100 ROIs × 2 measures [FA, MD]) and generate a cDTI score for neonatal HIE that correlated with the STO score for each individual. The LASSO regression model was chosen as a sparse model that addresses the overfitting and multicollinearity problem expected in whole-brain DTI analysis and includes only variables that have a significant impact on the STO scores. The DTI measures were converted to a z-score based on the mean and the standard deviation of each DTI-derived measurement of each ROI and served as input variables. The best lambda parameter was defined by 10-fold cross-validation, setting the alpha parameter as 1, to minimize a mean squared prediction error between the measured and the predicted STO scores. A software package, glmnet version 4.1-3, that runs on R (version 4.1.2) was used for the analysis (Friedman et al., 2010). Spearman's rank correlation tests with the cDTI score were performed for all factors selected in the prediction model, and the results are presented in scatterplots with regression lines and coefficients (Supplementary Figure 1).

Relationship between the cDTI score and the clinical variables

The Spearman's rank pairwise correlation test was used to evaluate the relationship between the categorical variables (i.e., STO score, Sarnat score, NICHD-NRN score, sex, field strength, with or without the use of each MR scanner) and the Pearson's pairwise correlation test was used to evaluate the relationship between the numerical variables (i.e., GA and BW at birth, and chronological age and PMA at MRI scan), both including the cDTI score. A $p < 0.05$ was regarded as a significant correlation.

Comparison of biomarkers between severe and mild groups over time

Based on the cDTI score, all patients were classified into mild or severe groups. A cDTI score of 1.5 or less was defined as the mild group and above 1.5 as the severe group. The cut point of cDTI score of 1.5 was set to separate neonates with mild MRI findings from those with typical lesions in the basal ganglia–thalamus, watershed area, and the internal capsule, with approximately the same number of subjects in the mild and severe groups. Using lme4 library version 1.1-27.1 on R (version 4.1.2), a linear mixed-effects analysis was performed for each biomarker (i.e., BDNF, IL-6, VEGF, GFAP, NRGN, IL-10, IL-8, and tau). The concentration values of biomarkers were set as a response, and the dichotomized severity (mild/severe), the four time points (i.e., baseline, during TH, end of TH/rewarming, and after rewarming), and the interaction of both were set as fixed effects, and the intercepts for subjects were set as random effects. A type II Wald F-test with a Kenward–Roger degree of freedom was conducted on each mixed model to see the overall difference in biomarker values among the four different time points, two levels of severity, and their interaction.

For biomarkers in which significant differences were identified between the mild and severe groups, Welch's t-test was further performed as a *post-hoc* test using the emmeans library version 1.7.2 on R (version 4.1.2) to identify at which time points there were differences. Furthermore, the correlation between the cDTI score and biomarker values at each time point was examined using Spearman's rank correlation method. For all series of analyses (i.e., F-test, *post-hoc* tests, and correlation test), the significance level of the p-value was set at 0.05.

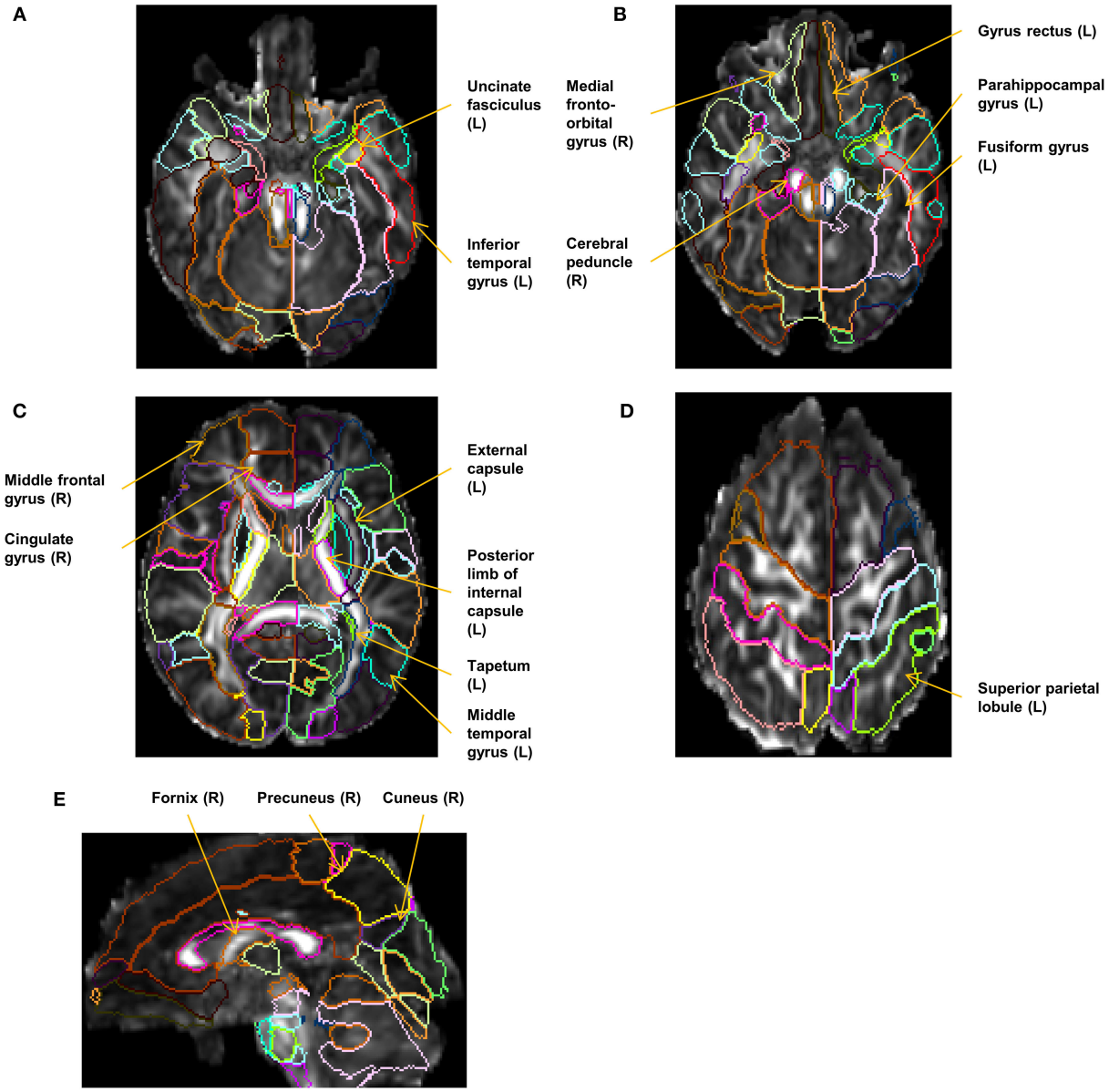

FIGURE 2
Representative parcellation maps superimposed on FA maps. The locations and laterality (L/R) of the selected 17 structures in the cDTI score calculation are annotated. **(A–D)** Axial images at the level of the corticospinal tract, the uncinate fasciculus **(A)**, the cerebral peduncle **(B)**, the basal ganglia **(C)**, and the superior parietal lobule **(D)**. **(E)** A sagittal image at the level of the right fornix and the right cuneus.

Results

Participants and distribution of clinical variables

Sixty patients met our clinical inclusion criteria and had high-quality DTI available for quantitative analysis. Overall, the group tended to have mild-to-moderate rather than moderate-to-severe injury, as evidenced by the distribution of the Sarnat scores and NICHD-NRN scores shown in Figures 1E,F and Table 1. The chronological age at the MRI scan averaged 7.7 days, indicating that the DTI captured the subacute phase of HIE when a diffusion-weighted image is most informative in determining the overall extent of injury (Huang and Castillo, 2008; Ouwehand et al., 2020).

The effect of different MR scanners and field strength levels

The result of the type II likelihood ratio test on the proportional odds model showed no significant differences in

TABLE 3 Results of the proportional odds model analysis for the evaluation of the distribution of the STO score among four MR scanners.

Analysis of deviance table (Type II test)

Variable	χ^2	df	*p*-value
MRI scanner	1.3	3	0.73

Brant test table for the proportional odds model

Variable tested for	χ^2	df	*p*-value[a]
Aera	0.18	2	0.91
Avanto	2.3	2	0.32
Skyra	0.19	2	0.91
TrioTim	10	6	0.11

[a]If there are no significant p-values, the model satisfies the proportional odds assumption.

the STO score distribution among four MR scanner types ($p = 0.73$) or between two levels of field strength ($p = 0.38$), as described in Table 3 and Supplementary Table 1. The Brant–Wald test was performed to assess the validity of the proportional odds model used for both tests. No significant *p*-values were found for any items, indicating that the proportional odds model assumption was not violated, and the results of the proportional odds model were valid. Thus, all 60 MR data were pooled together for the subsequent cDTI score calculation.

Generation of the cDTI score

Seventeen factors (FA of 10 ROIs and MD of 7 ROIs) were selected from 200 factors by the LASSO analysis and built into the final regression model. In this model, each variable (FA or MD derived from the 17 selected anatomical structures) was weighted and the sum (cDTI score) was calculated for each patient. The standardized regression coefficients for each of the image and non-image factors are presented in Table 4. Most of the 17 selected structures can be categorized as limbic fibers and related structures (parahippocampal gyrus, fornix, medial fronto-orbital gyrus, uncinate fasciculus, and cingulate gyrus); lateral frontotemporal cortices and related fibers (middle frontal gyrus, middle temporal gyrus, inferior temporal gyrus, and tapetum); and corticospinal projection fibers (cerebral peduncle and posterior limb of internal capsule). The locations and laterality of the selected factors are illustrated in Figure 2.

For the majority of the selected factors, increased MD and decreased FA were associated with higher cDTI scores, that is, worse neurological functions. On the contrary, a decrease in MD was shown to worsen the functions in five anatomical structures, including the lateral frontotemporal structures and the cerebral peduncle. Ten factors demonstrated moderate correlation with the cDTI score: cuneus MD (rho = 0.45); parahippocampal gyrus MD (rho = 0.32); middle temporal gyrus FA (rho = −0.28); superior parietal lobule FA (rho = −0.36); external capsule FA (rho = −0.34); gyrus rectus FA (rho = −0.40); fusiform gyrus FA (rho = −0.32); uncinate fasciculus FA (rho = −0.29); medial fronto-orbital gyrus FA (rho = −0.45); and fornix FA (rho = −0.59).

Relationship between the cDTI score and the clinical variables

Severity scale comparison (STO/cDTI/NICHD-NRN)

Figure 3 illustrates the relationship between three severity scales, namely, STO, cDTI, and NICHD-NRN. An excellent correlation was achieved between the STO score and the cDTI score, with a Spearman's rank correlation rho of 0.83 ($p = 2.8 \times 10^{-16}$, Figure 3A). For comparison, a correlation between the STO score and the NICHD-NRN score was also evaluated. The correlation (rho = 0.37, $p = 0.0037$) was significant, but weaker than the one between the STO and the cDTI scores (Figure 3B). As shown in the scatterplots in Figures 3B,C, higher NICHD-NRN and cDTI scores were associated with worse neurological functions. However, lower NICHD-NRN scores (e.g., 0, 1A, or 1B) were not necessarily associated with better neurological functions, whereas lower cDTI scores were associated with better neurological functions as represented by lower STO scores. This result suggested that the cDTI score is highly sensitive in detecting neuroanatomical alterations that are difficult to identify with conventional MRI sequences.

Relationships between cDTI score and demographics, clinical variables, and scanners

The pairwise Spearman's correlation test revealed that the cDTI score had a strong correlation with the STO score and had a weak or a moderate correlation with the Sarnat score (rho = 0.27, $p = 0.035$) and the NICHD-NRN score (rho = 0.43, $p = 6.6 \times 10^{-4}$) (Figure 4A and Table 5). Correlations between the cDTI scores and sex, field strength, MR scanner preference, and all numerical clinical variables were not significant, as summarized in Figure 4 and Tables 5, 6.

Comparison of biomarkers between severe and mild groups over time

A summary of the mixed-model analysis is presented in Table 7. The results of the *F*-test for the model indicated that there was a significant difference in biomarker values between

TABLE 4 Regression coefficients of the 17 factors selected by the LASSO regression analysis.

Regression coefficient	DTI	Anatomical structure	Side
Positive regression coefficients			
0.40	MD	Cuneus*	Right
0.064	MD	Parahippocampal gyrus*†	Right
Negative regression coefficients			
−0.31	MD	Middle frontal gyrus	Right
−0.23	FA	Fornix*†	Right
−0.22	MD	Inferior temporal gyrus	Left
−0.15	MD	Tapetum	Left
−0.13	FA	Medial fronto-orbital gyrus*†	Right
−0.12	FA	Uncinate fasciculus*†	Left
−0.072	FA	Fusiform gyrus*	Left
−0.068	FA	Gyrus rectus*	Left
−0.059	MD	Cerebral peduncle	Right
−0.057	FA	Precuneus	Right
−0.037	FA	External capsule*	Left
−0.031	FA	Superior parietal lobule*	Left
−0.017	FA	Middle temporal gyrus*	Left
−0.011	FA	Posterior limb of internal capsule	Left
−0.0091	MD	Cingulate gyrus†	Right

*Significant correlation with the cDTI score (Spearman's rank correlation, $p < 0.05$).
†Limbic fibers and related structures.

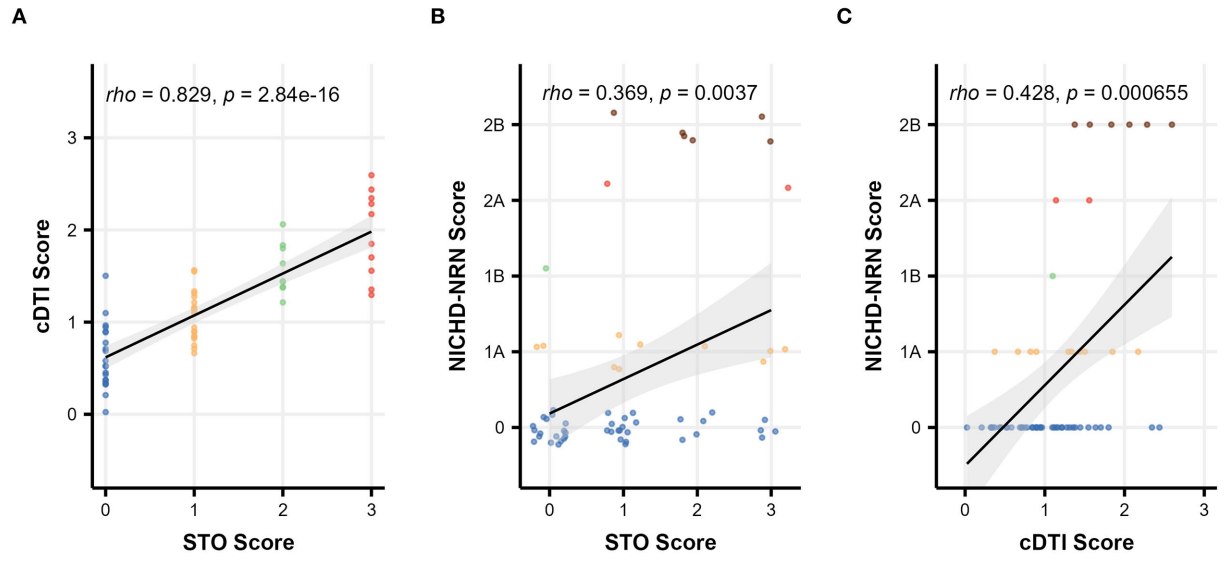

FIGURE 3
Scatterplots showing the relationship among severity scales: comparison between **(A)** the cDTI score and the STO score, **(B)** the NICHD-NRN score and the STO score, and **(C)** the NICHD-NRN score and the cDTI score. Solid black lines with gray areas represent the regression lines with 95% confidence intervals, and Spearman's correlation coefficients/*p*-values are shown in the upper left corner of each graph. For **(B)**, the data are jittered to show the sample size.

the cDTI mild and severe groups for IL-10 ($p = 4.1 \times 10^{-4}$) and tau ($p = 0.014$). Significant time effects were present for BDNF ($p = 0.0064$), IL-6 ($p = 0.030$), VEGF ($p = 6.1 \times 10^{-4}$), GFAP ($p = 0.016$), and IL-10 ($p = 5.9 \times 10^{-10}$). Significant interactions between time point and severity were found for VEGF ($p = 0.0043$) and IL-10 ($p = 1.7 \times 10^{-9}$).

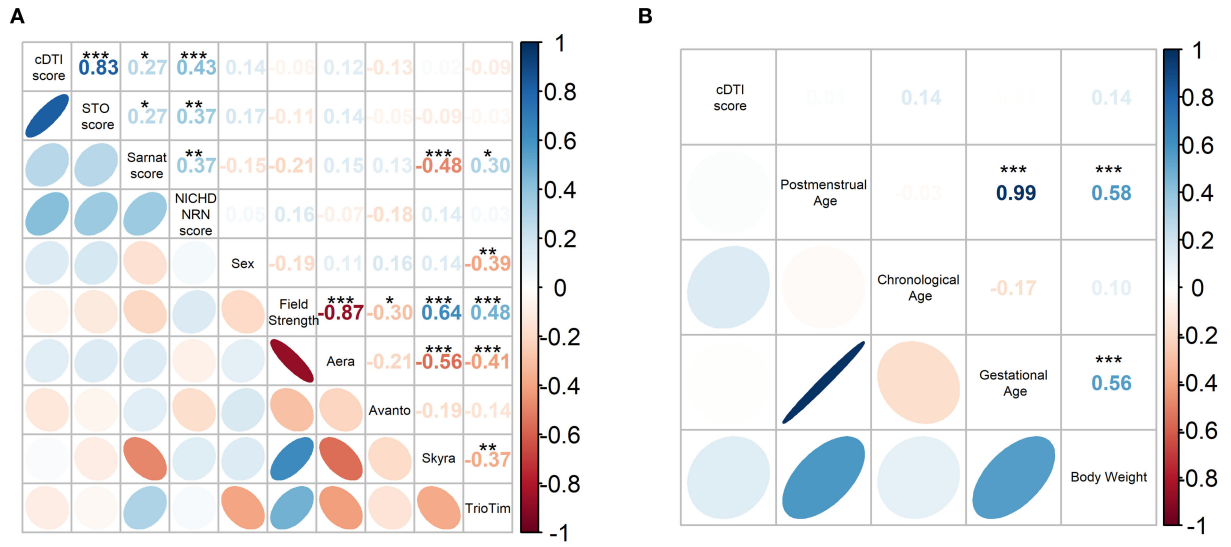

FIGURE 4
(A) Spearman's correlation coefficient matrix between the cDTI score and categorical clinical variables (i.e., STO, Sarnat, NICHD-NRN, sex, field strength, scanner preference). **(B)** Pearson's correlation coefficient matrix between the cDTI scores and numerical variables (postmenstrual age, chronological age, gestational age, and weight). Color-coded numbers in the upper right half of the matrix indicate correlation coefficients (*$p < 0.05$, **$p < 0.01$, and ***$p < 0.001$, blue: positive coefficient, red: negative coefficient). The color-coded ellipses in the lower left half of the matrix indicate the strength of correlation between variables, with blue indicating a negative correlation and red indicating a positive correlation. The shape of the ellipses indicates the strength of the correlation (ellipses are sharp when the correlation is strong and round when it is weak), positive slope indicates a positive correlation, and negative slope indicates a negative correlation.

TABLE 5 Spearman's correlation coefficients and *p*-values between the cDTI score and the categorical clinical variables.

Statistic	STO score	Sarnat score	NICHD NRN score	Sex	Field strength	Aera	Avanto	Skyra	TrioTim
rho	**0.83**	**0.27**	**0.43**	0.14	−0.057	0.12	−0.13	0.023	−0.095
p-value[a]	**2.8×10^{-16}*** **	**0.035***	**6.6×10^{-4}*** **	0.28	0.66	0.35	0.33	0.87	0.47

[a]*p < 0.05 and ***p < 0.001. Correlation coefficients (rho) and p-values in bold indicate significant correlations.

Table 8 summarizes the result of the subsequent pairwise Welch's *t*-tests for each biomarker. These *post-hoc* tests aimed to identify at which time point the difference between the mild and severe groups was observed. Among the biomarkers that had significant differences between mild and severe groups (IL-10, tau), significant differences were found at baseline ($p = 1.5 \times 10^{-13}$) for IL-10 and at the end of TH/rewarming ($p = 0.036$) and after rewarming ($p = 0.0015$) for tau. These group differences are observed in Figure 5, illustrating the time course of IL-10 and tau concentrations by the groups. The Spearman's rank correlation test indicated a moderate correlation between the cDTI score and IL-10 concentration after rewarming (rho = 0.44, $p = 0.024$) and between the cDTI score and tau concentration during TH (rho = 0.41, $p = 0.0056$) and at the end of TH/rewarming (rho = 0.31, $p = 0.029$; Figure 6).

The effect of including different *b*-values

The results from the group of 56 patients, excluding the four patients who were scanned using a *b*-value of 800 s/mm^2 to avoid the influence of the *b*-value on the DTI quantification, demonstrated a trend similar to that of the results that included all 60 patients. Although the number of anatomical structures selected by the LASSO regression model was slightly increased, all anatomical structures selected in the analysis of all 60 patients were included, and the magnitude of the regression coefficients for each anatomical structure tended to be similar (Supplementary Figure 2 and Supplementary Table 3). The significant correlations between the cDTI score and other severity scales (STO, NICHD-NRN, and Sarnat) and between the cDTI score and clinical variables were also unchanged (Supplementary Figures 3, 4

TABLE 6 Pearson's correlation coefficients and *p*-values between the cDTI score and the continuous clinical variables.

Statistic	Postmenstrual age at MRI scan (weeks)	Chronological age at MRI scan (days)	Gestational age at birth (weeks)	Body weight at birth (grams)
r	0.012	0.14	−0.0088	0.14
p-value	0.93	0.29	0.95	0.30

TABLE 7 Results of mixed-model analysis for each biomarker.

Biomarker[a]	Source[b]	df	df (residual)	*F*-value	*p*-value[c]
BDNF	**Timepoint**	3	105	4.3	**0.0064****
	Severity	1	50	0.41	0.53
	Timepoint * Severity	3	105	0.76	0.52
IL-6	**Timepoint**	3	112	3.1	**0.030***
	Severity	1	48	0.0073	0.93
	Timepoint * Severity	3	111	0.41	0.75
VEGF	**Timepoint**	3	99	6.3	**0.00061*****
	Severity	1	51	2.9	0.096
	Timepoint * Severity	3	100	4.7	**0.0043****
GFAP	**Timepoint**	3	103	3.6	**0.016***
	Severity	1	51	0.35	0.56
	Timepoint * Severity	3	103	0.11	0.96
NRGN	Timepoint	3	104	1.3	0.30
	Severity	1	50	0.35	0.56
	Timepoint * Severity	3	104	0.47	0.71
IL-10	**Timepoint**	3	95	20	**5.9×10^{-10}*****
	Severity	1	35	15	**0.00041*****
	Timepoint * Severity	3	94	18	**1.7×10^{-9}*****
IL-8	Timepoint	3	87	1.9	0.13
	Severity	1	39	0.30	0.59
	Timepoint * Severity	3	85	0.17	0.92
Tau	Timepoint	3	100	1.2	0.33
	Severity	1	46	6.6	**0.014***
	Timepoint * Severity	3	100	2.0	0.12

[a]Biomarkers with significant differences between the severe and mild groups are made bold. Severity is a binary variable of severity grouping (mild/severe) based on the cDTI score.
[b]Timepoint * Severity cells shows interactions of timepoint and severity variables.
[c]*$p < 0.05$, **$p < 0.01$, and ***$p < 0.001$.

and Supplementary Tables 4, 5). In the mixed-model analysis of serum biomarkers and the cDTI scores, all significant effects (time point, severity, and interaction between both) remained except for the interaction effects in VEGF (Supplementary Table 6). Significant differences between severity groups were also replicated for IL-10 and tau concentrations.

Discussion

Clinical relevance of the cDTI score

We applied an atlas-based, whole-brain approach to capture the neuroradiological features of neonatal HIE that are associated with short-term neurological function. Our novel

TABLE 8 Results of Welch's *t*-test for the difference in biomarker values between the mild and severe groups defined by the cDTI score for each time point.

Biomarker[a]	Timepoint	Estimated difference (mild - severe)	SE	df	T-ratio	*p*-value[b]
BDNF	Baseline	−209	561	147	−0.37	0.71
	During TH	248	410	112	0.60	0.55
	End of TH/Rewarming	500	406	111	1.2	0.22
	After Rewarming	−103	468	133	−0.22	0.83
IL-6	Baseline	105	103	148	1.0	0.31
	During TH	−9.6	71	141	−0.14	0.89
	End of TH/Rewarming	−8.7	70	140	−0.13	0.90
	After Rewarming	−19	83	146	−0.23	0.82
VEGF	Baseline	−103	74	129	−1.4	0.17
	During TH	95	60	81	1.6	0.12
	End of TH/Rewarming	131	60	84	2.2	**0.033***
	After Rewarming	122	65	102	1.9	0.064
GFAP	Baseline	0.088	0.93	131	0.095	0.92
	During TH	0.48	0.76	89	0.63	0.53
	End of TH/Rewarming	0.31	0.76	87	0.41	0.69
	After Rewarming	0.55	0.84	110	0.66	0.51
NRGN	Baseline	0.019	0.16	139	0.12	0.91
	During TH	−0.010	0.13	98	−0.077	0.94
	End of TH/Rewarming	0.12	0.13	96	0.89	0.38
	After Rewarming	0.13	0.15	120	0.86	0.39
IL-10	**Baseline**	−124	15	120	−8.3	**1.5×10^{-13}*** **
	During TH	−11	11	120	−1.0	0.30
	End of TH/Rewarming	0.013	11	120	0.0012	1.0
	After Rewarming	−0.49	13	120	−0.039	0.97
IL-8	Baseline	46	128	118	0.36	0.72
	During TH	59	96	92	0.61	0.54
	End of TH/Rewarming	58	98	94	0.59	0.56
	After Rewarming	−18	111	109	−0.16	0.88
Tau	Baseline	−50	310	140	−0.16	0.87
	During TH	−276	225	112	−1.2	0.22
	End of TH/Rewarming	−461	217	107	−2.1	**0.036***
	After Rewarming	−808	250	126	−3.2	**0.0015****

[a]Biomarkers with significant differences between the severe and mild groups are made bold.
[b]*$p < 0.05$, **$p < 0.01$, and ***$p < 0.001$.

severity scale, the cDTI score, has the potential to resolve conventional challenges. It has been extensively reported that even cases with a severe clinical prognosis have subtle or no abnormalities on DWI or conventional MRI, leading to an increase in false negatives in the early diagnosis of HIE brain injury (Liauw et al., 2009; Rollins et al., 2014; Krishnan and Shroff, 2016; ElBeheiry et al., 2019). This conclusion is also supported by this study, in which more than 20% of the patients scored low (0, 1A, 1B) on the NICHD-NRN score, but were found to have severe short-term functional impairments (STO score of 3 or 4). On the contrary, the cDTI scores were strongly correlated with the STO scores, even in cases with the NICHD-NRN scores of 0, 1a, and 1b. However, the interpretation of the cDTI scores of 1–2 remained difficult. Nevertheless, our cDTI score may overcome one of the previous challenges of finding severe cases that were difficult to detect by visual qualitative MRI evaluation and may provide an accurate prediction of short-term clinical prognosis for those cases.

Effect of variations in scanner and scan protocols

Although DTI is an essential imaging tool in terms of its ability to assess the brain quantitatively and is widely used in clinical research, it is necessary to consider the impact of different protocols on its quantitative data. For the acquisition of DTI parameters, we had matched voxel sizes ($1 \times 1 \times 2$ mm), but other parameters (scanner type, magnetic field

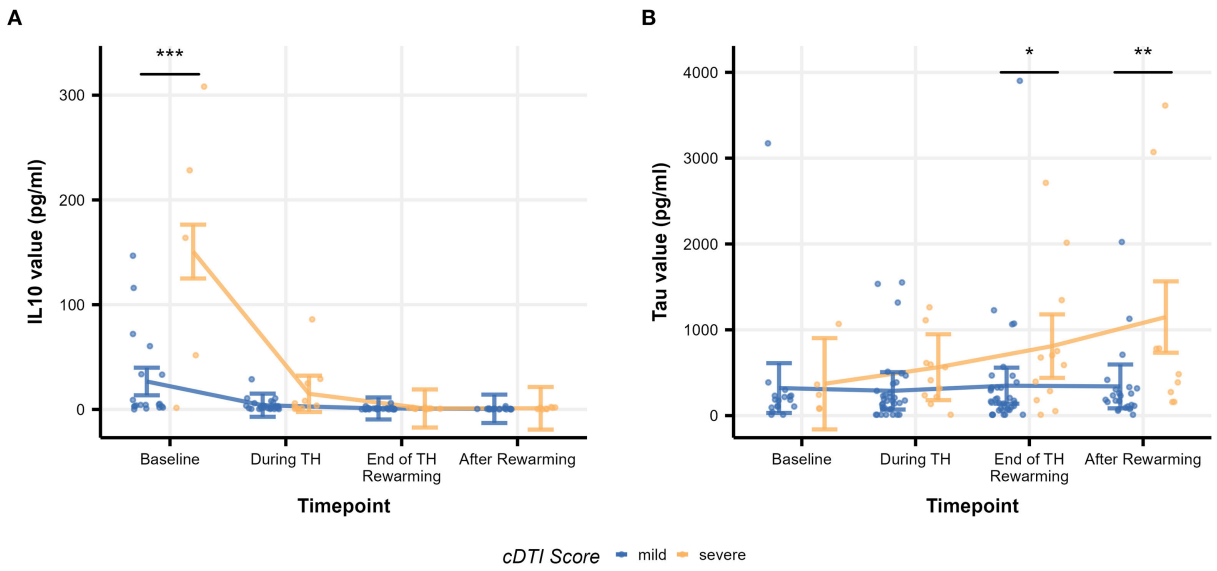

FIGURE 5
Time courses of biomarker values [**(A)**: IL-10 and **(B)**: tau] by severity group. Raw biomarker values are shown as scatterplots, and time courses are indicated as error bars. The error bars on each timepoint (baseline, during TH, end of TH/rewarming, and after rewarming) were calculated based on the results of the mixed-model analysis. Significance stars are embedded according to the result of the *post-hoc t*-test (*$p < 0.05$, **$p < 0.01$, and ***$p < 0.001$).

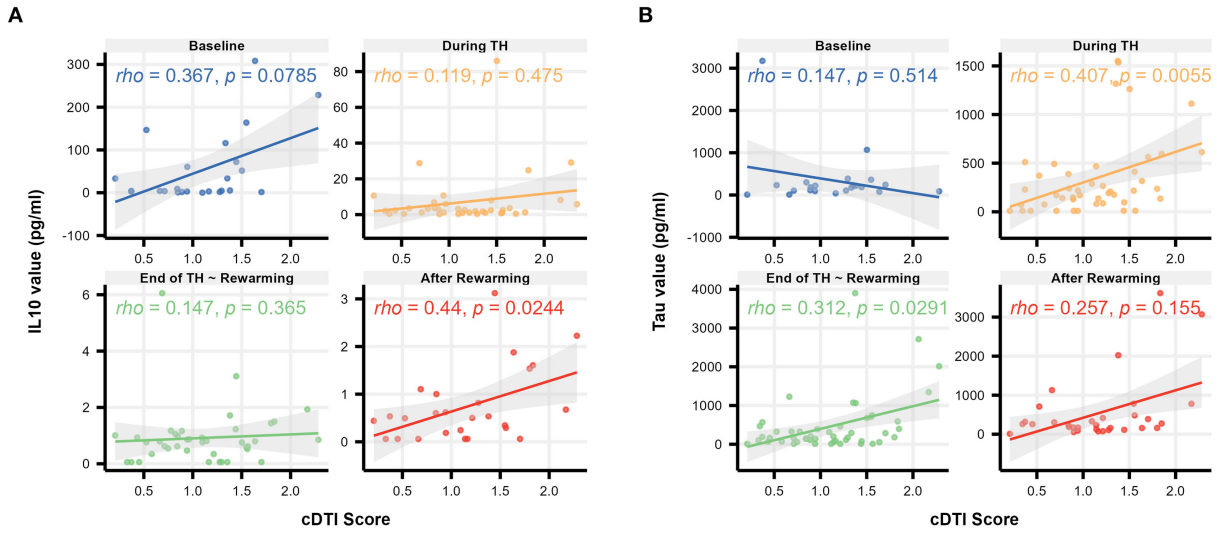

FIGURE 6
Scatterplots illustrating the relationship between the cDTI score and biomarker values [**(A)**: IL-10 and **(B)**: tau] over time (baseline, during TH, end of TH/rewarming, and after rewarming). Solid lines with gray areas indicate the regression lines with 95% confidence intervals, and Spearman's correlation coefficients/*p*-values are shown in the upper left corner of each graph.

strength, and *b*-value) could not be completely standardized; therefore, the results need to be interpreted carefully. Several studies have investigated the effect of these different protocols on FA/MD values. To assess the impact of using different scanners, Zhou et al. examined inter-manufacturer (GE vs. Siemens) and intra-manufacturer (Siemens Skyra vs. Siemens TrioTim) comparability and concluded there was a little impact between scanners on DTI metrics within the same manufacturer (Zhou et al., 2018), which we confirmed in this study. Regarding the magnetic field strength, although DTI theoretically is not affected by magnetic field strength, some papers report that it is affected (Huisman et al., 2006; Chung et al., 2013), while

others conclude that it is not affected (Hunsche et al., 2001; Alexander et al., 2006), indicating the effect of magnetic field strength on quantitative DTI values and its mechanisms are not fully understood. Given this situation, we used a proportional odds model to examine the uniformity of the distribution of the STO scores among scanners and between magnetic field strength to check that the effect between protocols was not significant. The pairwise Spearman's correlation test on categorical clinical variables showed no significant correlation between the cDTI/STO scores and field strength or scanner preference, and the correlation coefficients were, at most, 0.14, which supports the small effect size of the protocol difference.

In terms of the difference in *b*-values, several studies have suggested that the signal-to-noise ratio decreases as *b*-value increases (Bisdas et al., 2008; Chung et al., 2013). Diffusivity measures are also known to be affected by *b*-value (Barrio-Arranz et al., 2015). Taking these findings into consideration, we performed the same series of analyses, with the exclusion of the four patients with an 800 s/mm^2 *b*-value, and found that most of the results were similar to those before the exclusion, as shown in Section "The effect of including different b values" (Supplementary Figures 2–7 and Supplementary Tables 3–7). Although the impact of different *b*-values on the cDTI score was minor in this study, the influence of *b*-values on neurological prediction needs to be examined further.

DTI measurements selected by LASSO regression model

Throughout the LASSO regression, we identified two types of relationships between the neurological functions of HIE and DTI measures: for structures such as the lateral frontotemporal structures and the cerebral peduncle, decreased MD values were related to the poor neurological functions of HIE, whereas for other structures including the limbic system, decreased FA and increased MD values were associated with the poor neurological functions of HIE. Although the pathogenetic factors responsible for the alterations in FA and MD after neonatal HIE remain unknown, these results may be explained by multiple mechanisms (Wu et al., 2014), namely, cytotoxic edema for the former group of structures, vasogenic edema for the latter group of structures, and the potential effects of Wallerian degeneration (Groenendaal et al., 2006), which can be observed in the subacute phase of HIE (Neil and Inder, 2006).

The primary pathogenesis of HIE can be broadly divided into ischemic and reperfusion phases. Cytotoxic edema occurs during the ischemic phase, whereas vasogenic edema results from the effects of free radical-induced vascular endothelial damage during the reperfusion phase (Distefano and Praticò, 2010). In our study, DTI was acquired during the subacute phase, in which the effects of both the ischemic and reperfusion phases could be observed. Gutierrez et al. demonstrated that, in the subacute phase of ischemia, blood reperfusion induces vasogenic edema, whereas the restriction of water mobility due to high blood viscosity also causes the exacerbation of cytotoxic edema (Gutierrez et al., 2010).

Cytotoxic edema is a redistribution of water from the extracellular to the intracellular space due to the disruption of the Na^+/K^+ ATPase pump and intracellular calcium concentration maintenance mechanisms, caused by decreased oxygen and glucose due to reduced cerebral blood flow (Allen and Brandon, 2011). This condition is known to cause decreased MD values due to cell swelling (Rai et al., 2008). On the contrary, in vasogenic edema, disruption of the blood–brain barrier (BBB) and increased vascular permeability leads to extravascular leakage of serum proteins, resulting in extracellular fluid retention (Utsunomiya, 2011). As a result, unlike cytotoxic edema, increased MD and decreased FA values are observed due to the expansion of the extracellular compartment (Keller et al., 1999; Moritani et al., 2000). In addition to these pathological mechanisms, our findings may also reflect the early impact of Wallerian degeneration on the corticospinal tracts. In the early stage of the degeneration (onset to 1–2 weeks), the axonal and myelin debris causes restriction of water diffusion, resulting in a significant decrease in FA or MD values of the corticospinal tracts (Yu et al., 2009; Qin et al., 2012). The posterior limb of the internal capsule and cerebral peduncle have been reported as preferential sites of the degeneration (Venkatasubramanian et al., 2013), which is consistent with the present results.

Among the structures identified in this study that may be involved in vasogenic edema, limbic-related structures, in particular, are consistent with the recently reported findings that they are susceptible to hypoxic–ischemic injury in neonates (Zheng et al., 2021; Parmentier et al., 2022). Long-term studies have identified survivors of even mild HIE, without evidence of cerebral palsy, to have deficits in functions served by the limbic system, including memory, emotional processing, and behavior (van Handel et al., 2010; Lee-Kelland et al., 2020), which is also reported in preclinical studies (Burnsed et al., 2015; Diaz et al., 2017; Chavez-Valdez et al., 2018). Another study of 10-year-olds with a history of neonatal HIE found that smaller mammillary body and hippocampal volumes were associated with lower total IQ, performance IQ, processing speed, and episodic memory (Annink et al., 2021). Our results support that the severity of impairment of the limbic network by HIE may be related to the severity of neurological sequelae. Preclinical animal studies also support regionally specific temporal patterns of cell death and neurodegeneration (Northington et al., 2001a,b, 2022; Chavez-Valdez et al., 2021a). Thus, the results also suggested that the progression of cytotoxic and vasogenic edema and Wallerian degeneration occurs heterogeneously in different brain regions and that the pattern of progression and the severity may be associated with neurological functions.

Relationship between cDTI score and time course of serum biomarker

We also examined the potential biological mechanism supporting the cDTI score by comparing the time course of serum biomarker values between the cDTI score-defined severe and mild disease groups. The results of the mixed-model analysis showed that not only higher cDTI scores were associated with higher IL-10 and tau values, but also, more precisely, at which time points these relationships were observed: at baseline for IL-10 and at the end of TH/rewarming and after rewarming for tau. Moreover, tau was correlated with the cDTI score during TH and at the end of TH/rewarming, further supporting its association.

Our group has previously reported in a larger cohort, which included those patients studied here, that indicators of worse HIE severity, including the Sarnat scores correlated with higher IL-10 within the first 24 h of life, and tau at and after TH (Chavez-Valdez et al., 2021b). Increased levels of IL-10 (Orrock et al., 2016) and tau proteins (Dietrick et al., 2020) are closely linked to the worse prognosis of HIE. Previous animal (Li et al., 2014; Bai et al., 2021) and human (Youn et al., 2013) studies have identified a broad anti-inflammatory role for IL-10, such as the prevention of pro-inflammatory cytokine synthesis and the excessive phosphorylation of tau protein that leads to microtubule collapse and deposition in neurons, resulting in neurodegeneration (Wu et al., 2017c). Interpreting the present results in light of these findings, the cDTI score may be a composite measure that reflects the degree of both inflammatory responses in the early stages and accumulated neuronal damage in the later stages in HIE patients with TH.

Relationship between cDTI and STO scores

In a previous study by our group, neonates suffering from HIE who end up developing qualitative MRI evidence of brain injury despite TH took an average of 17 $\pm$ 9 days to reach full oral feeds, with >60% needing G-tube placement prior to discharge, and >10% dying, which contrasted with those HIE neonates with negative MRI, who took only 9 $\pm$ 5 days to reach full feeds and had no need for G-tube or mortality (Ennen et al., 2011). Others have also found similar feeding difficulties in this population (Krüger et al., 2019) and associations with brain injury in MRI and alterations in EEG (Badran et al., 2020; Takle et al., 2021). Thus, time to reach full oral feeds, the need for G-tube, and mortality after TH are appropriate functional assessments of the severity of short-term neurological functions and were used to build the STO score as described in Section "Short-term oral-feeding (STO) score." Here, we show that while the Sarnat or NICHD-NRN scores alone have a weak correlation with the STO scores, the cDTI score has a strong correlation, which was not related to sex, field strength, MRI scanner, or other clinical variables. Furthermore, unlike low cDTI scores, low NICHD-NRN scores do not necessarily relate to better neurological functions based on the STO scores. Therefore, the cDTI scores are superior in identifying poor neurological functions in HIE neonates without major abnormalities on qualitative MRI reading, suggesting a higher sensitivity in detecting mild neuronal damage.

Limitations

Our study has several limitations. First, the scanner and scan protocols varied among patients. We are fully aware of the impact of differences in scanners, magnetic field strength, and *b*-values on DTI measurements. Although our results indicated that such technological variations were negligible in obtaining cDTI scores, the potential impact of the technological variations on the predictive model and cDTI scores cannot be completely excluded. Nevertheless, the results suggest that the cDTI score is a robust measure against technological variability, and this robustness is crucial in clinical applications across institutions. Second, our cohort was comprised predominantly of neonates with mild-to-moderate rather than moderate-to-severe HIE injury by MRI, with relatively small contributions from basal ganglia and thalamic structures known to be involved in moderate-to-severe HIE before TH became standard of care for this subgroup of patients. Whether the cDTI scores from our model can predict the neurological function in more severely injured patients remains to be explored. Third, our analysis did not include standard neurological assessments such as the Hammersmith Neonatal Neurological Assessment, the NICU Network Neurobehavioral Scale, or the General Movements Assessment. Although an association between oral feeding difficulties and poor neurological prognosis has been reported, a direct comparison of the STO scores with gold standard assessments has not been made. Future studies are needed to test whether the STO scores accurately reflect short- and long-term neurological complications. Particularly, a longer follow-up is needed to assess whether the cDTI score is predictive of future neurological function. Fourth, the current single atlas analysis required manual correction to quantify DTI-derived scalar indices when errors in parcellation occur. This need for manual correction may limit its use in clinical practice. We are currently developing an atlas-based image parcellation tool based on the multi-atlas label fusion (MALF) algorithm that uses multiple atlases as teaching files to accurately parcellate neonatal brains (Tang et al., 2014; Otsuka et al., 2019). MALF algorithm, once validated, is expected to improve the accuracy of image parcellation and enable fully automated DTI quantification suitable for clinical applications. Fifth, a substantial number of patients in the original study cohort did not undergo brain MRI scans during their NICU admission. Because our study included

only neonates who had MRI scans, there may be a patient selection bias based on indications or contraindications for brain MRI scans. The cohort in this study had relatively mild Sarnat scores, which may have excluded HIE neonates with unstable clinical conditions that precluded them from undergoing MRI scans. Finally, although our cohort size was larger than previous studies using DTI in neonates, the number of participants was still small, considering the number of regions analyzed in a whole-brain approach. Larger cohorts may allow for more stable modeling with less prediction error and may identify more areas associated with disease severity.

Summary

Using an unbiased composite quantitative imaging measure across whole-brain structures, we developed the cDTI score, a novel severity measurement correlating with short-term neurological status in HIE patients who undergo TH. Limbic and frontotemporal regions and corticospinal projection fibers were identified as a lesion associated with short-term neurological functions. The relationship between the cDTI score and serum biomarkers suggested that the cDTI score reflects the inflammatory response prior to TH and the neuronal damage observed after TH. Larger studies that include more patients with moderate-to-severe HIE are needed to validate the cDTI score and assess how it can be implemented in clinical practice.

Data availability statement

The original contributions presented in the study are included in the article/Supplementary material, further inquiries can be directed to the corresponding author.

Ethics statement

This study was reviewed and approved by Johns Hopkins School of Medicine IRB. Written informed consent to participate in this study was provided by the participants' legal guardian/next of kin.

Author contributions

EC, RC-V, AE, FN, and KOi were involved in conceptualization and design of the study. KOn, EC, RC-V, and KOi were involved in methodology and drafted the significant portions of manuscript, tables, and figures. RC-V, AM, BS, AT, CP, DV, EG, AE, CS, FN, and KOi were involved in supervision and oversight. KOn, EC, JC, and KOi were involved in formal data analysis. RC-V, AM, BS, HS, SM, AT, CP, DV, EG, AE, and FN were involved in resources. All authors were involved in data acquisition, reviewing, and editing of the final manuscript.

Funding

This work was supported by the National Institutes of Health R01HD065955 (KOi), R01NS126549 (KOi), RO1HD086058 (AE and FN), RO1HD070996 (FN), R21AG061643 (FN), K08NS096115 (RC-V), and K08NS096115-03S1 (RC-V); the JHU-SOM Clinician Scientist Award (RC-V); and the Thomas Wilson Foundation (RC-V).

Acknowledgments

We thank the families of the extremely sick neonates included in this study for their willingness to participate. We also thank the nursing and ancillary staff at the Johns Hopkins Hospital NICU and core laboratory for their support in the collection of the samples. We also thank Dr. Brian Caffo for his statistical advice.

Conflict of interest

KOi is a consultant for "AnatomyWorks" and "Corporate-M." This arrangement is being managed by the Johns Hopkins University in accordance with its conflict-of-interest policies.

The remaining authors declare that the research was conducted in the absence of any commercial or financial relationships that could be construed as a potential conflict of interest.

Publisher's note

Supplementary material

The Supplementary Material for this article can be found online at: https://www.frontiersin.org/articles/10.3389/fnins.2022.931360/full#supplementary-material

References

Akazawa, K., Chang, L., Yamakawa, R., Hayama, S., Buchthal, S., Alicata, D., et al. (2016). Probabilistic maps of the white matter tracts with known associated functions on the neonatal brain atlas: application to evaluate longitudinal developmental trajectories in term-born and preterm-born infants. *Neuroimage* 128, 167–179. doi: 10.1016/j.neuroimage.2015.12.026

Alderliesten, T., de Vries, L. S., Benders, M. J., Koopman, C., and Groenendaal, F. (2011). MR imaging and outcome of term neonates with perinatal asphyxia: value of diffusion-weighted MR imaging and (1)H MR spectroscopy. *Radiology* 261, 235–242. doi: 10.1148/radiol.11110213

Alexander, A. L., Lee, J. E., Wu, Y.-C., and Field, A. S. (2006). Comparison of diffusion tensor imaging measurements at 3.0 T versus 1.5 T with and without parallel imaging. *Neuroimaging Clin. N. Am.* 16, 299–309. doi: 10.1016/j.nic.2006.02.006

Allen, K. A., and Brandon, D. H. (2011). Hypoxic ischemic encephalopathy: pathophysiology and experimental treatments. *Newborn Infant Nurs. Rev.* 11, 125–133. doi: 10.1053/j.nainr.2011.07.004

Annink, K. V., de Vries, L. S., Groenendaal, F., Eijsermans, R., Mocking, M., van Schooneveld, M. M. J., et al. (2021). Mammillary body atrophy and other MRI correlates of school-age outcome following neonatal hypoxic-ischemic encephalopathy. *Sci. Rep.* 11, 5017. doi: 10.1038/s41598-021-83982-8

Badran, B. W., Jenkins, D. D., Cook, D., Thompson, S., Dancy, M., DeVries, W. H., et al. (2020). Transcutaneous auricular vagus nerve stimulation-paired rehabilitation for oromotor feeding problems in newborns: an open-label pilot study. *Front. Hum. Neurosci.* 14, 77. doi: 10.3389/fnhum.2020.00077

Bai, X., Xiong, L.-L., Fang, C.-L., Zhou, H.-L., Xue, L.-L., Hu, Y., et al. (2021). Interleukin 10 plays an important role in neonatal rats with hypoxic-ischemia associated with B-cell lymphoma 2 and endoplasmic reticulum protein 29. *Analytical Cell. Pathol.* 2021, 6622713. doi: 10.1155/2021/6622713

Bano, S., Chaudhary, V., and Garga, U. C. (2017). Neonatal hypoxic-ischemic encephalopathy: a radiological review. *J. Pediatr. Neurosci.* 12, 1–6. doi: 10.4103/1817-1745.205646

Barrio-Arranz, G., de Luis-García, R., Tristán-Vega, A., Martín-Fernández, M., and Aja-Fernández, S. (2015). Impact of MR acquisition parameters on DTI Scalar indexes: a tractography based approach. *PLoS ONE* 10, e0137905. doi: 10.1371/journal.pone.0137905

Bisdas, S., Bohning, D. E., Besenski, N., Nicholas, J. S., and Rumboldt, Z. (2008). Reproducibility, interrater agreement, and age-related changes of fractional anisotropy measures at 3T in healthy subjects: effect of the applied b-value. *AJNR Am. J. Neuroradiol.* 29, 1128–1133. doi: 10.3174/ajnr.A1044

Burnsed, J. C., Chavez-Valdez, R., Hossain, M. S., Kesavan, K., Martin, L. J., Zhang, J., et al. (2015). Hypoxia-ischemia and therapeutic hypothermia in the neonatal mouse brain–a longitudinal study. *PLoS ONE* 10, e0118889. doi: 10.1371/journal.pone.0118889

Chavez-Valdez, R., Emerson, P., Goffigan-Holmes, J., Kirkwood, A., Martin, L. J., and Northington, F. J. (2018). Delayed injury of hippocampal interneurons after neonatal hypoxia-ischemia and therapeutic hypothermia in a murine model. *Hippocampus* 28, 617–630. doi: 10.1002/hipo.22965

Chavez-Valdez, R., Lechner, C., Emerson, P., Northington, F. J., and Martin, L. J. (2021a). Accumulation of PSA-NCAM marks nascent neurodegeneration in the dorsal hippocampus after neonatal hypoxic-ischemic brain injury in mice. *J. Cereb. Blood Flow Metab.* 41, 1039–1057. doi: 10.1177/0271678X20942707

Chavez-Valdez, R., Miller, S., Spahic, H., Vaidya, D., Parkinson, C., Dietrick, B., et al. (2021b). Therapeutic hypothermia modulates the relationships between indicators of severity of neonatal hypoxic ischemic encephalopathy and serum biomarkers. *Front. Neurol.* 12, 748150. doi: 10.3389/fneur.2021.748150

Chung, A. W., Thomas, D. L., Ordidge, R. J., and Clark, C. A. (2013). Diffusion tensor parameters and principal eigenvector coherence: Relation to b-value intervals and field strength. *Magn. Reson. Imaging* 31, 742–747. doi: 10.1016/j.mri.2012.11.014

Diaz, J., Abiola, S., Kim, N., Avaritt, O., Flock, D., Yu, J., et al. (2017). Therapeutic hypothermia provides variable protection against behavioral deficits after neonatal hypoxia-ischemia: a potential role for brain-derived neurotrophic factor. *Dev. Neurosci.* 39, 257–272. doi: 10.1159/000454949

Dietrick, B., Molloy, E., Massaro, A. N., Strickland, T., Zhu, J., Slevin, M., et al. (2020). Plasma and cerebrospinal fluid candidate biomarkers of neonatal encephalopathy severity and neurodevelopmental outcomes. *J. Pediatr.* 226, 71.e5–79.e5. doi: 10.1016/j.jpeds.2020.06.078

Distefano, G., and Praticò, A. D. (2010). Actualities on molecular pathogenesis and repairing processes of cerebral damage in perinatal hypoxic-ischemic encephalopathy. *Ital. J. Pediatr.* 36, 63. doi: 10.1186/1824-7288-36-63

Douglas-Escobar, M., and Weiss, M. D. (2015). Hypoxic-ischemic encephalopathy: a review for the clinician. *JAMA Pediatr.* 169, 397–403. doi: 10.1001/jamapediatrics.2014.3269

ElBeheiry, A. A., Elgamal, M. A., Ettaby, A. N., Omar, T. E., and Badeib, A. O. (2019). Can diffusion tensor imaging predict cerebral palsy in term neonates with hypoxic ischemic encephalopathy? *Egypt. J. Radiol. Nuclear Med.* 50, 66. doi: 10.1186/s43055-019-0077-9

Ennen, C. S., Huisman, T. A., Savage, W. J., Northington, F. J., Jennings, J. M., Everett, A. D., et al. (2011). Glial fibrillary acidic protein as a biomarker for neonatal hypoxic-ischemic encephalopathy treated with whole-body cooling. *Am. J. Obstet. Gynecol.* 205, 251.e251–257.e251. doi: 10.1016/j.ajog.2011.06.025

Friedman, J., Hastie, T., and Tibshirani, R. (2010). Regularization paths for generalized linear models via coordinate descent. *J. Stat. Softw.* 33, 1–22. doi: 10.18637/jss.v033.i01

Gerner, G. J., Newman, E. I., Burton, V. J., Roman, B., Cristofalo, E. A., Leppert, M., et al. (2019). Correlation between white matter injury identified by neonatal diffusion tensor imaging and neurodevelopmental outcomes following term neonatal asphyxia and therapeutic hypothermia: an exploratory pilot study. *J. Child Neurol.* 34, 556–566. doi: 10.1177/0883073819841717

Gluckman, P. D., Wyatt, J. S., Azzopardi, D., Ballard, R., Edwards, A. D., Ferriero, D. M., et al. (2005). Selective head cooling with mild systemic hypothermia after neonatal encephalopathy: multicentre randomised trial. *Lancet* 365, 663–670. doi: 10.1016/S0140-6736(05)70932-6

Graham, E. M., Ruis, K. A., Hartman, A. L., Northington, F. J., and Fox, H. E. (2008). A systematic review of the role of intrapartum hypoxia-ischemia in the causation of neonatal encephalopathy. *Am. J. Obstet. Gynecol.* 199, 587–595. doi: 10.1016/j.ajog.2008.06.094

Groenendaal, F., Benders, M. J., and de Vries, L. S. (2006). Pre-wallerian degeneration in the neonatal brain following perinatal cerebral hypoxia-ischemia demonstrated with MRI. *Semin. Perinatol.* 30, 146–150. doi: 10.1053/j.semperi.2006.04.005

Gutierrez, L. G., Rovira, À., Portela, L. A. P., Leite, C.,d,.C., and Lucato, L.T. (2010). CT and MR in non-neonatal hypoxic–ischemic encephalopathy: radiological findings with pathophysiological correlations. *Neuroradiology* 52, 949–976. doi: 10.1007/s00234-010-0728-z

Huang, B. Y., and Castillo, M. (2008). Hypoxic-ischemic brain injury: imaging findings from birth to adulthood. *Radiographics* 28, 417-439; quiz 617. doi: 10.1148/rg.282075066

Huisman, T. A. G. M., Loenneker, T., Barta, G., Bellemann, M. E., Hennig, J., Fischer, J. E., et al. (2006). Quantitative diffusion tensor MR imaging of the brain: field strength related variance of apparent diffusion coefficient (ADC) and fractional anisotropy (FA) scalars. *Eur. Radiol.* 16, 1651. doi: 10.1007/s00330-006-0175-8

Hunsche, S., Moseley, M. E., Stoeter, P., and Hedehus, M. (2001). Diffusion-tensor MR imaging at 1.5 and 3.0 T: initial observations. *Radiology* 221, 550–556. doi: 10.1148/radiol.2212001823

Jang, S. H., and Kwon, H. G. (2018). Injury of the hypothalamus in patients with hypoxic-ischemic brain injury: a diffusion tensor imaging study. *Am. J. Phys. Med. Rehabil.* 97, 160–163. doi: 10.1097/PHM.0000000000000813

Jiang, H., van Zijl, P. C., Kim, J., Pearlson, G. D., and Mori, S. (2006). DtiStudio: resource program for diffusion tensor computation and fiber bundle tracking. *Comput. Methods Programs Biomed.* 81, 106–116. doi: 10.1016/j.cmpb.2005.08.004

Keller, E., Flacke, S., Urbach, H., and Schild, H. H. (1999). Diffusion- and perfusion-weighted magnetic resonance imaging in deep cerebral venous thrombosis. *Stroke* 30, 1144–1146. doi: 10.1161/01.STR.30.5.1144

Krishnan, P., and Shroff, M. (2016). Neuroimaging in neonatal hypoxic ischemic encephalopathy. *Indian J. Pediatr.* 83, 995–1002. doi: 10.1007/s12098-016-2042-1

Krüger, E., Kritzinger, A., and Pottas, L. (2019). Oropharyngeal dysphagia in breastfeeding neonates with hypoxic-ischemic encephalopathy on therapeutic hypothermia. *Breastfeed. Med.* 14, 718–723. doi: 10.1089/bfm.2019.0048

Lee-Kelland, R., Jary, S., Tonks, J., Cowan, F. M., Thoresen, M., and Chakkarapani, E. (2020). School-age outcomes of children without cerebral palsy cooled for neonatal hypoxic-ischaemic encephalopathy in 2008-2010. *Arch. Dis. Child. Fetal Neonatal Ed.* 105, 8–13. doi: 10.1136/archdischild-2018-316509

Lemmon, M. E., Wagner, M. W., Bosemani, T., Carson, K. A., Northington, F. J., Huisman, T., et al. (2017). Diffusion tensor imaging detects occult cerebellar injury in severe neonatal hypoxic-ischemic encephalopathy. *Dev. Neurosci.* 39, 207–214. doi: 10.1159/000454856

Li, S. J., Liu, W., Wang, J. L., Zhang, Y., Zhao, D. J., Wang, T. J., et al. (2014). The role of TNF-α, IL-6, IL-10, and GDNF in neuronal apoptosis in neonatal rat with hypoxic-ischemic encephalopathy. *Eur. Rev. Med. Pharmacol. Sci.* 18, 905–909.

Li, Y., Shea, S. M., Lorenz, C. H., Jiang, H., Chou, M. C., and Mori, S. (2013). Image corruption detection in diffusion tensor imaging for post-processing and real-time monitoring. *PLoS ONE* 8, e49764. doi: 10.1371/journal.pone.0049764

Liauw, L., van Wezel-Meijler, G., Veen, S., van Buchem, M. A., and van der Grond, J. (2009). Do apparent diffusion coefficient measurements predict outcome in children with neonatal hypoxic-ischemic encephalopathy? *AJNR Am. J. Neuroradiol.* 30, 264–270. doi: 10.3174/ajnr.A1318

Longo, D., Bottino, F., Lucignani, G., Scarciolla, L., Pasquini, L., Rossi Espagnet, M. C., et al. (2020). DTI parameters in neonates with hypoxic-ischemic encephalopathy after total body hypothermia. *J. Matern. Fetal Neonatal Med*. 17, 1–8. doi: 10.1080/14767058.2020.1846180

Ly, M. T., Nanavati, T. U., Frum, C. A., and Pergami, P. (2015). Comparing tract-based spatial statistics and manual region-of-Interest labeling as diffusion analysis methods to detect white matter abnormalities in infants with hypoxic-Ischemic encephalopathy. *J. Magn. Reson. Imaging* 42, 1689–1697. doi: 10.1002/jmri.24930

Martinez-Biarge, M., Diez-Sebastian, J., Kapellou, O., Gindner, D., Allsop, J. M., Rutherford, M. A., et al. (2011). Predicting motor outcome and death in term hypoxic-ischemic encephalopathy. *Neurology* 76, 2055–2061. doi: 10.1212/WNL.0b013e31821f442d

Massaro, A. N. (2015). MRI for neurodevelopmental prognostication in the high-risk term infant. *Semin. Perinatol.* 39, 159–167. doi: 10.1053/j.semperi.2015.01.009

Massaro, A. N., Evangelou, I., Fatemi, A., Vezina, G., McCarter, R., Glass, P., et al. (2015). White matter tract integrity and developmental outcome in newborn infants with hypoxic-ischemic encephalopathy treated with hypothermia. *Dev. Med. Child Neurol.* 57, 441–448. doi: 10.1111/dmcn.12646

Moritani, T., Shrier, D. A., Numaguchi, Y., Takase, Y., Takahashi, C., Wang, H. Z., et al. (2000). Diffusion-weighted echo-planar MR imaging: clinical applications and pitfalls. A pictorial essay. *Clin. Imaging* 24, 181–192. doi: 10.1016/S0899-7071(00)00203-5

Neil, J. J., and Inder, T. E. (2006). Detection of wallerian degeneration in a newborn by diffusion magnetic resonance imaging (MRI). *J. Child Neurol.* 21, 115–118. doi: 10.1177/08830738060210021501

Northington, F. J., Ferriero, D. M., Graham, E. M., Traystman, R. J., and Martin, L. J. (2001a). Early neurodegeneration after hypoxia-ischemia in neonatal rat is necrosis while delayed neuronal death is apoptosis. *Neurobiol. Dis.* 8, 207–219. doi: 10.1006/nbdi.2000.0371

Northington, F. J., Ferriero, D. M., and Martin, L. J. (2001b). Neurodegeneration in the thalamus following neonatal hypoxia-ischemia is programmed cell death. *Dev. Neurosci.* 23, 186–191. doi: 10.1159/000046141

Northington, F. J., Kratimenos, P., Turnbill, V., Flock, D. L., Asafu-Adjaye, D., Chavez-Valdez, R., et al. (2022). Basal forebrain magnocellular cholinergic systems are damaged in mice following neonatal hypoxia-ischemia. *J. Comp. Neurol.* 530, 1148–1163. doi: 10.1002/cne.25263

Oishi, K., Mori, S., Donohue, P. K., Ernst, T., Anderson, L., Buchthal, S., et al. (2011). Multi-contrast human neonatal brain atlas: application to normal neonate development analysis. *Neuroimage* 56, 8–20. doi: 10.1016/j.neuroimage.2011.01.051

Orrock, J. E., Panchapakesan, K., Vezina, G., Chang, T., Harris, K., Wang, Y., et al. (2016). Association of brain injury and neonatal cytokine response during therapeutic hypothermia in newborns with hypoxic-ischemic encephalopathy. *Pediatr. Res.* 79, 742–747. doi: 10.1038/pr.2015.280

Otsuka, Y., Chang, L., Kawasaki, Y., Wu, D., Ceritoglu, C., Oishi, K., et al. (2019). A multi-atlas label fusion tool for neonatal brain MRI parcellation and quantification. *J. Neuroimaging* 29, 431–439. doi: 10.1111/jon.12623

Ouwehand, S., Smidt, L. C. A., Dudink, J., Benders, M., de Vries, L. S., Groenendaal, F., et al. (2020). Predictors of outcomes in hypoxic-ischemic encephalopathy following hypothermia: a meta-analysis. *Neonatology* 117, 411–427. doi: 10.1159/000505519

Parmentier, C. E. J., de Vries, L. S., and Groenendaal, F. (2022). Magnetic resonance imaging in (Near-)Term infants with hypoxic-ischemic encephalopathy. *Diagnostics* 12, 645. doi: 10.3390/diagnostics12030645

Qin, W., Zhang, M., Piao, Y., Guo, D., Zhu, Z., Tian, X., et al. (2012). Wallerian degeneration in central nervous system: dynamic associations between diffusion indices and their underlying pathology. *PLoS ONE* 7, e41441. doi: 10.1371/journal.pone.0041441

Rai, V., Nath, K., Saraswat, V. A., Purwar, A., Rathore, R. K. S., and Gupta, R. K. (2008). Measurement of cytotoxic and interstitial components of cerebral edema in acute hepatic failure by diffusion tensor imaging. *J. Magn. Reson. Imaging.* 28, 334–341. doi: 10.1002/jmri.21438

Rollins, N., Booth, T., Morriss, M. C., Sanchez, P., Heyne, R., and Chalak, L. (2014). Predictive value of neonatal MRI showing no or minor degrees of brain injury after hypothermia. *Pediatr. Neurol.* 50, 447–451. doi: 10.1016/j.pediatrneurol.2014.01.013

Salas, J., Reddy, N., Orru, E., Carson, K. A., Chavez-Valdez, R., Burton, V. J., et al. (2019). The role of diffusion tensor imaging in detecting hippocampal injury following neonatal hypoxic-ischemic encephalopathy. *J. Neuroimaging* 29, 252–259. doi: 10.1111/jon.12572

Sarnat, H. B., and Sarnat, M. S. (1976). Neonatal encephalopathy following fetal distress. A clinical and electroencephalographic study. *Arch. Neurol.* 33, 696–705. doi: 10.1001/archneur.1976.00500100030012

Seo, Y., Kim, G. T., and Choi, J. W. (2017). Early detection of neonatal hypoxic-ischemic white matter injury: an MR diffusion tensor imaging study. *Neuroreport* 28, 845–855. doi: 10.1097/WNR.0000000000000844

Shankaran, S., Laptook, A. R., Ehrenkranz, R. A., Tyson, J. E., McDonald, S. A., Donovan, E. F., et al. (2005). Whole-Body Hypothermia for Neonates with Hypoxic–Ischemic Encephalopathy. *N. Eng. J. Med.* 353, 1574–1584. doi: 10.1056/NEJMcps050929

Shankaran, S., McDonald, S. A., Laptook, A. R., Hintz, S. R., Barnes, P. D., Das, A., et al. (2015). Neonatal magnetic resonance imaging pattern of brain injury as a biomarker of childhood outcomes following a trial of hypothermia for neonatal hypoxic-ischemic encephalopathy. *J. Pediatr.* 167, 987 e983–993 e983. doi: 10.1016/j.jpeds.2015.08.013

Tagin, M. A., Woolcott, C. G., Vincer, M. J., Whyte, R. K., and Stinson, D. A. (2012). Hypothermia for neonatal hypoxic ischemic encephalopathy: an updated systematic review and meta-analysis. *Arch. Pediatr. Adolesc. Med*. 166, 558–566. doi: 10.1001/archpediatrics.2011.1772

Takle, M., Conaway, M., and Burnsed, J. (2021). Electroencephalogram background predicts time to full oral feedings in hypoxic-ischemic encephalopathy. *Am. J. Perinatol.* doi: 10.1055/s-0041-1725161. [Epub ahead of print].

Tang, X., Yoshida, S., Hsu, J., Huisman, T. A., Faria, A. V., Oishi, K., et al. (2014). Multi-contrast multi-atlas parcellation of diffusion tensor imaging of the human brain. *PLoS ONE* 9, e96985. doi: 10.1371/journal.pone.0096985

Thayyil, S., Chandrasekaran, M., Taylor, A., Bainbridge, A., Cady, E. B., Chong, W. K., et al. (2010). Cerebral magnetic resonance biomarkers in neonatal encephalopathy: a meta-analysis. *Pediatrics* 125, e382–395. doi: 10.1542/peds.2009-1046

Tusor, N., Wusthoff, C., Smee, N., Merchant, N., Arichi, T., Allsop, J. M., et al. (2012). Prediction of neurodevelopmental outcome after hypoxic-ischemic encephalopathy treated with hypothermia by diffusion tensor imaging analyzed using tract-based spatial statistics. *Pediatr. Res.* 72, 63–69. doi: 10.1038/pr.2012.40

Utsunomiya, H. (2011). Diffusion MRI abnormalities in pediatric neurological disorders. *Brain Dev.* 33, 235–242. doi: 10.1016/j.braindev.2010.08.015

van Handel, M., Swaab, H., de Vries, L. S., and Jongmans, M. J. (2010). Behavioral outcome in children with a history of neonatal encephalopathy following perinatal asphyxia. *J. Pediatr. Psychol.* 35, 286–295. doi: 10.1093/jpepsy/jsp049

van Laerhoven, H., de Haan, T. R., Offringa, M., Post, B., and van der Lee, J. H. (2013). Prognostic tests in term neonates with hypoxic-ischemic encephalopathy: a systematic review. *Pediatrics* 131, 88–98. doi: 10.1542/peds.2012-1297

Venkatasubramanian, C., Kleinman, J. T., Fischbein, N. J., Olivot, J. M., Gean, A. D., Eyngorn, I., et al. (2013). Natural history and prognostic value of corticospinal tract Wallerian degeneration in intracerebral hemorrhage. *J. Am. Heart Assoc.* 2, e000090. doi: 10.1161/JAHA.113.000090

Wu, D., Chang, L., Akazawa, K., Oishi, K., Skranes, J., Ernst, T., et al. (2017a). Change-point analysis data of neonatal diffusion tensor MRI in preterm and term-born infants. *Data Brief* 12, 453–458. doi: 10.1016/j.dib.2017.04.020

Wu, D., Chang, L., Akazawa, K., Oishi, K., Skranes, J., Ernst, T., et al. (2017b). Mapping the critical gestational age at birth that alters brain development in preterm-born infants using multi-modal MRI. *Neuroimage* 149, 33–43. doi: 10.1016/j.neuroimage.2017.01.046

Wu, D., Martin, L. J., Northington, F. J., and Zhang, J. (2014). Oscillating gradient diffusion MRI reveals unique microstructural information in normal and hypoxia-ischemia injured mouse brains. *Magn. Reson. Med.* 72, 1366–1374. doi: 10.1002/mrm.25441

Wu, H., Li, Z., Yang, X., Liu, J., Wang, W., and Liu, G. (2017c). SBDPs and Tau proteins for diagnosis and hypothermia therapy in neonatal hypoxic ischemic encephalopathy. *Exp. Ther. Med.* 13, 225–229. doi: 10.3892/etm.2016.3911

Youn, Y., Sung, I. K., and Lee, I. G. (2013). The role of cytokines in seizures: interleukin (IL)-1β, IL-1Ra, IL-8, and IL-10. *Korean J. Pediatr.* 56, 271–274. doi: 10.3345/kjp.2013.56.7.271

Yu, C., Zhu, C., Zhang, Y., Chen, H., Qin, W., Wang, M., et al. (2009). A longitudinal diffusion tensor imaging study on Wallerian degeneration of corticospinal tract after motor pathway stroke. *Neuroimage* 47, 451–458. doi: 10.1016/j.neuroimage.2009.04.066

Zarifi, M. K., Astrakas, L. G., Poussaint, T. Y., Plessis Ad, A., Zurakowski, D., and Tzika, A. A. (2002). Prediction of adverse outcome with cerebral lactate level and apparent diffusion coefficient in infants with perinatal asphyxia. *Radiology* 225, 859–870. doi: 10.1148/radiol.2253011797

Zheng, Q., Viaene, A. N., Freeman, C. W., and Hwang, M. (2021). Radiologic-pathologic evidence of brain injury: hypoperfusion in the Papez circuit results in poor neurodevelopmental outcomes in neonatal hypoxic ischemic encephalopathy. *Childs. Nerv. Syst.* 37, 63–68. doi: 10.1007/s00381-020-04795-0

Zhou, X., Sakaie, K. E., Debbins, J. P., Narayanan, S., Fox, R. J., and Lowe, M. J. (2018). Scan-rescan repeatability and cross-scanner comparability of DTI metrics in healthy subjects in the SPRINT-MS multicenter trial. *Magn. Reson. Imaging* 53, 105–111. doi: 10.1016/j.mri.2018.07.011

frontiers | Frontiers in Neuroscience

TYPE Original Research
PUBLISHED 16 September 2022
DOI 10.3389/fnins.2022.952322

OPEN ACCESS

EDITED BY
Dan Wu,
Zhejiang University, China

REVIEWED BY
Jessie Maxwell,
University of New Mexico,
United States
Yuma Kitase,
Johns Hopkins Medicine, United States

*CORRESPONDENCE
Rupa Radhakrishnan
rradhak@iu.edu

SPECIALTY SECTION
This article was submitted to Neurodevelopment, a section of the journal Frontiers in Neuroscience

RECEIVED 25 May 2022
ACCEPTED 01 September 2022
PUBLISHED 16 September 2022

CITATION
Vishnubhotla RV, Zhao Y, Wen Q, Dietrich J, Sokol GM, Sadhasivam S and Radhakrishnan R (2022) Brain structural connectome in neonates with prenatal opioid exposure. *Front. Neurosci.* 16:952322. doi: 10.3389/fnins.2022.952322

Brain structural connectome in neonates with prenatal opioid exposure

Ramana V. Vishnubhotla[1], Yi Zhao[2], Qiuting Wen[1], Jonathan Dietrich[3], Gregory M. Sokol[4], Senthilkumar Sadhasivam[5] and Rupa Radhakrishnan[1]*

[1]Department of Radiology and Imaging Sciences, Indiana University School of Medicine, Indianapolis, IN, United States, [2]Department of Biostatistics and Health Data Science, Indiana University School of Medicine, Indianapolis, IN, United States, [3]Indiana University School of Medicine, Indianapolis, IN, United States, [4]Department of Pediatrics, Indiana University School of Medicine, Indianapolis, IN, United States, [5]Department of Anesthesiology and Perioperative Medicine, University of Pittsburgh Medical Center, University of Pittsburgh School of Medicine, Pittsburgh, PA, United States

Introduction: Infants with prenatal opioid exposure (POE) are shown to be at risk for poor long-term neurobehavioral and cognitive outcomes. Early detection of brain developmental alterations on neuroimaging could help in understanding the effect of opioids on the developing brain. Recent studies have shown altered brain functional network connectivity through the application of graph theoretical modeling, in infants with POE. In this study, we assess global brain structural connectivity through diffusion tensor imaging (DTI) metrics and apply graph theoretical modeling to brain structural connectivity in infants with POE.

Methods: In this prospective observational study in infants with POE and control infants, brain MRI including DTI was performed before completion of 3 months corrected postmenstrual age. Tractography was performed on the whole brain using a deterministic fiber tracking algorithm. Pairwise connectivity and network measure were calculated based on fiber count and fractional anisotropy (FA) values. Graph theoretical metrics were also derived.

Results: There were 11 POE and 18 unexposed infants included in the analysis. Pairwise connectivity based on fiber count showed alterations in 32 connections. Pairwise connectivity based on FA values showed alterations in 24 connections. Connections between the right superior frontal gyrus and right paracentral lobule and between the right superior occipital gyrus and right fusiform gyrus were significantly different after adjusting for multiple comparisons between POE infants and unexposed controls. Additionally, alterations in graph theoretical network metrics were identified with fiber count and FA value derived tracts.

Conclusion: Comparisons show significant differences in fiber count in two structural connections. The long-term clinical outcomes related to these findings may be assessed in longitudinal follow-up studies.

KEYWORDS

NOWS, DTI, diffusion tensor imaging, brain development, prenatal opioid exposure, brain networks, opioid use disorder, structural connectivity

Introduction

Over 6% of pregnant women in the US indicate antepartum opioid use (Ko et al., 2020). From 1999 to 2014, opioid use in pregnant women increased more than 4-fold, (Haight et al., 2018) with consequent increase in incidence of infants born with prenatal opioid exposure (POE). Up to 94% of infants with POE develop drug withdrawal symptoms called neonatal opioid withdrawal syndrome (NOWS) (Khan, 2020). From 2004 to 2014, documented cases of NOWS rose 5-fold and NOWS management associated Medicaid costs rose from $65 million to $462 million, a greater than 7-fold increase (Winkelman et al., 2018).

Risks associated with POE go beyond signs and symptoms of NOWS. Children with POE are at a higher risk of adverse neurodevelopmental and neurobehavioral outcomes, such as learning and attention problems (Levine and Woodward, 2018), educational delay (Lee et al., 2019), and lower cognitive and motor scores than unexposed children (Yeoh et al., 2019). In addition, children with POE are at a higher risk for development of attention deficit hyperactive disorder (ADHD) (Azuine et al., 2019; Schwartz et al., 2021) and autism spectrum disorder (Rubenstein et al., 2019).

Older children and adolescents with a history of POE may have long-term alterations in brain development (Sirnes et al., 2017) compared to unexposed controls, including reduced basal ganglia, thalamus, and cerebellar white matter volumes (Walhovd et al., 2007; Yuan et al., 2014), reduced regional cortical thickness (Nygaard et al., 2018), and alterations in hippocampal volumes (Riggins et al., 2012; Robey et al., 2014). However, some of these alterations, such as cortical thickness, are not consistently identified in all studies (Walhovd et al., 2015; Sirnes et al., 2017) or the changes were negated by early childhood environment, Riggins et al. (2012) suggesting that perinatal and postnatal factors could potentially influence neuroplasticity in the developing pediatric brain. Older children and adolescents with POE also showed white matter microstructural alterations (Soares et al., 2013) alterations such as decreased fractional anisotropy (FA) (Walhovd et al., 2010) on diffusion tensor imaging (DTI), and alterations in working memory networks on functional MRI (fMRI) (Sirnes et al., 2018), all of which correlated with cognitive outcomes.

Recent studies have focused on early detection of evidence related to the impact of prenatal opioids on fetal and infant brain development. For example, fetal brains with POE demonstrated differences in brain morphometry (Radhakrishnan et al., 2022a) compared to unexposed controls based on fetal MRI. Alterations in functional network connectivity on resting state functional MRI (rs-fMRI) have also been described in infants with POE compared to controls using both seed-based and connectome-based approaches (Radhakrishnan et al., 2020, 2022b,c; Merhar et al., 2021; Liu et al., 2022). In a few small DTI studies, white matter microstructural alterations in infants with POE and substance exposure have been reported with voxel-wise analysis (Walhovd et al., 2012; Monnelly et al., 2018; Warton et al., 2018). In our study, we attempt to use a connectome-based approach to understand tract-based microstructural alterations in prenatal opioid exposure.

Brain connectivity is based on anatomical links (structural connectivity) and statistical dependencies (functional connectivity) (Rubinov and Sporns, 2010). It has been effectivity utilized to assess infant (Wen X. et al., 2019; Zhao et al., 2019) and even fetal brains (Turk et al., 2019). In infants, DTI has been used as a marker of white matter integrity and maturation in addition to POE, is shown to be altered in several conditions such as prematurity (Rose et al., 2014; Li et al., 2015; Pannek et al., 2018) and perinatal brain injury (Merhar et al., 2016; Kline-Fath et al., 2018). On rs-fMRI studies, the developing neonatal and infant brain shows increasing complexity in connectomes when assessed using graph theoretical models, with disruptions in network connectivity shown to be associated with perinatal brain insults (Zhao et al., 2019). Graph theory analysis involves studying relationships/connections mathematically utilizing systems composed of nodes and edges (connections between nodes). While the first paper involving graph theoretical analysis was first published in the 1736 by Swiss mathematician Leonhard Euler (Biggs et al., 1986), graph theory metrics

Abbreviations: R, right; L, left; POE, prenatal opioid exposure; NOWS, neonatal opioid withdrawal syndrome; ROI, region of interest; MRI, magnetic resonance imaging; DTI, diffusion tensor imaging; ADHD, attention deficit hyperactivity disorder.

have been applied in neuroimaging to understand networks in the human brain (Bassett and Bullmore, 2009; Bullmore and Sporns, 2009; Mears and Pollard, 2016; Sporns, 2018; Lee et al., 2020).

The direct effects of opioids on the developing brain are mainly through the opioid receptors which are expressed in variable concentrations in different regions of the developing brain as revealed in animal studies (Zhu et al., 1998). Opioid receptors are expressed on oligodendrocytes and their precursors as well as developing neurons. Specifically, these animal studies suggest that opioids impair regional brain myelination, probably through accelerated apoptosis of oligodendrocytes and microglial activation (Oberoi et al., 2019; Gibson et al., 2022). Studies also reveal increases in myelinated axons with compacted myelin sheaths (Vestal-Laborde et al., 2014) in prenatal methadone exposed rats, and dose dependent decreased number of myelinated axons and increased percentage of larger diameter axons with thinner myelin sheaths in prenatal buprenorphine exposed rats, with some of these changes being dose dependent (Sanchez et al., 2008). In addition, prenatal morphine exposure in rats have shown to be associated with regional decreases in neuronal dendritic length and branching (Mei et al., 2009). More recently, POE has been linked to increased neuroinflammation, reduced myelin basic protein, lower fractional anisotropy, and deficits in learning and executive control (Jantzie et al., 2020). These studies suggest an impact of prenatal opioid exposure on white matter developmental integrity that could be evaluated in the infant brain using DTI metrics. We therefore used a connectomics approach to assess microstructural brain development in infants with POE compared to control non-opioid exposed controls.

Materials and methods

Subject recruitment

Subject recruitment was performed similarly to previous studies (Radhakrishnan et al., 2022b,c). This prospective study was performed at Indiana University Health with approval by the Indiana University Institutional Review Board. We recruited infants with prenatal opioid exposure as well as control infants without prenatal opioid exposure at less than 3 months corrected postmenstrual age. Eligible participants were screened from medical records. Infants with major genetic or congenital anomalies, or significant postnatal abnormalities such as birth asphyxia or neonatal sepsis were excluded. Information regarding maternal and infant demographics, maternal opioid use, infant birth and postnatal details including any treatment for neonatal opioid withdrawal syndrome were collected from medical records and maternal self-report questionnaires. Written informed consent was obtained from at least one parent for all minor participants.

Diffusion tensor imaging acquisition

MRI data were acquired on a single Siemens Prisma 3T scanner with a 64-channel RF receiver head/neck coil. All participants underwent T1-weighted imaging and diffusion MRI. T1-weighted anatomical imaging used a 3-dimensional magnetization rapid gradient echo (MPRAGE) with 1 mm × 1 mm × 1mm resolution. The diffusion MRI protocol employed a single-shot spin-echo echo-planar imaging (SS-SE-EPI) sequence with two diffusion-encoding schemes. One used a hybrid diffusion imaging (HYDI)-encoding scheme that contained three zero diffusion-weighting (i.e., b-value = 0 s/mm^2) and multiple concentric diffusion-weighting shells (b-values = 5, 495, 500, 505, 795, 800, 805, 1590, 1595, 1600, 1605, 1610, 2590, 2595, 2600, 2605, and 2610 s/mm^2) for a total of 141 diffusion-weighting gradient directions (Wu and Alexander, 2007; Wen Q. et al., 2019). The second scheme used a single shell diffusion imaging with 64 diffusion directions at b-value = 1000 s/mm^2. The resolution was matched in both schemes, with a field of view of 160 × 160 mm, 66 slices, and a slice thickness of 1.5 mm, yielding 1.5-mm isotropic voxels. An additional b = 0 s/mm^2 with reversed-phase encoding was acquired for geometric distortion correction.

Preprocessing

Initial preprocessing of the MR images for each subject was performed using the FMRIB (for Functional MRI of the Brain) software Library (FSL, Oxford, UK) (Woolrich et al., 2009). Fieldmap and gradient-non-linearity distortion corrections were performed using FSL-topup (Smith et al., 2004). Eddy current-induced disruptions and subject motion were corrected using FSL-eddy (Andersson and Sotiropoulos, 2016). Samples were inspected for quality and those with deformations or greater than 20% loss were excluded. The b-tables were imported and corrected using DSI Studio[1] using a population average template (Yeh et al., 2018). Diffusion data was reconstructed in the MNI space using q-space diffeomorphic reconstruction (QSDR) (Yeh and Tseng, 2011) and aligned with the software neonatal template. We note that for the HYDI-encoding scheme, only the b-values between 505 and 800 s/mm^2 were included in the subsequent tractography analysis.

1 http://dsi-studio.labsolver.org

Tractography

Tractography was performed on the whole brain with DSI Studio using a deterministic fiber tracking algorithm (Yeh et al., 2013) with a diffusion sampling ratio of 1.25. Ten million tracts were calculated for each subject. Quantitative anisotropy (qa) threshold values were determined based visual inspection to maximize number of tracts while minimizing spurious fibers. The quantitative anisotropy threshold was set at 0.05 and 0.03 for DTI and HYDI samples, respectively. The angular threshold was set at 45 degrees and the step size was 0.75 mm. Track lengths shorter than 10 mm or longer than 150 mm were discarded. ICBM template (Fonov et al., 2009, 2011) was registered to subject space through non-linear transformation. Brain parcelation regions were based on the AAL2 atlas (Rolls et al., 2015). Connectivity matrices and graph network measures were calculated in DSI Studio based on fiber count and fractional anisotropy (FA) values.

Pairwise connectivity analysis

Connectivity matrices with 120 regions of interest (ROIs) were collected for each subject based on fiber count and FA values. Regions involving the cerebellum and vermis were excluded, leaving 94 ROIs for the analysis. Region pairs with zero values in over 50% of the samples were removed from the analysis ending up with 644 pairs of fiber count and 652 pairs of FA values. Linear regression models were fitted for each pair to compare between POE and control groups with infant sex, postmenstrual age (PMA) at time of MRI, and DTI scan sequence as the covariates. Multiplicity was corrected following the Benjamini-Hochberg procedure to control for the false discovery rate (Benjamini and Hochberg, 1995). A p-value of <0.05 was considered significant.

Network measures

Network measures for fiber count and FA values were collected for each subject within DSI Studio using the Brain Connectivity Toolbox (Rubinov and Sporns, 2010). Evaluated network measures include network density, global clustering coefficients, local clustering coefficients, average path length, global efficiency, local efficiency, eccentricity, rich club coefficients, node degree, node strength, betweenness centrality, eigenvector centrality, and pagerank centrality. Network measures were based on weighted values. The same type of analysis as in the pairwise connectivity analysis was conducted with the network measures as the outcome. Multiple testing correction was also performed following the Benjamini-Hochberg procedure. A p-value of <0.05 was considered significant.

TABLE 1 Demographic information of subjects.

	POE	Control	p-value
Subject number	11	18	
Males	5	9	1
Gestational age (weeks) (SD)	37.71 (2.77)	39.59 (0.8)	0.051
Postmenstrual age at MRI (weeks) (SD)	43.42 (3.28)	44.37 (1.86)	0.4
Birth weight (kg) (SD)	2.715 (0.52)	3.386 (0.4)	0.002
Birth head circumference (cm) (SD)	33.16 (2.0)	34.39 (1.04)	0.083
Maternal age (years) (SD)	28.73 (3.56)	28.39 (4.27)	0.82
NOWS	3	NA	NA
Postnatal opioid treatment	2	NA	NA
Maternal depression	5	2	0.071
Maternal hepatitis	2	0	0.14
Maternal college degree	0	6	0.058
Maternal buprenorphine	10	NA	NA
Maternal methadone	1	NA	NA
Maternal other opioids	3	NA	NA
Maternal non-opioids	5	NA	NA
Maternal smoking	6	1	0.006

P-values were calculated using Fisher's exact test or unpaired t-test as appropriate.

Results

Demographics

There were 37 subjects with DTI available and 8 infants were excluded due to poor DTI quality. Therefore, 29 infants were included in this study including 11 POE and 18 unexposed infants. Of these, 2 POE and 4 unexposed subjects were imaged using the HYDI protocol. The POE group demonstrated significantly lower birth weight than controls although mean birth weight for both groups was still within range of normal. There were no significant differences in gestational age at birth, postmenstrual age at time of MRI, or birth head circumference. There were differences in education levels as 6 of 18 mothers of unexposed infants had a college degree while none of the 11 mothers with POE infants were college graduates. Within the control group, there were no statistically significant differences in birth weight or birth head circumference in infants born to mothers with or without a college degree.

Mothers of the POE infant group received treatment with 10 receiving buprenorphine and 1 receiving methadone. Of the mothers with POE infants, 3 indicated use of opioids including heroin and 5 indicated use of other non-opioid substances including methamphetamines, marijuana,

and cocaine. Demographic information for the 29 infants is shown in Table 1.

Pairwise connectivity based on fiber count

Connectivity based on fiber count between multiple ROIs were significantly altered in POE infants compared to opioid naïve controls. Connections between the right superior frontal gyrus and right paracentral lobule and between the right superior occipital gyrus and right fusiform gyrus showed significance considering uncorrected *p*-values as well as p-FDR values (Figure 1). There were 30 other connections which were significant when considering uncorrected *p*-values but did not maintain significance when correcting for multiple comparisons. Diagram of connections based on fiber count is shown in Figure 2. Data is summarized in Table 2.

Pairwise connectivity based on fractional anisotropy

Connectivity based on FA between multiple ROIs were altered in POE infants compared to opioid naïve controls. Prior to multiple correction, there were 24 connections which were significant when considering uncorrected *p*-values, but none of these retained significance after correcting for multiple comparisons. Diagram of connections based on FA values is shown in Figure 3. Data is summarized in Table 3.

Network measures based on fiber count

Based on fiber count, there were 15 network metrics which were significantly altered in POE infants compared to opioid naïve controls when considering uncorrected *p*-values. None of the networks maintained statistical significance when correcting for multiple comparisons. Data is summarized in Table 4.

Network measures based on fractional anisotropy

Based on FA values, there were 22 networks which were significantly altered in POE infants compared to opioid naïve controls when considering uncorrected *p*-values. None of the networks maintained statistical significance when correcting for multiple comparisons. Data is summarized in Table 5.

Discussion

Our study is one of the first to show alterations in structural ROI-to-ROI pairwise connectivity and structural network measures in infants with POE compared to non-opioid exposed control infants. In infants with POE, there were greater number of fiber tracks between the right superior frontal gyrus and the right paracentral lobule and fewer fiber tracks between the right superior occipital gyrus and right fusiform gyrus when compared to control infants. We also identified several other regional alterations in graph network metrics in infants with

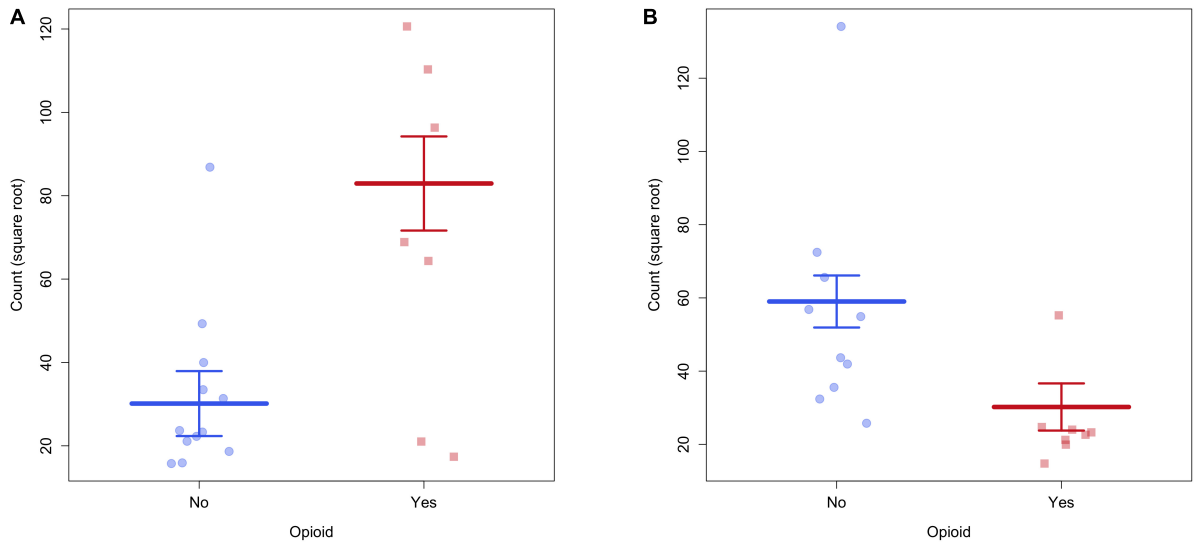

FIGURE 1
(A) There was greater structural connectivity between the right superior frontal gyrus and right paracentral lobule in POE infants. **(B)** There was greater structural connectivity between right superior occipital gyrus and right fusiform gyrus in unexposed infants.

TABLE 2 Connectivity values between POE and opioid naïve infants based on fiber count.

ROI 1	ROI 2	POE vs. Cont. (SE)	t-stat	*p*-value	*p*-corr
Superior Frontal - R	Paracentral Lobule - R	52.80 (6.02)	8.77	4.60E−07	2.96E−04
Superior Occipital - R	Fusiform - R	−28.81 (4.08)	−7.06	8.53E−06	0.003
Parahippocampal – R	Middle Temporal - R	79.13 (19.38)	4.08	5.33E−04	0.092
Fusiform - R	Middle Temporal - R	83.61 (21.06)	3.97	5.68E−04	0.092
Caudate - R	Pallidum - R	54.85 (14.13)	3.88	7.12E−04	0.092
Superior Parietal - R	Precuneus - L	63.83 (17.53)	3.64	0.003	0.263
Olfactory - R	Parahippocampal – R	37.22 (10.79)	3.45	0.003	0.263
Fusiform - R	Precuneus - R	−43.12 (12.16)	−3.55	0.005	0.427
Superior Frontal - L	Lateral OFC - L	35.05 (10.5)	3.34	0.007	0.453
Precuneus - R	Middle Temporal - R	53.15 (17.2)	3.09	0.007	0.453
Superior Temporal - R	Middle Temporal Pole - R	18.97421	2.79	0.012	0.631
Cuneus - R	Superior Parietal - R	51.08212	2.74	0.012	0.631
Cuneus - R	Middle Occipital - R	52.65 (19.63)	2.68	0.013	0.631
Hippocampus - R	Putamen - R	33.87 (12.69)	2.67	0.014	0.631
Hippocampus - R	Middle Temporal - R	82.98 (31.96)	2.60	0.016	0.677
Middle Cingulate - R	Posterior Cingulate - L	34.47 (13.27)	2.60	0.017	0.677
Inferior Frontal (Oper) - L	Rolandic Operculum - L	−31.07 (12.32)	−2.52	0.019	0.709
Precentral - R	Middle Cingulate - R	47.57 (19.07)	2.49	0.021	0.750
Rectus - R	Amygdala - R	27.67 (10.54)	2.63	0.024	0.750
Insula - R	Parahippocampal - R	30.89 (12.37)	2.50	0.024	0.750
Hippocampus - R	Superior Temporal - R	46.81 (19.26)	2.43	0.025	0.750
Middle Frontal - R	Anterior Cingulate - R	−51.87 (21.32)	−2.43	0.026	0.750
Inferior Parietal - R	Supramarginal - R	30.14 (12.98)	2.32	0.029	0.814
Superior Frontal 2 - L	Insula - L	71.08 (30.49)	2.33	0.032	0.847
Insula - L	Middle Temporal - L	45.74 (20.46)	2.24	0.036	0.901
Rectus - L	Putamen - L	26.11 (11.69)	2.23	0.038	0.901
Inferior Frontal (Tri) - L	Rolandic Operculum - L	−35.88 (15.84)	−2.26	0.038	0.901
Calcarine - R	Angular - R	28.17 (12.69)	2.22	0.042	0.931
Lingual - L	Lingual - R	66.69 (30.76)	2.17	0.048	0.931
Insula - R	Amygdala - R	35.53 (16.73)	2.12	0.049	0.931
Middle Frontal - L	Lateral OFC - L	26.36 (12.47)	2.11	0.049	0.931
Superior Occipital - R	Precuneus - R	−52.34 (25.25)	−2.07	0.049	0.931

POE; however, these did not maintain statistical significance after multiple corrections.

A few small studies have investigated brain diffusion metrics in infants with prenatal opioid exposure (Walhovd et al., 2012; Monnelly et al., 2018; Peterson et al., 2020). Using tract based spatial statistics, Monnelly et al. showed decreased fractional anisotropy in the internal capsule and inferior longitudinal fasciculus in prenatal methadone exposed infants compared to controls (Monnelly et al., 2018). Using similar methods, Walhovd et al. identified higher mean diffusivity (MD) in the superior longitudinal fasciculus in methadone exposed infants compared to control infants (Walhovd et al., 2012). Interestingly, another recent study showed higher FA values and reduced apparent diffusion coefficient (ADC) values in the frontal and parietal white matter in infants with prenatal methadone or heroin exposure (Peterson et al., 2020). In our current study, we used graph theoretical modeling to better understand global brain structural connectivity. The apparent differences in direction of FA values on prior studies is somewhat explained by our study, where we identified both stronger and weaker ROI-to-ROI connectivity based on FA strength in different brain region pairs in infants with POE compared to controls. We hypothesize therefore that there may be regional alterations in myelin and axonal microstructure that could be responsible for these results. Opioids likely exert their effects on the brain mainly through the opioid receptors and animal studies show differential opioid receptor expression in the developing fetal brain (Zhu et al., 1998). Opioid receptors are expressed on neurons and oligodendrocytes and their precursors, and are responsible for neuronal and glial development, and prenatal exposure to exogenous opioids may hence result in regional variations in degree of neuronal

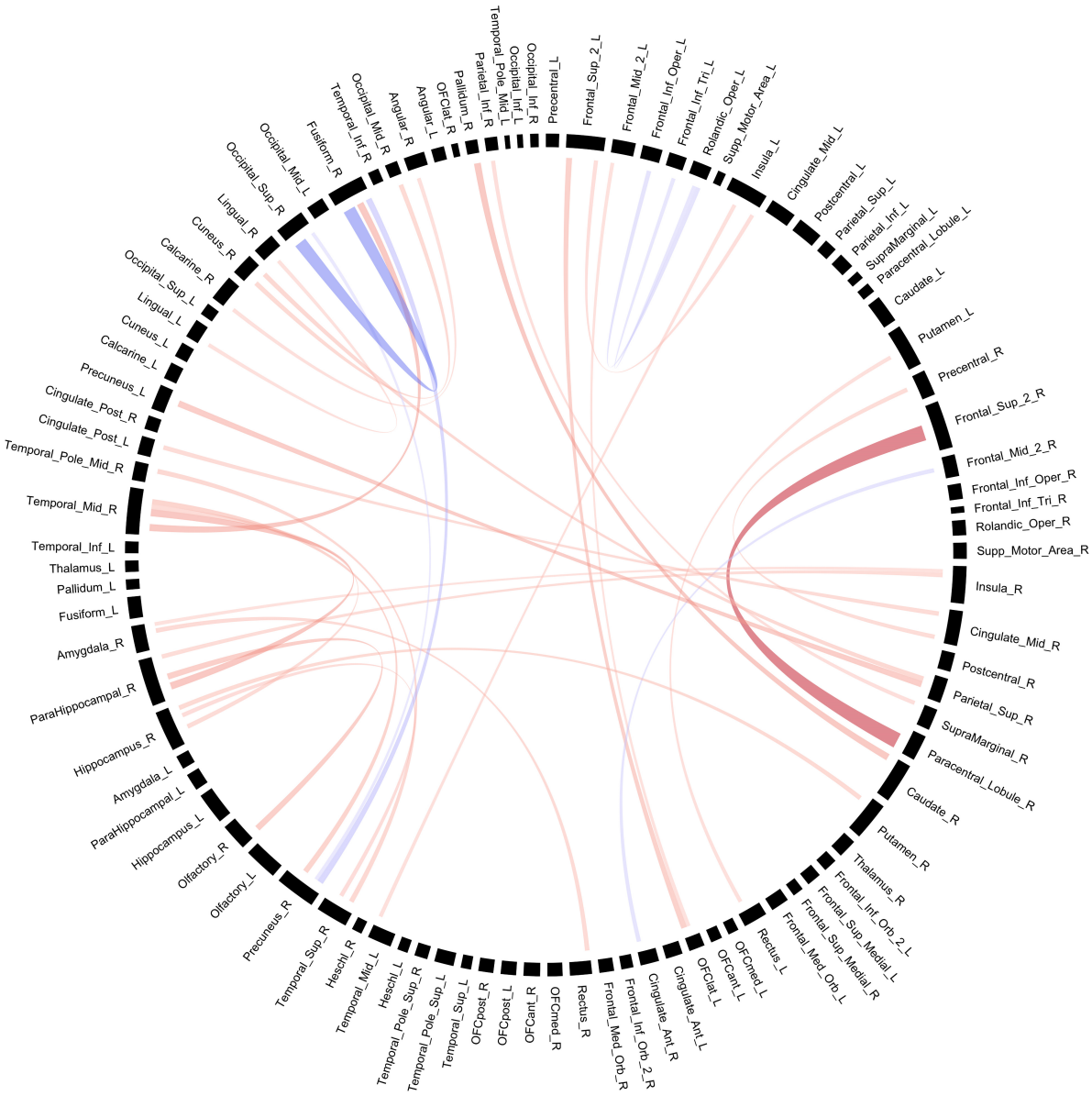

FIGURE 2
Structural connectivity between regions of interest based on fiber count. Red bands indicate a greater connectivity in the POE group while blue bands indicate greater connectivity in the control group. Band thickness is determined by the t-stat value.

apoptosis and myelination in the fetal and infant brain (Vestal-Laborde et al., 2014; Velasco et al., 2021).

We identified significantly higher FA based fiber tracts in the right superior frontal gyrus to the right paracentral lobule. The superior frontal gyrus has been associated with response inhibition and motor urgency (Hu et al., 2016), while the paracentral lobule is responsible for motor and sensory functions of the lower limbs (Johns, 2014). Cortical thickness in the right superior frontal gyrus and other areas of the right prefrontal cortex (Almeida et al., 2010) are also shown to be reduced in children and adults with attention deficit hyperactivity disorder (ADHD). Considering that those with POE are more likely to develop ADHD (Azuine et al., 2019; Schwartz et al., 2021), assessing structural connectivity of the superior frontal gyrus may be an important prognostic marker for developmental disorders such as ADHD.

We also identified a significant lower FA based fiber count between the right superior occipital gyrus and the right fusiform gyrus in infants with POE compared to controls. Both these regions correspond to visual processing and object and facial recognition (Weiner and Zilles, 2016). Our results are in keeping with other studies have also indicated visual deficits in children

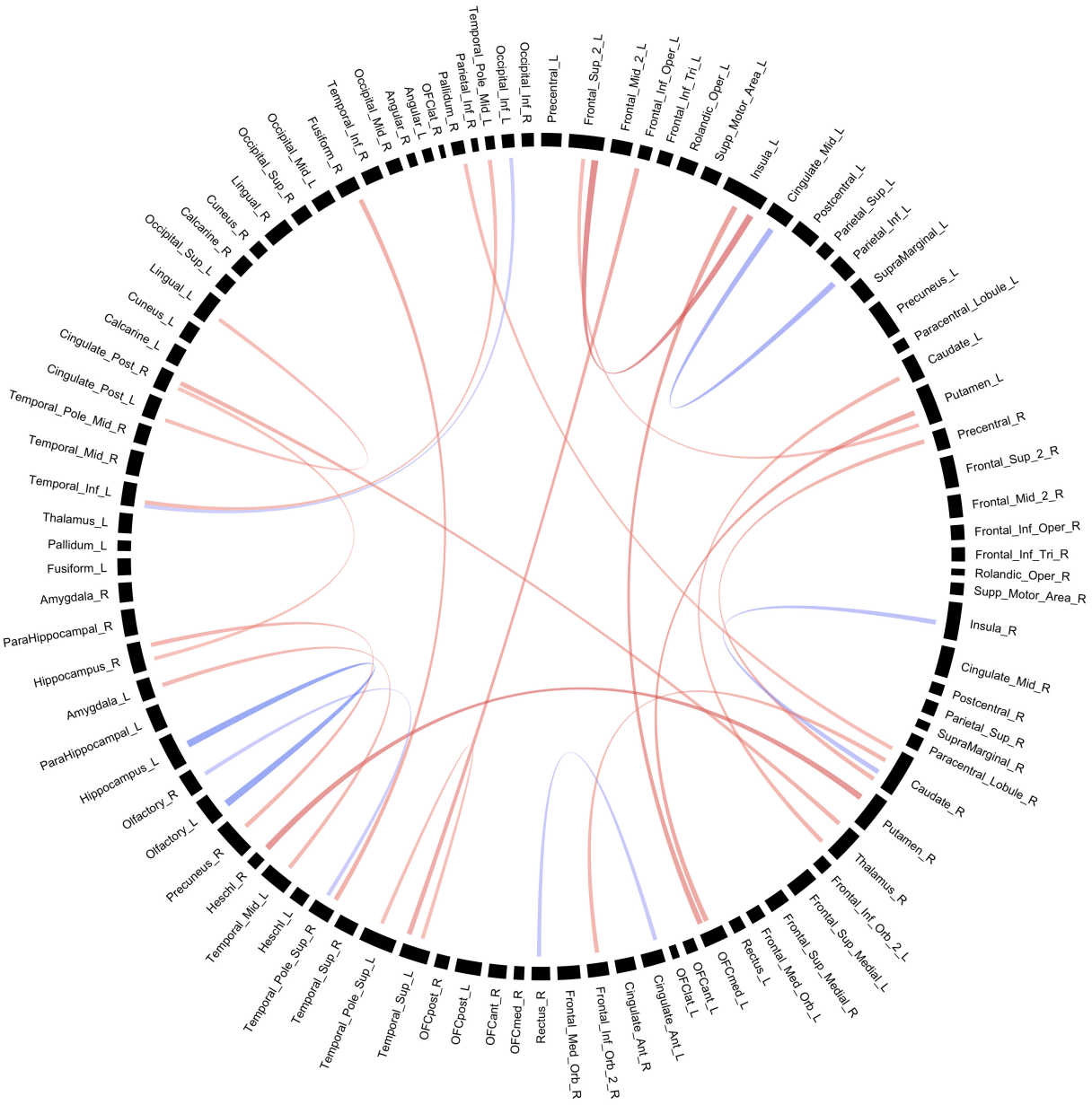

FIGURE 3
Structural connectivity between regions of interest based on FA values. Red bands indicate a greater connectivity in the POE group while blue bands indicate greater connectivity in the control group. Band thickness is determined by the t-stat value.

with POE (McGlone and Mactier, 2015; Maguire et al., 2016; Andersen et al., 2020). Children with POE have shown to have vision impairments compared to prenatally unexposed children (Andersen et al., 2020). Additionally, these children have been linked to poorer visual motor skills (Melinder et al., 2013; Sundelin-Wahlsten and Sarman, 2013).

Structural changes in brain functional connectivity have also been shown in infants with POE. Recent work showed alterations in amygdala and thalamocortical functional connectivity in infants with POE compared to controls (Radhakrishnan et al., 2020, 2022b). In addition, recent studies have also applied graph theoretical methods to understand further the brain functional connectivity alterations in POE and their associations with maternal comorbidities and clinical outcomes (Merhar et al., 2021; Radhakrishnan et al., 2022c). Due to differences in brain segmentation atlases, ROI selections and network connectivity analyses methods used in these prior rs-fMRI studies compared to our current DTI study, intermediary causal relationship of microstructural to functional network alterations is difficult to surmise. Since structural deficits often

10.3389/fnins.2022.952322

TABLE 3 Connectivity values between POE and opioid naïve infants based on fractional anisotropy (FA).

ROI 1	ROI 2	POE vs. Cont. (SE)	t-stat	*p*-value	*p*-corr
Superior Frontal – L	Insula - L	0.041 (0.011)	3.78	0.001	0.47
Olfactory – L	Hippocampus – L	−0.044 (0.011)	−3.96	0.001	0.47
Putamen – R	Heschl's- R	0.044 (0.013)	3.46	0.003	0.65
Middle Cingulate – L	Inferior Parietal - L	−0.026 (0.008)	−3.31	0.006	0.98
Medial OFC – L	Insula - L	0.04 (0.013)	3.07	0.010	0.98
Insula - R	Caudate - R	−0.041 (0.015)	-2.66	0.014	0.98
Inferior Frontal (Oper) – L	Superior Temporal - L	0.059 (0.021)	2.76	0.016	0.98
Medial OFC - L	Putamen - L	0.029 (0.01)	2.83	0.016	0.98
Fusiform - R	Superior Temporal Pole - R	0.036 (0.014)	2.62	0.021	0.98
Posterior Cingulate - R	Thalamus - R	0.082 (0.033)	2.50	0.023	0.98
Hippocampus - R	Precuneus - R	0.034 (0.014)	2.42	0.024	0.98
Inferior Frontal (Orb) – R	Caudate - R	0.032 (0.013)	2.42	0.029	0.98
Caudate – L	Thalamus - R	0.065 (0.027)	2.42	0.034	0.98
Middle Temporal_Pole - L	Inferior Temporal - L	0.018 (0.008)	2.28	0.034	0.98
Precentral - R	Caudate - R	0.038 (0.015)	2.45	0.034	0.98
Amygdala - L	Middle Temporal - L	0.031 (0.013)	2.33	0.035	0.98
Rectus - R	Anterior Cingulate - L	−0.071 (0.03)	−2.34	0.036	0.98
Caudate - R	Palladium - R	0.032 (0.015)	2.18	0.039	0.98
Olfactory - R	Superior Temporal Pole - R	−0.03 (0.013)	−2.24	0.039	0.98
Superior Frontal – L	Putamen - L	0.023 (0.011)	2.18	0.044	0.98
Posterior Cingulate - L	Lingual - L	0.043 (0.02)	2.15	0.046	0.98
Superior Temporal - L	Superior Temporal Pole - L	0.023 (0.011)	2.10	0.046	0.98
Inferior Occipital - L	Inferior Temporal - L	−0.021 (0.01)	−2.11	0.046	0.98
Posterior Cingulate - R	Hippocampus - R	0.05 (0.024)	2.06	0.050	0.98

TABLE 4 Network measures between POE and opioid naïve infants based on fiber count.

Network Measure	POE vs. Cont. (SE)	t-stat	*p*-value	*p*-corr
Betweenness centrality				
Transverse Temporal – L	10.52 (4.98)	2.11	0.045	0.694
Inferior Parietal – L	43.3 (19.65)	2.20	0.037	0.694
Supp. Motor – R	−44.66 (20.68)	−2.16	0.041	0.694
Thalamus – L	357.25 (121.32)	2.94	0.007	0.665
Cluster coefficient				
Caudate – R	0.005 (0.002)	2.43	0.023	0.691
Middle Cingulate – R	0.007 (0.002)	3.44	0.002	0.201
Hippocampus – R	0.01 (0.004)	2.43	0.023	0.691
Inferior Parietal – L	−0.013 (0.006)	−2.21	0.037	0.691
Middle Temporal – R	0.009 (0.004)	2.26	0.033	0.691
Eigenvector centrality				
Precentral – R	−0.025 (0.012)	−2.12	0.045	0.997
Local efficiency				
Caudate – R	0.009 (0.004)	2.43	0.023	0.724
Middle Cingulate – R	0.011 (0.004)	2.68	0.013	0.724
Hippocampus – R	0.018 (0.007)	2.58	0.016	0.724
Inferior Parietal – L	−0.019 (0.009)	−2.27	0.032	0.764
Pagerank centrality				
Precentral – R	−0.002 (0.001)	−2.48	0.020	0.771

TABLE 5 Network measures between POE and opioid naïve infants based on fractional anisotropy (FA).

Network Measure	POE vs. Cont. (SE)	t-stat	*p*-value	*p*-corr
Betweenness centrality				
Cuneus – R	93.3 (27.95)	3.34	0.003	0.086
Hippocampus – L	−194.23 (81.31)	−2.39	0.025	0.273
Hippocampus – R	−118.81 (42.54)	−2.79	0.010	0.19
Lateral OFC – L	−1.58 (0.74)	−2.13	0.043	0.369
Medial OFC – R	36.38 (15.59)	2.33	0.028	0.273
Inferior Parietal – L	65.37 (18.97)	3.45	0.002	0.086
Rectus – L	205.45 (75.78)	2.71	0.012	0.191
Rectus – R	168.55 (47.09)	3.58	0.002	0.086
Supp. Motor – R	−70.59 (29.11)	−2.43	0.023	0.273
Supramarginal – ‘R	47.63 (20.51)	2.32	0.029	0.273
Thalamus – R	−153.34 (54.79)	−2.80	0.010	0.19
Cluster coefficient				
Middle Occipital – L	−0.033 (0.014)	−2.28	0.032	0.925
Rectus – R	−0.042 (0.019)	−2.22	0.036	0.925
Supp. Motor – L	−0.027 (0.013)	−2.13	0.044	0.925
Thalamus – L	−0.04 (0.018)	−2.24	0.034	0.925
Local efficiency				
Middle Occipital – R	−0.048 (0.022)	−2.16	0.041	0.853
Paracentral Lobule – R	−0.052 (0.02)	−2.54	0.018	0.853
Pagerank centrality				
Middle Occipital – R	−0.001 (0.0006)	−2.08	0.049	0.761
Medial OFC – L	0.001 (0.0006)	2.22	0.036	0.761
Precuneus – L	−0.002 (0.0007)	−2.47	0.021	0.761
Supp. Motor – R	−0.002 (0.0006)	−3.15	0.004	0.408
Inferior Temporal – L	0.001 (0.0005)	2.12	0.044	0.761

underlie functional impairments, we may presume some degree of overlap in regional structural and functional connectivity. However, prenatal opioid exposure is known impact myelin, axonal and neuronal integrity based on the distribution of opioid receptors, and there may also be isolated effects of opioids on these structures. Brain morphometry, DTI and fMRI network studies may therefore be considered complementary in assessing the overall impact of opioids on the developing brain.

Several mothers in our study indicated use of substances such as methamphetamines, marijuana, cocaine, and tobacco. Prenatal exposure to some of these substances also show disruptions in the structural connectome. For example, neonates with prenatal methamphetamine exposure (PME) show lower FA values than unexposed infants in several connections between the striatum and midbrain, orbitofrontal cortex and associated limbic structures, all components of the striato-thalamo-orbitofrontal circuit and its limbic connections, which may be responsible for drug addiction related neurocircuitry (Warton et al., 2018, 2020). Detrimental effects due to prenatal substance exposure may linger as older children with PME demonstrated lower FA in the frontal and limbic regions and greater mean, radial, and axial diffusivities (Roos et al., 2015) as well as lower apparent diffusivity coefficients (Cloak et al., 2009). These early brain microstructural alterations noted on diffusion imaging in prenatal cocaine, marijuana and methadone or heroin exposure may also serve as predictors of 12 month behavioral and language outcomes (Peterson et al., 2020). Similarly, infants with prenatal alcohol exposure also showed altered FA values and reduced white matter microstructural integrity (Donald et al., 2015), and these early brain microstructural disruptions may persist until later life (Wozniak et al., 2009; Moore and Xia, 2021; Roos et al., 2021; Stephen et al., 2021).

Given the long-term developmental issues associated with prenatal substance exposure, especially in the realm of mental processing, impulse control, and executive functions (Wozniak and Muetzel, 2011), identification of early brain developmental microstructural alterations with DTI may offer a mechanistic understanding and be a predictive biomarker for these future outcomes. However, more work needs to be done to further our understanding on how the brain structural connectome may correlate with developmental outcomes.

This study had a few limitations. First, this study was restricted by the number of subjects that were evaluated.

While 37 infants were imaged, only 29 studies were able to be used for analysis due to poor image quality, mostly due to motion artifact. Since diffusion imaging has a low signal to noise ratio, it is particularly susceptible to motion artifacts (Farrell et al., 2007). Infants pose a particular challenge as they cannot follow instructions. While imaging of neonates in this study was conducted during sleep, head motion was still a noticeable issue. Two different diffusion techniques were used, however we had infants with POE and control subjects that were scanned with both these techniques, and DTI scan technique was used in the regression model to account for scan related issues. Polysubstance use was not controlled for in this study due to limited prevalence of individuals with single substance use. Polysubstance use (e.g., SSRIs, nicotine, benzodiazepines, etc.) is known to affect opioid metabolism and development of NOWS (Patrick et al., 2015) and may impact brain development. Future larger studies would be better powered to understand these associations. Maternal comorbidities (e.g., stress, depression, socioeconomic, genetic) were not included in this small sample study. We and other researchers have shown the effects of maternal comorbidities on infant brain functional connectivity, and we hope that future studies would be able to assess this impact. Nevertheless, our study has shown novel findings in graph theoretical networks of brain structural connectivity in POE that adds to the existing limited knowledge in this field. Future longitudinal studies can also help understand the clinical outcomes associated with brain microstructural alterations in prenatal substance exposure.

Conclusion

Children with prenatal opioid exposure may be at greater risk to have a developmental disorder. Assessing structural connectivity could have important prognostic value for these conditions. This study identified two structural connections where tract counts were significantly different in POE infants compared to unexposed infants. These microstructural alterations may be positive or negative based on brain region and may reflect differences in development and opioid related impact. Future longitudinal studies with larger sample sizes would help understand how these preliminary results of altered structural connectivity relate to long-term developmental implications in children with prenatal substance exposure.

Data availability statement

The raw data supporting the conclusions of this article will be made available by the authors, without undue reservation.

Ethics statement

The studies involving human participants were reviewed and approved by the Indiana University Institutional Review Board. Written informed consent to participate in this study was provided by the participants' legal guardian/next of kin.

Author contributions

RV contributed to the sample processing, analysis, design, and manuscript preparation. YZ contributed to the analysis and manuscript preparation. QW contributed to the analysis, design, and manuscript preparation. JD contributed to the sample processing. GS and SS contributed to the recruitment and design. RR contributed to the recruitment, design, and manuscript preparation. All authors contributed to the article and approved the submitted version.

Funding

RR was supported by the American Roentgen Ray Scholarship Award 2018 and Radiological Society of North America Seed Grant 2018. SS and RR were supported by the Eunice Kennedy Shriver National Institute of Child Health and Human Development of the National Institutes of Health under Award, R01HD096800 (PI: SS).

Conflict of interest

The authors declare that the research was conducted in the absence of any commercial or financial relationships that could be construed as a potential conflict of interest.

Publisher's note

All claims expressed in this article are solely those of the authors and do not necessarily represent those of their affiliated organizations, or those of the publisher, the editors and the reviewers. Any product that may be evaluated in this article, or claim that may be made by its manufacturer, is not guaranteed or endorsed by the publisher.

Author disclaimer

The content is solely the responsibility of the authors and does not necessarily represent the official views of the National Institutes of Health.

References

Almeida, L. G., Ricardo-Garcell, J., Prado, H., Barajas, L., Fernandez-Bouzas, A., Avila, D., et al. (2010). Reduced right frontal cortical thickness in children, adolescents and adults with ADHD and its correlation to clinical variables: A cross-sectional study. *J. Psychiatr. Res.* 44, 1214–1223. doi: 10.1016/j.jpsychires.2010.04.026

Andersen, J. M., Hoiseth, G., and Nygaard, E. (2020). Prenatal exposure to methadone or buprenorphine and long-term outcomes: A meta-analysis. *Early Hum. Dev.* 143:104997. doi: 10.1016/j.earlhumdev.2020.104997

Andersson, J. L. R., and Sotiropoulos, S. N. (2016). An integrated approach to correction for off-resonance effects and subject movement in diffusion MR imaging. *Neuroimage* 125, 1063–1078. doi: 10.1016/j.neuroimage.2015.10.019

Azuine, R. E., Ji, Y., Chang, H. Y., Kim, Y., Ji, H., DiBari, J., et al. (2019). Prenatal Risk Factors and Perinatal and Postnatal Outcomes Associated With Maternal Opioid Exposure in an Urban. *Low-Income, Multiethnic US Population. JAMA Netw. Open* 2:e196405. doi: 10.1001/jamanetworkopen.2019.6405

Bassett, D. S., and Bullmore, E. T. (2009). Human brain networks in health and disease. *Curr. Opin. Neurol.* 22, 340–347. doi: 10.1097/WCO.0b013e32832d93dd

Benjamini, Y., and Hochberg, Y. (1995). Controlling the False Discovery Rate: A Practical and Powerful Approach to Multiple Testing. *J. R. Stat. Soc. Series B* 57, 289–300.

Biggs, N., Lloyd, E. K., and Wilson, R. J. (1986). *Graph Theory, 1736-1936*. Oxford: Clarendon Press.

Bullmore, E., and Sporns, O. (2009). Complex brain networks: Graph theoretical analysis of structural and functional systems. *Nat. Rev. Neurosci.* 10, 186–198. doi: 10.1038/nrn2575

Cloak, C. C., Ernst, T., Fujii, L., Hedemark, B., and Chang, L. (2009). Lower diffusion in white matter of children with prenatal methamphetamine exposure. *Neurology* 72, 2068–2075. doi: 10.1212/01.wnl.0000346516.49126.20

Donald, K. A., Roos, A., Fouche, J. P., Koen, N., Howells, F. M., Woods, R. P., et al. (2015). A study of the effects of prenatal alcohol exposure on white matter microstructural integrity at birth. *Acta Neuropsychiatr.* 27, 197–205. doi: 10.1017/neu.2015.35

Farrell, J. A., Landman, B. A., Jones, C. K., Smith, S. A., Prince, J. L., van Zijl, P. C., et al. (2007). Effects of signal-to-noise ratio on the accuracy and reproducibility of diffusion tensor imaging-derived fractional anisotropy, mean diffusivity, and principal eigenvector measurements at 1.5 T. *J. Magn. Reson .Imaging* 26, 756–767. doi: 10.1002/jmri.21053

Fonov, V., Evans, A., McKinstry, R., Almli, C. R., and Collins, L. (2009). Unbiased nonlinear average age-appropriate brain templates from birth to adulthood. *Neuroimage* 47:S102. doi: 10.1016/S1053-8119(09)70884-5

Fonov, V., Evans, A. C., Botteron, K., Almli, C. R., McKinstry, R. C., Collins, D. L., et al. (2011). Unbiased average age-appropriate atlases for pediatric studies. *Neuroimage* 54, 313–327. doi: 10.1016/j.neuroimage.2010.07.033

Gibson, J. M., Chu, T., Zeng, W., Wethall, A. C., Kong, M., Mellen, N., et al. (2022). Perinatal methadone exposure attenuates myelination and induces oligodendrocyte apoptosis in neonatal rat brain. *Exp. Biol. Med.* 247, 1067–1079. doi: 10.1177/15353702221090457

Haight, S. C., Ko, J. Y., Tong, V. T., Bohm, M. K., and Callaghan, W. M. (2018). Opioid Use Disorder Documented at Delivery Hospitalization - United States, 1999–2014. *MMWR Morb. Mortal. Wkly. Rep.* 67, 845–849. doi: 10.15585/mmwr.mm6731a1

Hu, S., Ide, J. S., Zhang, S., and Li, C. R. (2016). The Right Superior Frontal Gyrus and Individual Variation in Proactive Control of Impulsive Response. *J. Neurosci.* 36, 12688–12696. doi: 10.1523/JNEUROSCI.1175-16.2016

Jantzie, L. L., Maxwell, J. R., Newville, J. C., Yellowhair, T. R., Kitase, Y., Madurai, N., et al. (2020). Prenatal opioid exposure: The next neonatal neuroinflammatory disease. *Brain Behav. Immun.* 84, 45–58. doi: 10.1016/j.bbi.2019.11.007

Johns, P. (2014). "Chapter 3 - Functional neuroanatomy," in *Clinical Neuroscience*, ed. P. Johns (London: Churchill Livingstone), 27–47.

Khan, L. (2020). Neonatal Abstinence Syndrome. *Pediatr. Ann.* 49:e3–e7. doi: 10.3928/19382359-20191211-01

Kline-Fath, B. M., Horn, P. S., Yuan, W., Merhar, S., Venkatesan, C., Thomas, C. W., et al. (2018). Conventional MRI scan and DTI imaging show more severe brain injury in neonates with hypoxic-ischemic encephalopathy and seizures. *Early Hum. Dev.* 122, 8–14. doi: 10.1016/j.earlhumdev.2018.05.008

Ko, J. Y., D'Angelo, D. V., Haight, S. C., Morrow, B., Cox, S., Salvesen, et al. (2020). Vital Signs: Prescription Opioid Pain Reliever Use During Pregnancy - 34 U.S. Jurisdictions, 2019. *MMWR Morb. Mortal. Wkly. Rep.* 69, 897–903. doi: 10.15585/mmwr.mm6928a1

Lee, J. M., Kim, P. J., Kim, H. G., Hyun, H. K., Kim, Y. J., Kim, J. W., et al. (2020). Analysis of brain connectivity during nitrous oxide sedation using graph theory. *Sci. Rep.* 10:2354. doi: 10.1038/s41598-020-59264-0

Lee, S. J., Woodward, L. J., and Henderson, J. M. T. (2019). Educational achievement at age 9.5 years of children born to mothers maintained on methadone during pregnancy. *PLoS One* 14:e0223685. doi: 10.1371/journal.pone.0223685

Levine, T. A., and Woodward, L. J. (2018). Early inhibitory control and working memory abilities of children prenatally exposed to methadone. *Early Hum. Dev.* 116, 68–75. doi: 10.1016/j.earlhumdev.2017.11.010

Li, K., Sun, Z., Han, Y., Gao, L., Yuan, L., and Zeng, D. (2015). Fractional anisotropy alterations in individuals born preterm: A diffusion tensor imaging meta-analysis. *Dev. Med. Child Neurol.* 57, 328–338. doi: 10.1111/dmcn.12618

Liu, J., Grewen, K., and Gao, W. (2022). Evidence for the Normalization Effects of Medication for Opioid Use Disorder on Functional Connectivity in Neonates with Prenatal Opioid Exposure. *J. Neurosci.* 42, 4555–4566. doi: 10.1523/JNEUROSCI.2232-21.2022

Maguire, D. J., Taylor, S., Armstrong, K., Shaffer-Hudkins, E., Germain, A. M., Brooks, S. S., et al. (2016). Long-Term Outcomes of Infants with Neonatal Abstinence Syndrome. *Neonatal. Netw.* 35, 277–286. doi: 10.1891/0730-0832.35.5.277

McGlone, L., and Mactier, H. (2015). Infants of opioid-dependent mothers: Neurodevelopment at six months. *Early Hum. Dev.* 91, 19–21. doi: 10.1016/j.earlhumdev.2014.10.006

Mears, D., and Pollard, H. B. (2016). Network science and the human brain: Using graph theory to understand the brain and one of its hubs, the amygdala, in health and disease. *J. Neurosci. Res.* 94, 590–605. doi: 10.1002/jnr.23705

Mei, B., Niu, L., Cao, B., Huang, D., and Zhou, Y. (2009). Prenatal morphine exposure alters the layer II/III pyramidal neurons morphology in lateral secondary visual cortex of juvenile rats. *Synapse* 63, 1154–1161. doi: 10.1002/syn.20694

Melinder, A., Konijnenberg, C., and Sarfi, M. (2013). Deviant smooth pursuit in preschool children exposed prenatally to methadone or buprenorphine and tobacco affects integrative visuomotor capabilities. *Addiction* 108, 2175–2182. doi: 10.1111/add.12267

Merhar, S. L., Gozdas, E., Tkach, J. A., Harpster, K. L., Schwartz, T. L., Yuan, W., et al. (2016). Functional and structural connectivity of the visual system in infants with perinatal brain injury. *Pediatr. Res.* 80, 43–48. doi: 10.1038/pr.2016.49

Merhar, S. L., Jiang, W., Parikh, N. A., Yin, W., Zhou, Z., Tkach, J. A., et al. (2021). Effects of prenatal opioid exposure on functional networks in infancy. *Dev. Cogn. Neurosci.* 51:100996. doi: 10.1016/j.dcn.2021.100996

Monnelly, V. J., Anblagan, D., Quigley, A., Cabez, M. B., Cooper, E. S., Mactier, H., et al. (2018). Prenatal methadone exposure is associated with altered neonatal brain development. *Neuroimage Clin.* 18, 9–14. doi: 10.1016/j.nicl.2017.12.033

Moore, E. M., and Xia, Y. (2021). Neurodevelopmental Trajectories Following Prenatal Alcohol Exposure. *Front. Hum. Neurosci.* 15:695855. doi: 10.3389/fnhum.2021.695855

Nygaard, E., Slinning, K., Moe, V., Due-Tonnessen, P., Fjell, A., and Walhovd, K. B. (2018). Neuroanatomical characteristics of youths with prenatal opioid and poly-drug exposure. *Neurotoxicol. Teratol.* 68, 13–26. doi: 10.1016/j.ntt.2018.04.004

Oberoi, R., Chu, T., Mellen, N., Jagadapillai, R., Ouyang, H., Devlin, L. A., et al. (2019). Diverse changes in myelin protein expression in rat brain after perinatal methadone exposure. *Acta Neurobiol. Exp.* 79, 367–373.

Pannek, K., Fripp, J., George, J. M., Fiori, S., Colditz, P. B., Boyd, R. N., et al. (2018). Fixel-based analysis reveals alterations is brain microstructure and macrostructure of preterm-born infants at term equivalent age. *Neuroimage Clin.* 18, 51–59. doi: 10.1016/j.nicl.2018.01.003

Patrick, S. W., Dudley, J., Martin, P. R., Harrell, F. E., Warren, M. D., Hartmann, K. E., et al. (2015). Prescription opioid epidemic and infant outcomes. *Pediatrics* 135, 842–850. doi: 10.1542/peds.2014-3299

Peterson, B. S., Rosen, T., Dingman, S., Toth, Z. R., Sawardekar, S., Hao, X., et al. (2020). Associations of Maternal Prenatal Drug Abuse With Measures of Newborn Brain Structure, Tissue Organization, and Metabolite Concentrations. *JAMA Pediatr.* 174, 831–842. doi: 10.1001/jamapediatrics.2020.1622

Radhakrishnan, R., Brown, B. P., Haas, D. M., Zang, Y., Sparks, C., and Sadhasivam, S. (2022a). Pilot study of fetal brain development and morphometry in prenatal opioid exposure and smoking on fetal MRI. *J. Neuroradiol.* 49, 53–58. doi: 10.1016/j.neurad.2020.12.004

Radhakrishnan, R., Vishnubhotla, R. V., Guckien, Z., Zhao, Y., Sokol, G. M., Haas, D. M., et al. (2022b). Thalamocortical functional connectivity in infants with prenatal opioid exposure correlates with severity of neonatal opioid withdrawal syndrome. *Neuroradiology* 64, 1649-1659. doi: 10.1007/s00234-022-02939-4

Radhakrishnan, R., Vishnubhotla, R. V., Zhao, Y., Yan, J., He, B., Steinhardt, N., et al. (2022c). Global Brain Functional Network Connectivity in Infants With Prenatal Opioid Exposure. *Front. Pediatr.* 10:847037. doi: 10.3389/fped.2022.847037

Radhakrishnan, R., Elsaid, N. M. H., Sadhasivam, S., Reher, T. A., Hines, A. C., Yoder, K. K., et al. (2020). Resting state functional MRI in infants with prenatal opioid exposure-a pilot study. *Neuroradiology* 63, 585-591. doi: 10.1007/s00234-020-02552-3

Riggins, T., Cacic, K., Buckingham-Howes, S., Scaletti, L. A., Salmeron, B. J., and Black, M. M. (2012). Memory ability and hippocampal volume in adolescents with prenatal drug exposure. *Neurotoxicol. Teratol.* 34, 434–441. doi: 10.1016/j.ntt.2012.05.054

Robey, A., Buckingham-Howes, S., Salmeron, B. J., Black, M. M., and Riggins, T. (2014). Relations among prospective memory, cognitive abilities, and brain structure in adolescents who vary in prenatal drug exposure. *J. Exp. Child Psychol.* 127, 144–162. doi: 10.1016/j.jecp.2014.01.008

Rolls, E. T., Joliot, M., and Tzourio-Mazoyer, N. (2015). Implementation of a new parcellation of the orbitofrontal cortex in the automated anatomical labeling atlas. *Neuroimage* 122, 1–5. doi: 10.1016/j.neuroimage.2015.07.075

Roos, A., Kwiatkowski, M. A., Fouche, J. P., Narr, K. L., Thomas, K. G., Stein, D. J., et al. (2015). White matter integrity and cognitive performance in children with prenatal methamphetamine exposure. *Behav. Brain Res.* 279, 62–67. doi: 10.1016/j.bbr.2014.11.005

Roos, A., Wedderburn, C. J., Fouche, J. P., Subramoney, S., Joshi, S. H., Woods, R. P., et al. (2021). Central white matter integrity alterations in 2-3-year-old children following prenatal alcohol exposure. *Drug Alcohol. Depend.* 225:108826. doi: 10.1016/j.drugalcdep.2021.108826

Rose, J., Vassar, R., Cahill-Rowley, K., Stecher Guzman, X., Hintz, S. R., Stevenson, D. K., et al. (2014). Neonatal physiological correlates of near-term brain development on MRI and DTI in very-low-birth-weight preterm infants. *Neuroimage Clin.* 5, 169–177. doi: 10.1016/j.nicl.2014.05.013

Rubenstein, E., Young, J. C., Croen, L. A., DiGuiseppi, C., Dowling, N. F., Lee, L. C., et al. (2019). Brief Report: Maternal Opioid Prescription from Preconception Through Pregnancy and the Odds of Autism Spectrum Disorder and Autism Features in Children. *J. Autism. Dev. Disord.* 49, 376–382. doi: 10.1007/s10803-018-3721-8

Rubinov, M., and Sporns, O. (2010). Complex network measures of brain connectivity: Uses and interpretations. *Neuroimage* 52, 1059–1069. doi: 10.1016/j.neuroimage.2009.10.003

Sanchez, E. S., Bigbee, J. W., Fobbs, W., Robinson, S. E., and Sato-Bigbee, C. (2008). Opioid addiction and pregnancy: Perinatal exposure to buprenorphine affects myelination in the developing brain. *Glia* 56, 1017–1027. doi: 10.1002/glia.20675

Schwartz, A. N., Reyes, L. M., Meschke, L. L., and Kintziger, K. W. (2021). Prenatal Opioid Exposure and ADHD Childhood Symptoms: A Meta-Analysis. *Children* 8:106. doi: 10.3390/children8020106

Sirnes, E., Griffiths, S. T., Aukland, S. M., Eide, G. E., Elgen, I. B., and Gundersen, H. (2018). Functional MRI in prenatally opioid-exposed children during a working memory-selective attention task. *Neurotoxicol. Teratol.* 66, 46–54. doi: 10.1016/j.ntt.2018.01.010

Sirnes, E., Oltedal, L., Bartsch, H., Eide, G. E., Elgen, I. B., and Aukland, S. M. (2017). Brain morphology in school-aged children with prenatal opioid exposure: A structural MRI study. *Early Hum. Dev.* 106-107, 33–39. doi: 10.1016/j.earlhumdev.2017.01.009

Smith, S. M., Jenkinson, M., Woolrich, M. W., Beckmann, C. F., Behrens, T. E., Johansen-Berg, H., et al. (2004). Advances in functional and structural MR image analysis and implementation as FSL. *Neuroimage* 23:S208–S219. doi: 10.1016/j.neuroimage.2004.07.051

Soares, J. M., Marques, P., Alves, V., and Sousa, N. (2013). A hitchhiker's guide to diffusion tensor imaging. *Front. Neurosci.* 7:31. doi: 10.3389/fnins.2013.00031

Sporns, O. (2018). Graph theory methods: Applications in brain networks. *Dialog. Clin. Neurosci.* 20, 111–121.

Stephen, J. M., Hill, D. E., and Candelaria-Cook, F. T. (2021). Examining the effects of prenatal alcohol exposure on corticothalamic connectivity: A multimodal neuroimaging study in children. *Dev. Cogn. Neurosci.* 52:101019. doi: 10.1016/j.dcn.2021.101019

Sundelin-Wahlsten, V., and Sarman, I. (2013). Neurobehavioural development of preschool-age children born to addicted mothers given opiate maintenance treatment with buprenorphine during pregnancy. *Acta Paediatr.* 102, 544–549. doi: 10.1111/apa.12210

Turk, E., van den Heuvel, M. I., Benders, M. J., de Heus, R., Franx, A., Manning, J. H., et al. (2019). Functional Connectome of the Fetal Brain. *J. Neurosci.* 39, 9716–9724. doi: 10.1523/JNEUROSCI.2891-18.2019

Velasco, B., Mohamed, E., and Sato-Bigbee, C. (2021). Endogenous and exogenous opioid effects on oligodendrocyte biology and developmental brain myelination. *Neurotoxicol. Teratol.* 86:107002. doi: 10.1016/j.ntt.2021.107002

Vestal-Laborde, A. A., Eschenroeder, A. C., Bigbee, J. W., Robinson, S. E., and Sato-Bigbee, C. (2014). The opioid system and brain development: Effects of methadone on the oligodendrocyte lineage and the early stages of myelination. *Dev. Neurosci.* 36, 409–421. doi: 10.1159/000365074

Walhovd, K. B., Bjornebekk, A., Haabrekke, K., Siqveland, T., Slinning, K., Nygaard, E., et al. (2015). Child neuroanatomical, neurocognitive, and visual acuity outcomes with maternal opioid and polysubstance detoxification. *Pediatr. Neurol.* 52:e321–e323. doi: 10.1016/j.pediatrneurol.2014.11.008

Walhovd, K. B., Moe, V., Slinning, K., Due-Tonnessen, P., Bjornerud, A., Dale, A. M., et al. (2007). Volumetric cerebral characteristics of children exposed to opiates and other substances in utero. *Neuroimage* 36, 1331–1344. doi: 10.1016/j.neuroimage.2007.03.070

Walhovd, K. B., Watts, R., Amlien, I., and Woodward, L. J. (2012). Neural tract development of infants born to methadone-maintained mothers. *Pediatr. Neurol.* 47, 1–6. doi: 10.1016/j.pediatrneurol.2012.04.008

Walhovd, K. B., Westlye, L. T., Moe, V., Slinning, K., Due-Tonnessen, P., Bjornerud, A., et al. (2010). White matter characteristics and cognition in prenatally opiate- and polysubstance-exposed children: A diffusion tensor imaging study. *AJNR Am. J. Neuroradiol.* 31, 894–900. doi: 10.3174/ajnr.A1957

Warton, F. L., Taylor, P. A., Warton, C. M. R., Molteno, C. D., Wintermark, P., Lindinger, N. M., et al. (2018). Prenatal methamphetamine exposure is associated with corticostriatal white matter changes in neonates. *Metab. Brain Dis.* 33, 507–522. doi: 10.1007/s11011-017-0135-9

Warton, F. L., Taylor, P. A., Warton, C. M. R., Molteno, C. D., Wintermark, P., Zollei, L., et al. (2020). Reduced fractional anisotropy in projection, association, and commissural fiber networks in neonates with prenatal methamphetamine exposure. *Dev. Neurobiol.* 80, 381–398. doi: 10.1002/dneu.22784

Weiner, K. S., and Zilles, K. (2016). The anatomical and functional specialization of the fusiform gyrus. *Neuropsychologia* 83, 48–62. doi: 10.1016/j.neuropsychologia.2015.06.033

Wen, Q., Mustafi, S., Harezlak, J., Li, J., Risacher, S., West, J., et al. (2019). White matter alterations in early stage Alzheimer's disease: A tract specific study. *Alzheimer's Dement.* 11, 576–587.

Wen, X., Zhang, H., Li, G., Liu, M., Yin, W., Lin, W., et al. (2019). First-year development of modules and hubs in infant brain functional networks. *Neuroimage* 185, 222–235. doi: 10.1016/j.neuroimage.2018.10.019

Winkelman, T. N. A., Villapiano, N., Kozhimannil, K. B., Davis, M. M., and Patrick, S. W. (2018). Incidence and Costs of Neonatal Abstinence Syndrome Among Infants With Medicaid: 2004-2014. *Pediatrics* 141:e20173520. doi: 10.1542/peds.2017-3520

Woolrich, M. W., Jbabdi, S., Patenaude, B., Chappell, M., Makni, S., Behrens, T., et al. (2009). Bayesian analysis of neuroimaging data in FSL. *Neuroimage* 45:S173–S186. doi: 10.1016/j.neuroimage.2008.10.055

Wozniak, J. R., and Muetzel, R. L. (2011). What does diffusion tensor imaging reveal about the brain and cognition in fetal alcohol spectrum disorders? *Neuropsychol. Rev.* 21, 133–147. doi: 10.1007/s11065-011-9162-1

Wozniak, J. R., Muetzel, R. L., Mueller, B. A., McGee, C. L., Freerks, M. A., Ward, E. E., et al. (2009). Microstructural corpus callosum anomalies in children with prenatal alcohol exposure: An extension of previous diffusion tensor imaging findings. *Alcohol. Clin. Exp. Res.* 33, 1825–1835. doi: 10.1111/j.1530-0277.2009.01021.x

Wu, Y. C., and Alexander, A. L. (2007). Hybrid diffusion imaging. *Neuroimage* 36, 617–629. doi: 10.1016/j.neuroimage.2007.02.050

Yeh, F. C., Panesar, S., Fernandes, D., Meola, A., Yoshino, M., Fernandez-Miranda, J. C., et al. (2018). Population-averaged atlas of the macroscale human structural connectome and its network topology. *Neuroimage* 178, 57–68. doi: 10.1016/j.neuroimage.2018.05.027

Yeh, F. C., and Tseng, W. Y. (2011). NTU-90: A high angular resolution brain atlas constructed by q-space diffeomorphic reconstruction. *Neuroimage* 58, 91–99. doi: 10.1016/j.neuroimage.2011.06.021

Yeh, F. C., Verstynen, T. D., Wang, Y., Fernandez-Miranda, J. C., and Tseng, W. Y. (2013). Deterministic diffusion fiber tracking improved by quantitative anisotropy. *PLoS One* 8:e80713. doi: 10.1371/journal.pone.0080713

Yeoh, S. L., Eastwood, J., Wright, I. M., Morton, R., Melhuish, E., Ward, M., et al. (2019). Cognitive and Motor Outcomes of Children With Prenatal Opioid Exposure: A Systematic Review and Meta-analysis. *JAMA Netw. Open* 2:e197025. doi: 10.1001/jamanetworkopen.2019.7025

Yuan, Q., Rubic, M., Seah, J., Rae, C., Wright, I. M., Kaltenbach, K., et al. (2014). Do maternal opioids reduce neonatal regional brain volumes? A pilot study. *J. Perinatol.* 34, 909–913. doi: 10.1038/jp.2014.111

Zhao, T., Xu, Y., and He, Y. (2019). Graph theoretical modeling of baby brain networks. *Neuroimage* 185, 711–727. doi: 10.1016/j.neuroimage.2018.06.038

Zhu, Y., Hsu, M. S., and Pintar, J. E. (1998). Developmental expression of the mu, kappa, and delta opioid receptor mRNAs in mouse. *J. Neurosci.* 18, 2538–2549. doi: 10.1523/JNEUROSCI.18-07-02538.1998

frontiers | Frontiers in Neuroscience

TYPE Original Research
PUBLISHED 11 November 2022
DOI 10.3389/fnins.2022.1027084

OPEN ACCESS

EDITED BY
L. Tugan Muftuler,
Medical College of Wisconsin,
United States

REVIEWED BY
Can Ceritoglu,
Johns Hopkins University,
United States
Robert Fekete,
New York Medical College,
United States
Vijay Venkatraman,
The University of Melbourne, Australia

*CORRESPONDENCE
Emma G. Duerden
eduerden@uwo.ca

†These authors have contributed equally to this work

SPECIALTY SECTION
This article was submitted to Brain Imaging Methods, a section of the journal Frontiers in Neuroscience

RECEIVED 24 August 2022
ACCEPTED 19 October 2022
PUBLISHED 11 November 2022

CITATION
Wang J, Nichols ES, Mueller ME, de Vrijer B, Eagleson R, McKenzie CA, de Ribaupierre S and Duerden EG (2022) Semi-automatic segmentation of the fetal brain from magnetic resonance imaging.
Front. Neurosci. 16:1027084.
doi: 10.3389/fnins.2022.1027084

Semi-automatic segmentation of the fetal brain from magnetic resonance imaging

Jianan Wang[1], Emily S. Nichols[2,3], Megan E. Mueller[2], Barbra de Vrijer[4], Roy Eagleson[1,3,5], Charles A. McKenzie[6], Sandrine de Ribaupierre[1,3,7,8†] and Emma G. Duerden[1,2,3*†]

[1]Biomedical Engineering, Western University, London, ON, Canada, [2]Applied Psychology, Faculty of Education, Western University, London, ON, Canada, [3]Western Institute for Neuroscience, Western University, London, ON, Canada, [4]Department of Obstetrics and Gynaecology, Schulich School of Medicine & Dentistry, Western University, London, ON, Canada, [5]Department of Electrical and Computer Engineering, Western University, London, ON, Canada, [6]Department of Medical Biophysics, Schulich School of Medicine & Dentistry, Western University, London, ON, Canada, [7]Department of Clinical Neurological Sciences, Schulich School of Medicine & Dentistry, Western University, London, ON, Canada, [8]Department of Anatomy and Cell Biology, Schulich School of Medicine & Dentistry, Western University, London, ON, Canada

Background: Volumetric measurements of fetal brain maturation in the third trimester of pregnancy are key predictors of developmental outcomes. Improved understanding of fetal brain development trajectories may aid in identifying and clinically managing at-risk fetuses. Currently, fetal brain structures in magnetic resonance images (MRI) are often manually segmented, which requires both time and expertise. To facilitate the targeting and measurement of brain structures in the fetus, we compared the results of five segmentation methods applied to fetal brain MRI data to gold-standard manual tracings.

Methods: Adult women with singleton pregnancies (n = 21), of whom five were scanned twice, approximately 3 weeks apart, were recruited [26 total datasets, median gestational age (GA) = 34.8, IQR = 30.9–36.6]. T2-weighted single-shot fast spin echo images of the fetal brain were acquired on 1.5T and 3T MRI scanners. Images were first combined into a single 3D anatomical volume. Next, a trained tracer manually segmented the thalamus, cerebellum, and total cerebral volumes. The manual segmentations were compared with five automatic methods of segmentation available within Advanced Normalization Tools (ANTs) and FMRIB's Linear Image Registration Tool (FLIRT) toolboxes. The manual and automatic labels were compared using Dice similarity coefficients (DSCs). The DSC values were compared using Friedman's test for repeated measures.

Results: Comparing cerebellum and thalamus masks against the manually segmented masks, the median DSC values for ANTs and FLIRT were 0.72 [interquartile range (IQR) = 0.6–0.8] and 0.54 (IQR = 0.4–0.6), respectively. A Friedman's test indicated that the ANTs registration methods, primarily nonlinear methods, performed better than FLIRT ($p < 0.001$).

Conclusion: Deformable registration methods provided the most accurate results relative to manual segmentation. Overall, this semi-automatic subcortical segmentation method provides reliable performance to segment subcortical volumes in fetal MR images. This method reduces the costs of manual segmentation, facilitating the measurement of typical and atypical fetal brain development.

KEYWORDS

fetal, MRI, brain, linear registration, nonlinear registration, volumetric reconstruction

Introduction

Magnetic resonance imaging (MRI) of the fetal brain for clinical purposes has advanced considerably in recent years due to its application in assessing atypical brain development and brain injury and its potential utility in predicting functional outcomes in high-risk fetuses (Banović et al., 2014; Brossard-Racine et al., 2014, 2019; Cesaretti et al., 2016; Andescavage et al., 2017). Additionally, research-based MRI studies of typical fetal brain development have provided important normative data for subsequent comparison with clinical populations (De Asis-Cruz et al., 2021). MRI methods for the characterization of fetal brain abnormalities are of key clinical relevance due to the high incidence of central nervous system malformations (i.e., anencephaly, ventriculomegaly, schizencephaly, and callosal agenesis) in as many as 1/1,000 fetuses (Werner et al., 2018). In particular, detection of delayed brain growth offers new opportunities to identify objective biomarkers that can facilitate a better understanding of fetal brain development, improved management of high-risk pregnancies (Rutherford et al., 2008; Cesaretti et al., 2016; Knezović et al., 2019; Wu et al., 2020), and potentially early detection of neurodevelopmental outcome (Banović et al., 2014; Bonnet-Brilhault et al., 2018). Additionally, longitudinal studies point to fetal brain abnormalities as an important contributor to later life neurodevelopmental and psychiatric disorders (Thomason, 2020). Better understanding of typical fetal brain developmental trajectories may aid in predicting functional outcomes.

Quantitative measurements of the fetal brain and subcortical volumes can support characterizing normal brain development and identifying early predictors of brain dysmaturation (Boardman et al., 2010; Rathbone et al., 2011). However, the traditional manual segmentation of MR images is time-consuming and requires high-level expertise; thus, it is impractical to implement these methods to large datasets. For functional imaging, manual segmentation of 4D fetal images can take upwards of 30 h to complete a single scanning run in an individual participant's data (Nichols et al., 2022). Automatic segmentation pipelines and routines developed for neonatal and child imaging protocols are not appropriate for studying fetal brain tissue due to the variations in image acquisition, and maturational differences leading to poorer contrast of the gray and white matter. Therefore, reliable automatic segmentation methods for fetal MR images are needed to study typical and atypical fetal brain development.

We applied two atlas-based segmentation techniques, linear and nonlinear atlas registration algorithms, to perform the regional segmentation of the cortex and subcortical areas in the fetal brain to examine their macrostructural development. The cerebellum and thalamus are key deep brain structures related to alterations in neuro-cognition and motor behaviors that are typically seen in infants impacted by growth restriction as well as preterm birth. Early growth impairments or alterations in the trajectory of growth in the cerebellum have been found to be associated with an increased risk of autism (Beversdorf et al., 2005; Limperopoulos et al., 2007). Further, cerebellar lesions in adulthood can impair decision-making, working memory, and planning (Koziol et al., 2014; Clausi et al., 2015). Deficits in linguistic abilities, anxiety, and impaired social behavior have also been associated with cerebellar lesions (Schmahmann, 2004; Ramphal et al., 2021). Early cerebellar lesions at the vermis area can produce impaired eye gaze, anxiety, and lack of mental flexibility such as stereotyped behavior (Wells et al., 2008; Clausi et al., 2015). The thalamus, is the primary relay station to the cortex and plays an important role in motor and cognitive functions (Dehghani and Wimmer, 2019). Atypical development of the thalamus is associated with impaired emotional processing, language, and social cognition in children and adult populations with neurodevelopmental disorders (Hardan et al., 2006). Volumetric segmentations of the cerebellum and thalamus can aid in morphological analysis of the growth of the two brain structures, which may be beneficial

Abbreviations: ANTs, advanced normalization tools; ANTs Lin MI, ANTs linear registration with mutual information similarity metric; ANTs Lin CC, ANTs linear registration with cross-correlation similarity metric; ANTs NL MI, ANTs nonlinear registration with mutual information similarity metric; ANTs NL CC, ANTs nonlinear registration with cross-correlation similarity metric; CSF, Cerebrospinal Fluid; CNN, convolutional neural network; FGR, fetal growth restriction; FLIRT, FMRIB's Linear Image Registration Tool; FSE, fast spin echo; GUI, graphical user interface; IUGR, Intrauterine Growth Restriction; MRI, magnetic resonance imaging; TR, repetition time; TE, echo time; ROI, regions of interest; SyN, symmetric image normalization.

to exploring *in utero* origins of cognitive and motor functions in the typically developing fetus.

Manual based segmentation methods have been employed to segment subcortical fetal brain tissues (Twickler et al., 2002). However, these methods are very time consuming and require high level expertise. Deep-learning methods such as deep convolutional neural networks (CNNs) have been used to segment subcortical structures in fetal MR images (Khalili et al., 2019; Zhao et al., 2022). Atlas-based segmentation methods have been used to target deep brain structures in fetal MR images (Habas et al., 2010). Landmark-based rigid image transformation has been applied to fetal MR images to obtain volumetric and cortical measures (Wu et al., 2020). However, deformable registrations may be more robust. They may be able to more accurately segment subcortical structures in fetal MR images compared to linear registration, but are more computationally intensive and may be more challenging to implement in clinical settings. Using an atlas-based method, we examined whether more computationally intensive deformation image registration methods, using the Advanced Normalization Tools (ANTs), are needed for adequate subcortical segmentation compared to an affine image registration FLIRT (FMRIB's Linear Image Registration Tool). This research aimed to develop and implement a semi-automatic pipeline combining semi-automatic fetal brain reconstruction, segmentation, volumetric reconstruction, and atlas registration algorithms for subcortical segmentation in fetal brains to extract and analyze subcortical volumes.

Materials and methods

Participants

Pregnant individuals with singleton fetuses were recruited to the study. All participants self-identified as native English speakers and reported no history of psychiatric illness, neurological disorder, or hearing impairment.

The study was approved by the Health Sciences Research Ethics Board at Western University. The research was conducted according to the principles expressed in the Declaration of Helsinki. The letter of information was sent to participants in advance of the study, and a member of the research team reviewed the protocol. All participants provided informed consent.

Magnetic resonance imaging protocol

Participants were scanned at two sites, and the study procedures were maintained at both locations. The majority of the scans ($n = 21$) were acquired on a 3T MRI [General Electric (GE), Milwaukee, WI, SA; MR7500] with a 32-channel GE torso coil and a 60 cm bore at the Translational Imaging Research Facility at the Robarts Research Institute. Of the 21 scans, 5 were repeat scans whereby the mothers returned for an identical scanning session. The other five scans were collected on a 70 cm bore 1.5T (GE, MR450w) with a GEM posterior and anterior array coil at London Health Science Center.

The T2-weighted MR images were acquired using a single shot fast spin echo (SSFSE) sequence [repetition time (TR) > 1,200 ms, echo time (TE): 81.36–93.60 ms, voxel size: 0.98 mm × 1.96 mm × 8 mm and 0.125 mm × 0.17 mm × 9 mm], applied in three image planes (**Figure 1**).

Volumetric reconstruction of magnetic resonance images

NiftyMIC (Ebner et al., 2020) was used for fetal brain segmentation and 3D reconstruction. The main processing pipeline for detection and segmentation of the fetal brain included with NiftyMIC involves only a single command (*fetal_brain_seg*) and can be executed unsupervised. Various features of different slice-to-volume reconstructions methods including NitfyMIC have been compared for fetal MRI, and have reported comparable results (Payette et al., 2021).

It was essential to first estimate the fetal brain location in the MR image such that a bounding box was created to reduce both unrelated contents and image space, as well as the algorithm processing time for the later more precise fetal brain segmentation algorithm using 2D P-Net CNN (Yamashita et al., 2018). NiftyMIC's *fetal_brain_seg* command was then executed on the MR image, generating a mask of the fetal brain in the surrounding tissue for each slice within the image. This step took under 2 min per stack of 2D slices.

The resulting masks were then reviewed using FSLeyes.[1] These automatically generated 2D fetal brain masks from NiftyMIC were suboptimal for most participants, resulting in either over- or under-estimating fetal brain tissue in the slices; surrounding maternal gray and white tissue were still evident in the slices, depending on the acquisition and field of view. Therefore, manual adjustments of the masks, such as filling and excluding pixels, were performed on all automatically generated 2D masks ($n = 26$). Time spent manually editing ranged from 1 to 15 min per stack of 2D slices, with the majority taking under 5 min to complete.

After segmenting fetal brains in the 2D planes, the stacks of 2D slices were reconstructed into 3D volumes, and the 2D fetal brain segmentations were also reconstructed into 3D space. The 2D MR image slices could be corrupted by low-frequency bias field signals to blur the high-frequency contents, such

1 https://fsl.fmrib.ox.ac.uk/fsl/fslwiki/FSLeyes

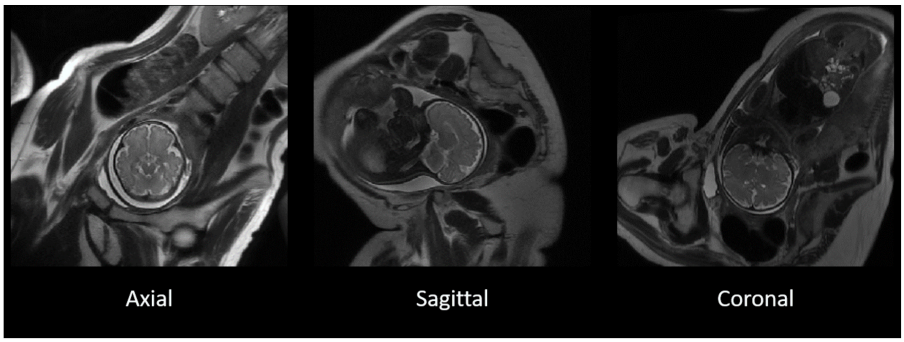

FIGURE 1
The original T2-weighted acquisition of a fetal MR image in axial, sagittal, and coronal planes. T2-weighted images acquired separately in three separate image planes in the axial **(left)**, sagittal **(middle)**, and coronal **(right)** in a representative participant. The three image planes were subsequently used for the reconstruction of 3D images.

as edges and contours. Intensity variance also resulted from existing bias field signals where the same tissue had a uniformed pixel gray level in the images. Thus, the stacks of segmented 2D fetal brain slices were first bias-field corrected. Second, the bias-field corrected 2D slices were reconstructed into a 3D volume by the slice-to-volume process that rigidly registered the 2D slices to one randomly selected target slice from the fetal brain MR images so that all the slices were volumetrically aligned. The slice-to-volume process also used linear regression to correct and match the slices' voxel intensities to the target slice's voxel intensity. Third, the volume-to-volume process was performed on the 2D slices and previously segmented 2D masks to reconstruct into 3D volumes and 3D fetal brain masks in native space. Processing times varied but were up to 2 h in some participants' data (Uus et al., 2022).

Subsequently, the native-space 3D volumes were rigidly registered to a spatiotemporal atlas developed from images acquired at 3T MRI from typically developing fetuses to obtain the volumetric reconstruction in the standard anatomical planes of atlas space.

Registration-based subcortical segmentation

The reconstructed 3D fetal brain masks were applied onto the reconstructed 3D brain volumes for fetal brain skull stripping (**Figure 2**). The 3D brain volumes were segmented with the binary masks for fetal brain-only MR images. This segmentation was a prerequisite for later subcortical segmentation utilizing image registration since image registration for tissue alignment assumes the target object and the moving object are the same tissue with similar shapes. Registering the skull-stripped fetal brain atlas to the subject's fetal brain, excluding maternal tissue, would reduce unrelated content for meaningful registration results. The skull stripping step was performed using 3dcalc from the AFNI toolkit that multiplied the reconstructed 3D fetal brain image with the binary 3D masks. Then the orientations of the skull-stripped MR images were manually adjusted according to the orientations of the age-appropriate fetal brain atlas using the ITK-SNAP GUI (**Figure 2**; graphical user interface[2]).

Two different registration toolkits were applied to the reconstructed images and compared to determine an optimal fetal subcortical segmentation strategy. Deformable registration was performed using ANTs (Avants et al., 2008) using the well-known SyN (symmetric image normalization) method, and linear (affine) atlas registration was performed using FLIRT (Jenkinson et al., 2012). The fetal brain atlas (**Figure 3**; Gholipour et al., 2017) is an averaged atlas from fetuses imaged at 36 weeks GA with predefined labels of deep-brain structures, including the thalamus and cerebellum. The atlas was nonlinearly and linearly registered into the native participant 3D MRI space. The transformation matrix was saved and applied onto the atlas mask to warp the tissue labels into subject space. The transformed atlas labels were used as thalamus and cerebellum masks and were compared with manual masks by calculating DSCs for the reliability test.

The applied FLIRT registration tool implemented the correlation ratio similarity metric for linear (affine) registration as the default parameters. The ANTs registration tool used a mutual information (MI) similarity metric for linear (rigid and affine) registration and nonlinear (SyN) registration. Different combinations of similarity metrics for both linear and nonlinear image registration of ANTs were also applied and compared to find the more suitable image registration method for our MR image data. The cross-correlation (CC) and MI similarity metrics, provided in the ANTs toolbox, which are both sufficient for intra-modality registration were used for rigid, affine, and SyN registration algorithms.

The FLIRT linear image registration was performed using the command line tool with the DOF (degree of freedom) option set at 12. The ANTs linear image registration (12

2 http://itksnap.org

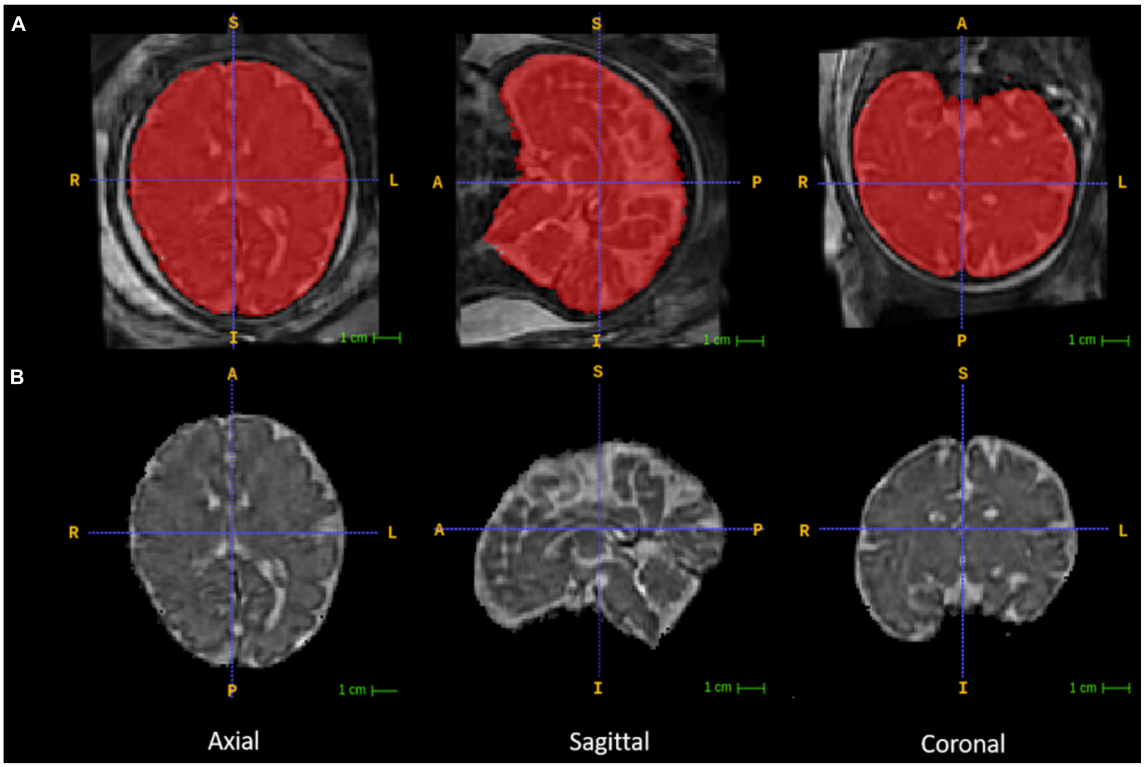

FIGURE 2
Fetal brain segmentation. Row **(A)** includes the volumetrically reconstructed fetal brains in three planes. The red areas are the manually segmented fetal brain binary masks. Row **(B)** includes the orientation-corrected and skull-stripped (using the binary masks in red) fetal brain volumes in three planes.

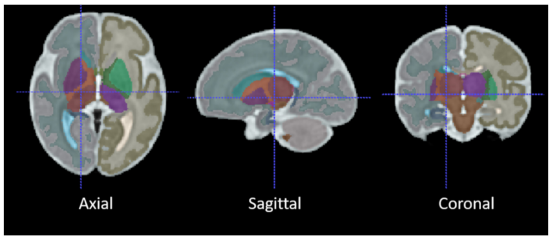

FIGURE 3
The average 36-week GA fetal brain atlas, including cerebellum and thalamus labels. The axial, sagittal, coronal, and 3D rendered views of the age-appropriate fetal brain atlas whereby deep brain tissues are color-coded.

TABLE 1 Maternal ages and fetal gestational ages.

Characteristic	Total (n = 26)
Maternal ages, median years (IQR)	33.5 (29.3–36)
Fetal gestational age, median weeks (IQR)	34.8 (30.9–36.6)

Ages of the mothers (years) and fetuses (weeks' gestation), IQR, interquartile range (25%ile–75%ile).

DOF) was performed using the antsRegistration command line tool by defining the rigid and affine transformations. The ANTs nonlinear registration (millions of DOF) algorithm using the MI metric was performed using the default antsRegistraionSyNQuick.sh script. Keeping every other parameter the same as the antsRegistraionSyNQuick.sh script, the ANTs nonlinear registration using the CC metric was also performed using the antsRegistration command line tool by adding the SyN transformation definition upon the linear registration parameters. To apply the transformation matrices to the atlas masks, the FLIRT command line tool was defined with the applyxfm option, and the ANTs command line tool was antsApplyTransformations. The whole fetal brain, cerebellum, and thalamus volumes were computed from the skull-stripped fetal brain masks and subcortical masks.

Manual subcortical segmentation protocol

Anonymized with respect to GA, the left and right thalamus and cerebellum were delineated in all reconstructed T2-weighted images. The 3D reconstructed T2-weighted images were visualized and segmented using ITK SNAP. The displays provided simultaneous coronal, sagittal and axial views of the brain and created a 3D image of the thalamus and cerebellum.

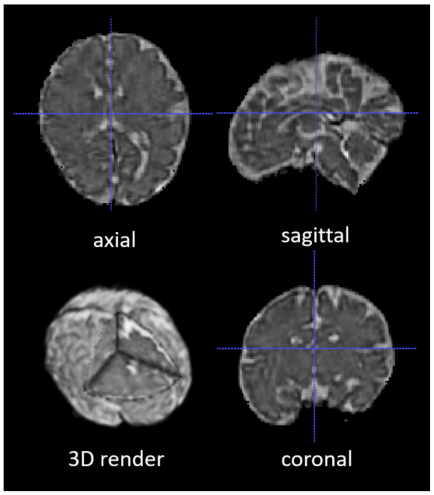

FIGURE 4
A segmented and volumetrically reconstructed fetal brain image using NiftyMIC. The original 2D slices of fetal MR images were automatically segmented and manually adjusted for fetal brain 2D masks. Then the 2D slices and 2D brain masks were reconstructed into 3D volumes and 3D masks with motion correction. This figure shows an example of the skull-stripped, orientation-adjusted 3D fetal brain volumes in axial, sagittal, coronal, and 3D-rendered views.

TABLE 2 Fetal brain volumes.

Characteristic	Total (n = 25)
Cerebellum, median volumes mm^3 (IQR)	13,365 (10,167–17,783)
Thalamus, median volumes mm^3 (IQR)	3,850 (2,714–8,381)
Whole brain, median volumes mm^3 (IQR)	373,186 (285,450–405,289)
GA, median weeks (IQR)	34.6 (30.9–36.4)

GA, Gestational age (weeks), IQR, interquartile range (25%ile–75%ile).

Bilateral thalamus and cerebellum masks were created through the visual identification and tracing of these brain regions in each slice. A three-step segmentation protocol was applied to each image to segment the cerebellum and thalamus. The thalamus was segmented first, followed by the cerebellum. In each scan, the thalamus was present in approximately 40 slices, whereas the cerebellum was present in approximately 50 slices. Segmentations were based on the intensity differences between white and gray matter.

Step 1: Segmentation of the cerebellum and thalamus. Dependent on the participants and the resolution of the images, the rater segmenting the images manually composed segmentations through all three viewpoints (sagittal, coronal, and axial) to ensure that the masks were accurate in all viewpoints. The initially completed segmentations were verified in the other views, and any incorrectly identified areas were omitted and revised.

Step 2: Inspection of the 3D surface. The segmented cerebellum and thalamus masks were represented in a 3D display through ITK-SNAP. The surface of the cerebellum and thalamus is expected to be smooth throughout, so any areas on the masks that protruded excessively were trimmed through a smoothing feature on ITK-SNAP.

Step 3: Segmentation of left and right hemispheres. Once complete, cerebellum and thalamus masks were segmented into left and right hemispheres. Each mask was segmented and split into the left and right hemispheres by identifying the brain's midline. These segmentations were verified across all three viewpoints to ensure accuracy and to revise the original segmentations.

Protocol reliability testing

Three fetal MR images were randomly selected and re-segmented by the same rater to assess the reliability of the three-step manual segmentation protocol. The re-segmentations of the left and right thalamus and cerebellum in the fetal MR images were performed 6 months after the original segmentations to ensure that the rater's memory would not unduly influence the results. This type of test-retest metric, intra-rater reliability, can be used as an upper bound metric to assess the accuracy of the segmentations of the thalamus and cerebellum. The protocol's reliability was measured using the Dice similarity metric, which evaluates the spatial and volumetric overlap of the original and re-segmented label volumes.

Manually adjusting automatically generated masks from NiftyMIC

Anonymized with respect to GA, whole brain masks were manually segmented in all 25 fetal brain scans. A three-step segmentation protocol (described below) was applied to each image to segment the whole brain masks. The whole brain appeared in approximately 90 slices.

Step 1: Automatic segmentation. Whole brain masks were generated automatically for each subject using NiftyMIC software.

Step 2: Manual segmentation. Brain masks generated automatically through NiftyMIC were contrasted against the original brain scan for each subject on ITK-SNAP. Each mask was manually edited to ensure that the mask fit the image. Dependent on the subject and the clarity of the image, the individual segmenting the images manually worked through all three viewpoints (sagittal, coronal, and axial) to ensure that the masks were accurate in all viewpoints. The initially completed segmentations were

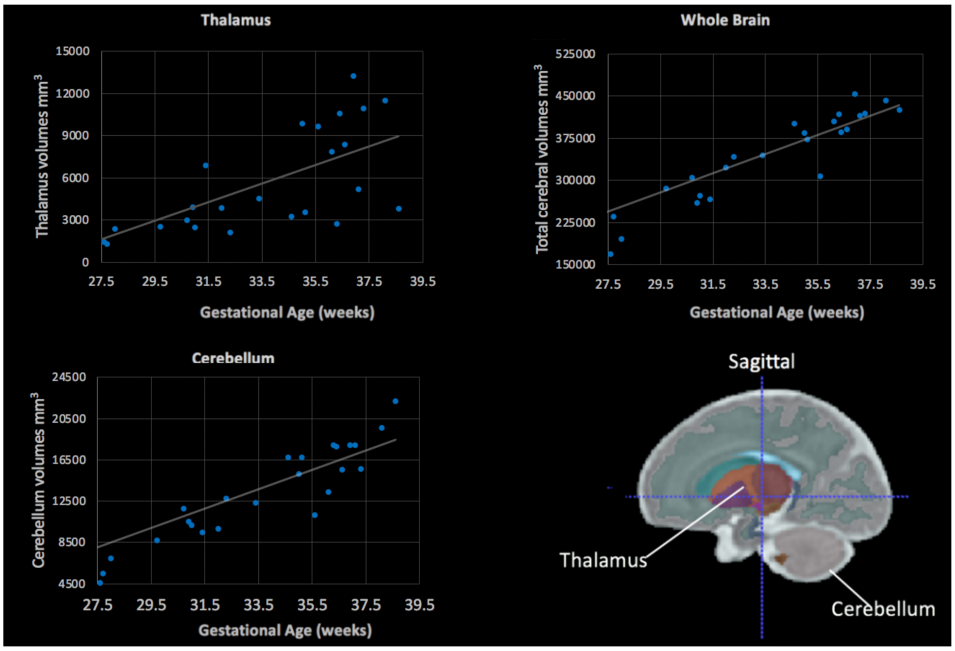

FIGURE 5
Fetal subcortical volumes (*y*-axis) plotted in relation to gestational age (*x*-axis). Fetal thalamus **(top, left)**, whole brain **(top, right)** and cerebellum **(bottom, left)** volumes were plotted in relation to gestational age in weeks. The cerebellum, thalamus and total cerebral volumes showed a positive linear association with gestational age (all, $p < 0.05$). **(Bottom, right)** The color-coded fetal atlas overlaid on a atlas MRI demonstrates the location of the thalamus (orange/purple) and the cerebellum (gray).

verified in the other views, and any incorrectly identified areas were omitted and revised. Any area of the mask that protruded excessively outside the brain region was removed. Additionally, any areas of the brain that were not covered by the mask were filled in appropriately.

Step 3: Segmentation of left and right hemispheres. Once the segmentations were complete, the whole brain masks were segmented into left and right hemispheres. Each mask was segmented and split into the corresponding hemisphere by identifying the midline of the brain. These segmentations were verified across all three viewpoints to ensure accuracy and to revise the original segmentations.

Software installation and operating system decency

The computer used in this study was built with the 10th generation of intel i7 CPU (central processing unit) with 8 cores and 16 threads, 32 GB of RAM (random access memory). The operating system used for this study was Ubuntu 18.04. ITK-SNAP (version 3.6.0), AFNI (version 20.3.01), convert3d package (version 1.0.0), FSL package (version 6.0.4) including FLIRT was installed locally from source. ANTs was provided by and installed on the SciNet supercomputer center at the University of Toronto (i.e., Digital Research Alliance of Canada). NiftyMIC was installed with the provided Docker image.

Statistical analysis

The robustness of the entire automatic fetal deep brain structure segmentation workflow was tested by comparing the automatically segmented masks and manually segmented masks by calculating the DSCs of the common areas covered. The DSC, which computes the ratio of two times the common area to the sum of both areas, was calculated using the formula $D = \frac{2(A \cap B)}{A+B}$, where A and B represent the automatic and manual masks. The masks for the left and right thalamus and cerebellum were combined.

Statistical analyses were performed using SPSS (version 27, Armonk, NY, USA). The resulting DSCs were non-normally distributed, based on Shapiro–Wilk's tests (all, $p < 0.02$). Therefore, a nonparametric Friedman's test for repeated measures data was applied to the DSCs. We had a single hypothesis regarding deformable registration methods, so the alpha level was set at $p < 0.05$. The DSCs range from 0, indicating no spatial overlap between the binary segmentation results calculated automatically versus gold-standard manual segmentations, to 1, indicating complete overlap (Cohen, 1960).

Moderate overlap occurs when DSCs are 0.5–0.6, while very good overlap occurs at >0.7.

To calculate the DSCs, four regions of interest (ROI): the right cerebellum, left cerebellum, right thalamus, and left thalamus, were extracted from the registration-based subcortical masks using the combination of 3dcalc and 3dcluster command line tools from AFNI. The reason for this step is that the manually drawn subcortical masks of one participant were traced separately for the four ROIs described above. The DSCs were then calculated by overlaying the automatically extracted ROIs from the five different registration methods with the corresponding manual ROIs using the c3d-overlay command line tool of the convert3d package from ITK-SNAP. The c3d command line tool produced the DSCs and redirected the output numbers to print into text files. An in-house Python script was developed to read and write the DSCs from the text files into CSV format.

Results

Participants

A total of 21 pregnant adult women participated in the MRI study. Five women returned for a second scan (median time between scans = 3.5 weeks). This resulted in a total of 26 scans that were subsequently used for the analysis. The majority of scans were acquired during the women's third trimester of pregnancy (n = 24, 92%), with the other scans occurring in the near third trimester (range: 27.6–39 weeks of GA). The median GA for all 26 scans was 34.8 weeks (Table 1).

Two-dimensional fetal brain segmentation and 3D volumetric reconstruction

The 2D fetal brain masks of the stacks of the original fetal brain MR images were automatically segmented using NiftyMIC in the axial, coronal, and sagittal image planes. For the NiftyMIC volumetric reconstruction algorithm to perform optimally, the 2D auto-masks were manually adjusted using ITK-SNAP for the over- and under-estimations of fetal brain tissue by the NiftyMIC segmentation algorithm. The volumetric reconstruction process was performed on all 26 scans from the 21 total participants. On a total of 25 scans from 20 participants were 2D masks (96%) successfully reconstructed into 3D space (Figure 4). One participant's data, from the total of 21 participants, was excluded due to a complete failure of the fetal brain segmentation and volumetric reconstruction routine. Once reconstructed, the image dimensions were X = 122, Y = 127, Z = 103 and the voxel size was 1 mm^3.

TABLE 3 Intra-reliability test – Dice similarity coefficients.

	Dice similarity coefficients
Cerebellum	0.78 (0.7–0.8)
Thalamus	0.6 (0.5–0.7)
Overall	0.7 (0.5–0.7)

The median Dice similarity coefficients for cerebellar and thalamic segmentations, and both segmentations combined. IQR, interquartile range (25%ile–75%ile).

Skull stripping and orientation tags correction were successfully applied to the reconstructed 3D volumes. Based on the skull-stripped automatically reconstructed 3D fetal brain MR images, manual segmentations of the thalamus and cerebellum on both left and right sides were successfully performed. The median volumes of the subcortical ROI and whole brain volumes are presented in Table 2, along with the interquartile ranges (IQR). Left and right volumes were combined.

Of the 25 scans, the majority (n = 21) were completed on a 3T MRI and 4 were completed at 1.5T. None of the manually segmented volumes for the thalamus, cerebellum or total cerebral volumes differed based on the Tesla strength of the magnets when adjusting for gestational age (all, $p > 0.05$). The averaged left and right thalamus and cerebellum volumes were plotted against gestational age (Figure 5). All regions, the cerebellum (r = 0.74, $p < 0.001$), thalamus (r = 0.7, $p < 0.001$) and the total cerebral volumes (r = 0.8, $p < 0.001$) were positively associated with gestational age, indicative of larger volumes at older gestational ages.

Manual segmentation protocol validation: Intra-reliability test

The thalamus and cerebellum were re-segmented by a single rater (MM) to assess the consistency of the three-step manual segmentation protocol. Re-segmentations of both the left and right thalamus and cerebellum in these images were performed at least 6 months after the original segmentations were performed to minimize memory effects in the rater. The intra-reliability test results are listed in Table 3. The IQR of the median DSCs of cerebellar and thalamic segmentations were 0.78 and 0.6, respectively. The overall median DSC was 0.7.

Registration-based segmentation reliability test: Comparisons of dice similarity coefficients

The ANTs- (5–10 h/dataset) and FLIRT-based (10 min/dataset) registrations of the 36-week GA fetal brain atlas into the native spaces of the individual fetal MR images were successfully processed in all participants. The

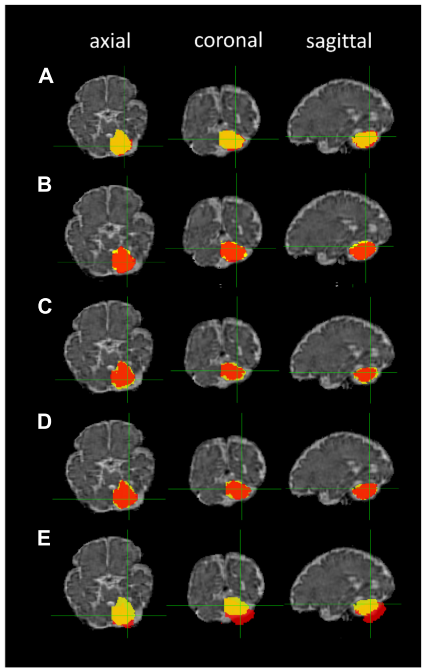

FIGURE 6
Cerebellar masks: registration-based segmentation (red) versus manual segmentation (yellow). The masks are shown in axial, coronal, and sagittal planes from left to right. Row **(A)** ANTs linear registration (MI); **(B)** ANTs linear registration (CC); **(C)** ANTs nonlinear registration (CC); **(D)** ANTs nonlinear registration (MI); and **(E)** FLIRT linear registration.

TABLE 4 Median Dice similarity coefficients.

Registration method	Both	Cerebellum	Thalamus
FLIRT	0.54 (0.44–0.63)	0.62 (0.46–0.73)	0.52 (0.39–0.66)
ANTs Lin MI	0.70 (0.58–0.74)	0.80 (0.73–0.83)	0.59 (0.48–0.7)
ANTs Lin CC	0.72 (0.59–0.75)	0.80 (0.74–0.83)	0.61 (0.48–0.71)
ANTs NL MI	0.72 (0.63–0.76)	0.79 (0.75–0.83)	0.62 (0.49–0.68)
ANTs NL CC	0.74 (0.65–0.76)	0.79 (0.76–0.82)	0.65 (0.52–0.71)

The median Dice similarity coefficients and the interquartile ranges of the cerebellum, thalamus, and both subcortical segmentations using five registration methods compared to manual segmentations.

TABLE 5 *Post hoc* comparisons of mean ranks: fetal cerebellar segmentations.

Sample 1–sample 2	Standard test statistic	*P*-value*
FLIRT – ANTs NL CC	**6.77**	**<0.001**
FLIRT – ANTs Lin MI	**7.65**	**<0.001**
FLIRT – ANTs NL MI	**8.41**	**<0.001**
FLIRT – ANTs Lin	**−8.48**	**<0.001**
ANTs NL CC – ANTs Lin MI	0.89	0.9
ANTs NL CC – ANTs NL MI	1.64	0.9
ANTs NL CC – ANTs Lin	−1.71	0.88
ANTs Lin MI – ANTs NL MI	0.76	0.9
ANTs Lin MI – ANTs Lin CC	−0.82	0.9
ANTs NL MI – ANTs Lin CC	−0.06	0.9

Results of a Dunn's pairwise *post hoc* tests on the mean ranks. *Bonferroni corrected for multiple comparisons. Significant values are in bold.

median DSCs comparing the five image registration methods to the manual segmentation method were: (1) FLIRT linear registration (affine) using the correlation ratio similarity metric, (2) ANTs linear registration (rigid and affine) using the MI similarity metric (ANTs Lin MI), (3) ANTs linear registration using the CC similarity metric (ANTs Lin CC), (4) ANTs nonlinear registration (rigid, affine, and SyN) using the MI similarity metric (ANTs NL MI), and (5) ANTs nonlinear registration using the CC similarity metric (ANTs NL CC) for left and right cerebellum and thalamus segmentations. The cerebellar masks produced by the five registration methods using different similarity metrics are shown in Figure 6.

The median DSCs of the five registration methods for the cerebellum segmentations, thalamus segmentations, and both segmentations are listed in Table 4. Overall, the FLIRT linear registration resulted in non-optimal estimation with gross misalignment of the masks on the fetal MR image. The ANTs nonlinear registration (CC) had the highest median Dice similarity index. The ANTs non linear registration (MI) also demonstrated a very good performance.

The median DSCs of both subcortical segmentations revealed that ANTs NL CC and ANTS NL MI were high with the linear registrations being comparable, while those produced by FLIRT were the lowest. The DSCs for the linear (i.e., ANTs rigid and affine, and FLIRT affine) and nonlinear (i.e., ANTs nonlinear with MI and CC similarity metrics) methods for the thalamus and cerebellum segmentations were compared using Friedman's Repeated Measure Analysis of Variance by Ranks. Upon comparison of the left and right cerebellar DSCs (n = 50), the calculated mean ranks were significantly different from one another (df = 4, test statistic = 100.84, $p < 0.001$). *Post hoc* pairwise comparisons revealed that the mean ranks were significantly different for the FLIRT-based registrations compared to the ANTs linear and nonlinear methods (all, $p < 0.001$; Table 5). Additionally, none of the mean ranks differed for any of the ANTs based registration methods (all $p > 0.88$).

Subsequently, the DSCs produced by the linear and nonlinear registrations algorithms compared to the manual segmentations were examined for the left and right thalamic segmentations and were also significantly different (n = 50, df = 4, test statistic = 47.36, $p < 0.001$). Pairwise comparisons indicated slightly different results than seen for the cerebellar segmentations, whereby FLIRT-based registrations were associated with significantly different mean ranks compared to the ANTs-based

TABLE 6 *Post hoc* comparisons for mean ranks: fetal thalamic segmentations.

	Standard test statistic	*P*-value*
FLIRT – ANTs Lin MI	2.15	0.32
FLIRT – ANTs Lin CC	**−3.67**	**0.002**
FLIRT – ANTs NL MI	**4.49**	**<0.001**
FLIRT – ANTs NL CC	**6.45**	**<0.001**
ANTs Lin MI – ANTs Lin CC	−1.52	0.9
ANTs Lin MI – ANTs NL MI	2.34	0.19
ANTs Lin MI – ANTs NL CC	**−4.30**	**<0.001**
ANTs Lin CC – ANTs NL MI	0.82	0.1
ANTs Lin CC – ANTs NL CC	2.78	0.05
ANTs NL MI – ANTs NL CC	−1.96	0.5

Results of a Dunn's pairwise *post hoc* tests on the mean ranks. *Bonferroni corrected for multiple comparisons. Significant values are in bold.

nonlinear registration methods, including ANTs NL MI and NL CC, but also the ANTs Lin CC method (all $p < 0.002$; Table 6).

Comparison of the mean ranks indicated that ANTs NL CC performed significantly better than ANTs Lin MI ($p < 0.001$).

We further compared the volumes extracted by the 5 registration methods relative to the manually segmented volumes. The extracted volumes for the cerebellum and thalamus based on the FLIRT and ANTs-based methods were subtracted from the manually segmented volumes. The differences in the volumes were then divided by the manually segmented volumes and the resulting values were converted to percentages (Figure 7). Overall, the cerebellar segmentations were more likely to be underestimated by ANTs-based methods. FLIRT-based registration of the thalamus and the cerebellum resulted in overestimation of the volumes.

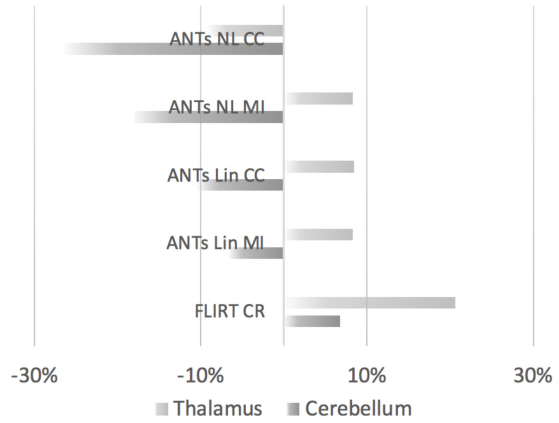

FIGURE 7
Comparisons of thalamic and cerebellar volumes produced by FLIRT- or ANTs-based methods relative to manually segmented volumes. The overlap (positive values indicate overestimation, negative values indicate underestimation) is displayed according to the registration methods from top to bottom. Top to bottom: ANTs nonlinear registration (CC, cross-correlation); ANTs nonlinear registration (MI, mutual information); ANTs linear registration (CC); ANTs linear registration (MI); and FLIRT linear registration.

Discussion

Fetal MRI represents one of the next frontiers in clinical, translational and basic science research, not only to improve our understanding of the developing fetal brain, but to aid in early diagnosis, particularly for fetuses at-risk for adverse neurodevelopmental outcomes (Andescavage et al., 2017; Mufti et al., 2021; Rajagopalan et al., 2021). The study of the brain and other organs in the fetus has been limited to primarily non-invasive ultrasound technology. While ultrasound offers many advantages due to its low cost and ease of use in hospital settings, it is limited in terms of its spatial resolution to study fetal brain structure. MRI of the fetal brain offers superior 3D image resolution and can be used to study brain volumetric development.

This work aimed to develop a semi-automatic pipeline to segment fetal brain volumes acquired in third-trimester images. A recently developed deep learning algorithm was employed to mask the fetal brain and reconstruct MR images in second-trimester fetuses. Analyzing fetal MR images using brain segmentation toolkits designed for adult populations is impractical due to the presence of motion artifacts from fetal movements. This study aimed to overcome this obstacle in fetal MRI by applying segmentation, volumetric reconstruction, and image normalization toolkits to build a semi-automated process for fetal brain subcortical segmentation in T2-weighted fetal MR images that were acquired during the third trimester of pregnancy.

The fetal brain was masked in three anatomical 2D planes (axial, sagittal, and coronal) in the first step. Then the segmented 2D fetal brains and brain masks in three planes were reconstructed into 3D brain volumes and masks. After skull-stripping and orientation tag correction, linear and nonlinear image registration methods were evaluated in terms of their accuracy in segmenting cortical and subcortical structures by applying an age-appropriate MRI atlas. In turn, the subcortical labels of the chosen atlas were aligned with the individual fetal MR images using two different image registration toolkits (ANTs and FLIRT) using linear (ANTs Lin MI/CC and FLIRT) and nonlinear registration methods (ANTs NL MI/CC). The optimal cortical and subcortical segmentation performance was determined by applying and comparing two image registration toolkits for both nonlinear and linear image registration

algorithms with different configurations of similarity metrics. The aligned subcortical labels were then compared with manually segmented thalamus and cerebellum subcortical masks. The manually labeled masks were considered ground truth for later comparison with the atlas-based registration. The nonlinear registration methods within ANTs provided improved results compared to a linear transformation (FLIRT) for the cerebellum segmentations as well as in comparison to the linear methods within ANTs, primarily for the thalamic segmentations. The ANTs MI and CC similarity metrics are optimized in terms of translation, rotation, scaling, and shearing during the registration of the images. Nonlinear registration methods, while computationally more intensive, may be more suitable for small samples of fetal brain images acquired during the third trimester to have higher quality results. Overall, our findings indicated that ANTs-based nonlinear registration methods using the MI and CC similarity metric performed adequately and may be more practical for processing larger datasets but with additional computational processing time.

Semi-automatic registration-based fetal subcortical segmentation

This research utilized a machine learning-based segmentation algorithm from the NiftyMIC toolkit (Ebner et al., 2020) to significantly mitigate motion artifacts, segment the fetal brain images acquired during the third trimester in 2D, and reconstruct 2D images in three planes into 3D volumes. The NiftyMIC toolkit (Ebner et al., 2020) is open-source, Python-based software for research within the Guided Instrumentation for Fetal Therapy and Surgery (GIFT-Surg) project, which is an international research consortium focused on developing technology, tools and training to facilitate fetal surgery (Joyeux et al., 2018). The software can reconstruct an isotropic, high-resolution brain volume from multiple low-resolution 2D image slices acquired in fetuses. The NiftyMIC 2D segmentation was originally trained and developed for second-trimester fetal MR images. This masking step is essential for the remaining workflow steps. In the current work, each fetal mask required visual inspection and manual editing to aid the performance of the automatically generated labels. With the adequate 2D fetal brain masks serving as input, the NiftyMIC volumetric reconstruction process performed smoothly. Overall, NiftyMIC performed well on most images, and the performance was comparable to what was published in second-trimester images.

Machine learning algorithms are known to theoretically perform well to learn and predict data patterns when the process is trained with enough data (Cardenas et al., 2019). This performance depends on the problem's complexity and the sophistication of the machine learning algorithm. The NiftyMIC 2D brain segmentation of third-trimester fetal MR images did not always perform reliably on the third-trimester MRI data. The NiftyMIC (*niftymic_segment_fetal_brains*) machine learning algorithm was originally trained with MR images of second-trimester healthy fetuses and fetuses diagnosed with spina bifida. Exponential growth of the fetal brain from the second to the third trimester results in significant cortical and subcortical morphology changes.

Additionally, during the third trimester, the fetal brain becomes increasingly myelinated (Dubois et al., 2008a,b, 2014; Wilson et al., 2021). Structural MR images weighted by T1 or T2 relaxation times will be influenced by different water and fat contents in the fetal brain compared to that seen in adults. This difference results in different signal intensities in the voxels of MR images of the fetal brain, which can vary in fetuses even compared to 6-month-old infants due to the rapid changes in overall growth and myelination (Dubois et al., 2014). Less is known about tissue intensity changes between second-trimester and third-trimester fetuses; however, in relation to the current work, the image intensity of the voxels of the gray and white matter tissues of the training data used for NiftyMIC may have been quite different from that of our third-trimester data. These factors could have notably influenced the machine learning algorithm's performance.

The linear and nonlinear registration algorithms paired with various similarity metrics were successfully applied to register the labeled atlas into native space for cortical and subcortical segmentation of the MRI scans acquired in third-trimester fetuses. The use of different similarity metrics applied to fetal deep-brain segmentation was explored. The registered thalamic and cerebellar masks were compared to manually segmented masks. The ANTs nonlinear registration tool (Avants et al., 2008) reliably segmented deep brain structures of fetal brains on MR images for both the cerebellum and thalamus. The DSCs of ANTs Lin CC indicated a good agreement between the atlas-based and manual segmentations. The ANTs Lin MI registration had similar DSCs for both thalamic and cerebellar segmentations. According to the guidelines for interpreting DSCs (Cohen, 1960), the median DSCs of ANTs Lin MI and CC indicated a substantial agreement between the registration-based semi-automatic segmentation and manual segmentation for estimating fetal deep brain structures. However, there was a notable performance difference between thalamic and cerebellar segmentations using all five registration methods. The median DSCs of the thalamic segmentations were lower than that of the cerebellar segmentations, which indicated very good agreement (>0.7) and only moderate agreement (0.5–0.6) between the registration-based and manual thalamic segmentations using ANTs Lin MI and CC. Findings indicated that ANTs-based nonlinear image registration did not outperform ANTs-based linear image registration for segmenting the cerebellar structures. The CC similarity metric, suitable for intra-modality MR image normalization, was sufficient for our fetal MRI data. The additional calculations involving histogram matching from the MI metric did not substantially improve the image

registration quality. Therefore, using the CC metric, which requires less computation time to register the data, is sufficient for processing datasets, particularly those with larger sample sizes.

This semi-automatic fetal subcortical segmentation method may be very beneficial for future studies of fetal neurodevelopment. The *in utero* origin of neurodevelopmental delay reflected in smaller cortical and subcortical volumes can be studied by applying this methodology to a larger fetal MR image dataset that has the potential for significant savings in terms of time and labor devoted to manual segmentations. The whole brain volume and deep brain structures such as the hippocampus are important for learning and memory processes and can be segmented from the MR images for comparison, analysis and developmental outcome prediction (Eichenbaum, 1997; Bird and Burgess, 2008; Milivojevic and Doeller, 2013). The proposed methodology could also be utilized to study second-trimester fetal volumetric development. From the second to the third trimester, fetal neurodevelopment could be monitored by segmenting and calculating subcortical and brain growth in high-risk groups. This method could potentially reveal when the variations in brain morphology occur to aid in the early diagnosis of fetal brain abnormalities in clinical settings.

The ANTs-based nonlinear image registration performed slightly better than the ANTS-based linear image registration for aligning the fetal brain atlas to our dataset's native MR image space. However, this difference was not strongly evident statistically. The amount of deformation of the image when warping the atlas might have been minimal, given that the difference in the shape of the fetal brain of the atlas and our acquired fetal MR images was comparable in terms of the anatomy. Linear mislocalization of the fetal brains between the atlas image and the target image may have contributed to spatial differences. The ANTs-based nonlinear registration is more time-consuming than linear registration, with a higher requirement of computation abilities while providing reliable subcortical segmentation performance.

Conclusion

Antenatal development of the fetal cortex and subcortical structures is a complex neurophysiological process. The development of the nervous occurs through genetically predetermined events, including cellular proliferation, neuronal migration, and differentiation of cells into specialized subtypes, followed by synaptogenesis, which provides the formation of cortical and subcortical circuitry. Environmental influences such as maternal diet and even stress can alter these processes and, in more severe cases, can lead to growth restriction of the fetus. The study of fetal brain development using volumetric MRI provides a window into the development of the cortex and subcortical structures in typical and atypically developing fetuses. This work developed and evaluated a semi-automatic pipeline to segment the cortex and subcortical structures in third-trimester images. A novel deep learning-based algorithm was used to segment and reconstruct 3D MR images of the entire fetal brain. An atlas to segment cortical and subcortical structures was aligned to the fetal brain images. Five registration algorithms were compared to gold-standard manual segmentations of subcortical structures. Overall a deformable registration method, ANTs using a CC metric provided optimal performance to segment the cortical structures, and may be favorable for large datasets or for use in high-resource settings without access to high throughput computational facilities. Future work, using deep-learning methods for image registration and segmentation may facilitate more automated methods for cortical and subcortical parcellation in the fetus. Larger datasets with wider gestational age ranges would aid in facilitating artificial intelligent approaches to fetal brain development. Additionally, applying this atlas-based method to study deep-brain macrostructural development in high-risk fetuses would be a future step. Fetal brain growth is a key marker for developmental outcomes. Methods to characterize subcortical development in typically and atypically fetuses could aid in the detection of potential biomarkers associated with delayed or arrested growth. Utilizing multi-modal MR methods may also further facilitate fetal brain tissue extraction.

Data availability statement

The raw data supporting the conclusions of this article will be made available by the authors upon reasonable request.

Ethics statement

The studies involving human participants were reviewed and approved by the Health Sciences Research Ethics Board at Western University. The participants provided their written informed consent to participate in this study.

Author contributions

JW, EN, MM, BV, RE, CM, SR, and ED were involved in the study design, database variable creation, test material selection, and data acquisition design and execution of the data analytic strategy, and reviewed and revised the final version of the manuscript. JW, EN, SR, and ED conceptualized the execution of the data analytic strategy, contributed to the data analysis, and reviewed and revised the final draft of the manuscript.

All authors approved the final manuscript as submitted and agree to be accountable for all aspects of the work.

Funding

This study was supported by funding from the New Frontiers in Research Fund, the Canadian Institutes of Health Research (CIHR), the Molly Towell Perinatal Research Foundation, and the Canada First Research Excellence Fund through BrainsCAN.

Acknowledgments

We thank the women who participated in this study.

Conflict of interest

The authors declare that the research was conducted in the absence of any commercial or financial relationships that could be construed as a potential conflict of interest.

Publisher's note

All claims expressed in this article are solely those of the authors and do not necessarily represent those of their affiliated organizations, or those of the publisher, the editors and the reviewers. Any product that may be evaluated in this article, or claim that may be made by its manufacturer, is not guaranteed or endorsed by the publisher.

References

Andescavage, N., duPlessis, A., Metzler, M., Bulas, D., Vezina, G., Jacobs, M., et al. (2017). In vivo assessment of placental and brain volumes in growth-restricted fetuses with and without fetal Doppler changes using quantitative 3D MRI. *J. Perinatol.* 37, 1278–1284. doi: 10.1038/jp.2017.129

Avants, B. B., Epstein, C. L., Grossman, M., and Gee, J. C. (2008). Symmetric diffeomorphic image registration with cross-correlation: evaluating automated labeling of elderly and neurodegenerative brain. *Med. Image Anal.* 12, 26–41. doi: 10.1016/j.media.2007.06.004

Banović, V., Škrablin, S., Banović, M., Radoš, M., Gverić-Ahmetašević, S., and Babiæ, I. (2014). Fetal brain magnetic resonance imaging and long-term neurodevelopmental impairment. *Int. J. Gynaecol. Obstet* 125, 237–240.

Beversdorf, D. Q., Manning, S. E., Hillier, A., Anderson, S. L., Nordgren, R. E., Walters, S. E., et al. (2005). Timing of prenatal stressors and autism. *J. Autism Dev. Disord.* 35, 471–478.

Bird, C. M., and Burgess, N. (2008). The hippocampus and memory: insights from spatial processing. *Nat. Rev. Neurosci.* 9, 182–194.

Boardman, J. P., Craven, C., Valappil, S., Counsell, S. J., Dyet, L. E., Rueckert, D., et al. (2010). A common neonatal image phenotype predicts adverse neurodevelopmental outcome in children born preterm. *Neuroimage* 52, 409–414. doi: 10.1016/j.neuroimage.2010.04.261

Bonnet-Brilhault, F., Rajerison, T. A., Paillet, C., Guimard-Brunault, M., Saby, A., Ponson, L., et al. (2018). Autism is a prenatal disorder: evidence from late gestation brain overgrowth. *Autism Res.* 11, 1635–1642. doi: 10.1002/aur.2036

Brossard-Racine, M., du Plessis, A. J., Vezina, G., Robertson, R., Bulas, D., Evangelou, I. E., et al. (2014). Prevalence and spectrum of in utero structural brain abnormalities in fetuses with complex congenital heart disease. *AJNR Am. J. Neuroradiol.* 35, 1593–1599. doi: 10.3174/ajnr.A3903

Brossard-Racine, M., McCarter, R., Murnick, J., Tinkleman, L., Vezina, G., Limperopoulos, C., et al. (2019). Early extra-uterine exposure alters regional cerebellar growth in infants born preterm. *Neuroimage Clin.* 21:101646. doi: 10.1016/j.nicl.2018.101646

Cardenas, C. E., Yang, J., Anderson, B. M., Court, L. E., and Brock, K. B. (2019). Advances in auto-segmentation. *Semin. Radiat. Oncol.* 29, 185–197.

Cesaretti, C., Nanni, M., Ghi, T., Parazzini, C., Conte, G., Contro, E., et al. (2016). Variability of forebrain commissures in callosal agenesis: a prenatal MR imaging study. *AJNR Am. J. Neuroradiol.* 37, 521–527.

Clausi, S., Coricelli, G., Pisotta, I., Pavone, E. F., Lauriola, M., Molinari, M., et al. (2015). Cerebellar damage impairs the self-rating of regret feeling in a gambling task. *Front. Behav. Neurosci.* 9:113. doi: 10.3389/fnbeh.2015.00113

Cohen, J. (1960). A coefficient of agreement for nominal scales. *Educ. Psychol. Meas.* 20, 37–46.

De Asis-Cruz, J., Andescavage, N., and Limperopoulos, C. (2021). Adverse prenatal exposures and fetal brain development: insights from advanced fetal MRI. *Biol. Psychiatry Cogn. Neurosci. Neuroimaging* 7, 480–490.

Dehghani, N., and Wimmer, R. D. (2019). A computational perspective of the role of the thalamus in cognition. *Neural Comput.* 31, 1380–1418.

Dubois, J., Dehaene-Lambertz, G., Kulikova, S., Poupon, C., Hüppi, P. S., and Hertz-Pannier, L. (2014). The early development of brain white matter: a review of imaging studies in fetuses, newborns and infants. *Neuroscience* 276, 48–71.

Dubois, J., Dehaene-Lambertz, G., Perrin, M., Mangin, J. F., Cointepas, Y., Duchesnay, E., et al. (2008a). Asynchrony of the early maturation of white matter bundles in healthy infants: quantitative landmarks revealed noninvasively by diffusion tensor imaging. *Hum. Brain Mapp.* 29, 14–27. doi: 10.1002/hbm.20363

Dubois, J., Dehaene-Lambertz, G., Soarès, C., Cointepas, Y., Le Bihan, D., Hertz-Pannier, L., et al. (2008b). Microstructural correlates of infant functional development: example of the visual pathways. *J. Neurosci.* 28, 1943–1948. doi: 10.1523/JNEUROSCI.5145-07.2008

Ebner, M., Wang, G., Li, W., Aertsen, M., Patel, P. A., Aughwane, R., et al. (2020). An automated framework for localization, segmentation and super-resolution reconstruction of fetal brain MRI. *Neuroimage* 206:116324. doi: 10.1016/j.neuroimage.2019.116324

Eichenbaum, H. (1997). Declarative memory: insights from cognitive neurobiology. *Annu. Rev. Psychol.* 48, 547–572.

Gholipour, A., Rollins, C. K., Velasco-Annis, C., Ouaalam, A., Akhondi-Asl, A., Afacan, O., et al. (2017). A normative spatiotemporal MRI atlas of the fetal brain for automatic segmentation and analysis of early brain growth. *Sci. Rep.* 7:476. doi: 10.1038/s41598-017-00525-w

Habas, P. A., Kim, K., Rousseau, F., Glenn, O. A., Barkovich, A. J., and Studholme, C. (2010). Atlas-based segmentation of developing tissues in the human brain with quantitative validation in young fetuses. *Hum. Brain Mapp.* 31, 1348–1358. doi: 10.1002/hbm.20935

Hardan, A. Y., Girgis, R. R., Adams, J., Gilbert, A. R., Keshavan, M. S., and Minshew, N. J. (2006). Abnormal brain size effect on the thalamus in autism. *Psychiatry Res.* 147, 145–151.

Jenkinson, M., Beckmann, C. F., Behrens, T. E., Woolrich, M. W., and Smith, S. M. (2012). FSL. *Neuroimage* 62, 782–790.

Joyeux, L., De Bie, F., Danzer, E., Van Mieghem, T., Flake, A. W., and Deprest, J. (2018). Safety and efficacy of fetal surgery techniques to close a spina bifida defect in the fetal lamb model: a systematic review. *Prenat Diagn.* 38, 231–242. doi: 10.1002/pd.5222

Khalili, N., Turk, E., Benders, M. J. N. L., Moeskops, P., Claessens, N. H. P., de Heus, R., et al. (2019). Automatic extraction of the intracranial volume in fetal

and neonatal MR scans using convolutional neural networks. *Neuroimage Clin.* 24:102061. doi: 10.1016/j.nicl.2019.102061

Knezović, V., Kasprian, G., Štajduhar, A., Schwartz, E., Weber, M., Gruber, G. M., et al. (2019). Underdevelopment of the human hippocampus in callosal agenesis: an in vivo fetal MRI study. *AJNR Am. J. Neuroradiol.* 40, 576–581. doi: 10.3174/ajnr.A5986

Koziol, L. F., Budding, D., Andreasen, N., D'Arrigo, S., Bulgheroni, S., Imamizu, H., et al. (2014). Consensus paper: the cerebellum's role in movement and cognition. *Cerebellum* 13, 151–177.

Limperopoulos, C., Bassan, H., Gauvreau, K., Robertson, R. L. Jr., Sullivan, N. R., Benson, C. B., et al. (2007). Does cerebellar injury in premature infants contribute to the high prevalence of long-term cognitive, learning, and behavioral disability in survivors? *Pediatrics* 120, 584–593. doi: 10.1542/peds.2007-1041

Milivojevic, B., and Doeller, C. F. (2013). Mnemonic networks in the hippocampal formation: from spatial maps to temporal and conceptual codes. *J. Exp. Psychol. Gen.* 142, 1231–1241. doi: 10.1037/a0033746

Mufti, N., Aertsen, M., Ebner, M., Fidon, L., Patel, P., Rahman, M. B. A., et al. (2021). Cortical spectral matching and shape and volume analysis of the fetal brain pre- and post-fetal surgery for spina bifida: a retrospective study. *Neuroradiology* 63, 1721–1734. doi: 10.1007/s00234-021-02725-8

Nichols, E. S., Correa, S., Van Dyken, P., Kai, J., Kuehn, T., de Ribaupierre, S., et al. (2022). An automated BIDS-App for brain segmentation of human fetal functional MRI data. *bioRxiv* Available online at: https://doi.org/10.1101/2022.09.02.506391 (accessed September 5, 2022).

Payette, K., de Dumast, P., Kebiri, H., Ezhov, I., Paetzold, J. C., Shit, S., et al. (2021). An automatic multi-tissue human fetal brain segmentation benchmark using the Fetal Tissue Annotation Dataset. *Sci. Data* 8:167. doi: 10.1038/s41597-021-00946-3

Rajagopalan, V., Deoni, S., Panigrahy, A., and Thomason, M. E. (2021). Is fetal MRI ready for neuroimaging prime time? An examination of progress and remaining areas for development. *Dev. Cogn. Neurosci.* 51:100999. doi: 10.1016/j.dcn.2021.100999

Ramphal, B., Pagliaccio, D., Thomas, L. V., He, X., and Margolis, A. E. (2021). Contributions of cerebellar white matter microstructure to social difficulty in nonverbal learning disability. *Cerebellum* 20, 931–937. doi: 10.1007/s12311-021-01265-4

Rathbone, R., Counsell, S. J., Kapellou, O., Dyet, L., Kennea, N., Hajnal, J., et al. (2011). Perinatal cortical growth and childhood neurocognitive abilities. *Neurology* 77, 1510–1517. doi: 10.1212/WNL.0b013e318233b215

Rutherford, M., Jiang, S., Allsop, J., Perkins, L., Srinivasan, L., Hayat, T., et al. (2008). MR imaging methods for assessing fetal brain development. *Dev. Neurobiol.* 68, 700–711.

Schmahmann, J. D. (2004). Disorders of the cerebellum: ataxia, dysmetria of thought, and the cerebellar cognitive affective syndrome. *J. Neuropsychiatry Clin. Neurosci.* 16, 367–378.

Thomason, M. E. (2020). Development of brain networks in utero: relevance for common neural disorders. *Biol. Psychiatry* 88, 40–50. doi: 10.1016/j.biopsych.2020.02.007

Twickler, D. M., Reichel, T., McIntire, D. D., Magee, K. P., and Ramus, R. M. (2002). Fetal central nervous system ventricle and cisterna magna measurements by magnetic resonance imaging. *Am. J. Obstet Gynecol.* 187, 927–931.

Uus, A. U., Egloff Collado, A., Roberts, T. A., Hajnal, J. V., Rutherford, M. A., and Deprez, M. (2022). Retrospective motion correction in foetal MRI for clinical applications: existing methods, applications and integration into clinical practice. *Br. J. Radiol.* [Online ahead of print]. doi: 10.1259/bjr.20220071

Wells, E. M., Walsh, K. S., Khademian, Z. P., Keating, R. F., and Packer, R. J. (2008). The cerebellar mutism syndrome and its relation to cerebellar cognitive function and the cerebellar cognitive affective disorder. *Dev. Disabil. Res. Rev.* 14, 221–228. doi: 10.1002/ddrr.25

Werner, H., Gasparetto, T. D., Daltro, P., Leandro Gasparetto, E., and Araujo Júnior, E. (2018). Typical lesions in the fetal nervous system: correlations between fetal magnetic resonance imaging and obstetric ultrasonography findings. *Ultrasonography* 37, 261–274. doi: 10.14366/usg.17040

Wilson, S., Pietsch, M., Cordero-Grande, L., Price, A. N., Hutter, J., Xiao, J., et al. (2021). Development of human white matter pathways in utero over the second and third trimester. *Proc. Natl. Acad. Sci. U. S. A.* 118:e2023598118. doi: 10.1073/pnas.2023598118

Wu, Y., Lu, Y. C., Jacobs, M., Kapse, K., Zhao, L., Niforatos-Andescavage, N., et al. (2020). Association of prenatal maternal psychological distress with fetal brain growth, metabolism, and cortical maturation. *JAMA Netw. Open* 3:e1919940. doi: 10.1001/jamanetworkopen.2019.19940

Yamashita, R., Nishio, M., Do, R. K. G., and Togashi, K. (2018). Convolutional neural networks: an overview and application in radiology. *Insights Imaging* 9, 611–629.

Zhao, L., Asis-Cruz, J. D., Feng, X., Wu, Y., Kapse, K., Largent, A., et al. (2022). Automated 3D fetal brain segmentation using an optimized deep learning approach. *AJNR Am. J. Neuroradiol.* 43, 448–454. doi: 10.3174/ajnr.A7419

frontiers | Frontiers in Neuroscience

TYPE Original Research
PUBLISHED 18 November 2022
DOI 10.3389/fnins.2022.952355

OPEN ACCESS

EDITED BY
Hao Huang,
University of Pennsylvania,
United States

REVIEWED BY
Catherine Limperopoulos,
Children's National Hospital,
United States
Andras Jakab,
University Children's Hospital Zurich,
Switzerland

*CORRESPONDENCE
Ashok Panigrahy
panigrahya@upmc.edu

†These authors have contributed equally to this work and share first authorship

SPECIALTY SECTION
This article was submitted to Neurodevelopment, a section of the journal Frontiers in Neuroscience

RECEIVED 25 May 2022
ACCEPTED 01 November 2022
PUBLISHED 18 November 2022

CITATION
Votava-Smith JK, Gaesser J, Harbison AL, Lee V, Tran N, Rajagopalan V, del Castillo S, Kumar SR, Herrup E, Baust T, Johnson JA, Gabriel GC, Reynolds WT III, Wallace J, Meyers B, Ceschin R, Lo CW, Schmithorst VJ and Panigrahy A (2022) Clinical factors associated with microstructural connectome related brain dysmaturation in term neonates with congenital heart disease. *Front. Neurosci.* 16:952355. doi: 10.3389/fnins.2022.952355

Clinical factors associated with microstructural connectome related brain dysmaturation in term neonates with congenital heart disease

Jodie K. Votava-Smith[1†], Jenna Gaesser[2†], Anna Lonyai Harbison[3†], Vince Lee[4,5], Nhu Tran[6], Vidya Rajagopalan[7], Sylvia del Castillo[8], S. Ram Kumar[9], Elizabeth Herrup[10], Tracy Baust[10], Jennifer A. Johnson[11], George C. Gabriel[12], William T. Reynolds III[4], Julia Wallace[4], Benjamin Meyers[4], Rafael Ceschin[4,13], Cecilia W. Lo[12], Vanessa J. Schmithorst[4] and Ashok Panigrahy[4,5,13]*

[1]Division of Cardiology, Department of Pediatrics, Children's Hospital Los Angeles, Keck School of Medicine of USC, Los Angeles, CA, United States, [2]Department of Neurology, Children's Hospital of Pittsburgh of UPMC, University of Pittsburgh School of Medicine, Pittsburgh, PA, United States, [3]Stanford Children's Health, Palo Alto, CA, United States, [4]Department of Pediatric Radiology, Children's Hospital of Pittsburgh of UPMC, University of Pittsburgh School of Medicine, Pittsburgh, PA, United States, [5]Department of Bioengineering, Swanson School of Engineering, University of Pittsburgh, Pittsburgh, PA, United States, [6]Division of Neonatology, Department of Pediatrics, Keck School of Medicine of USC, Children's Hospital Los Angeles, Fetal and Neonatal Institute, Los Angeles, CA, United States, [7]Department of Radiology, Children's Hospital Los Angeles, Keck School of Medicine of USC, Los Angeles, CA, United States, [8]Department of Anesthesiology Critical Care Medicine Anesthesiology, Children's Hospital Los Angeles, Keck School of Medicine of USC, Los Angeles, CA, United States, [9]Division of Cardiothoracic Surgery, Department of Surgery, Children's Hospital Los Angeles, Keck School of Medicine of USC, Los Angeles, CA, United States, [10]Division of Pediatric Cardiac Intensive Care, Department of Critical Care, University of Pittsburgh School of Medicine, Pittsburgh, PA, United States, [11]Division of Pediatric Cardiology, Department of Pediatrics, University of Pittsburgh School of Medicine, Pittsburgh, PA, United States, [12]Department of Developmental Biology, University of Pittsburgh, Pittsburgh, PA, United States, [13]Department of Biomedical Informatics, University of Pittsburgh, Pittsburgh, PA, United States

Objective: Term congenital heart disease (CHD) neonates display abnormalities of brain structure and maturation, which are possibly related to underlying patient factors, abnormal physiology and perioperative insults. Our primary goal was to delineate associations between clinical factors and postnatal brain microstructure in term CHD neonates using diffusion tensor imaging (DTI) magnetic resonance (MR) acquisition combined with complementary data-driven connectome and seed-based tractography quantitative analyses. Our secondary goal was to delineate associations between mild dysplastic structural brain abnormalities and connectome and seed-base tractography quantitative analyses. These mild dysplastic structural abnormalities have been derived from prior human infant CHD MR studies and neonatal mouse models of CHD that were collectively used to calculate to calculate a brain dysplasia score (BDS) that included assessment

of subcortical structures including the olfactory bulb, the cerebellum and the hippocampus.

Methods: Neonates undergoing cardiac surgery for CHD were prospectively recruited from two large centers. Both pre- and postoperative MR brain scans were obtained. DTI in 42 directions was segmented into 90 regions using a neonatal brain template and three weighted methods. Clinical data collection included 18 patient-specific and 9 preoperative variables associated with preoperative scan and 6 intraoperative (e.g., cardiopulmonary bypass and deep hypothermic circulatory arrest times) and 12 postoperative variables associated with postoperative scan. We compared patient specific and preoperative clinical factors to network topology and tractography alterations on a preoperative neonatal brain MRI, and intra and postoperative clinical factors to network topology alterations on postoperative neonatal brain MRI. A composite BDS was created to score abnormal findings involving the cerebellar hemispheres and vermis, supratentorial extra-axial fluid, olfactory bulbs and sulci, hippocampus, choroid plexus, corpus callosum, and brainstem. The neuroimaging outcomes of this study included (1) connectome metrics: cost (number of connections) and global/nodal efficiency (network integration); (2) seed based tractography methods of fractional anisotropy (FA), radial diffusivity, and axial diffusivity. Statistics consisted of multiple regression with false discovery rate correction (FDR) comparing the clinical risk factors and BDS (including subcortical components) as predictors/exposures and the global connectome metrics, nodal efficiency, and seed based- tractography (FA, radial diffusivity, and axial diffusivity) as neuroimaging outcome measures.

Results: A total of 133 term neonates with complex CHD were prospectively enrolled and 110 had analyzable DTI. Multiple patient-specific factors including d-transposition of the great arteries (d-TGA) physiology and severity of impairment of fetal cerebral substrate delivery (i.e., how much the CHD lesion alters typical fetal circulation such that the highest oxygen and nutrient rich blood from the placenta are not directed toward the fetal brain) were predictive of preoperative reduced cost ($p < 0.0073$) and reduced global/nodal efficiency ($p < 0.03$). Cardiopulmonary bypass time predicted postoperative reduced cost ($p < 0.04$) and multiple postoperative factors [extracorporeal membrane oxygenation (ECMO), seizures and cardiopulmonary resuscitation (CPR)] were predictive of postoperative reduced cost and reduced global/nodal efficiency ($p < 0.05$). Anthropometric measurements (weight, length, and head size) predicted tractography outcomes. Total BDS was not predictive of brain network topology. However, key subcortical components of the BDS score did predict key global and nodal network topology: abnormalities of the cerebellum predicted reduced cost ($p < 0.0417$) and of the hippocampus predicted reduced global efficiency ($p < 0.0126$). All three subcortical structures predicted unique alterations of nodal efficiency ($p < 0.05$), including hippocampal abnormalities predicting widespread reduced nodal efficiency in all lobes of the brain, cerebellar abnormalities predicting increased prefrontal nodal efficiency, and olfactory bulb abnormalities predicting posterior parietal-occipital nodal efficiency.

Conclusion: Patient-specific (d-TGA anatomy, preoperative impairment of fetal cerebral substrate delivery) and postoperative (e.g., seizures, need for ECMO, or CPR) clinical factors were most predictive of diffuse postnatal

microstructural dysmaturation in term CHD neonates. Anthropometric measurements (weight, length, and head size) predicted tractography outcomes. In contrast, subcortical components (cerebellum, hippocampus, olfactory) of a structurally based BDS (derived from CHD mouse mutants), predicted more localized and regional postnatal microstructural differences. Collectively, these findings suggest that brain DTI connectome and seed-based tractography are complementary techniques which may facilitate deciphering the mechanistic relative contribution of clinical and genetic risk factors related to poor neurodevelopmental outcomes in CHD.

KEYWORDS

congenital heart disease, diffusion tensor imaging, connectome analysis, seed-based tractography, subcortical brain dysmaturation, magnetic resonance imaging, clinical factors

Background

Congenital heart disease (CHD) is the most prevalent birth defect, accounting for nearly one third of all major congenital anomalies (van der Linde et al., 2011). While surgical techniques have vastly improved survival in the past few decades, with most children with complex CHD now living to adulthood, neurodevelopmental impairments have emerged as one of the most common long-term sequelae of CHD survivors, including the realms of cognition, memory, social interaction, communication and language, attention, and executive function (Bellinger et al., 2009; Marino et al., 2012; Mussatto et al., 2014; Cassidy et al., 2015; Gaynor et al., 2015; Pike et al., 2016). Neonates with CHD display findings of brain dysmaturation as well as vulnerability to brain injury, assessed by magnetic resonance imaging (MRI) (Miller et al., 2007; Licht et al., 2009; Panigrahy et al., 2016). The cause of the widespread neurodevelopmental delays seen in CHD children are likely multifactorial, stemming from prenatal, genetic, and postnatal factors. Abnormalities of brain growth and microstructure in CHD have fetal origins (Limperopoulos et al., 2010; Rajagopalan et al., 2018), and may result from impaired oxygen and substrate delivery to the developing brain based on alterations of fetoplacental circulation related to the CHD (Sun et al., 2015). Neurodevelopmental impairments in the CHD population correlate more with brain immaturity rather than injury (Beca et al., 2013; Rollins et al., 2014). Therefore, the traditional "lesion-based approach" to specific brain injuries driving the widespread cognitive dysfunction seen in CHD seems to fall short.

A brain connectome approach has emerged in recent years as a new paradigm to understand the complexity of functional neural networks and how they influence human behavior. This type of analysis has also been used to evaluate adolescents with d-transposition of the great arteries (d-TGA), in which network topology differences were found to mediate multiple domains of adverse neurocognitive outcomes (Panigrahy et al., 2015a). We have recently described a quantitative data-driven network topology (connectome) graph analysis to compare neonates with CHD to normal controls, and demonstrated the early presence of brain reorganization in CHD neonates (Schmithorst et al., 2018; Bhroin et al., 2020; Feldmann et al., 2020; Ji et al., 2020; Ramirez et al., 2022). Other recent studies have described aberrant diffusion tensor - based connectome in CHD neonates and infants in both preoperative and postoperative periods, finding distinct patterns of structural network topology alterations (Schmithorst et al., 2018; Bhroin et al., 2020; Feldmann et al., 2020; Ji et al., 2020; Ramirez et al., 2022). There is also recent literature to suggest that genetic factors might impact the structural connectome in CHD (Ji et al., 2020; Patt et al., 2022). While the connectome technique is a robust analytical tool, there are other hypothesis-driven approaches that have been applied to quantifying diffusion tensor-based data in CHD which includes seed-based tractography that facilitates quantitative metrics of cortical association tracts. Of note, pre-clinical surgical based animal models of CHD show that the postnatal subventricular zone is vulnerable to neurotoxicity from volatile anesthetic agents (Brambrink et al., 2010, 2012) and hypoxia, resulting in diffuse white matter injury (WMI) of white matter tracts, including the superior longitudinal fasciculus (SLF), inferior longitudinal fasciculus (ILF), and fronto-occipital fasciculus (FOF), assessed by diffusion tensor imaging (DTI) tractography techniques. Diffuse WMI also correlates with cortical long-range connectivity dysmaturation. In contrast, focal WMI, acquired in CHD infants on serial preoperative/immediate postoperative brain MRIs (usually performed on 7–14 postnatal days and are detected with 3D-T1 based MR imaging), involve punctate periventricular fronto-parietal white matter lesions involving long-range connectivity crossing-fibers (Beca et al., 2009, 2013;

Petit et al., 2009; Block et al., 2010; McQuillen and Miller, 2010; Gaynor et al., 2016; Peyvandi et al., 2019), also caused by hypoxia/inflammation.

A recent published study comparing critical/serious CHD prior to surgery and 116 matched healthy controls as part of the developing Human Connectome Project imaged with high angular resolution diffusion MRI (HARDI) and processed with multi-tissue constrained spherical deconvolution, anatomically constrained probabilistic tractography (ACT) and spherical-deconvolution informed filtering of tractograms (SIFT2) was used to construct weighted structural networks, and identified one subnetwork with reduced structural connectivity in CHD infants involving basal ganglia, amygdala, hippocampus, and the cerebellar vermis (Bhroin et al., 2020; Feldmann et al., 2020). We have recently described a similar pattern of structural subcortical dysmaturation both in human infants with CHD and genetically relevant ciliary motion dysfunction, and also in relation to preclinical models of CHD including hypoplastic left heart syndrome (HLHS) (Panigrahy et al., 2014, 2015b, 2016; Votava-Smith et al., 2017; Ceschin et al., 2018; Gabriel et al., 2018; Subramanian et al., 2019). This pattern of subcortical dysmaturation was predominantly seen in the olfactory bulb (dysmorphometry of left and right olfactory bulbs and sulci), the cerebellum (hypoplasia and/or dysplasia in cerebellar hemispheres and vermis) and the hippocampus (hypoplasia or malrotation) are components of a larger spectrum of structural abnormalities including extra-axial CSF fluid increases, corpus callosum abnormalities, choroid plexus abnormalities and brainstem dysplasia that we have recently observed in both human CHD patients and preclinical CHD mouse models (Panigrahy et al., 2014, 2015b, 2016; Votava-Smith et al., 2017; Ceschin et al., 2018; Gabriel et al., 2018; Subramanian et al., 2019). As such, we have derived a composite Brain Dysplasia Score (BDS) which was previously created with one point given for each positive finding in any of thirteen parameters including: hypoplasia in cerebellar hemispheres and vermis; dysplasia in cerebellar hemispheres and vermis; supratentorial extra-axial fluid; dysmorphometry of left and right olfactory bulbs and sulci; abnormalities in hippocampus and choroid plexus; malformation of corpus callosum; and brainstem dysplasia (Panigrahy et al., 2014, 2015b, 2016; Votava-Smith et al., 2017; Ceschin et al., 2018; Gabriel et al., 2018; Subramanian et al., 2019). There is little known about the relationship of these milder structural dysplastic abnormalities (relative to more gross brain malformation) to white matter connectivity.

Here, we sought to use our quantitative data-driven approach to primarily correlate clinical risk factors in CHD neonates to abnormalities of white matter connectivity using two complementary techniques: structural network topology (connectome) and seed based tractography. We first compared patient specific and preoperative clinical factors to network topology and tractography alterations on a preoperative neonatal brain MRI, and intra and postoperative clinical factors to network topology alterations on postoperative neonatal brain MRI. Secondarily, we correlated our previously derived total BDS score (and its subcortical components including olfactory, cerebellar, and hippocampal dysmaturation) with similar methodologies as our primary aim including structural network topology (connectome) and seed-based tractography measurements. As such, we tested the hypothesis that clinical risk factors would predict distinct patterns of microstructural brain dysmaturation compared to those patterns predicted by the total BDS score/subcortical components.

Materials and methods

Patients with critical CHD were recruited both pre- and postnatally for consecutive enrollment in this prospective, observational neuroimaging study at two large children's hospitals [Children's Hospital Los Angeles (CHLA) and Children's Hospital of Pittsburgh (CHP)]. Critical CHD was defined as defects expected to require corrective or palliative cardiac surgery within the first month of life. Patients that had a known major chromosomal abnormality, were premature (=36 weeks of age), died prior to MRI or had no MRI performed, or did not require neonatal cardiac surgery were excluded. The data collection sources included the electronic medical record. Clinical data collection included 18 patient-specific and 9 preoperative variables associated with preoperative scan and 6 intra-operative (e.g., cardiopulmonary bypass, deep hypothermic circulatory arrest times) and 12 postoperative variables associated with postoperative scan that were selected based on prior literature on neurodevelopmental research in CHD as well as criteria included in the RACHS-1 scoring system; these are listed in **Table 1** (Jenkins et al., 2002; Limperopoulos et al., 2002; Mahle et al., 2002; Beca et al., 2013). CHD lesions were classified in several ways (not mutually exclusive) including cyanotic vs. acyanotic defects, presence of aortic arch obstruction, single vs. double ventricle defects, presence of d-TGA, presence of a conotruncal defect (which includes d-TGA as well as other lesions with altered conal septal/outflow tract relationships such as tetralogy of Fallot, double outlet right ventricle, truncus arteriosus, etc.), and presence of heterotaxy. CHD lesions were additionally classified by impairment of fetal substrate delivery, i.e., how a CHD lesion impacts the fetal circulation which aims to direct the highest oxygen and nutrient rich blood from the placenta toward the fetal brain. This severity score included normal (isolated septal and arch defects), altered (which includes single ventricles, tetralogy of Fallot, and other lesions which have fetal intracardiac mixing), and severely altered (which includes d-TGA and its variants which results in direction of the least oxygen and nutrient rich blood to the fetal brain) (Sun et al., 2015). Parental consent was obtained, and the

TABLE 1 Demographic characteristics of final 110 subjects with analyzable diffusion tensor imaging (DTI) in study group.

	Factor	Total or average (% or SD)
Innate factors and cardiac lesions	Male sex	80 (73%)
	Gestational age at birth, weeks	38.9 (0.9)
	Birth weight, gm	3,216 (517)
	Birth weight percentile	39 (30)
	Head circumference, cm	34.3 (2.8)
	Head circumference percentile	41 (31)
	Birth length, cm	49.0 (5.9)
	Birth length percentile	36.0 (31.4)
	APGAR at 1 and 5 min	7.5 (2), 8.4 (1.2)
	22q11 microdeletion	10 (9%)
	Cyanotic heart disease	99 (90%)
	Arch obstruction	45 (41%)
	Single ventricle	49 (45%)
	With arch obstruction	39 (35%)
	d-TGA	38 (35%)
	Conotruncal defect	70 (64%)
	Heterotaxy	8 (7%)
	Severity of altered fetal cerebral substrate delivery	
	Normal	11 (10%)
	Altered	69 (63%)
	Severely altered (d-TGA physiology)	30 (27%)
Preoperative factors	Preop arterial blood gas Ph	7.44 (0.066)
	Preop arterial blood gas pO_2	50.5 (31.8)
	Preop arterial lactate (mmol/L)	1.7 (0.7)
	Preop renal dysfunction	0
	Preop hepatic dysfunction	1 (1%)
	Preop inotrope use	44 (40%)
	Age at surgery (days)	6.9 (5)
	Age at surgery $\leq$ 7 days	81 (67)
	Post-conceptional age at surgery (weeks)	40 (1)
Intraoperative factors	Cardiopulmonary bypass used	97 (88%)
	Cardiopulmonary bypass time (minutes)	86 (56)
	Aortic cross-clamp used	65 (59%)
	Aortic cross-clamp time (minutes)	41 (39)
	Circulatory arrest/DHCA used	91 (80)
	Circulatory arrest/DHCA time (minutes)	17 (20)
Postoperative factors	ECMO during 1st hospitalization	22 (20%)
	Time on ECMO (days)	5 (2.5)
	Delayed sternal closure	86 (78%)
	Unplanned intervention(s), 1st hospitalization (patients)	66 (60%)
	Required CPR, 1st hospitalization	10 (9%)
	Had seizures during 1st hospitalization	15 (14%)
	ICU length of stay, 1st hospitalization (days)	30 (32)
	Hospital length of stay (days)	41 (36)
	Expired during 1st hospitalization	6 (6%)
	Discharged on antiepileptics	12 (11%)
	Discharged with gastrostomy-tube	26 (24%)
	Discharged with tracheostomy and/or ventilator	7 (6%)

d-TGA, d-transposition of the great arteries; CPR, cardiopulmonary resuscitation; DHCA, deep hypothermic circulatory arrest; ECMO, extra corporeal membrane oxygenation; ICU, intensive care unit.

institutional review boards of both institutions approved the study.

Neonatal brain magnetic resonance imaging protocol

Preoperative brain imaging was conducted when the cardiothoracic intensive care unit (CTICU)/cardiology team determined the patient was stable for transport to the MRI scanner. A postoperative scan was performed when the patient was younger than 3 months of postnatal age either as an inpatient or outpatient. Most of our scans were research indicated and, as such, no additional sedation/anesthesia was given for purpose of the scan. Most of the preoperative scans were performed on non-intubated, non-sedated patients; however, if a patient was intubated and sedated for clinical reasons at the time of the scan, their clinically indicated sedation continued under care of the primary CTICU team. The postoperative scans were performed after the infant had stepped down from the CTICU and were done as "feed and bundle" scans without sedation.

MR data were acquired on a Philips 3T Achieva MR System (Ver. 3.2.1.1; Philips Healthcare, Foster City, California) with the use of either a neonatal SENSE coil or a standard 8-channel SENSE head coil. To minimize movement during imaging, infants were secured in Med-Vac Immobilization Bag (CFI Medical, Fenton, Michigan) with multiple levels of ear protection, including ear plugs, MiniMuffs (Natus Medical Inc., Pleasanton, California), and standard headphones. Conventional T1-weighted, T2-weighted, and diffusion-weighted images were acquired and reviewed by 2 pediatric neuroradiologists for evidence of punctate white matter lesion, acute focal infarction, and hemorrhage as described previously (Brambrink et al., 2012).

Magnetic resonance acquisition

At both sites, a 3T scanner was used for all studies; scans were acquired on a Phillips Achieva at CHLA and Siemens Skyra. Newborns were positioned in the coil to minimize head tilting. Newborns were fitted with earplugs (Quiet Earplugs; Sperian Hearing Protection, San Diego, CA) and neonatal earmuffs (MiniMuffs; Natus, San Carlos, CA). An MR-compatible, vital signs monitoring system (Veris, MEDRAD, Inc., Indianola, PA) was used to monitor neonatal vital signs. All scans were performed using a multi-channel head coil. Volumetric 3D T1 and T2 imaging and a blood sensitive sequence (GRE or SWI) were performed to evaluate for punctate WMI and to evaluate for other major forms of brain injury (infarcts and hemorrhage) and congenital brain malformations. 2D EPI-DTI with 42 directions, TE/TR = 92 ms/12,600 ms, b = 1,000 s/mm (Marino et al., 2012), 2 mm slice thickness were acquired; in-plane resolution was close to 2 mm but varied slightly for some participants.

Data analysis

Analyses were performed using in-house routines in IDL (ENVI, Boulder, CO); and routines in SPM8 (Wellcome Department of Cognitive Neurology, London, UK), FSL (fMRIB, Oxford, UK), and Brain Connectivity Toolbox (BCT; Indiana University, Bloomington, IN). A schematic of the graph analysis pipeline is presented in Figure 1.

Pre-processing and generation of fractional anisotropy-independent developing white matter segmentation

Data that was automatically upsampled (factor = 2) by the scanner reconstruction software (in GE scanners) was corrected by rebinning the data in the in-plane directions by a factor of 2. Frames with slice drop-out artifacts were removed using an automated routine in IDL. Motion and eddy current artifacts were corrected using routines in FSL, and maps of FA, axial diffusivity, radial diffusivity, and direction of principal eigenvector computed. The B_0 maps were normalized to the neonatal anatomical template (Shi et al., 2011) using routines

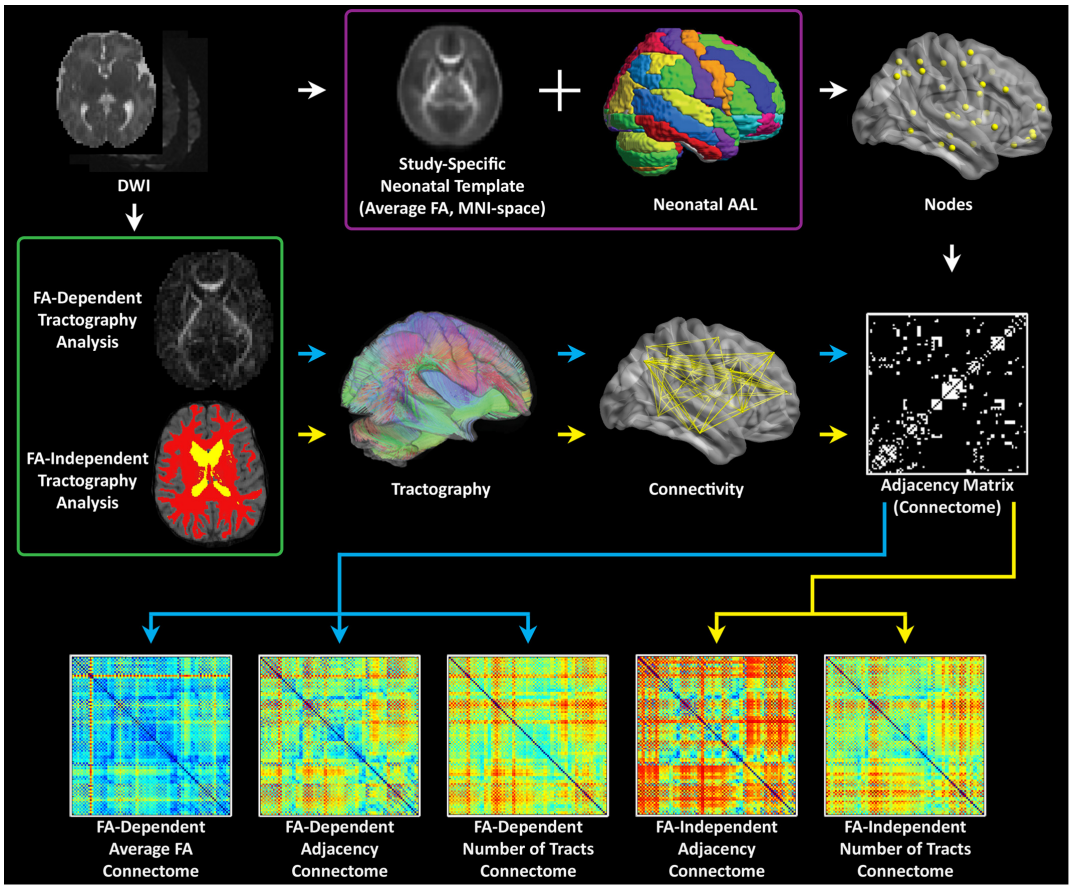

FIGURE 1
Computational pipeline for processing neonatal diffusion tensor imaging data: first a white matter template is generated in MNI space. Second, parcellation is performed using a neonatal AAL template; third, different weighted matrixes are generated to facilitate network topology measures at the global and the nodal levels.

in SPM8 and these transformations were used to applied to the FA maps (resampled to 2 mm isotropic resolution). An average study specific FA template was then constructed in template space. The FA template was back-transformed into native space for each participant (using routines in SPM8 and the individual FA map as the reference) and the neonatal cortical parcellation atlas (Shi et al., 2011) was also transformed into native space using that transformation.

In the population studied, FA maps cannot be directly used in deterministic tractography due to within participant variations in FA values associated with post-conceptional age, CHD status, regional differences in myelination status, and other factors. To account for FA variations, WM probabilistic maps were computed from segmentations performed using the FA map, the neonatal WM, gray matter, and CSF templates (Shi et al., 2011) using spm_preproc8 routine in SPM8. These WM probability map computed are not dependent on the absolute values of FA in white matter and were used for the deterministic tractography.

Tractography and construction of unweighted and weighted graph matrices

Deterministic tractography in native space was carried out using routines in IDL. Streamlines were constructed starting from each voxel with WM probability > 0.78 and were continued in both directions with stopping criteria of turning angle > 45 degrees or WM probability < 0.78 (using the white matter template). This threshold was determined via visual inspection to optimize the tradeoff between ensuring all streamlines remain in white matter and ensuring streamlines do not end prematurely due to a misclassified voxel. Secondary analyses showed that variation of this parameter did not appreciably affect cost and global efficiency. Using the parcellation atlas (transformed into native space) to identify the cortical regions at both ends of each streamline we generated three 90×90 matrices using two different weighted matrices and one unweighted matrix). One of the two weighted approaches was termed "average FA" (each non-diagonal element contains the FA averaged over all streamlines connecting two regions), and the other weighted approach was termed "number of tracts" (each non-diagonal element contains the total number of streamlines connecting the two regions). The unweighted approach was termed "adjacency" (each non-diagonal element is either 0 or 1, depending on whether at least one tract connects the corresponding cortical regions). See **Figure 2** for a schematic of these 3 weighted methods. We interpreted these difference in weighting as follows: "microstructural" changes reflect more in mean FA weighting while "macrostructural" change reflects more the other weighted approach "number of tracts" and the unweighted approach "adjacency." Of note, the "number of tracts" approach likely also weights toward total white matter volume. Our previous publication using this pipeline provides more information about the value of these different weighting within respect to the microstructural architecture (Schmithorst et al., 2018). The sensitivity of the various graph analyses (adjacency/# tracts/average FA) lies on a continuum with the average FA connectome being more sensitive to microstructural change, as the graph weights are directly related to a DTI microstructural parameter (FA). Adjacency, on the other hand, is the least sensitive to microstructural change as it needs only one streamline to connect between areas, irrespective of the FA values. In our previously published study in which the neonates with CHD that are included in this manuscript were initially compared to healthy controls we found that the highest degrees of statistical significance for cost/global efficiency were found in the mean FA and # tracts connectomes, consistent with the changes in DTI microstructure and with our secondary analyses relating DTI metrics to network topology parameters. Macrostructural changes may also be distinguished from microstructural changes seen here via controlling for cost in the analysis. Higher significance was seen in the # tracts and average FA connectomes for the small-worldness metric controlling for cost, which we interpret as hierarchical fiber reorganization involving changes in relative strength of connections (which adjacency is unable to measure) rather than creation and destruction of connections (Schmithorst et al., 2018).

Graph analysis

Unweighted (for adjacency matrices) and weighted (for number of tracts and average FA matrices) metrics were computed using routines in the C++ version of BCT and in-house routines in IDL. Global metrics computed included cost (number of connections), global efficiency, transitivity, modularity, and small-worldness. Nodal metrics (which have a value for each of the 90 nodes) (see **Supplementary Table 1** for anatomic labels) included nodal efficiency (adjacency matrices only). As the modularity and small-world calculations depend on a stepwise optimization from a random starting point, 100 iterations were used and the results were averaged (small-world) or maximum value was used (modularity). Additionally, we examined our nodal level results in context of the developing brain network topology in the last trimester and early infancy (Gao et al., 2011, 2013, 2014; Menon, 2011; Thomason et al., 2014, 2015; Alcauter et al., 2015).

Graph analysis

Graph metrics (global efficiency, modularity, transitivity, and small-worldness) were computed via the C++ modules available from the Brain Connectivity Toolbox (BCT; Indiana University). A brief description for each metric is given below (Rubinov and Sporns, 2010; Panigrahy et al., 2015a). *Global efficiency*is a measure of network integration

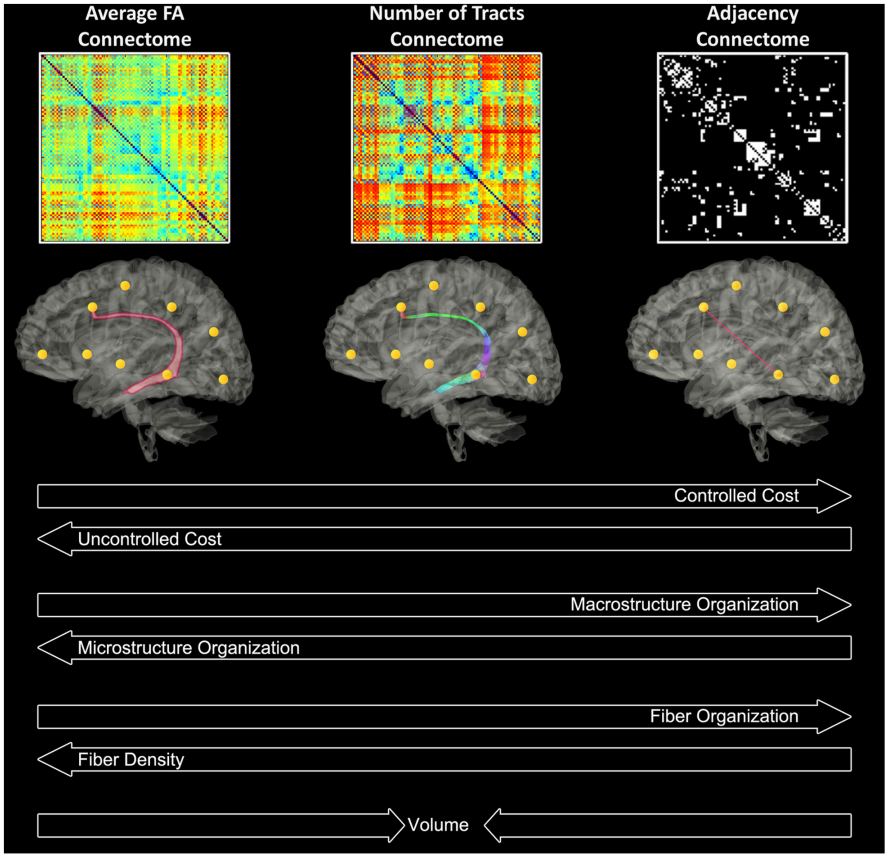

FIGURE 2
Theoretical interpretations of the different weighted matrices in relation to cost, micro/macro- organization, fiber density/organization, and volume.

(Bullmore and Sporns, 2012; Panigrahy et al., 2015a). The *path length* between two nodes is defined as the shortest distance between them. Global efficiency is defined as the mean of the reciprocal path length over all pairs of nodes (e.g., if every node was directly connected to every other node, the path lengths would all be one, and global efficiency [mean(1/path length) would be 1]. In a highly integrated network, the typical number of steps it takes to get from one node to another is low. *Modularity* is a measure of network segregation (Meunier et al., 2010; Uehara et al., 2012). Modularity is defined as the fraction of the edges that fall within given modules minus the expected such fraction if the edges were distributed at random. In a more modular—or segregated—network, nodes within a given module are more highly interconnected, and less connected to nodes outside the module. Modularity was calculated using the Louvain algorithm (Blondel et al., 2008). *Transitivity*, another measure of segregation at the local or nodal level, is calculated as the proportion of triangles (i.e., where A-B, A-C, and B-C are all directly connected) relative to incomplete triangles (i.e., where A-B and A-C are directly connected, but B-C are not) and quantifies the frequency of localized clusters within the overall network. *Small-worldness* represents the balance of integration and segregation (Bassett and Bullmore, 2006; Telesford et al., 2011). Small-worldness is calculated as the ratio of transitivity to characteristic path length, divided by the ratio of transitivity to characteristic path length for a random graph with the same degree distribution; and quantifies the extent to which the network balances overall efficiency and localized clustering (Humphries and Gurney, 2008). In a small-world network, there is only a slight increase in characteristic path length as compared to a random network (and hence only slightly less integration), but a large increase in transitivity (and hence much greater segregation).

Brain dysplasia score methods

The BDS was based on previous correlative analysis of brain phenotype from CHD mouse mutant and human infant MRI including a spectrum of subtle brain dysplasia (hypoplasia or aplasia) including increased extra-axial CSF and abnormalities of the olfactory bulbs, cerebellum, hippocampus and corpus callosum and a composite BDS, as previously described

(Panigrahy et al., 2014, 2015b, 2016; Votava-Smith et al., 2017; Ceschin et al., 2018; Gabriel et al., 2018; Subramanian et al., 2019). Basic pediatric neuroradiological definitions and criteria were used from Barkovich and Raybaud (2012) for overall assessment of brain abnormalities. For olfactory abnormalities, we assessed for aplasia/hypoplasia of the olfactory blub within the olfactory groove and aplasia/hypoplasia of the olfactory sulcus on high resolution coronal T2 images (Blustajn et al., 2008). Hippocampal abnormalities (hypoplasia/malrotation/inversion) were identified as previously described on coronal T1 and T2 images (Sato et al., 2001; Montenegro et al., 2006; Righini et al., 2006; Bajic et al., 2008, 2012). Brainstem dysplasia including either hyperplasia/hypoplasia and asymmetry/disproportion of the any part of the brainstem (medulla, pons, midbrain) using sagittal and axial T1/T2 imaging based on prior studies by Barkovich et al. (2007). Corpus callosum dysplasia included focal hypogenesis, asymmetry/disproportion of different portions of the corpus callosal (genu, body, splenium, rostrum), or overall abnormal "arching" or morphology best identified on Sagittal T1/T2 imaging as previously described by Hetts et al. (2006). A composite was created with one point given for each positive finding in any of thirteen parameters including: hypoplasia in cerebellar hemispheres and vermis; dysplasia in cerebellar hemispheres and vermis; supratentorial extra-axial fluid; dysmorphometry of left and right olfactory bulbs and sulci; abnormalities in hippocampus and choroid plexus; malformation of corpus callosum; and brainstem dysplasia. Brain injury was assessed using the method described by Licht et al. (2009).

Seed-based tractography analysis

Iterative mask set refinement

To measure the accuracy of our iteratively developed semi-automated method, we first generated a "gold-standard" set by manually delineating the mask sets for the following tracts: genu, body, and splenium of the corpus callosum; anterior and posterior segments of the superior longitudinal fasciculus (SLFA and SLFP, respectively); ILF, FOF, and cortical spinal tract (CST). Manual mask set delineation was performed following the guidelines published by Fernandez-Miranda et al. (2012). The ROIs and ROAs comprising each mask set, and visualization of each manual mask set has recently been published (Meyers et al., 2022). All subjects from the CHP and CHLA cohorts were manually delineated.

The automated tractography was performed by propagating the above mask sets from a cohort-specific template onto each subject's native space diffusion images. We generated cohort-specific templates using a modified version of the FSL TBSS pipeline (Smith et al., 2006). First we non-linearly co-registering all subject FA maps into a standard space, selecting the most representative subject and setting it as the new standard space for subsequent registrations. All subjects were then non-linearly transformed into this new space, generating a new cohort-specific atlas. This process is iterated until no measurable improvement in registration is perceived. We then duplicating the above mask sets, following the identical anatomical guidelines, onto each the generated cohort template. The masks were then propagated into each subject's native diffusion space using the previously calculated non-linear transforms. Each tract was delineated in DSI studio using a deterministic tracking algorithm an FA threshold of 0.1 and angular threshold of 45 degrees with no manual pruning. We used four increasingly granular metrics to measure the accuracy of the semi-automated approach. At each successive mask-refinement iteration, more emphasis is placed on the more granular measure. First, as a qualitative measure of cohort-level accuracy, we projected both the manually delineated tracts and automated tracts onto the cohort-specific atlas, displaying the spatial distribution of each tract and level of agreement. This allows for the detection of obvious points of failure in the pipeline, as well as a general overview of the variance in anatomical tract location. Further refinement used DICE coefficients to compare automated vs. manual tractography, and finally, along-tract measures of dispersion within cohort was the final quality check to validate the automated approach. All tractography values used in this hypothesis-driven analysis used the output of the automated pipeline.

Statistical analysis

Multivariable regression with false discovery rate (FDR) correction was used, with covariates including postmenstrual age at time of scan. The FDR is one way of conceptualizing the rate of type I errors in null hypothesis testing when conducting multiple comparisons. We defined our "exposure" as the patient and clinical factors and the "neuroimaging outcome measure" as cost (number of connections) and global and nodal efficiency (network integration) as the outcome, in each of the 3 differentially weighted connectome methods (average FA, number of tracts, and adjacency connectomes). The patient and clinical risk factors were then additionally compared against seed-based tractography (including FA, radial diffusivity, and axial diffusivity). Patient specific, cardiac lesion subtype, and preoperative variables were compared only with the preoperative MRI scans. The intraoperative and postoperative exposures were compared only with the postoperative MRI scans. The BDS, its individual components of cerebellar, olfactory and hippocampal abnormalities, as well as presence of brain injury (punctate WMI and stroke) were evaluated against the three connectome methods on both pre and postoperative MRI timepoints. The BDS and its individual components of cerebellar, olfactory, and hippocampal abnormalities were

evaluated against tractography by FA, radial and axial diffusivity at preoperative and postoperative time points as well as on all scans combined.

We have controlled for effect of scanner by not only including scanner as a covariate but modeling different between-subject variances dependent on scanner and shown that these variances are in fact similar in an our prior publication on the dataset (Schmithorst et al., 2018). We have also demonstrated from human phantom data a high degree of reliability for graph metrics (nodal/global efficiency) and DTI metrics (FA/AD) (Schmithorst et al., 2018).

Outcomes

The primary neuroimaging outcomes for the study were cost and global and nodal efficiency (connectome) and fractional anisotropy (FA) (seed-based tractography). The secondary outcomes were (connectome) modularity and small-worldness (connectome) and radial and axial diffusivity (seed-based tractography). These outcomes were based on our prior publication which compared the network topology of these CHD patients with healthy controls (Schmithorst et al., 2018).

Results

Two hundred ninety-one subjects were enrolled from June 2009 to October 2016. Of these subjects, 158 met exclusion criteria including 57 with no MRI done, 38 due to prematurity, 38 passed the age threshold, 11 expired preoperatively, 10 had no neonatal surgery and 4 had a postnatal major genetic diagnosis. Of the 133 term CHD infants with brain MRI meeting inclusion criteria, 110 subjects had sufficient imaging quality for DTI analysis and comprised the study group, including 57 from CHLA and 53 from CHP. This group included 67 preoperative MRI scans and 77 postoperative MRI scans (Figure 3). Those excluded for insufficient imaging quality mirrored the demographics of the study group, with 12 from CHLA and 11 from CHP, and consisted of 10 pre- and 13 postoperative scans.

Table 1 lists patient demographic data and clinical factors. The majority of the CHD neonates were male (73%), had cyanotic forms of CHD (90%) including 48% with single ventricle CHD and 35% with d-TGA, and had surgery involving cardiopulmonary bypass (88%), with an average cardiopulmonary bypass time of 86 ± 56 min. Postoperatively, 20% were on extracorporeal membrane oxygenation (ECMO), 14% had seizures, and 9% required cardiopulmonary resuscitation (CPR) during the first hospitalization. The mortality rate for the study population prior to discharge was 6%.

Clinical risk factors vs. connectome

Patient and prenatal factors-correlation with connectome measures

We analyzed the patient-specific and CHD subtype factors against the 3 differentially weighted connectome analyses on preoperative scans and found several CHD subtypes were related to alterations in global network topology (Tables 2A–C). Aortic arch obstruction (in both single and 2-ventricle patients combined) predicted altered modularity by all 3 connectome methods (p = −0.0106 for adjacency, −0.0098 for number of tracts, and −0.0183 for average FA connectome), as well as small-worldness in the number of tracts (p = −0.0141) and average FA (p = −0.0039) connectomes. D-TGA predicted altered modularity (p = 0.0009) and reduced cost (p = −0.0442) in the adjacency connectome, as well as

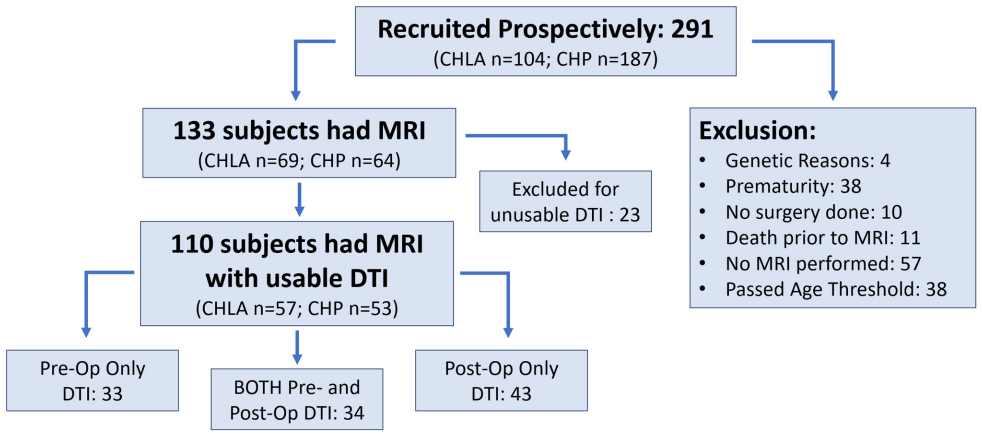

FIGURE 3
Study flow chart and recruitment.

TABLE 2(A) Correlation between clinical risk factors and global connectome metrics: Adjacency matrix (FDR-corrected).

		Cost	Global efficiency	Transitivity	Modularity	Small world	Assortativity
Innate factors and cardiac lesions	Gestational age at birth	0.3393	0.4742	−0.9632	0.7849	−0.5117	−0.7608
	Birth weight	−0.3771	−0.5902	−0.7142	0.8003	0.8375	−0.9972
	Birth weight percentile	−0.0567	−0.1512	−0.5948	0.2046	0.1767	0.2328
	Head circumference	0.8768	−0.7604	0.9361	−0.9694	0.956	−0.5454
	Head circumference percentile	−0.2892	**−0.0439**	0.8222	0.3757	0.2501	0.7831
	Birth length	0.8093	0.9694	−0.4568	−0.5394	−0.3504	−0.8874
	Birth length percentile	1	−0.4935	−0.4365	−0.3042	−0.168	0.0565
	APGAR, 1 min	−0.533	0.5919	−0.2054	−0.4152	−0.8175	−0.334
	APGAR, 5 min	−0.9119	0.4618	0.4893	−0.833	0.5417	−0.8021
	22q11 microdeletion	−0.5514	−0.2186	−0.6524	0.9916	−0.7051	0.9463
	Single ventricle	0.1528	−0.8881	0.6944	−0.071	−0.232	0.8596
	Arch obstruction	0.572	−0.8024	−0.503	**−0.0106**	**−0.0141**	0.2608
	Single ventricle with arch obstruction	0.4095	−0.5173	0.6432	−0.2468	−0.3673	0.1547
	d-TGA	**−0.0442**	−0.3057	−0.4542	0.0517	0.0849	0.8169
	Conotruncal defect	−0.3726	−0.5388	0.7487	**0.009**	0.1013	−0.8047
	Altered fetal cerebral substrate delivery	−0.4349	−0.2581	0.784	0.2262	0.3117	−0.4175
	Altered fetal substrate delivery, severity score	−0.0559	−0.2424	−0.4373	0.0731	0.3005	0.751
	Heterotaxy	0.3437	0.4249	0.577	−0.9005	−0.7657	−0.7109
Preoperative factors	Preoperative arterial blood gas pH	**−0.0444**	−0.0532	−0.128	0.2902	0.6587	0.8897
	Preoperative arterial blood gas pO_2	0.7139	0.1438	0.8756	−0.6411	0.6388	−0.2578
	Preoperative arterial lactate	0.609	0.6729	0.4887	0.9987	0.4399	−0.2661
	Preoperative renal dysfunction	0.5678	−0.6186	−0.8305	0.989	−0.1747	0.1117
	Preoperative hepatic dysfunction	0.1413	0.2046	0.1575	0.8789	0.8958	0.8389
	Preoperative inotrope use	−0.6446	−0.1852	−0.6888	−0.967	−0.0832	−0.4767
	Age at surgery, days	0.5973	0.4562	0.3746	0.1595	0.6875	−0.4308
	Age at surgery $\leq$ 7 days	−0.7191	−0.5292	0.8511	−0.3441	0.5453	0.9782
	Post-conceptional age at surgery, weeks	0.473	0.3836	0.6587	0.2224	0.9365	−0.5161
Intraoperative factors	Cardiopulmonary bypass used	−0.6136	−0.737	−0.66	−0.864	0.7605	−0.1917
	Cardiopulmonary bypass time	−0.4517	−0.5571	−0.1952	0.4127	−0.593	−0.5451
	Aortic cross-clamp used	−0.8278	−0.7459	−0.4735	−0.16	−0.8284	−0.2995
	Aortic cross-clamp time	−0.8423	−0.9097	−0.4466	0.8169	−0.3826	−0.524
	Circulatory arrest/DHCA used	−0.7393	0.671	0.4861	−0.8968	0.165	**−0.0051**
	Circulatory arrest/DHCA time	−0.418	−0.861	0.8306	0.8215	**0.031**	−0.1187
Postoperative factors	ECMO during 1st hospitalization	−0.9575	−0.6103	−0.7278	−0.2475	−0.088	−0.827
	Time on ECMO (days)	−0.4635	−0.3165	−0.4087	−0.4905	−0.2352	−0.7835
	Delayed sternal closure	−0.9673	0.4216	0.8002	0.6009	0.4257	−0.4587
	Had unplanned intervention(s), 1st hospitalization	−0.8938	−0.7	−0.3149	−0.7572	−0.1424	−0.8704
	ICU length of stay, 1st hospitalization	−0.7763	−0.6725	−0.4364	−0.9797	−0.6921	0.9291
	Hospital length of stay	−0.5218	−0.6434	−0.246	0.8926	−0.8239	−0.779
	Expired during 1st hospitalization	−0.5742	−0.3424	−0.5219	0.9913	−0.4949	0.9834
	Required CPR during 1st hospitalization	0.6693	−0.9399	−0.4697	−0.1615	−0.2419	0.7517
	Had seizures during 1st hospitalization	**−0.0388**	−0.0714	−0.0704	0.1237	0.3648	−0.7843
	Discharged on antiepileptics	0.8048	0.4454	−0.6969	0.9339	0.4292	−0.7385
	Discharged with gastrostomy tube	0.9248	−0.9773	−0.1932	−0.3559	−0.1179	0.1806
	Discharged with tracheostomy and/or ventilator	−0.215	−0.6838	−0.4707	0.6231	0.1736	−0.833

Bold values indicate reference FDR-corrected values.

TABLE 2(B) Correlation between clinical risk factors and global connectome metrics: Number tracts matrix (FDR-corrected).

		Cost	Global efficiency	Transitivity	Modularity	Small world	Assortativity
Innate and cardiac lesions	Gestational age at birth	0.2918	0.1846	0.524	−0.5181	0.4814	−0.7608
	Birth weight	0.9739	0.6472	0.6176	−0.2367	0.0759	−0.9972
	Birth weight percentile	−0.299	−0.3999	−0.8739	−0.8968	0.0725	0.2328
	Head circumference	0.2385	0.2246	0.4581	−0.5984	0.8289	−0.5454
	Head circumference percentile	0.7785	1	0.429	−0.7041	0.1823	0.7831
	Birth length	0.3057	0.2915	−0.8689	−0.5285	−0.2581	−0.8874
	Birth length percentile	0.1748	0.2791	0.7156	−0.2275	−0.12	0.0565
	APGAR, 1 min	−0.9608	0.4852	−0.6635	−0.2196	0.4353	−0.334
	APGAR, 5 min	−0.7745	0.7962	0.9329	−0.5814	0.6284	−0.8021
	22q11 microdeletion	0.3997	0.4856	0.7645	−0.5744	0.9477	0.9463
	Single ventricle	0.0825	0.1872	0.1694	−0.2159	−0.1002	0.8596
	Arch obstruction	0.575	0.6645	0.8957	**−0.0098**	**−0.0361**	0.2608
	Single ventricle with arch obstruction	0.1453	0.3584	0.1226	−0.4095	−0.1829	0.1547
	d-TGA	**−0.0043**	**−0.0058**	**−0.0203**	**0.0435**	0.101	0.8169
	Conotruncal defect	−0.5529	−0.4627	−0.7289	**0.0111**	0.2363	−0.8047
	Altered fetal cerebral substrate delivery	−0.458	−0.2826	−0.8858	0.1006	0.3929	−0.4175
	Altered cerebral substrate delivery severity score	**−0.0073**	**−0.0054**	**−0.046**	0.0585	0.3361	0.751
	Heterotaxy	0.1544	0.1302	0.3229	−0.6267	−0.3342	−0.7109
Preoperative factors	Preoperative arterial blood gas pH	−0.1056	−0.0875	−0.0558	0.5133	0.7699	0.8897
	Preoperative arterial blood gas pO_2	0.8971	0.5152	0.8042	−0.6566	0.5429	−0.2578
	Preoperative arterial lactate	0.8769	0.9856	0.8261	0.4515	−0.8143	−0.2661
	Preoperative renal dysfunction	0.8891	−0.5072	−0.5942	−0.872	−0.0802	0.1117
	Preoperative hepatic dysfunction	0.8081	0.9093	0.8589	0.8398	−0.9418	0.8389
	Preoperative inotrope use	−0.6951	−0.4534	−0.562	0.8415	−0.1463	−0.4767
	Age at surgery, days	0.9474	−0.8745	−0.9641	0.3906	−0.5035	−0.4308
	Age at surgery $\leq$ 7 days	0.9424	0.8055	0.455	−0.5178	0.1021	0.9782
	Post-conceptional age at surgery, weeks	0.607	0.5579	0.8236	0.9837	0.9641	−0.5161
Intraoperative factors	Cardiopulmonary bypass used	−0.1086	−0.1435	−0.3265	0.187	0.3983	−0.1917
	Cardiopulmonary bypass time	−0.0759	−0.0765	−0.0663	−0.9521	−0.6056	−0.5451
	Aortic cross-clamp used	−0.1836	−0.2674	−0.1699	0.2248	0.5837	−0.2995
	Aortic cross-clamp time	−0.5709	−0.5751	−0.5269	−0.9326	−0.671	−0.524
	Circulatory arrest/DHCA used	−0.9488	0.8619	0.6678	−0.5385	0.6901	**−0.0051**
	Circulatory arrest/DHCA time	−0.8855	0.9394	0.6792	−0.9018	0.2848	−0.1187
Postoperative factors	ECMO during 1st hospitalization	−0.3713	−0.2622	−0.2767	−0.6661	−0.0545	−0.827
	Time on ECMO (days)	−0.1446	−0.1052	−0.0973	0.9931	−0.0878	−0.7835
	Delayed sternal closure	−0.5379	−0.6143	−0.6814	0.3623	0.9183	−0.4587
	Had unplanned intervention(s), 1st hospitalization	−0.3879	−0.3596	−0.1475	−0.6329	−0.0733	−0.8704
	ICU length of stay, 1st hospitalization	−0.6355	−0.5327	−0.3574	−0.3949	−0.2001	0.9291
	Hospital length of stay	−0.3037	−0.283	−0.1566	−0.448	−0.1779	−0.779
	Expired during 1st hospitalization	−0.6103	−0.4601	−0.3885	−0.194	−0.1493	0.9834
	Required CPR during 1st hospitalization	−0.7533	−0.5378	−0.3742	−0.1507	−0.1666	0.7517
	Had seizures during 1st hospitalization	−0.1804	−0.1351	−0.1467	0.279	−0.8936	−0.7843
	Discharged on antiepileptics	−0.9114	−0.8641	−0.8618	0.3822	0.5556	−0.7385
	Discharged with gastrostomy tube	−0.5563	−0.6523	−0.1695	0.9847	−0.3562	0.1806
	Discharged with tracheostomy and/or ventilator	−0.0674	−0.1208	−0.1959	0.1477	0.3242	−0.833

Bold values indicate reference FDR-corrected values.

TABLE 2(C) Correlation between clinical risk factors and global connectome metrics: Average fractional anisotropy matrix (FDR-corrected).

		Cost	Global Efficiency	Transitivity	Modularity	Small World	Assortativity
Innate and cardiac lesions	Gestational age at birth	0.2129	0.2726	0.6258	−0.938	−0.9175	−0.7608
	Birth weight	−0.7891	−0.9483	−0.8389	0.6793	0.9634	−0.9972
	Birth weight percentile	−0.2619	−0.3833	−0.7516	0.0946	0.2292	0.2328
	Head circumference	0.7205	0.9823	0.8313	0.8605	0.9079	−0.5454
	Head circumference percentile	−0.5598	−0.2367	0.8029	0.4178	0.192	0.7831
	Birth length	0.7429	0.856	−0.6331	−0.6738	−0.3599	−0.8874
	Birth length percentile	0.9289	−0.7633	−0.47	−0.2075	−0.2277	0.0565
	APGAR, 1 min	−0.6998	0.6338	−0.3445	−0.4049	−0.8701	−0.334
	APGAR, 5 min	0.6623	0.3672	0.3478	−0.4664	0.6321	−0.8021
	22q11 microdeletion	−0.1672	−0.1146	−0.2041	−0.8494	−0.8558	0.9463
	Single ventricle	0.2122	0.918	0.6752	−0.0998	−0.1202	0.8596
	Arch obstruction	0.4403	0.8931	−0.6476	**−0.0183**	**−0.0039**	0.2608
	Single ventricle with arch obstruction	0.8128	−0.4546	−0.9548	−0.1547	−0.1898	0.1547
	d-TGA	−0.1558	−0.4273	−0.7334	**0.0237**	**0.0353**	0.8169
	Conotruncal defect	−0.2603	−0.3807	0.8804	**0.0075**	**0.0305**	−0.8047
	Altered fetal cerebral substrate delivery	−0.2248	−0.1727	−0.7726	0.3247	0.1395	−0.4175
	Altered cerebral substrate delivery severity score	−0.1602	−0.4154	−0.7166	0.1529	0.1429	0.751
	Heterotaxy	0.4118	0.5625	0.55	0.6015	−0.6252	−0.7109
Preoperative factors	Preoperative arterial blood gas pH	−0.1064	−0.1201	−0.2402	0.5332	0.7033	0.8897
	Preoperative arterial blood gas pO_2	−0.8363	0.5042	−0.5876	−0.789	0.7652	−0.2578
	Preoperative arterial lactate	0.722	0.7662	0.5436	−0.9811	0.2692	−0.2661
	Preoperative renal dysfunction	−0.789	−0.4613	−0.5181	−0.6232	−0.2445	0.1117
	Preoperative hepatic dysfunction	0.8424	0.9009	0.8052	−0.7401	0.6648	0.8389
	Preoperative inotrope use	−0.2349	−0.0956	−0.2937	−0.7737	−0.128	−0.4767
	Age at surgery, days	0.7364	0.6158	0.544	0.1907	−0.9121	−0.4308
	Age at surgery $\leq$ 7 days	−0.9697	−0.8198	0.7901	−0.5234	0.307	0.9782
	Post-conceptional age at surgery, weeks	0.2976	0.2375	0.3806	0.3008	0.9289	−0.5161
Intraoperative factors	Cardiopulmonary bypass used	−0.1915	−0.2437	−0.2629	−0.5077	0.5177	−0.1917
	Cardiopulmonary bypass time	**−0.0271**	**−0.0373**	**−0.0173**	0.8561	−0.9387	−0.5451
	Aortic cross-clamp used	−0.4251	−0.4333	−0.2282	−0.1459	0.9109	−0.2995
	Aortic cross-clamp time	−0.192	−0.2131	−0.0727	0.6495	−0.4238	−0.524
	Circulatory arrest/DHCA used	−0.6456	0.8999	0.6391	−0.3985	0.2857	**−0.0051**
	Circulatory arrest/DHCA time	−0.594	−0.9883	0.7047	−0.7415	**0.0247**	−0.1187
Postoperative factors	ECMO during 1st hospitalization	−0.193	−0.0566	−0.2699	−0.1254	−0.1765	−0.827
	Time on ECMO (days)	**−0.0404**	**−0.0116**	−0.0938	−0.2941	−0.379	−0.7835
	Delayed sternal closure	−0.9928	0.4595	0.6821	−0.5052	0.5109	−0.4587
	Had unplanned intervention(s), 1st hospitalization	−0.2819	−0.16	−0.2036	−0.4477	−0.3391	−0.8704
	ICU length of stay, 1st hospitalization	−0.2399	−0.1934	−0.2395	−0.9562	−0.898	0.9291
	Hospital length of stay	−0.166	−0.2456	−0.1726	0.8774	0.9816	−0.779
	Expired during 1st hospitalization	−0.0926	**−0.0318**	−0.1541	0.6219	−0.6581	0.9834
	Required CPR during 1st hospitalization	−0.2268	**−0.0361**	−0.0608	−0.7409	−0.2031	0.7517
	Had seizures during 1st hospitalization	**−0.0496**	−0.0908	−0.1527	0.2009	0.4436	−0.7843
	Discharged on antiepileptics	−0.9194	0.9117	−0.6587	−0.9203	0.8254	−0.7385
	Discharged with gastrostomy tube	−0.8844	−0.8286	−0.2652	−0.257	−0.1839	0.1806
	Discharged with tracheostomy and/or ventilator	−0.1789	−0.4994	−0.4402	−0.7227	0.2231	−0.833

Bold values indicate reference FDR-corrected values.

reduced cost (p = −0.0043), global efficiency (p = −0.0058), and transitivity (p = −0.0203) in the number of tracts connectome, and increased modularity (p = 0.0237) and small-worldness (p = 0.0353) in the average FA connectome. The prenatal cerebral substrate delivery severity score, which separated CHD lesions by how much alteration there is in the typical fetal circulation which directs the highest oxygen and nutrient rich blood from the placenta to the fetal brain, was also a strong predictor of lower cost (p = −0.0073) and global efficiency (p = −0.0054) in the number of tracts connectome. Conotruncal CHD subtype (which includes d-TGA as well as other lesions with altered conal septal/outflow tract relationships such as tetralogy of Fallot, double outlet right ventricle, truncus arteriosus, etc.) predicted modularity (p = 0.0075) and small-worldness (p = 0.0305) in the average FA connectome. Assortativity was not associated with the CHD subtypes by any of the methods. The only biometric parameter found to have an association was head circumference percentile which had a weak relationship with reduced global efficiency (p = −0.0439) and the only preoperative variable with a network topology association was preoperative arterial blood gas pH predicting reduced cost (p = −0.0444). These results are given in Tables 2A–C.

In the analysis of nodal network topology, increased severity of fetal cerebral substrate delivery was associated with reduced nodal efficiency in multiple areas, shown in Figure 4 (anatomic location of nodes—Precuneus Right (PCUN-R), Postcentral Gyrus Right (PoCG-R), Precentral Gyrus Right (PreCG-R), Supplementary Motor Area Right (SMA-R), Middle Frontal Gyrus Right (MFG-R), Thalamus Right (THA-R), Superior Temporal Gyrus Right (STG-R), Hippocampus Right (HIP-R), Insula Right (INS-R), Caudate Right (CAU-R), Anterior Cingulate Gyrus Right (ACG-R), Superior Frontal Gyrus Medial Right (SFGmed-R).

Intraoperative factors

Associations between intraoperative factors and global network topology on the postoperative MRI (Tables 2A–C) were as follows: Time on cardiopulmonary bypass was associated with decreased cost (p = −0.0271), global efficiency (p = −0.0373), and transitivity (p = −0.0173) in the average FA connectome. Use of circulatory arrest/DHCA (deep hypothermic circulatory arrest) was associated with decreased assortativity in all 3 connectome methods (p = −0.0051 for adjacency, number of tracts and average FA) and minutes of circulatory arrest/DHCA were associated with alterations of small-worldness in the adjacency (p = 0.031) and average FA (p = 0.0247) connectomes (Tables 2A–C). There were no significant associations at a nodal level with the intraoperative factors.

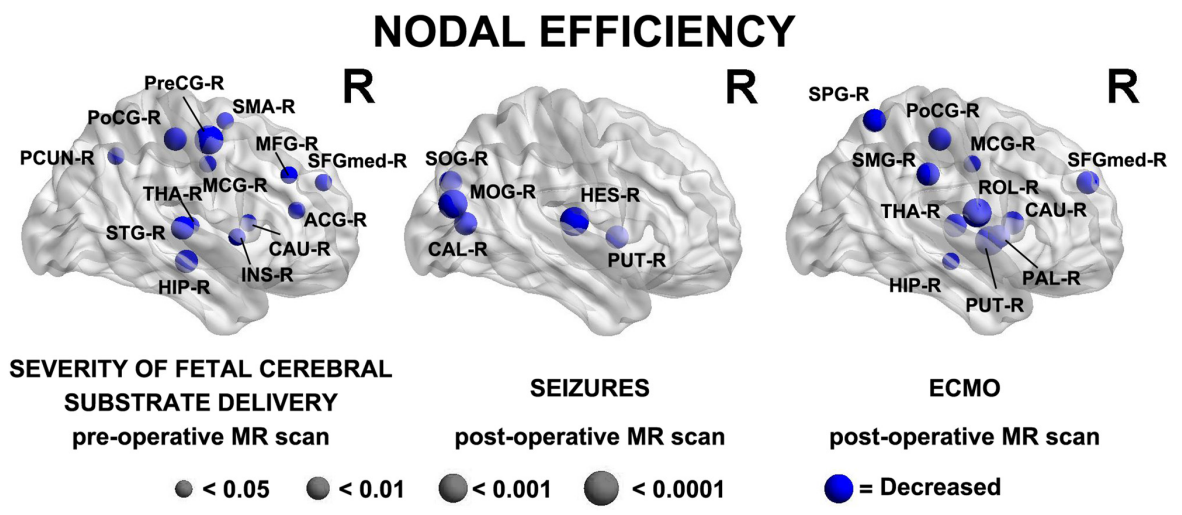

FIGURE 4
Three major clinical risk factors: (prenatal) severity of fetal cerebral substrate delivery correlates with preoperative reduced nodal efficiency in fronto-temporal, paralimbic, and parietal regions; (postoperative) presence of seizures and ECMO predict reduced nodal efficiency in similar regions on the postoperative MRI scan. Severity of Fetal Cerebral Substrate Delivery Pre-Operative MR Scan: Hippocampus Right (HIP-R), Superior Temporal Gyrus Right (STG-R), Thalamus Right (THA-R), Precuneus Right (PCUN-R), Postcentral Gyrus Right (PoCG-R), Precentral Gyrus Right (PreCG-R), Middle Cingulate Gyrus Right (MCG-R), Insula Right (INS-R), Caudate Right (CAU-R), Anterior Cingulate Gyrus Right (ACG-R), Superior Frontal Gyrus Medial Right (SFGmed-R), Middle Frontal Gyrus Right (MFG-R), Supplementary Motor Area Right (SMA-R). Seizures Post-Operative MR Scan: Superior Occipital Gyrus Right (SOG-R), Middle Occipital Gyrus Right (MOG-R), Calcarine Right (CAL-R), Heschl GyrusRight (HES-R), Putamen Right (PUT-R). ECMO Post-Operative MR Scan: Superior Parietal Gyrus Right (SPG-R), Postcentral Gyrus Right (PoCG-R), Supramarginal Gyrus Right (SMG-R), Middle Central Gyrus Right (MCG-R), Rolandic Operculum Right (ROL-R), Thalmus Right (THA-R), Hippocampus Right (HIP-R), Putamen Right (PUT-R), Pallidum Right (PAL-R), Caudate Right (CAU-R), Superior Frontal Gyrus Medial Right (SFGmed-R).

Postoperative factors

In the global network topology analysis (Tables 2A–C), postoperative seizures were associated with decreased cost in the adjacency connectome ($p = -0.0388$) and with reduced global efficiency in the average FA connectome ($p = -0.0496$). Time on ECMO predicted reduced cost ($p = -0.404$) and global efficiency ($p = -0.0116$) in the average FA connectome. Undergoing CPR (including chest compressions) and expiration during the first hospitalization both predicted reduced global efficiency in the average FA connectome ($p = -0.0318, -0.0361$, respectively).

In the nodal analysis by postoperative time points, having seizures postoperatively and time on ECMO both demonstrated multiple associations with decreased efficiency in nodal areas, shown in Figure 4 [anatomic location of nodes- *Seizures Post-Operative MR Scan:* Superior Occipital Gyrus Right (SOG-R), Middle Occipital Gyrus Right (MOG-R), Calcarine Right (CAL-R), Heschl Right (HES-R), Putamen Right (PUT-R) *ECMO Post-Operative MR Scan:* Superior Parietal Gyrus Right (SPG-R), Postcentral Gyrus Right (PoCG-R), Supramarginal Gyrus Right (SMG-R), Middle Central Gyrus Right (MCG-R), Rolandic Operculum Right (ROL-R), Thalmus Right (THA-R), Hippocampus Right (HIP-R), Putamen Right (PUT-R), Pallidum Right (PAL-R), Caudate Right (CAU-R), Superior Frontal Gyrus Medial Right (SFGmed-R)].

Clinical risk factor vs. tractography

The clinical risk factors were analyzed against tractography including FA, radial diffusivity, and axial diffusivity of the following areas: genu, body, and splenium of the corpus callosum, right and left CST, FOF, ILF, SLF.

Clinical risk factor vs. fractional anisotropy

When the clinical risk factors were compared against DTI tractography by FA (Supplementary Tables 2A–D), several intraoperative variables were found to have association with postoperative FA tractography outcomes. Time on cardiopulmonary bypass correlated with mean FA of the left FOF ($p = 0.0242$). Aortic cross-clamp time was associated with abnormal FA of the genu and splenium of the corpus callosum ($p = 0.0033$ for both, Supplementary Table 2C). After FDR correction, tractography by FA did not have significance with any of the patient-specific, CHD subtype, preoperative, or postoperative clinical parameters (Supplementary Tables 2A,B,D).

Clinical risk factor vs. radial diffusivity

When the clinical risk factors were compared against DTI tractography by radial diffusivity, multiple associations were found with the patient-specific factors specifically the neonatal anthropometric parameters and preoperative scans (Supplementary Table 2A). Newborn biometry was predictive of increased radial diffusivity of the genu, body, and splenium of the corpus callosum including birth weight ($p = 0.041$ genu, 0.0066 body, 0.0176 splenium), birth weight percentile ($p = 0.0055$ genu, 0.0022 body, 0.0055 splenium), head circumference ($p = 0.0147$ genu and body, 0.0198 splenium), and birth length percentile ($p = 0.0407$ for all 3). Birth weight was also predictive of increased radial diffusivity of the left SLF ($p = 0.0187$) and birth weight percentile with increased radial diffusivity of the right CST ($p = 0.02$), left FOF and right ILF ($p = 0.0426$), both right and left SLF ($p = 0.0297$ R and 0.02 L). Head circumference percentile predicted increased radial diffusivity of the left FOF ($p = 0.0147$), and birth length percentile of the inferior ($p = 0.0407$ R and L) and SLF ($p = 0.0407$ R, 0.0418 L). The 1-min APGAR score correlated with increased radial diffusivity of the corpus callosum body, left FOF, left ILF, and right SLF ($p = 0.0204$ for all).

Among the intra-operative factors, cardiopulmonary bypass time predicted increased radial diffusivity of the left FOF ($p = 0.0242$) and aortic cross-clamp time predicted increased radial diffusivity of the genu and splenium of the corpus callosum on postoperative scans ($p = 0.0033$) (Supplementary Table 2C). None of the CHD subtype categories, preoperative clinical factors, or postoperative clinical factors predicted radial diffusivity of any of the structures assessed (Supplementary Tables 2A,B,D).

Clinical risk factor vs. axial diffusivity

When the clinical risk factors were compared against DTI tractography by axial diffusivity, the findings were quite similar to those for radial diffusivity. For axial diffusivity, again multiple associations were found with the patient-specific factors specifically the neonatal anthropometric parameters on preoperative scans (Supplementary Table 2A). Birth weight was predictive of increased axial diffusivity of the corpus callosum body and left SLF ($p = 0.0182$). Birth weight percentile predicted increased axial diffusivity of the corpus callosum ($p = 0.0072$ genu, 0.0066 body, 0.0176 splenium), right CST ($p = 0.0114$), left FOF ($p = 0.0327$), and both SLF ($p = 0.0207$ R and 0.0157 L). Head circumference percentile predicted increased axial diffusivity of the of the corpus callosum ($p = 0.0017$ genu, 0.0077 body, 0.0132 splenium) and the left FOF ($p = 0.0017$), left ILF ($p = 0.0132$), and bilateral SLF ($p = 0.0478$ R, 0.0257 L). Birth length percentile predicted increased axial diffusivity of the corpus callosum body ($p = 0.0226$) and splenium ($p = 0.0315$), right CST ($p = 0.0315$), and bilateral ILF ($p = 0.0315$ R, 0.0187 L) and SLF ($p = 0.0352$ R, 0.0330 L). The 1-min APGAR score correlated with increased radial diffusivity of the left FOF ($p = 0.0231$).

Among the intra-operative factors, cardiopulmonary bypass time predicted increased postoperative axial diffusivity of the left FOF ($p = 0.0242$) and aortic cross-clamp time predicted increased axial diffusivity of the genu and splenium of the corpus

callosum (p = 0.0033) (Supplementary Table 2C). None of the CHD subtype categories, preoperative clinical factors, or postoperative clinical factors predicted radial diffusivity of any of the structures assessed (Supplementary Tables 2A,B,D).

Brain injury and brain dysplasia score (including subcortical components) findings

A total of 24 subjects had brain injury (22%) including 12 (11%) with punctate WMI, and 6 (5%) with stroke. The majority of the injury was seen on the preoperative scan (83% of punctate WMI and 67% of stroke occurred on preoperative scan). BDS was 3.6 ± 3.3. Brain dysplasia included 21 (19%) with cerebellar hypoplasia/dysplasia, 49 (45%) with olfactory bulb/sulcus abnormality, 45 (41%) with hippocampal hypoplasia/dysplasia.

Brain dysplasia score (including subcortical components) vs. connectome

Brain dysplasia was evaluated against global network topology via the 3 differentially weighted connectome analysis methods at both pre and postoperative time points (Table 3). BDS was not predictive of brain network topology by any of the methods. However, abnormalities of the cerebellum on preoperative scans predicted reduced cost in all 3 connectomes (p = −0.0417 adjacency, p = −0.0117 number of tracts, p = −0.0388 average FA) and reduced global efficiency in the number of tracts connectome (p = −0.0467). Abnormalities of the hippocampus on preoperative scans predicted reduced global efficiency (p = −0.0126) in the adjacency connectome. Olfactory abnormalities on the preoperative scan predicted increased modularity by the number of tracts connectome (p = 0.021).

Among the brain injury variables, punctate WMI on the preoperative scan predicted reduced cost in the adjacency connectome (p = −0.0401), and stroke on the postoperative scan predicted multiple abnormalities in the adjacency connectome including reduced cost (p = −0.0437), global efficiency (p = −0.0285), transitivity (p = −0.0439), and increased modularity (p = 0.0381). The composite brain injury did not predict any connectome metrics (Table 3).

Abnormalities of the subcortical structures including hypoplasia/dysplasia of the cerebellum, hippocampus, and olfactory bulb/sulci predicted altered nodal efficiency in multiple areas (p < 0.05, Figure 5). The patterns of nodal prediction were unique for each subcortical structures with the hippocampus abnormalities predicting widespread reduced nodal efficiency in all lobes of the brain, the cerebellum abnormalities predicting increased prefrontal nodal efficiency and the olfactory bulb abnormalities predicting posterior parietal-occipital nodal efficiency. The anatomic location of these nodes were: (1) Hippocampal Hypoplasia/Dysplasia: Inferior Temporal Gyrus Left (ITG-L), Amygdala Left (AMYG-L), Putamen Left (PUT-L), Insula Left (INS-L), Caudate Left (CAU-L), Inferior Frontal Gyrus Pars Triangularis Left (IFGtriang-L), Pallidum Left (PAL-L), Superior Frongal Gyrus Medial Left (SFGmed-L), Midddle Frontal Gyrus Left (MFG-L), Superior Frontal Gyrus Left (SFGdor-L), Supplementary Motor Area Left (SMA-L), Precentral Gyrus Left (PreCG-L), Paracental Lobule Left (PCL-L), Postcentral Gyrus Left (PoCG-L), Superior Parietal Gyrus Left (SPG-L), Precuneus Left (PCUN-L), Cuneus Left (CUN-L), Calcarine Left (CAL-L), Thalamus Left (THA-L), Hippocampus Left (HIP-L); (2) Cerebellar Hypoplasia/Dysplasia: Gyrus Rectus Left (REC-L), Inferior Frontal Gyrus Pars Triangularis Left (IFGtriang-L), Superior Frontal Gyrus Medial Left (SFGmed-L), Middle Frontal Gyrus Left (MFG-L), Superior Frontal Gyrus Left (SFGdor-L), Precentral Gyrus Left (PreCG-L), Postcentral Gyrus Left (PoCG-L); (3) Olfactory Hypoplasia/Dysplasia: Superior Temporal Pole Left (TPOsup-L), Hippocampus Left (HIP-L), Middle Occipital Gyrus Left (MOG-L), Superior Occipital Gyrus Left (SOG-L), Superior Parietal Gyrus Left (SPG-L), Middle Central Gyrus Left (MCG-L).

Brain dysplasia score (including subcortical components) vs. tractography

The brain dysplasia metrics were analyzed against tractography including FA, radial diffusivity, and axial diffusivity of the following areas: genu, body, and splenium of the corpus callosum, right and left CST, FOF, ILF, SLF. This analysis took place on preoperative scans, postoperative scans, and all scans combined (Table 4).

FA of the right CST on all scans combined correlated with global BDS (p = 0.0495) and FA of the bilateral CST correlated with cerebellar dysplasia (p = 0.0036 R, p = 0.0223 L) for all scans combined as well as for the preoperative scans only (p = 0.0288 R).

Radial diffusivity of multiple tracts demonstrated multiple correlations with brain dysplasia parameters. Radial diffusivity of the corpus callosum correlated with BDS on preoperative scans alone (p = 0.0029 genu, 0.0173 body, 0.002 splenium) and all scans combined (p = 0.025 genu, 0.0086 splenium), with cerebellar hypoplasia/dysplasia on preoperative only scans (p = 0.0275 genu, 0.0391 body, < 0.0001 splenium) and all scans combined (p = 0.0004 splenium), and hippocampal hypoplasia/dysplasia on both preoperative only scans (p = 0.0133 genu, 0.0002 body, 0.0004 splenium) and all scans combined (p = 0.0282 genu, 0.0029 body, 0.0005 splenium). Radial diffusivity of the left FOF correlated with BDS (p = 0.0415) and hippocampal abnormalities (p = 0.0034) and of the right FOF with cerebellar anomalies (p = 0.0459) all on preoperative scans. Radial diffusivity of the left ILF correlated with BDS on preoperative (p = 0.018) and all scans (p = 0.0044), with cerebellar abnormalities on preoperative (p = 0.0287) and all scans (p = 0.0088), and with hippocampal abnormalities on preoperative (p = 0.0054) and all scans (p = 0.082).

TABLE 3 Correlation between subcortical brain dysplasia score (BDS), brain injury and global connectome metrics (FDR-corrected).

		Cost	Global efficiency	Transitivity	Modularity	Small world	Assortativity
Adjacency matrix, Preoperative MRI	BDS	−0.0817	−0.0525	−0.1839	0.1353	0.218	−0.6677
	Cerebellum	**−0.0417**	−0.2953	−0.2506	0.5293	0.1854	−0.3837
	Olfactory	−0.6433	−0.7436	−0.8967	0.0766	0.1612	−0.3406
	Hippocampal	−0.1005	**−0.0126**	−0.0776	0.3526	0.9879	0.1771
	Brain Injury	−0.0773	−0.0936	−0.2051	0.1927	0.9104	0.6224
	Stroke	0.7366	−0.8034	−0.5851	−0.6983	−0.4022	−0.3788
	Punctate white mater injury	**−0.0401**	−0.0552	−0.1822	0.2154	−0.7936	0.1389
Adjacency matrix, Postoperative MRI	BDS	0.1183	0.0806	0.1422	0.3276	−0.1717	−0.4248
	Cerebellum	0.3625	0.3195	0.1936	−0.9118	−0.4835	−0.1075
	Olfactory	0.137	0.0916	0.0663	0.2404	−0.323	−0.393
	Hippocampal	0.3582	0.4186	−0.9307	0.3746	−0.0616	−0.8561
	Brain Injury	−0.2206	−0.204	−0.2319	0.1666	0.284	0.6022
	Stroke	**−0.0437**	**−0.0285**	**−0.0439**	0.2592	0.8144	**0.0381**
	Punctate white mater injury	−0.7189	−0.6146	−0.4661	0.2569	0.6579	−0.6747
Numbers tracts matrix, Preoperative MRI	BDS	−0.4672	−0.3245	−0.7039	0.0846	0.4401	−0.6677
	Cerebellum	**−0.0117**	**−0.0467**	−0.0762	−0.9661	0.1175	−0.3837
	Olfactory	0.6876	0.8216	0.4707	**0.021**	0.2736	−0.3406
	Hippocampal	−0.4156	−0.2242	−0.2342	0.997	−0.4147	0.1771
	Brain Injury	−0.2819	−0.3661	−0.5621	0.7756	0.3986	0.6224
	Stroke	0.4722	0.4767	0.7012	−0.1498	−0.8963	−0.3788
	Punctate white mater injury	−0.1582	−0.2679	−0.344	0.8958	0.5207	0.1389
Numbers tracts postoperative MRI	BDS	0.1484	0.2503	0.1179	−0.8474	−0.3386	−0.4248
	Cerebellum	0.0567	0.0654	0.0697	−0.2503	−0.5315	−0.1075
	Olfactory	0.3392	0.4785	0.181	0.488	−0.613	−0.393
	Hippocampal	0.1894	0.2657	0.231	−0.1688	−0.2635	−0.8561
	Brain Injury	−0.0988	−0.0615	−0.1599	−0.9669	0.4344	0.6022
	Stroke	−0.3329	−0.4203	−0.0995	−0.7676	0.5287	**0.0381**
	Punctate white mater injury	−0.5409	−0.4706	−0.5737	−1	0.8858	−0.6747
Average fractional anisotropy preoperative MRI	BDS	−0.5744	−0.544	0.6988	0.4685	0.1233	−0.6677
	Cerebellum	**−0.0388**	−0.2154	−0.2026	0.5875	0.1404	−0.3837
	Olfactory	0.5741	0.4828	0.5078	0.4721	0.1548	−0.3406
	Hippocampal	−0.3403	−0.118	−0.2409	0.4253	0.9481	0.1771
	Brain Injury	−0.2765	−0.3748	−0.445	0.5613	−0.8481	0.6224
	Stroke	0.9845	−0.6852	−0.5091	−0.72	−0.1931	−0.3788
	Punctate white matter injury	−0.1288	−0.2154	−0.3457	0.5821	−0.694	0.1389
Average fractional anisotropy postoperative MRI	BDS	0.4757	0.5487	0.3432	0.7551	−0.2918	−0.4248
	Cerebellum	0.4413	0.5061	0.1702	−0.8609	−0.7585	−0.1075
	Olfactory	0.3753	0.394	0.1805	0.6156	−0.4073	−0.393
	Hippocampal	−0.6546	−0.3959	−0.3226	0.796	−0.1053	−0.8561
	Brain Injury	−0.0994	−0.1034	−0.1698	0.365	0.3303	0.6022
	Stroke	−0.1593	−0.1399	−0.1677	0.2267	0.9753	**0.0381**
	Punctate white matter injury	−0.6274	−0.5925	−0.5907	0.3855	0.7528	−0.6747

Bold values indicate reference FDR-corrected values.

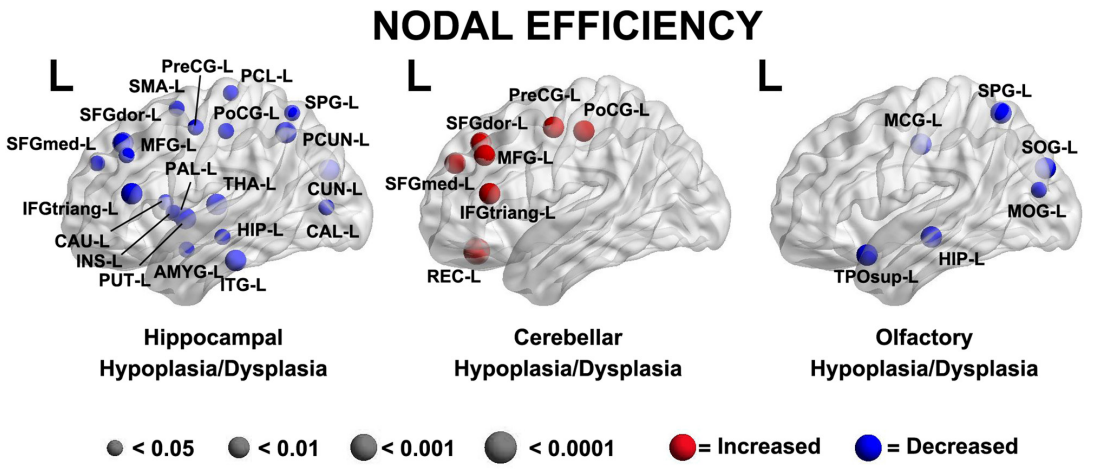

FIGURE 5
A brain dysplasia score (BDS) (composed of hippocampal, cerebellar and olfactory hypoplasia/dysplasia components) predicted specific regional patterns of nodal efficiency suggestive regional brain reorganization and distinct patterns when compared to clinical risk factors demonstrated in **Figure 4**. Hippocampal Hypoplasia/Dysplasia: Inferior Temporal Gyrus Left (ITG-L), Amygdala Left (AMYG-L), Putamen Left (PUT-L), Insula Left (INS-L), Caudate Left (CAU-L), Inferior Frontal Gyrus Pars Triangularis Left (IFGtriang-L), Pallidum Left (PAL-L), Frontal Superior Gyrus Medial Left (SFGmed-L), Middle Frontal Gyrus Left (MFG-L), Frontal Superior Gyrus Dorsolateral Left (SFGdor-L), Supplementary Motor Area Left (SMA-L), Precentral Gyrus Left (PreCG-L), Paracental Lobule Left (PCL-L), Postcentral Gyrus Left (PoCG-L), Superior Parietal Gyrus Left (SPG-L), Precuneus Left (PCUN-L), Cuneus Left (CUN-L), Calcarine Left (CAL-L), Thalamus Left (THA-L), Hippocampus Left (HIP-L). Cerebellar Hypoplasia/Dysplasia: Gyrus Rectus Left (REC-L), Inferior Frontal Gyrus Pars Triangularis Left (IFGtriang-L), Superior frontal Gyrus Medial Left (SFGmed-L), Middle Frontal Gyrus Left (MFG-L), Superior Frontal Gyrus Left (SFGdor-L), Precentral Gyrus Left (PreCG-L), Postcentral Gyrus Left (PoCG-L). Ofactory Hypoplasia/Dysplasia: Superior Temporal Pole Left (TPOsup-L), Hippocampus Left (HIP-L), Middle Occipital Gyrus Left (MOG-L), Superior Occipital Gyrus Left (SOG-L), Superior Parietal Gyrus Left (SPG-L), Middle Cingulate Gyrus Left (MCG-L).

Radial diffusivity of the right SLF was associated with hippocampal abnormalities on preoperative only scans ($p = 0.0449$).

Axial diffusivity of multiple tracts also demonstrated correlations with brain dysplasia parameters. Axial diffusivity of the corpus callosum correlated with BDS on preoperative scans alone ($p = 0.0194$ genu, 0.0371 body, 0.0029 splenium) and all scans combined ($p = 0.0262$ splenium), with cerebellar abnormality on preoperative only scans ($p = 0.0251$ genu, < 0.0001 splenium) and all scans combined ($p = 0.0004$ splenium), and hippocampal abnormality on both preoperative only scans ($p = 0.0212$ genu, 0.0005 body, 0.0003 splenium) and all scans combined ($p = 0.0007$ splenium). Axial diffusivity of the left CST was associated with hippocampal abnormality on all scans combined ($p = 0.0428$). Axial diffusivity of the left FOF correlated with hippocampal abnormalities ($p = 0.006$) and of the right FOF with cerebellar anomalies ($p = 0.0495$) on preoperative scans. Axial diffusivity of the left ILF correlated with BDS on preoperative ($p = 0.0464$) and all scans ($p = 0.0127$), with cerebellar abnormalities on preoperative ($p = 0.0422$) and all scans ($p = 0.007$), and with hippocampal abnormalities on preoperative ($p = 0.0082$) and all scans ($p = 0.0109$). Axial diffusivity of the right SLF was associated with hippocampal abnormalities on preoperative scans (=0.0263).

Discussion

Neurodevelopmental deficits are common in infants with CHD who undergo neonatal open-heart surgery (Bellinger et al., 1995, 2003, 2009, 2011). Some risk factors for these deficits are innate (e.g., genetic), but others involve modifiable medical management (McQuillen et al., 2010; Li et al., 2015; Gaynor et al., 2016; Marelli et al., 2016; Wernovsky and Licht, 2016; Zahid et al., 2018). The pathophysiology of CHD-related neuropsychological impairment is multifactorial, likely acting through two broad mechanistic pathways, destructive and developmental (Volpe, 2014). This *destructive-developmental amalgam* is mediated by exposure to potentially toxic agents (e.g., volatile anesthetic agents, inflammation) or deprivation of essential exposures (e.g., oxygen) (Volpe, 2014). This amalgam includes diffuse WMI, cortical long-range connectivity, and focal WMI all of which is likely to impact DTI measures, either post-processed by connectome or tractography techniques. Overall, this is the first study to use the brain connectome to look at the interaction of clinical factors and novel properties of brain tractography, specifically cost, global efficiency, and modularity.

One of our major findings was that d-TGA anatomy and a 3-tiered severity score based on alteration of fetal substrate delivery were both found to be associated with white matter network topology including lower cost and reduced global efficiency when looked at through a number of tracts

TABLE 4 Correlation between brain dysplasia score (BDS) (including subcortical components) and seed-based tractography metrics (FDR-corrected).

		Fractional anisotropy			Radial diffusivity			Axial diffusivity		
		Pre	Post	All	Pre	Post	All	Pre	Post	All
Corpus callosum genu	BDS	**0.0489**	0.6865	0.1426	**0.0029**	0.8118	**0.025**	**0.0194**	0.8855	0.2067
	Cerebellum	0.4839	0.5308	0.9382	**0.0275**	0.6841	0.1982	**0.0251**	0.7969	0.1702
	Olfactory	0.2686	0.9773	0.4723	0.2837	0.6018	0.5085	0.7493	0.7435	0.9642
	Hippocampal	0.2468	0.8402	0.6056	**0.0133**	0.5037	0.0282	**0.0212**	0.5277	0.061
Corpus callosum body	BDS	0.2271	0.5468	0.2399	**0.0173**	0.8118	0.0921	**0.0371**	0.782	0.3028
	Cerebellum	0.4581	0.9952	0.6303	**0.0391**	0.6841	0.1746	0.0947	0.6346	0.3295
	Olfactory	0.8371	0.7989	0.7452	0.9785	0.6018	0.6941	0.9095	0.6089	0.7182
	Hippocampal	0.1839	0.8296	0.3511	**0.0002**	0.5037	**0.0029**	**0.0005**	0.7277	**0.0122**
Corpus callosum splenium	BDS	0.1747	0.9669	0.3038	**0.002**	0.7703	**0.0086**	**0.0029**	0.8771	**0.0262**
	Cerebellum	0.4251	0.7146	0.6587	**<0.0001**	0.7349	**0.0004**	**<0.0001**	0.8891	**0.0004**
	Olfactory	0.3839	0.9184	0.5273	0.3568	0.8085	0.4968	0.3885	0.7682	0.6243
	Hippocampal	0.3557	0.7932	0.6366	**0.0004**	0.2667	**0.0005**	**0.0003**	0.2483	**0.0007**
Cortical spinal tract left	BDS	0.5901	0.9105	0.5348	0.9743	0.4924	0.6447	0.8467	0.4859	0.4524
	Cerebellum	0.0826	0.1654	**0.0223**	0.9191	0.9768	0.9458	0.4199	0.5598	0.2825
	Olfactory	0.7273	0.564	0.4249	0.4553	0.6249	0.7845	0.3632	0.3673	0.9907
	Hippocampal	0.3988	0.6435	0.3048	0.4696	0.3219	0.2178	0.1532	0.1974	**0.0428**
Cortical spinal tract right	BDS	0.1017	0.4165	**0.0495**	0.6399	0.83	0.8542	0.8008	0.5668	0.4538
	Cerebellum	**0.0288**	0.0601	**0.0036**	0.8618	0.6913	0.7149	0.4189	0.6118	0.304
	Olfactory	0.2036	0.4406	0.1241	0.1285	0.8603	0.2518	0.2291	0.5701	0.5722
	Hippocampal	0.2161	0.3139	0.086	0.4347	0.9691	0.5279	0.1214	0.6186	0.1152
Fronto-occipital fasciculus left	BDS	0.13	0.719	0.5897	**0.0415**	0.4147	0.5228	0.0766	0.3593	0.7491
	Cerebellum	0.1437	0.4141	0.6858	0.2875	0.8409	0.5211	0.701	0.7798	0.6798
	Olfactory	0.8631	0.4291	0.6268	0.5179	0.3852	0.8711	0.4226	0.6026	0.885
	Hippocampal	0.1234	0.6281	0.6567	**0.0034**	0.4102	0.246	**0.006**	0.3129	0.4062
Fronto-occipital fasciculus right	BDS	0.5517	0.4682	0.6938	0.1853	0.209	0.8943	0.1579	0.203	0.9817
	Cerebellum	0.4365	0.7093	0.8125	**0.0459**	0.7901	0.1887	**0.0495**	0.9664	0.1502
	Olfactory	0.7617	0.3383	0.3335	0.9519	0.1469	0.296	0.8176	0.156	0.4367
	Hippocampal	0.293	0.3687	0.8473	0.1328	0.1471	0.8483	0.1997	0.0976	0.6319
Inferior longitudinal fasciculus left	BDS	0.1906	0.9454	0.2937	**0.018**	0.1219	**0.0044**	**0.0464**	0.1557	**0.0127**
	Cerebellum	0.6072	0.2079	0.8331	**0.0287**	0.1928	**0.0088**	**0.0422**	0.0869	**0.007**
	Olfactory	0.7237	0.6934	0.6289	0.2189	0.1329	0.0548	0.2429	0.1469	0.0638
	Hippocampal	0.3554	0.9786	0.7845	**0.0054**	0.4265	**0.0082**	**0.0082**	0.4136	**0.0109**
Inferior longitudinal fasciculus right	BDS	0.2306	0.4673	0.5476	0.1753	0.9759	0.281	0.2829	0.9581	0.4614
	Cerebellum	0.5603	0.7997	0.8938	0.4044	0.9935	0.4452	0.5562	0.5805	0.4227
	Olfactory	0.6648	0.7904	0.8086	0.3863	0.9766	0.4474	0.366	0.7085	0.3456
	Hippocampal	0.1477	0.7262	0.4223	0.0635	0.8869	0.123	0.1317	0.9192	0.2955
Superior longitudinal fasciculus left	BDS	0.0788	0.4744	0.1092	0.3259	0.8205	0.5096	0.6847	0.4671	0.9068
	Cerebellum	0.9084	0.3257	0.9145	0.888	0.1867	0.441	0.8351	0.2193	0.4204
	Olfactory	0.283	0.2389	0.3002	0.783	0.9614	0.836	0.9008	0.8025	0.8044
	Hippocampal	0.1171	0.2793	0.4844	0.2186	0.4673	0.1552	0.4839	0.5139	0.3374
Superior longitudinal fasciculus right	BDS	0.9582	0.9454	0.5138	0.5083	0.3462	0.7487	0.3416	0.3821	0.81
	Cerebellum	0.7902	0.2079	0.413	0.3184	0.2997	0.8822	0.1067	0.6421	0.4454
	Olfactory	0.386	0.6934	0.1821	0.5341	0.3417	0.255	0.8247	0.5582	0.5314
	Hippocampal	0.4305	0.9786	0.6757	**0.0449**	0.8933	0.1611	**0.0263**	0.7581	0.1362

Bold values indicate reference FDR-corrected values.

connectome analysis, which is weighted toward brain volume. We found that d-TGA additionally resulted in in lower cost, revealed from a macrostructure perspective in our adjacency analysis. The altered fetal substrate delivery severity score also had multiple nodal-level connectome alterations (Figure 4). Interestingly, the fact that d-TGA patients tend to have the most impaired prenatal cerebral oxygen and substrate delivery (Sun et al., 2015) may be a driving factor for these perturbations given that patients with d-TGA rarely have identifiable chromosomal or genetic abnormalities, making genetic underpinnings seem less likely. Remarkably, a previous connectome study also showed that adolescents with d-TGA had reduced global efficiency and, importantly, these network properties mediated poor neurocognitive outcomes in d-TGA

patients compared to their referent adolescents across every domain assessed (Panigrahy et al., 2015a). This has important implications to suggest that neurocognitive perturbation is mediated by global differences in white matter network topology, which are already present in the preoperative neonatal time period.

Our secondary connectome outcome measures included brain network modularity and small-worldness. Conotruncal cardiac defect subtype (which includes d-TGA but also several other cardiac lesions) predicted increased modularity by all 3 weighted methods, and predicted increased small-worldness by the number of tracts and average FA methods (based on volume and microstructure). D-TGA alone, but not altered fetal cerebral substrate delivery, predicted increased modularity and small-worldness in the microstructure/fiber density-weighted model only. Interestingly, a previous study in adolescents with d-TGA also showed both increased modularity and small-worldness, suggesting that both our primary and secondary outcome network abnormalities seen in neonates have potential to persist over the lifetime (Panigrahy et al., 2015a). Despite their low postoperative morbidity and the rarity of need for reinterventions after an initial arterial switch operation, d-TGA patients have been shown to have suboptimal neurodevelopmental outcomes extending into adolescence as shown by the Boston Circulatory Arrest Study (BCAS) (Bellinger et al., 1995, 2003, 2009, 2011).

In contrast to increased modularity seen in conotruncal and d-TGA subjects, aortic arch obstruction was found to be associated with decreased modularity and decreased small-worldness by all 3 weighted connectome methods. Our study's arch obstruction group consisted largely of single ventricle subjects with arch obstruction (87% of that group), i.e., infants with HLHS and its variants, a group with a large burden of neurodevelopmental disability (Mahle et al., 2000; Tabbutt et al., 2008; Sananes et al., 2021). Others have implicated problems with modularity with childhood-onset schizophrenia (Alexander-Bloch et al., 2010) and autism (Shi et al., 2013), but this has yet to be studied in neonates with CHD. Further work is needed to understand specifically why modularity is decreased in patients that had arch obstruction and what implications that has on their neurodevelopment.

Our connectome results are in contrast to another study evaluating global network organization in neonates with CHD prior to heart surgery (De Asis-Cruz et al., 2017). De Asis-Cruz et al. (2017) found similar global efficiency, cost and small world levels in CHD infants compared to healthy controls, and concluded that the brain's ability to transfer information efficiently is maintained in CHD. Of note, this differs from our present study because it was a grouped analysis of 30 CHD subjects of which 7 had d-TGA, whereas our significant findings involving cost and global efficiency were in a subset of infants with d-TGA; additionally they utilized connectome analysis of blood oxygen level dependent imaging while our study utilized DTI. Similar to our present findings, our group's prior work which compared a group of CHD infants to control infants using a similar DTI-based connectome via 3 weighted methods, detected reductions in cost and global efficiency in CHD infants compared to controls, as well as increased small-worldness after controlling for cost, in a population which overlaps the group of our present study and included about 25% d-TGA in the CHD subjects, compared to 35% in our present study.

Our second major finding was that certain intraoperative and post-operative risk factors correlated with decreased cost and global efficiency in the average FA matrix postoperatively. This is the connectome method weighted to microstructure and fiber density, and we found that both longer time on cardiopulmonary bypass intraoperatively and longer time on ECMO postoperatively were associated with reduced numbers of connections and reduced network global efficiency. While we know that patients with CHD that survive ECMO have worse neurodevelopmental outcomes (Bellinger et al., 2009), little is known about early markers of differences in brain connectivity in relation to life-support needs. In fact, one group looked at infants that were placed on ECMO compared to healthy full term controls and found that the ECMO patients (albeit not with CHD) had significant differences in FA measured on DTI in multiple regions (Schiller et al., 2017). Similarly we found significant differences in our ECMO patients when using FA, specifically decreased number of connections and brain integration (global efficiency). Recently in a porcine model, Stinnett et al. (2017) looked at cardiopulmonary bypass-induced FA alterations after heart surgery and found, similar to our findings, decreased FA (Stinnett et al., 2017). Specifically they found the most alterations in the frontal cortex and suggested that that may be an early biomarker for WMI after cardiopulmonary bypass. An additional postoperative association in our data was with postoperative seizures and lower cost seen in both the average FA and adjacency connectome models. This suggests that seizures are associated with reduced number of connections on both macrostructure and microstructure levels. It is interesting that these the 2 clinical factors of time on ECMO and presence of seizures showed similar alterations in brain cost, as in our previous study we found these same clinical factors to both be related to altered brain metabolism (reduced white matter N-acytyl aspartate postoperatively) in a similar way (Harbison et al., 2017). Finally, our present study found that reduction in global efficiency on a microstructural level correlated with infants who received CPR (including chest compressions) and in infants who did not ultimately survive to hospital discharge.

The preclinical justification for also using tractography measurements was demonstrated by Morton et al. (2017) who recently showed that hypoxic exposure of the gyrencephalic piglet brain reduced proliferation and neurogenesis in the postnatal subventricular zone. This resulted in microstructural diffuse WMI as assessed by FA quantitative DTI of long range

connectivity of the SLF the FOF, and the ILF the metrics used to calculate the diffuse WMI (Morton et al., 2017). This preclinical piglet model also showed reduced cortical maturation similar to human CHD infants, supporting the concept that diffuse WMI also correlates with cortical long-range connectivity-related dysmaturation. Clinically, these DTI findings correlate with neonatal perioperative factors and long-term neurocognitive outcomes in the adolescent BCAS TGA study (Panigrahy et al., 2015a; Schmithorst et al., 2016). Unlike the preterm literature, there are few long-term outcome studies of diffuse WMI in CHD. Beca et al. (2013) found relative brain immaturity at 3 months of age was associated with reduced performance in cognition at 2 years of age. Serial total brain volumes of d-TGA infants were recently shown to be predictive of 18-month outcomes (Lim et al., 2019). Focal WMI is defined as punctate hyperintensity punctate periventricular fronto-parietal white matter lesions on 3D-T1 peri-operative imaging or "focal non-cystic coagulative necrosis," involving long-range connectivity crossing-fibers (Beca et al., 2009, 2013; Petit et al., 2009; Block et al., 2010; McQuillen and Miller, 2010; Gaynor et al., 2016; Peyvandi et al., 2019), in full-term CHD neonates. Focal WMI has been shown to be predictive of short-term motor impairment in CHD (Beca et al., 2009, 2013; Petit et al., 2009; Block et al., 2010; McQuillen and Miller, 2010; Brambrink et al., 2012; Gaynor et al., 2016).

When the clinical risk factors were assessed against conventional DTI tractography, microstructural dysmaturation correlated strongly with birth weight and percentile of weight, length, and head circumference across multiple white matter tracts, suggesting that even among term CHD neonates there is range of brain maturation which varies with the child's biometry and physical maturation. Reduced FA, and radial and axial diffusivity of the left FOF was correlated with cardiopulmonary bypass time, in line with piglet models of cardiopulmonary bypass using similar techniques (Stinnett et al., 2017), and reductions of all 3 DTI metrics in the corpus callosum with aortic cross-clamp time.

It was not surprising that when brain injury was utilized as an exposure for the connectome metrics, punctate WMI on preoperative scan predicted reduced cost and stroke on postoperative scan predicted reduced cost and global efficiency; however, these alterations were only seen on a macrostructural level, in the adjacency matrix, and no connectome alterations were seen by the other weighted methods. Of note, the previously discussed connectome analysis excluded patients with injury, so grossly visible injury was not the underpinning of our connectome results discussed above.

Subcortical brain dysplasia associations with connectome alterations included (1) cerebellar dysplasia associating with reduced cost by all three weighted methods, (2) reduced global efficiency in the volume-based number of tracts analysis, and (3) hippocampal dysplasia predicting reduced global efficiency on a macrostructural level, in the adjacency connectome. Additionally, hippocampal, cerebellar, and olfactory dysplasia predicted multiple regional patterns of inefficiency on a nodal level, suggestive of regional brain reorganization. Taken together with the associations seen between subcortical dysplasia and tractography analyses, including abnormalities of the hippocampus, cerebellum, and overall BDS predicting widespread microstructural dysmaturation in all white matter tracts evaluated, shared genetic underpinnings to abnormalities of subcortical structure and white matter microstructure are likely.

Limitations and future work

There were several limitations to our study. First, we had a heterogenous group of CHD patients, although they all required neonatal surgery and we subcategorized them into various conceptual categories (single ventricle, arch obstruction, TGA, heterotaxy), a larger sample size of individual defects would help better describe the differences in the brain's connectome. Additionally, we did not have a healthy control group, rather we compared groups to each other by looking at the clinical variable of interest. We also had normal values for brain network topology from previous studies as well as our previous study comparing CHD to controls that we utilized. In addition, while most of our newborns were not sedated for the MRI, some were sedated for clinical reasons, and we do not know what effect sedation has on brain network topology. Lastly, it will be important to correlate our neuroimaging findings with longer term neurodevelopmental outcomes. How these connectome metrics impact longer-term neurocognition is an important knowledge gap that our study could address with longitudinal follow-up of this enrolled cohort.

With regards to statistical considerations, despite FDR correction of each individual independent model proposed, our study did have a large number of models related to both the exposure/predictors (40 separate clinical risk factors and 7 components of the BDS) and primary neuroimaging outcomes for reach of the three weight [global efficiency (total # of individual model = 141)] and nodal efficiency (total # of individual models/node = 141). We did also explore secondary neuroimaging outcomes including other global connectome metrics (total # of individual model = 141/metric including cost, transitivity, modularity, assortativity) and 11 exploratory tractography measures (total # of individual models = 44/tract). Despite this, our findings are in alignment with existing connectome-related and DTI literature in neonates/infants with CHD as detailed above. Importantly, future work is needed to replicate these findings with larger-scale more focused multi-center studies, particularly if any of the most promising metrics are eventually incorporated into clinical trials of neuroprotection in CHD. Future work machine learning techniques may be needed to help establish more succinct models. Future work is also needed to understand how these MR brain studies should become part of clinical practice in

the management of these high-risk neonates and be potentially standardized with neurodevelopmental testing.

Conclusion

In summary, our work suggests that microstructural brain connectivity is disrupted in neonates with complex CHD. Prenatal clinical risk factors (heart lesion subtype and prenatal cerebral substrate delivery alterations), major intra and postoperative events (cardiopulmonary bypass time, ECMO time, and seizures) and preclinical CHD-derived subcortical dysplasia were the most predictive of connectome-based neuroimaging outcome measures relative to other pre and postoperative period clinical risk factors, while patient-specific anthropometric measurements (weight, length, and head size percentiles) predicted tractography outcomes. This is in alignment with the evolving literature that most of the neurodevelopmental impairment in CHD is related to patient-specific, prenatal, and unknown genetic factors. Postoperative factors with implications for high neurological severity, including seizures and time on ECMO, were highly predictive of diffuse connective nodal efficiency, identifying high risk patients with poor outcomes. In addition, intraoperative factors (including cardiopulmonary bypass and aortic cross-clamp times) correlated with reduction in tractography metrics, recapitulating microstructural diffusion correlations of white mater injury seen in developmental piglet models of cardiac surgery. Lastly, preclinical-CHD-derived subcortical brain dysplasia scoring predicted more distinct, localized structural network topology patterns in conjunction with tractography-based diffuse microstructural changes, likely reflecting genetic pathways that are known to impact the connectome and alter the organization of white matter development in CHD.

Data availability statement

The raw data supporting the conclusions of this article will be made available by the authors, without undue reservation.

Ethics statement

The studies involving human participants were reviewed and approved by the University of Pittsburgh. Written informed consent to participate in this study was provided by the participants or their legal guardian/next of kin.

Author contributions

JV-S, JG, AH, AP, and CL contributed to the conception and design of the study. NT, SK, EH, TB, and JJ contributed to the subject recruitment. VL, VR, GG, WR, BM, and RC contributed to the data analysis. VL and VS organized the database and performed the statistical analysis. AP and JV-S wrote the first draft of the manuscript. JV-S, JG, AH, SC, and GG wrote sections of the manuscript. All authors contributed to the manuscript revision, read, and approved the submitted version.

Funding

This work was supported by the Department of Defense (W81XWH-16-1-0613), the National Heart, Lung, and Blood Institute (R01 HL152740-1 and R01 HL128818-05), and the National Heart, Lung and Blood Institute with National Institute on Aging (R01HL128818-05 S1). Southern California Clinical and Translational Sciences Institute (NCATS) through Grant UL1TR0001855. We also acknowledge Additional Ventures for support (AP, VR, and RC). VR was supported by the Saban Research Institute, Additional Ventures Foundation and NIH-NHLBI K01HL153942. NT was supported by the Children's Hospital Los Angeles Clinical Services Research Grant and the NINR K23 Grant 1K23NR019121-01A1.

Conflict of interest

The authors declare that the research was conducted in the absence of any commercial or financial relationships that could be construed as a potential conflict of interest.

Publisher's note

All claims expressed in this article are solely those of the authors and do not necessarily represent those of their affiliated organizations, or those of the publisher, the editors and the reviewers. Any product that may be evaluated in this article, or claim that may be made by its manufacturer, is not guaranteed or endorsed by the publisher.

Author disclaimer

Its contents are solely the responsibility of the authors and do not necessarily represent the official views of the NIH.

Supplementary material

The Supplementary Material for this article can be found online at: https://www.frontiersin.org/articles/10.3389/fnins.2022.952355/full#supplementary-material

References

Alcauter, S., Lin, W., Smith, J. K., Gilmore, J. H., and Gao, W. (2015). Consistent anterior–posterior segregation of the insula during the first 2 years of life. *Cereb. Cortex* 25, 1176–1187. doi: 10.1093/cercor/bht312

Alexander-Bloch, A. F., Gogtay, N., Meunier, D., Birn, R., Clasen, L., Lalonde, F., et al. (2010). Disrupted modularity and local connectivity of brain functional networks in childhood-onset schizophrenia. *Front. Syst. Neurosci.* 4:147. doi: 10.3389/fnsys.2010.00147

Bajic, D., Moreira, N. C., Wikström, J., and Raininko, R. (2012). Asymmetric development of the hippocampal region is common: A fetal MR imaging study. *Am. J. Neuroradiol.* 33, 513–518. doi: 10.3174/ajnr.A2814

Bajic, D., Wang, C., Kumlien, E., Mattsson, P., Lundberg, S., Eeg-Olofsson, O., et al. (2008). Incomplete inversion of the hippocampus—a common developmental anomaly. *Eur. Radiol.* 18, 138–142. doi: 10.1007/s00330-007-0735-6

Barkovich, A. J., Millen, K. J., and Dobyns, W. B. (2007). A developmental classification of malformations of the brainstem. *Ann. Neurol.* 62, 625–639. doi: 10.1002/ana.21239

Barkovich, A. J., and Raybaud, C. (2012). *Pediatric Neuroimaging*. Philadelphia: Lippincott Williams and Wilkins.

Bassett, D. S., and Bullmore, E. (2006). Small-world brain networks. *Neuroscientist* 12, 512–523. doi: 10.1177/1073858406293182

Beca, J., Gunn, J., Coleman, L., Hope, A., Whelan, L. C., Gentles, T., et al. (2009). Pre-operative brain injury in newborn infants with transposition of the great arteries occurs at rates similar to other complex congenital heart disease and is not related to balloon atrial septostomy. *J. Am. Coll. Cardiol.* 53, 1807–1811. doi: 10.1016/j.jacc.2009.01.061

Beca, J., Gunn, J. K., Coleman, L., Hope, A., Reed, P. W., Hunt, R. W., et al. (2013). New white matter brain injury after infant heart surgery is associated with diagnostic group and the use of circulatory arrest. *Circulation* 127, 971–979. doi: 10.1161/CIRCULATIONAHA.112.001089

Bellinger, D. C., Bernstein, J. H., Kirkwood, M. W., Rappaport, L. A., and Newburger, J. (2003). Visual-spatial skills in children after open-heart surgery. *J. Dev. Behav. Pediatr.* 24, 169–79. doi: 10.1097/00004703-200306000-00007

Bellinger, D. C., Jonas, R. A., Rappaport, L. A., Wypij, D., Wernovsky, G., Kuban, K. C., et al. (1995). Developmental and neurologic status of children after heart surgery with hypothermic circulatory arrest or low-flow cardiopulmonary bypass. *N. Engl. J. Med.* 332, 549–555. doi: 10.1056/NEJM199503023320901

Bellinger, D. C., Newburger, J. W., Wypij, D., Kuban, K. C., duPlesssis, A. J., and Rappaport, L. A. (2009). Behaviour at eight years in children with surgically corrected transposition: The Boston Circulatory Arrest Trial. *Cardiol. Young* 19, 86–97. doi: 10.1017/S1047951108003454

Bellinger, D. C., Wypij, D., Rivkin, M. J., DeMaso, D. R., Robertson, R. L. Jr., Dunbar-Masterson, C., et al. (2011). Adolescents with d-transposition of the great arteries corrected with the arterial switch procedure: Neuropsychological assessment and structural brain imaging. *Circulation* 124, 1361–1369. doi: 10.1161/CIRCULATIONAHA.111.026963

Bhroin, M. N., Seada, S. A., Bonthrone, A. F., Kelly, C. J., Christiaens, D., Schuh, A., et al. (2020). Reduced structural connectivity in cortico-striatal-thalamic network in neonates with congenital heart disease. *NeuroImage* 28:102423 doi: 10.1016/j.nicl.2020.102423

Block, A. J., McQuillen, P. S., Chau, V., Glass, H., Poskitt, K. J., Barkovich, A. J., et al. (2010). Clinically silent preoperative brain injuries do not worsen with surgery in neonates with congenital heart disease. .*J. Thorac. Cardiovasc. Surg.* 140, 550–557. doi: 10.1016/j.jtcvs.2010.03.035

Blondel, V. D., Guillaume, J.-L., Lambiotte, R., and Lefebvre, E. (2008). Fast unfolding of communities in large networks. *J. Stat. Mech.* 2008:10008. doi: 10.1088/1742-5468/2008/10/P10008

Blustajn, J., Kirsch, C., Panigrahy, A., and Netchine, I. (2008). Olfactory anomalies in CHARGE syndrome: Imaging findings of a potential major diagnostic criterion. *Am. J. Neuroradiol.* 29, 1266–1269. doi: 10.3174/ajnr.A1099

Brambrink, A. M., Back, S. A., Riddle, A., Gong, X., Moravec, M. D., Dissen, G. A., et al. (2012). Isoflurane-induced apoptosis of oligodendrocytes in the neonatal primate brain. *Ann. Neurol.* 72, 525–535. doi: 10.1002/ana.23652

Brambrink, A. M., Evers, A. S., Avidan, M. S., Farber, N. B., Smith, D. J., Zhang, X., et al. (2010). Isoflurane-induced neuroapoptosis in the neonatal rhesus macaque brain. *Anesthesiology* 112, 834–841. doi: 10.1097/ALN.0b013e3181d049cd

Bullmore, E., and Sporns, O. (2012). The economy of brain network organization. *Nat. Rev. Neurosci.* 13, 336–349. doi: 10.1038/nrn3214

Cassidy, A. R., White, M. T., DeMaso, D. R., Newburger, J. W., and Bellinger, D. C. (2015). Executive Function in Children and Adolescents with Critical Cyanotic Congenital Heart Disease. *J. Int. Neuropsychol. Soc.* 21, 34–49. doi: 10.1017/S1355617714001027

Ceschin, R., Zahner, A., Reynolds, W., Gaesser, J., Zuccoli, G., Lo, C. W., et al. (2018). A computational framework for the detection of subcortical brain dysmaturation in neonatal MRI using 3D Convolutional Neural Networks. *NeuroImage* 178, 183–197. doi: 10.1016/j.neuroimage.2018.05.049

De Asis-Cruz, J., Donofrio, M. T., Vezina, G., and Limperopoulos, C. (2017). Aberrant brain functional connectivity in newborns with congenital heart disease before cardiac surgery. *NeuroImage* 17, 31–42. doi: 10.1016/j.nicl.2017.09.020

Feldmann, M., Guo, T., Miller, S. P., Knirsch, W., Kottke, R., Hagmann, C., et al. (2020). Delayed maturation of the structural brain connectome in neonates with congenital heart disease. *Brain Commun.* 2:fcaa209 doi: 10.1093/braincomms/fcaa209

Fernandez-Miranda, J. C., Pathak, S., Engh, J., Jarbo, K., Verstynen, T., Yeh, F. C., et al. (2012). High-definition fiber tractography of the human brain: Neuroanatomical validation and neurosurgical applications. *Neurosurgery* 71, 430–453. doi: 10.1227/NEU.0b013e3182592faa

Gabriel, G. C., Salamacha, N., Reynolds, W. T., Tan, T., Liu, X., Yagi, H., et al. (2018). Characterization of Neurodevelopmental Defects Associated With a Mouse Model of Hypoplastic Left Heart Syndrome. *Circulation* 138, A16609–A16609.

Gao, W., Alcauter, S., Smith, J. K., Gilmore, J. H., and Lin, W. (2014). Development of human brain cortical network architecture during infancy. *Brain Struct. Funct.* 220, 1173–1186. doi: 10.1007/s00429-014-0710-3

Gao, W., Gilmore, J. H., Giovanello, K. S., Smith, J. K., Shen, D., Zhu, H., et al. (2011). Temporal and spatial evolution of brain network topology during the first two years of life. *PLoS One* 6:e25278. doi: 10.1371/journal.pone.0025278

Gao, W., Gilmore, J. H., Shen, D., Smith, J. K., Zhu, H., and Lin, W. (2013). The synchronization within and interaction between the default and dorsal attention networks in early infancy. *Cereb. Cortex* 23, 594–603. doi: 10.1093/cercor/bhs043

Gaynor, J. W., Stopp, C., Wypij, D., Andropoulos, D. B., Atallah, J., Atz, A. M., et al. (2015). Neurodevelopmental outcomes after cardiac surgery in infancy. *Pediatrics* 135, 816–825. doi: 10.1542/peds.2014-3825

Gaynor, J. W., Stopp, C., Wypij, D., Andropoulos, D. B., Atallah, J., Atz, A. M., et al. (2016). Impact of operative and postoperative factors on neurodevelopmental outcomes after cardiac operations. *Ann. Thorac. Surg.* 102, 843–849. doi: 10.1016/j.athoracsur.2016.05.081

Harbison, A. L., Votava-Smith, J. K., Del Castillo, S., Kumar, S. R., Lee, V., Schmithorst, V., et al. (2017). Clinical Factors Associated with Cerebral Metabolism in Term Neonates with Congenital Heart Disease. *J. Pediatr.* 183, 67–73.e1. doi: 10.1016/j.jpeds.2016.12.061

Hetts, S. W., Sherr, E. H., Chao, S., Gobuty, S., and Barkovich, A. J. (2006). Anomalies of the corpus callosum: An MR analysis of the phenotypic spectrum of associated malformations. *Am. J. Roentgenol.* 187, 1343–1348. doi: 10.2214/AJR.05.0146

Humphries, M. D., and Gurney, K. (2008). Network 'small-world-ness': A quantitative method for determining canonical network equivalence. *PLoS One* 3:e0002051. doi: 10.1371/journal.pone.0002051

Jenkins, K. J., Gauvreau, K., Newburger, J. W., Spray, T. L., Moller, J. H., and Iezzoni, L. I. (2002). Consensus-based method for risk adjustment for surgery for congenital heart disease. *J. Thorac. Cardiovasc. Surg.* 123, 110–118. doi: 10.1067/mtc.2002.119064

Ji, W., Ferdman, D., Copel, J., Scheinost, D., Shabanova, V., Brueckner, M., et al. (2020). De novo damaging variants associated with congenital heart diseases contribute to the connectome. *Sci. Rep.* 10:7046. doi: 10.1038/s41598-020-63928-2

Li, Y., Klena, N. T., Gabriel, G. C., Liu, X., Kim, A. J., Lemke, K., et al. (2015). Global genetic analysis in mice unveils central role for cilia in congenital heart disease. *Nature* 521, 520–524. doi: 10.1038/nature14269

Licht, D. J., Shera, D. M., Clancy, R. R., Wernovsky, G., Montenegro, L. M., Nicolson, S. C., et al. (2009). Brain maturation is delayed in infants with complex congenital heart defects. *J. Thorac. Cardiovasc. Surg.* 137, 529–36. doi: 10.1016/j.jtcvs.2008.10.025

Lim, J. M., Porayette, P., Marini, D., Chau, V., Au-Young, S. H., Saini, A., et al. (2019). Associations between age at arterial switch operation, brain growth, and

development in infants with transposition of the great arteries. *Circulation* 139, 2728–2738. doi: 10.1161/CIRCULATIONAHA.118.037495

Limperopoulos, C., Majnemer, A., Shevell, M. I., Rohlicek, C., Rosenblatt, B., Tchervenkov, C., et al. (2002). Predictors of developmental disabilities after open heart surgery in young children with congenital heart defects. *J. Pediatr*. 141, 51–8. doi: 10.1067/mpd.2002.125227

Limperopoulos, C., Tworetzky, W., McElhinney, D. B., Newburger, J. W., Brown, D. W., Robertson, R. L. Jr., et al. (2010). Brain volume and metabolism in fetuses with congenital heart disease: Evaluation with quantitative magnetic resonance imaging and spectroscopy. *Circulation* 121, 26–33. doi: 10.1161/CIRCULATIONAHA.109.865568

Mahle, W. T., Clancy, R. R., Moss, E. M., Gerdes, M., Jobes, D. R., and Wernovsky, G. (2000). Neurodevelopmental outcome and lifestyle assessment in school-aged and adolescent children with hypoplastic left heart syndrome. *Pediatrics* 105, 1082–1089. doi: 10.1542/peds.105.5.1082

Mahle, W. T., Tavani, F., Zimmerman, R. A., Nicolson, S. C., Galli, K. K., Gaynor, J. W., et al. (2002). An MRI study of neurological injury before and after congenital heart surgery. *Circulation* 106, I109–14. doi: 10.1161/01.cir.0000032908.33237.b1

Marelli, A., Miller, S. P., Marino, B. S., Jefferson, A. L., and Newburger, J. W. (2016). Brain in Congenital Heart Disease Across the Lifespan The Cumulative Burden of Injury. *Circulation* 133, 1951–1962. doi: 10.1161/CIRCULATIONAHA.115.019881

Marino, B. S., Lipkin, P. H., Newburger, J. W., Peacock, G., Gerdes, M., Gaynor, J. W., et al. (2012). Neurodevelopmental outcomes in children with congenital heart disease: Evaluation and management: A scientific statement from the American Heart Association. *Circulation* 126, 1143–1172. doi: 10.1161/CIR.0b013e318265ee8a

McQuillen, P. S., Goff, D. A., and Licht, D. J. (2010). Effects of congenital heart disease on brain development. *Prog. Pediatr. Cardiol*. 29, 79–85. doi: 10.1016/j.ppedcard.2010.06.011

McQuillen, P. S., and Miller, S. P. (2010). Congenital heart disease and brain development. *Ann. N Y Acad. Sci.* 1184, 68–86. doi: 10.1111/j.1749-6632.2009.05116.x

Menon, V. (2011). Large-scale brain networks and psychopathology: A unifying triple network model. *Trends Cogn. Sci.* 15, 483–506. doi: 10.1016/j.tics.2011.08.003

Meunier, D., Lambiotte, R., and Bullmore, E. T. (2010). Modular and hierarchically modular organization of brain networks. *Front. Neurosci*. 4:200. doi: 10.3389/fnins.2010.00200

Meyers, B., Lee, V. K., Dennis, L., Wallace, J., Schmithorst, V., Votava-Smith, J. K., et al. (2022). Harmonization of multi-center diffusion tensor tractography in neonates with congenital heart disease: Optimizing post-processing and application of ComBat. *Neuroimage* 2:100114. doi: 10.1016/j.ynirp.2022.100114

Miller, S. P., McQuillen, P. S., Hamrick, S., Xu, D., Glidden, D. V., Charlton, N., et al. (2007). Abnormal brain development in newborns with congenital heart disease. *N. Engl. J. Med.* 357, 1928–1938. doi: 10.1056/NEJMoa067393

Montenegro, M. A., Kinay, D., Cendes, F., Bernasconi, A., Bernasconi, N., Coan, A. C., et al. (2006). Patterns of hippocampal abnormalities in malformations of cortical development. *J. Neurol. Neurosurg. Psychiatry* 77, 367–371. doi: 10.1136/jnnp.2005.070417

Morton, P. D., Korotcova, L., Lewis, B. K., Bhuvanendran, S., Ramachandra, S. D., Zurakowski, D., et al. (2017). Abnormal neurogenesis and cortical growth in congenital heart disease. *Sci. Transl. Med.* 9:eaah7029. doi: 10.1126/scitranslmed.aah7029

Mussatto, K. A., Hoffmann, R. G., Hoffman, G. M., Tweddell, J. S., Bear, L., Cao, Y., et al. (2014). Risk and prevalence of developmental delay in young children with congenital heart disease. *Pediatrics* 133, e570–e577. doi: 10.1542/peds.2013-2309

Panigrahy, A., Ceschin, R., Lee, V., Beluk, N., Khalifa, O., Zuccoli, G., et al. (2014). Respiratory Ciliary Motion Defect Predict Regional Brain Abnormalities and Increased Extra Axial CSF Fluid in Neonates With Complex Congenital Heart Disease. *Circulation* 130, A16570–A16570.

Panigrahy, A., Lee, V., Ceschin, R., Zuccoli, G., Beluk, N., Khalifa, O., et al. (2016). Brain Dysplasia Associated with Ciliary Dysfunction in Infants with Congenital Heart Disease. *J. Pediatr.* 178, 141–148.e1. doi: 10.1016/j.jpeds.2016.07.041

Panigrahy, A., Schmithorst, V. J., Wisnowski, J. L., Watson, C. G., Bellinger, D. C., Newburger, J. W., et al. (2015a). Relationship of white matter network topology and cognitive outcome in adolescents with d-transposition of the great arteries. *NeuroImage Clin.* 7, 438–448. doi: 10.1016/j.nicl.2015.01.013

Panigrahy, A., Votava-Smith, J., Lee, V., Gabriel, G., Klena, N., Gibbs, B., et al. (2015b). Abnormal Brain Connectivity and Poor Neurodevelopmental Outcome in Congenital Heart Disease Patients With Subtle Brain Dysplasia. *Circulation* 132, A16541–A16541. doi: 10.1161/circ.132.suppl_3.16541

Patt, E., Singhania, A., Roberts, A. E., and Morton, S. U. (2022). The genetics of neurodevelopment in congenital heart disease. *Can. J. Cardiol*. [Epub ahead of print]. doi: 10.1016/j.cjca.2022.09.026

Petit, C. J., Rome, J. J., Wernovsky, G., Mason, S. E., Shera, D. M., Nicolson, S. C., et al. (2009). Preoperative brain injury in transposition of the great arteries is associated with oxygenation and time to surgery, not balloon atrial septostomy. *Circulation* 119, 709–16. doi: 10.1161/CIRCULATIONAHA.107.760819

Peyvandi, S., Latal, B., Miller, S. P., and McQuillen, P. S. (2019). The neonatal brain in critical congenital heart disease: Insights and future directions. *Neuroimage* 185, 776–782. doi: 10.1016/j.neuroimage.2018.05.045

Pike, N. A., Woo, M. A., Poulsen, M. K., Evangelista, W., Faire, D., Halnon, N. J., et al. (2016). Predictors of memory deficits in adolescents and young adults with congenital heart disease compared to healthy controls. *Front. Pediatr*. 4:117. doi: 10.3389/fped.2016.00117

Rajagopalan, V., Votava-Smith, J. K., Zhuang, X., Brian, J., Marshall, L., Panigrahy, A., et al. (2018). Fetuses with single ventricle congenital heart disease manifest impairment of regional brain growth. *Prenat. Diagn*. 38, 1042–1048. doi: 10.1002/pd.5374

Ramirez, A., Peyvandi, S., Cox, S., Gano, D., Xu, D. Y., Tymofiyeva, O., et al. (2022). Neonatal brain injury influences structural connectivity and childhood functional outcomes. *PLoS One* 17:e0262310. doi: 10.1371/journal.pone.0262310

Righini, A., Zirpoli, S., Parazzini, C., Bianchini, E., Scifo, P., Sala, C., et al. (2006). Hippocampal infolding angle changes during brain development assessed by prenatal MR imaging. *Am. J. Neuroradiol*. 27, 2093–2097.

Rollins, C. K., Watson, C. G., Asaro, L. A., Wypij, D., Vajapeyam, S., Bellinger, D. C., et al. (2014). White Matter Microstructure and Cognition in Adolescents with Congenital Heart Disease. *J. Pediatr.* 165, 936–44.e1–2. doi: 10.1016/j.jpeds.2014.07.028

Rubinov, M., and Sporns, O. (2010). Complex network measures of brain connectivity: Uses and interpretations. *Neuroimage* 52, 1059–1069. doi: 10.1016/j.neuroimage.2009.10.003

Sananes, R., Goldberg, C. S., Newburger, J. W., Hu, C., Trachtenberg, F., Gaynor, J. W., et al. (2021). Six-year neurodevelopmental outcomes for children with single-ventricle physiology. *Pediatrics* 147:e2020014589. doi: 10.1542/peds.2020-014589

Sato, N., Hatakeyama, S., Shimizu, N., Hikima, A., Aoki, J., and Endo, K. (2001). MR evaluation of the hippocampus in patients with congenital malformations of the brain. *Am. J. Neuroradiol*. 22, 389–393.

Schiller, R. M., van den Bosch, G. E., Muetzel, R. L., Smits, M., Dudink, J., Tibboel, D., et al. (2017). Neonatal critical illness and development: White matter and hippocampus alterations in school-age neonatal extracorporeal membrane oxygenation survivors. *Dev. Med. Child Neurol*. 59, 304–310. doi: 10.1111/dmcn.13309

Schmithorst, V. J., Panigrahy, A., Gaynor, J. W., Watson, C. G., Lee, V., Bellinger, D. C., et al. (2016). Organizational topology of brain and its relationship to ADHD in adolescents with d-transposition of the great arteries. *Brain Behav*. 6:e00504. doi: 10.1002/brb3.504

Schmithorst, V. J., Votava-Smith, J. K., Tran, N., Kim, R., Lee, V., Ceschin, R., et al. (2018). Structural network topology correlates of microstructural brain dysmaturation in term infants with congenital heart disease. *Hum. Brain Mapp*. 39, 4593–4610. doi: 10.1002/hbm.24308

Shi, F., Wang, L., Peng, Z., Wee, C.-Y., and Shen, D. (2013). Altered modular organization of structural cortical networks in children with autism. *PLoS One* 8:e63131. doi: 10.1371/journal.pone.0063131

Shi, F., Yap, P.-T., Wu, G., Jia, H., Gilmore, J. H., Lin, W. Y., et al. (2011). Infant brain atlases from neonates to 1-and 2-year-olds. *PLoS One* 6:e18746. doi: 10.1371/journal.pone.0018746

Smith, S. M., Jenkinson, M., Johansen-Berg, H., Rueckert, D., Nichols, T. E., Mackay, C. E., et al. (2006). Tract-based spatial statistics: Voxelwise analysis of multi-subject diffusion data. *Neuroimage* 31, 1487–1505. doi: 10.1016/j.neuroimage.2006.02.024

Stinnett, G. R., Lin, S., Korotcov, A. V., Korotcova, L., Morton, P. D., Ramachandra, S. D., et al. (2017). Microstructural Alterations and Oligodendrocyte Dysmaturation in White Matter After Cardiopulmonary Bypass in a Juvenile Porcine Model. *J. Am. Heart Assoc*. 6:e005997. doi: 10.1161/JAHA.117.005997

Subramanian, S., Soundara Rajan, D., Gaesser, J., Wen-Ya Lo, C., and Panigrahy, A. (2019). Olfactory bulb and olfactory tract abnormalities in acrocallosal syndrome and Greig cephalopolysyndactyly syndrome. *Pediatr. Radiol.* 49, 1368–1373. doi: 10.1007/s00247-019-04480-8

Sun, L., Macgowan, C. K., Sled, J. G., Yoo, S. J., Manlhiot, C., Porayette, P., et al. (2015). Reduced fetal cerebral oxygen consumption is associated with smaller brain size in fetuses with congenital heart disease. *Circulation* 131, 1313–1323. doi: 10.1161/CIRCULATIONAHA.114.013051

Tabbutt, S., Nord, A. S., Jarvik, G. P., Bernbaum, J., Wernovsky, G., Gerdes, M., et al. (2008). Neurodevelopmental outcomes after staged palliation for hypoplastic left heart syndrome. *Pediatrics* 121, 476–483. doi: 10.1542/peds.2007-1282

Telesford, Q. K., Joyce, K. E., Hayasaka, S., Burdette, J. H., and Laurienti, P. J. (2011). The ubiquity of small-world networks. *Brain Connect*. 1, 367–375. doi: 10.1089/brain.2011.0038

Thomason, M. E., Brown, J. A., Dassanayake, M. T., Shastri, R., Marusak, H. A., Hernandez-Andrade, E., et al. (2014). Intrinsic functional brain architecture derived from graph theoretical analysis in the human fetus. *PLoS One* 9:e94423. doi: 10.1371/journal.pone.0094423

Thomason, M. E., Grove, L. E., Lozon, T. A. Jr., Vila, A. M., Ye, Y., Nye, M. J., et al. (2015). Age-related increases in long-range connectivity in fetal functional neural connectivity networks in utero. *Dev. Cogn. Neurosci.* 11, 96–104. doi: 10.1016/j.dcn.2014.09.001

Uehara, T., Tobimatsu, S., Kan, S., and Miyauchi, S. (2012). *Modular Organization of Intrinsic Brain Networks: A Graph Theoretical Analysis of Resting-state fMRI*. Kobe: IEEE. doi: 10.1109/ICCME.2012.6275597

van der Linde, D., Konings, E. E., Slager, M. A., Witsenburg, M., Helbing, W. A., Takkenberg, J. J., et al. (2011). Birth prevalence of congenital heart disease worldwide: A systematic review and meta-analysis. *J. Am. Coll. Cardiol.* 58, 2241–2247. doi: 10.1016/j.jacc.2011.08.025

Volpe, J. J. (2014). Encephalopathy of Congenital Heart Disease- Destructive and Developmental Effects Intertwined. *J. Pediatr.* 164, 962–965. doi: 10.1016/j.jpeds.2014.01.002

Votava-Smith, J. K., Schmithorst, V. J., Tran, N., Soleymani, S., Abbott, J., Lee, V., et al. (2017). Impaired Pre-Operative Cerebral Autoregulation is Associated With Functional Brain Dysmaturation in Neonatal Congenital Heart Disease. *Circulation* 136, A15580–A15580.

Wernovsky, G., and Licht, D. J. (2016). Neurodevelopmental Outcomes in Children With Congenital Heart Disease-What Can We Impact? *Pediatr. Crit. Care Med.* 17, S232–S242. doi: 10.1097/PCC.0000000000000800

Zahid, M., Bais, A., Tian, X., Devine, W., Lee, D. M., Yau, C., et al. (2018). Airway ciliary dysfunction and respiratory symptoms in patients with transposition of the great arteries. *PLoS One* 13:e0191605. doi: 10.1371/journal.pone.0191605

frontiers | Frontiers in Neuroscience

TYPE Original Research
PUBLISHED 25 November 2022
DOI 10.3389/fnins.2022.932386

OPEN ACCESS

EDITED BY
Dan Wu,
Zhejiang University, China

REVIEWED BY
Linda De Vries,
Leiden University Medical Center (LUMC), Netherlands
Tengda Zhao,
Beijing Normal University, China

*CORRESPONDENCE
Jessica Dubois
jessica.dubois@centraliens.net

†These authors have contributed equally to this work and share first authorship

SPECIALTY SECTION
This article was submitted to Neurodevelopment, a section of the journal Frontiers in Neuroscience

RECEIVED 29 April 2022
ACCEPTED 10 November 2022
PUBLISHED 25 November 2022

CITATION
Neumane S, Gondova A, Leprince Y, Hertz-Pannier L, Arichi T and Dubois J (2022) Early structural connectivity within the sensorimotor network: Deviations related to prematurity and association to neurodevelopmental outcome. *Front. Neurosci.* 16:932386. doi: 10.3389/fnins.2022.932386

Early structural connectivity within the sensorimotor network: Deviations related to prematurity and association to neurodevelopmental outcome

Sara Neumane[1,2,3†], Andrea Gondova[1,2†], Yann Leprince[2], Lucie Hertz-Pannier[1,2], Tomoki Arichi[3,4] and Jessica Dubois[1,2*]

[1]Inserm, NeuroDiderot, Université Paris Cité, Paris, France, [2]CEA, NeuroSpin UNIACT, Université Paris-Saclay, Paris, France, [3]School of Biomedical Engineering and Imaging Sciences, Centre for the Developing Brain, King's College London, London, United Kingdom, [4]Paediatric Neurosciences, Evelina London Children's Hospital, Guy's and St Thomas' NHS Foundation Trust, London, United Kingdom

Consisting of distributed and interconnected structures that interact through cortico-cortical connections and cortico-subcortical loops, the sensorimotor (SM) network undergoes rapid maturation during the perinatal period and is thus particularly vulnerable to preterm birth. However, the impact of prematurity on the development and integrity of the emerging SM connections and their relationship to later motor and global impairments are still poorly understood. In this study we aimed to explore to which extent the early microstructural maturation of SM white matter (WM) connections at term-equivalent age (TEA) is modulated by prematurity and related with neurodevelopmental outcome at 18 months corrected age. We analyzed 118 diffusion MRI datasets from the developing Human Connectome Project (dHCP) database: 59 preterm (PT) low-risk infants scanned near TEA and a control group of full-term (FT) neonates paired for age at MRI and sex. We delineated WM connections between the primary SM cortices (S1, M1 and paracentral region) and subcortical structures using probabilistic tractography, and evaluated their microstructure with diffusion tensor imaging (DTI) and neurite orientation dispersion and density imaging (NODDI) models. To go beyond tract-specific univariate analyses, we computed a *maturational distance related to prematurity* based on the multi-parametric Mahalanobis distance of each PT infant relative to the FT group. Our results confirmed the presence of microstructural differences in SM tracts between PT and FT infants, with effects increasing with lower gestational age at birth. Maturational distance analyses highlighted that prematurity has a differential effect on SM tracts with higher distances and thus impact on (i) cortico-cortical than cortico-subcortical connections; (ii) projections involving S1 than M1 and paracentral region; and (iii) the most rostral cortico-subcortical tracts, involving the lenticular nucleus. These different alterations at TEA suggested that vulnerability follows a specific pattern coherent with the established

WM caudo-rostral progression of maturation. Finally, we highlighted some relationships between NODDI-derived maturational distances of specific tracts and fine motor and cognitive outcomes at 18 months. As a whole, our results expand understanding of the significant impact of premature birth and early alterations on the emerging SM network even in low-risk infants, with possible relationship with neurodevelopmental outcomes. This encourages further exploration of these potential neuroimaging markers for prediction of neurodevelopmental disorders, with special interest for subtle neuromotor impairments frequently observed in preterm-born children.

KEYWORDS

brain development, tractography, diffusion MRI (dMRI), Diffusion Tensor Imaging (DTI), NODDI (neurite orientation dispersion and density imaging), multivariate Mahalanobis distance, preterm at term-equivalent age, white matter microstructure maturation

Introduction

The cerebral somatosensory and motor systems consist of distributed networks of specialized interconnected cortical and subcortical gray matter (GM) regions, interacting through white matter (WM) tracts, that support a wide variety of sensory and motor functions that are essential for nearly every human behavior across the lifespan. In somatosensation, inputs from peripheral receptors are first conveyed by peripheral nerves, then through the spinal cord to the *brainstem* dorsal column nuclei. These nuclei further connect to the thalamus which sends projections to cortical somatosensory areas, particularly the *primary somatosensory cortex* (S1) located on the *postcentral gyrus*. On the other hand, the *primary motor cortex* (M1) in the *precentral gyrus*, is critical for motor behavior, exerting its influence over the body's muscles through its output to a variety of descending pathways, the main being the direct cortical innervation of motoneurons *via* the corticospinal tract (CST). S1 and M1 are reciprocally connected, *directly via* short-range intra-hemispheric and homotopic interhemispheric pathways, and *indirectly via* some cortico-subcortical pathways predominately involving the *thalamus* and the *basal ganglia* (BG). The BG notably include the *caudate nucleus*, *putamen* and *globus pallidus*: the first two functionally constitute the striatum (receiving most of the BG inputs), while the last two are grouped anatomically in the lenticular nucleus, with the globus pallidus representing one of the key output structures of the BG (Leisman et al., 2014).

Interactions between somatosensory and motor systems, observable in mature brains (Hatsopoulos and Suminski, 2011; Tomasino and Gremese, 2016), are particularly important during the early stages of neurodevelopment. The late second and third trimesters of gestation, as well as the neonatal period, are a critical time for the dynamic refinement and maturation of brain networks through several complex processes (Dubois et al., 2014; Kostović et al., 2019), laying the foundations of structural connectivity that underlie later neurodevelopment (Gilmore et al., 2018). As projection and interhemispheric tracts show rapid growth before 28 weeks of gestational age (wGA) (Keunen et al., 2017; Kostović et al., 2019), the general architecture of the *sensorimotor* (SM) network is already established during the preterm period, making it one of the earliest brain systems to mature (Dubois et al., 2014; Ouyang et al., 2019; Machado-Rivas et al., 2021). It may therefore play a pivotal role for the optimal development of secondary and associative networks in their earliest stages and for organizing the structural and functional connectome throughout the neonatal period (Ball et al., 2014; van den Heuvel et al., 2015; Zhao et al., 2019).

This crucial maturation phase is also highlighted by the adverse effects of preterm birth (before 37wGA) on neurodevelopment. The sudden need to adapt to extra-uterine life does not provide the optimal conditions for

Abbreviations: AD, axial diffusivity; BG, basal ganglia; BSID-III, Bayley Scales of Infant and Toddler Development, 3rd edition; Bstem, brainstem; Caud, caudate nucleus; CLD, chronic lung disease; CSF, cerebrospinal fluid; CST, corticospinal tract; cUS, cranial ultrasonography; dHCP, developing Human Connectome Project; dMRI, diffusion-weighted MRI; DTI, diffusion tensor imaging; FA, fractional anisotropy; FDR, false discovery rate; FT, full-term born infants [FT_{EVCt}, "extreme to very preterms" matched FT controls, FT_{MLCt}, "moderate to late preterms" matched FT controls]; GA, gestational age; GM, gray matter; IMD, index of multiple deprivation; IUGR, intrauterine growth restriction; Lenti, lenticular nucleus; M1, lateral portion of the primary motor cortex (precentral region); mCA, months of corrected age; MD, Mean diffusivity; MRI, magnetic resonance imaging; NDI, neurite density index; NEC, necrotizing enterocolitis; NICU, neonatal intensive care unit; NODDI, neurite orientation dispersion and density imaging; ODI, orientation dispersion index; ParaC, medial portions of the primary sensori-motor cortices (paracentral region); PMA, post-menstrual age; PT, preterm infants [PT_{EV}, extreme to very preterms, PT_{ML}, moderate to late preterms]; RD, radial diffusivity; ROIs, regions of interest; ROP, retinopathy of prematurity; S1, lateral portion of the primary somatosensory cortex (postcentral region); SES, socio-economic status; Thal, thalamus; TEA, term-equivalent age; wGA, weeks of GA; WM, white matter.

physiological neurodevelopmental mechanisms, resulting in variable structural and/or functional abnormalities (Suzuki, 2007). The related diffuse cerebral dysmaturation (Back, 2015; Volpe, 2021) alters the integrity of the emerging neural networks (Suzuki, 2007; Back, 2015), with early maturing regions suffering the largest adverse effects with a greater degree of prematurity (lower GA at birth) (Knight et al., 2018).

Magnetic resonance imaging (MRI) including diffusion MRI (dMRI) has been extensively used to evaluate the consequences of preterm birth on brain development. Even in the absence of focal cerebral lesions, prematurity is associated with disturbances in brain growth, in particular in GM structures including the BG and thalamus (Keunen et al., 2012; Padilla et al., 2015; Loh et al., 2020), and pervasive widespread abnormalities in GM and WM microstructure, maturation and connectivity (Ball et al., 2013b; Batalle et al., 2018). In particular, the WM of preterm infants at term-equivalent age (TEA) has a more "immature" microstructural profile compared with term-born neonates, consistent with delayed and/or disrupted WM development and maturation (Thompson et al., 2011; Kelly et al., 2016a, 2020). The extent of early WM abnormalities (even in the absence of overt brain lesion) has been related to poorer neurodevelopmental outcome (Duerden et al., 2015; Barnett et al., 2018; Kelly et al., 2020; Pannek et al., 2020). Preterm infants are also at higher risk of impaired neuromotor function (Williams et al., 2010; Odd et al., 2013; Spittle and Orton, 2014), that can manifest as poorer fine and gross motor skills compared with term-born controls (Evensen et al., 2020). Although long-lasting WM alterations in SM tracts have been observed during childhood and adolescence in these populations (Groeschel et al., 2014; Dewey et al., 2019; Thompson et al., 2020), the relationship between neonatal SM network structural alterations and neuromotor impairment in *low-risk preterm* infants (including moderate to late preterm and/or preterm babies without perinatal brain injury) has been less systematically explored. Also, assessing early WM *maturational delays* across the different SM tracts and analyzing the correlation with outcome would enable a better understanding of the pathophysiology of the disorders resulting from deviations in typical developmental processes.

In this study, we thus aimed to assess how preterm birth impacts SM network maturation at TEA in the absence of overt cerebral lesions, and the potential effect on later neurodevelopmental outcome. We hypothesized that SM network would show significantly altered microstructure in preterm infants compared to full-term neonates, with distinct patterns of maturation delay across the SM tracts, and that these alterations are associated with motor and global neurodevelopmental outcomes. For this purpose, we studied a large cohort of low-risk preterm infants at TEA and full-term neonates from the *developing Human Connectome Project* (dHCP) (Edwards et al., 2022), and investigated the effects of prematurity on WM microstructure and maturation of SM tracts using complementary approaches based on diffusion MRI data and tractography (Dubois et al., 2014, 2016; Ouyang et al., 2019). We dissected an unprecedented set of SM cortico-cortical and cortico-subcortical tracts and computed quantitative metrics from two complementary models: the widely used Diffusion Tensor Imaging (DTI) model (Dubois et al., 2014; Pecheva et al., 2018; Ouyang et al., 2019) and the more specific 3 tissue compartments model of neurite orientation dispersion and density imaging (NODDI) (Zhang et al., 2012; Kunz et al., 2014; Batalle et al., 2017; Kimpton et al., 2021). To overcome the limitations inherent to univariate dMRI approaches which cannot reflect the inter-related complexity of processes involved in early brain maturation, we used the *multivariate Mahalanobis distance* approach to compare the preterm and full-term groups (Kulikova et al., 2015; Dean et al., 2017; Li et al., 2022). This allowed us to consider multiple metrics and to quantify the tract-specific maturational gap at TEA between a preterm infant and the reference group of full-term neonates, with the added advantage of taking into account inter-subject variability in the reference group, as well as correlations between input metrics. Moreover, using the Mahalonobis distance measure with different sets of DTI and NODDI complementary metrics allowed the effect of maturation and complex underlying WM microstructural processes to be accounted for. Finally, we evaluated the relationships between the aforementioned distances for the different SM connections and neurodevelopmental outcome at 18 months of corrected age (mCA).

Materials and methods

Subjects

This study included a sample of preterm and full-term neonates taken from the dHCP cohort, collected at St Thomas' Hospital London, UK from 2015 to 2020.[1] This project received UK NHS research ethics committee approval (14/LO/1169, IRAS 138070), and written informed consent was obtained from the parents of all participant infants. From the overall cohort, we identified 59 preterm (PT) infants (33 males, gestational age at birth – GA at birth: median 31.7 weeks, range [23.7w–36.0w]) scanned near TEA (median post-menstrual age – PMA: 41.3w, range [38.4w–44.9w]), and a control group of 59 full-term born (FT) infants (GA at birth: median 40.1w, range [37.4w–42.3w]) matched to the preterm population on age at MRI and sex. Preterm infants were subdivided into infants born extremely to very preterm (GA at birth < 32w, $N = 33$; PT_{EV} group) or moderate to late preterm (GA at birth ≥ 32w, $N = 26$; PT_{ML} group). The corresponding controls

1 http://www.developingconnectome.org/

are subsequently noted FT_{EVCt} and FT_{MLCt}, respectively. All included infants were deemed healthy at TEA, i.e., were without major brain focal lesions or any overt abnormality of clinical significance on structural MRI as evaluated by an expert pediatric neuroradiologist (dHCP radiological score in the range 1–3).[2]

Neonatal characteristics at birth

Obstetric factors (i.e., multiple pregnancy status, intrauterine growth restriction –IUGR, maternal antenatal steroids and magnesium therapy, delivery method) as well as *infant characteristics at birth* (i.e., Apgar scores at 1 and 5 min, birth weight, length, and head circumference) were extracted from the dHCP records.

Specific *postnatal risk factors* previously recognized to be related with neonatal brain abnormalities, including diffuse and regional WM microstructural alterations (Pogribna et al., 2013; Brouwer et al., 2017; Barnett et al., 2018; Parikh et al., 2021), were also considered. These included NICU variables (i.e., total duration of ventilatory support and oxygen therapy, and parenteral nutrition) which were binarized using thresholds established in previous studies (need of mechanical ventilation beyond 7 days, and of parenteral nutrition longer than 21 days) (Brouwer et al., 2017). Sepsis was considered as any situation where an infant received antibiotics, as there was not enough information to retain only confirmed episodes of postnatal sepsis. Additionally, we derived a *neonatal morbidities* binary factor to summarize the presence of at least one of the following 4 morbidities associated with prematurity (or the absence of all 4): chronic lung disease, necrotizing enterocolitis (NEC), retinopathy of prematurity (ROP) and abnormal cranial ultrasonography (cUS). Of note, detailed neonatal medical records were available only for infants admitted to the neonatal intensive care unit (NICU) after birth: 51 PT (86%) and 2 FT (3%, admitted for sepsis treatment, without further complications).

Comparisons between PT and FT groups in terms of the described variables and factors were performed with suitable tests (Wilcoxon rank sum test for ordinal and continuous variables; Fisher's exact test for binary factors; Pearson's Chi-squared test for non-binary nominal factors) in R (version 4.0.5, 2021.03.31).

Outcome assessment and infant characteristics at 18 months

Family socio-economic status (SES) was measured using the index of multiple deprivation (IMD) which is a UK geographically defined composite social risk score comprising data on income, employment, health, education, living environment, and crime calculated from the mother's home address at the time of birth.

Neurodevelopmental outcome was assessed at St Thomas' Hospital, London by two experienced assessors using the Bayley Scales of Infant and Toddler Development, Third Edition – BSID-III (Bayley, 2006). We only considered assessments performed at around 18 mCA (between 17 and 21 m), which was available for 44 (75%) PT infants and 53 (90%) FT infants (median age: 18.3 m). Five distinct developmental categories (cognition, receptive and expressive language, and fine and gross motor function) were assessed yielding age-standardized respective *scaled scores* (mean 10, SD 3), with higher values indicating better infant development and scores lower than 7 indicating developmental delay in that domain.

Comparisons between PT and the FT groups were performed with *t*-tests corrected for multiple comparisons using Benjamini–Hochberg false discovery rate (FDR) correction across scores. The effect of sub-groups (PT_{EV}, PT_{ML}, FT_{EVCt}, and FT_{MLCt}) on neurodevelopmental outcomes was assessed using one-way ANOVA.

Of note, the 5 BSID-III scaled scores can be summarized into the widely used 3 *composite* cognitive, language, and motor scores (mean 100, SD 15). The results of the entire analyses performed using them can be found in the **Supplementary materials**: *BSID-III composite score results* section.

Magnetic resonance imaging data acquired at term-equivalent age

Magnetic resonance imaging (MRI) data was acquired using a Philips 3-Tesla Achieva scanner (Philips Medical Systems, Best, Netherlands). All infants were scanned during natural sleep using a neonatal head coil and imaging system optimized for the dHCP study as previously described (Hughes et al., 2017).

We used anatomical and diffusion MRI data available in its pre-processed state from the dHCP database (third release) (Edwards et al., 2022). The *structural* data was a result of acquisition and reconstruction using optimized protocols (Cordero-Grande et al., 2018) leading to super-resolved T2w images with an isotropic spatial voxel size of 0.5 mm. Processing followed a dedicated pipeline for segmentation and cortical surface extraction for T2w images of neonatal brains (Makropoulos et al., 2018), with bias-correction, brain extraction, and segmentation using Draw-EM (Developing brain Region Annotation with Expectation Maximisation) algorithm (Makropoulos et al., 2014). White matter surface (inner cortical surface) meshes provided within the dHCP database were used for the segmentation of cortical regions of interest (ROIs), while volumetric segmentations were directly used to extract subcortical ROIs (cf. section *Selection and delineation of regions of interest*). Additionally, derived hemispheric, WM and cortical masks (also referred to as cortical ribbons) were also used for the tractography analysis (cf. section *SM connectivity reconstruction*).

2 https://biomedia.github.io/dHCP-release-notes/download.html

Acquisition and reconstruction of the *diffusion* data followed a multi-shell high angular resolution diffusion imaging (HARDI) protocol with 4 b-shells (b = 0 s/mm^2: 20 repeats; and b = 400, 1,000, 2,600 s/mm^2: 64, 88, and 128 directions, respectively) (Hutter et al., 2018) and was pre-processed with correction for motion artifacts and slice-to-volume reconstruction using the SHARD approach, leading to an isotropic voxel size of 1.5 mm (Christiaens et al., 2021).

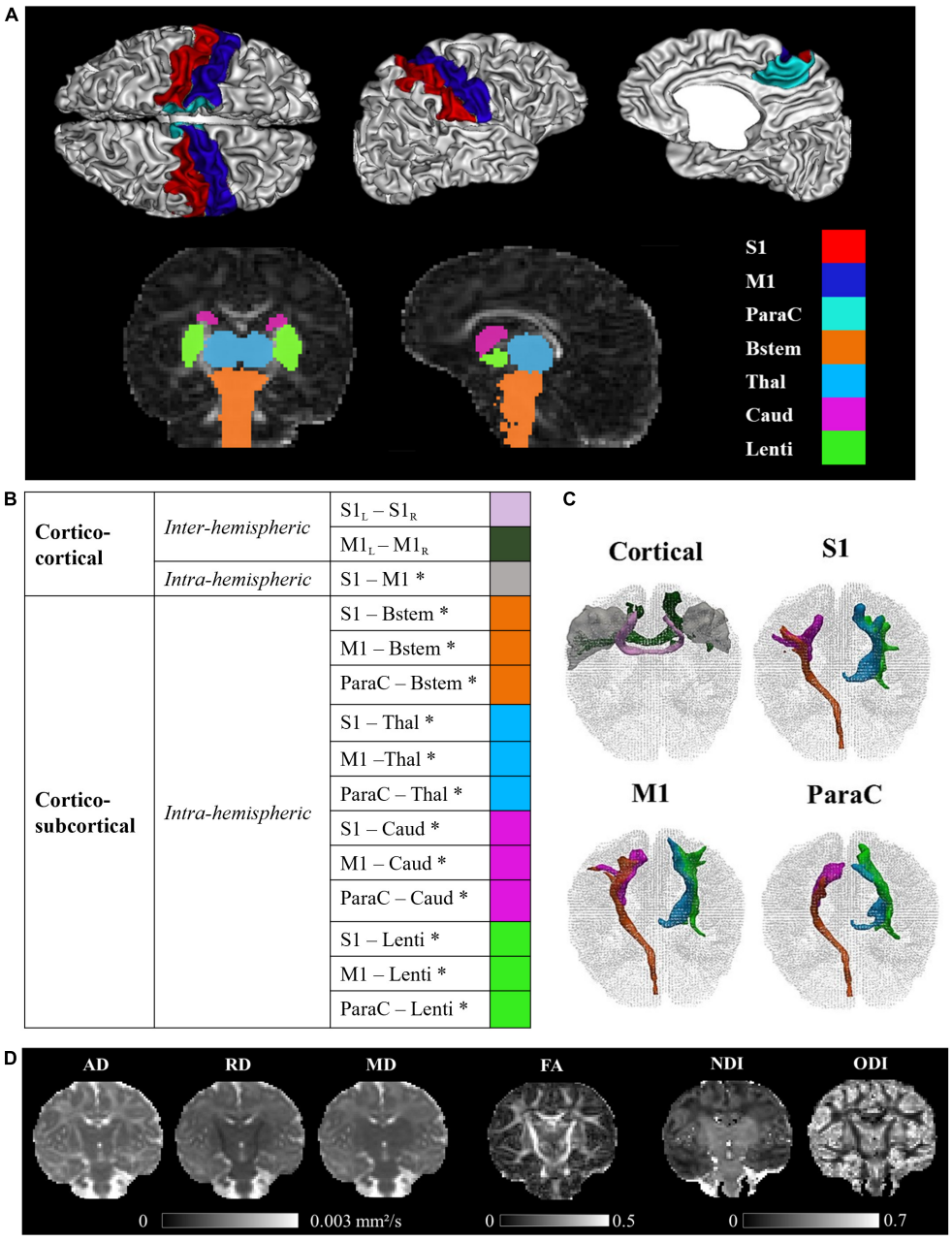

FIGURE 1
Regions of interest, sensorimotor tracts, and diffusivity metrics for a representative full-term infant (GA at birth 40.4w, PMA at MRI 44.1w). **(A)** Visualization of the cortical and subcortical ROIs used as tractography seeds. **(B)** List of the SM tracts of interest. **(C)** 3D reconstructions of SM tracts. **(D)** Metric maps resulting from DTI (AD, RD, MD, FA) and NODDI (NDI, ODI) models. GA, gestational age (in weeks); PMA, post-menstrual age (in weeks); ROIs, regions of interest; SM, sensorimotor; S1, lateral portion of the primary somatosensory cortex (postcentral gyrus); M1, lateral portion of the primary motor cortex (precentral gyrus); ParaC, medial portions of the primary sensorimotor cortices (paracentral area); Bstem, brainstem; Thal, thalamus; Caud, caudate nucleus; Lenti, lenticular nucleus; L, left; R, right. *Intra-hemispheric tracts, evaluated in left and right hemispheres separately. DTI, diffusion tensor imaging; metrics: AD, axial diffusivity; RD, radial diffusivity; MD, mean diffusivity; FA, fractional anisotropy; NODDI, neurite orientation dispersion and density imagingmetrics; NDI, neurite density index; ODI, orientation dispersion index.

Pre-processed data was used for the fitting of diffusion models (cf. section *Estimation of diffusion models*) and for the tractography analysis (cf. section *SM connectivity reconstruction*).

Assessment of sensorimotor network microstructure

To estimate WM microstructural characteristics within the SM network, we first quantified complementary diffusion metrics from the available diffusion data. Structural connections between pairs of anatomically defined SM regions, including cortical primary SM cortices and key sub-cortical structures, were delineated using probabilistic tractography. The diffusion metrics were then extracted for the selected connections of interest and used to study developmental differences between the cohort subgroups.

Estimation of diffusion models

The DTI model was fitted to the diffusion data using a single shell (b = 1,000 s/mm^2) and calculated with FSL's DTIFIT. The choice of using only a single b-value was made because the utility of including more diffusion directions may be outweighed by the non-Gaussian contribution of high b-value acquisitions (Pines et al., 2020). DTI maps were computed for four metrics: fractional anisotropy (FA) and Mean Diffusivity (MD) which are a composite of axial diffusivity (AD) and radial diffusivity (RD).

Additionally, multi-shell diffusion data were used to derive the NDI and ODI maps from the NODDI model (Zhang et al., 2012) using the CUDA 9.1 Diffusion Modelling Toolbox (cuDIMOT) NODDI Watson model implementation for GPUs (Hernandez-Fernandez et al., 2019). We used the MCMC optimization algorithm and default settings to fit the NODDI model to our infant data. The NODDI-derived maps were then post-processed to reduce the observed noise. Briefly, we used ODI maps to detect possible errors using an alpha-trimming strategy. The voxels presenting values outside the threshold range (fixed upper value of 0.95 and the lower limit being the first groove of the histogram of values) were either (i) normalized by the immediate surrounding values (i.e., the mean of the voxel's immediate environment after the removal of extreme values), or (ii) set to 0, if no voxels in the "normal" range were found in their environment. The same erroneous voxels were also corrected in NDI maps in the same fashion.

Selection and delineation of regions of interest

Pre-processed structural data was used to parcellate 13 ROIs (6 in each hemisphere and 1 bilateral, **Figure 1A**) relevant for the developing SM network, focusing on the primary core of cortical and deep GM structures. Regarding cortical regions, we considered *primary sensory* and *motor cortices* which are essential for processing peripheral somatosensory inputs and for initiating and controlling motor behaviors, through cortico-subcortical loops including *thalamus*, *BG* and *brainstem*. We then disregarded non-primary cortical areas, which mature later during typical development. Three cortical ROIs were thus defined on the cortical surface of each hemisphere using the M-CRIB-S surface-based parcellation tool optimized for the term-born neonates (Adamson et al., 2020) whose labeling scheme replicates the Desikan-Killiany-Tourville (DKT) atlas (Klein and Tourville, 2012): the postcentral gyrus as the anatomical proxy of the lateral portion of the primary somatosensory cortex (hereafter referred to as *S1* for the sake of simplification), the precentral gyrus as the lateral portion of the primary motor cortex (referred to as *M1*), and the paracentral lobule (referred to as *ParaC*) corresponding to the medial surface of the hemisphere in the continuation of the precentral and postcentral gyri, including the medial portions of the primary SM cortices. The central sulcus was required as a landmark to delineate these pre- and post-central regions, explaining the choice of a surfacic parcellation tool. Individual surface ROIs were then projected to the cortical ribbon defined in the anatomical volumes, and further dilated by one voxel into the WM to ease the tractography process.

Regarding sub-cortical structures, the most relevant to be studied at early developmental stages are the main input/output and relay structures, implicating in particular the brainstem, the thalamus, the dorsal striatum (composed of the putamen and caudate nucleus) that can be considered as the main BG input structure for SM projections, and the internal segment of the globus pallidus (GPi), one of the major output structures of the BG (Leisman et al., 2014). Identifying these specific GM structures on MR images is quite challenging in infants due to the inter-subject variability and rapid changes in morphological characteristics and sizes during the perinatal period. In addition, the precise segmentation of structures of interest also depends on the possibilities offered by the tool validated for neonatal population. The subcortical ROIs were thus defined using a volumetric GM parcellation based on Draw-EM algorithm segmentation (Makropoulos et al., 2014) provided within the dHCP data release, namely medial brainstem (*Bstem*) and for each hemisphere: thalamus (*Thal*, fusing high and low intensity regions), caudate nucleus (*Caud*, part of the striatum) and lenticular nucleus (*Lenti*, containing the putamen as well as the GPi).

These cortical ROIs (bilateral M1, S1, and ParaC region) and subcortical ROIs (brainstem and bilateral thalamus, caudate and lenticular nuclei), used as seeds for the tractography, were aligned to the diffusion space with FSL 6.0's FLIRT.

Sensorimotor connectivity reconstruction

Individual dissections of SM connections, which to our knowledge have never been achieved in neonates and infants until now, were performed using an automated tractography-based approach benefitting from multi-shell MRI data. For each

subject, probabilistic tractography estimating multiple diffusion orientations within a voxel (Behrens et al., 2007) was used to reconstruct connections between the selected ROI pairs (designated as *tracts* thereafter). Briefly, for each subject, we first modeled crossing fibers within each voxel of the multi-shell diffusion data using a GPU accelerated version of FSL's Bayesian Estimation of Diffusion Parameters Obtained using Sampling Techniques modelling Crossing Fibres (BEDPOSTX), with default settings apart from the deconvolution model with zeppelins (Hernández et al., 2013). Then, the pre-selected ROIs were used as seed masks to derive region-to-region structural connections using the GPU implementation of the Probabilistic Tractography with crossing fibers (ProbTrackX) available with FSL 6.0 (Hernandez-Fernandez et al., 2019), and the default (one-way) setting with a loop check. The resulting output describe the density of WM connections between the ROI pair.

To improve the tractography results, and to reduce the incidence of erroneous streamlines, we employed exclusion masks. These exclusion masks were based on a mask of CSF created by thresholding the MD maps (voxels with $MD > 2.10^{-3} mm^2/s$ were considered as CSF) and corrected by removing voxels with $FA > 0.25$ (which might correspond to WM voxels in the corpus callosum but close to the ventricles with CSF partial volume effects). The exclusion masks were further adapted to exclude all other brain structures apart from the considered ROIs pair. Additionally, where the pair of ROIs were ipsilateral, i.e., in a single hemisphere, the entire contralateral hemisphere was also excluded. No supplementary constraints were included in the tractography runs.

Reconstructed tracts were then thresholded at 5% of the maximum fiber density of the evaluated tract. This was not performed for cortico-cortical inter-hemispheric tracts, whose reconstructions were used in their original state due to low streamline numbers.

The final list of SM tracts of interest (corresponding to homotopic inter-hemispheric tracts, short-range S1–M1 intra-hemispheric tracts, and long-range intra-hemispheric cortico-subcortical tracts) is described in **Figure 1B** We visually validated the accuracy of the tracts reconstructions for several subjects and observed expected topographies (e.g., the S1 and M1 projections toward the ventral anterior and lateral portions of the thalami). Note that the (inter- and intra-hemispheric) cortico-cortical tracts involving paracentral regions could not be evaluated due to frequent and variable tractography errors identified upon visual examination. Also, connections between subcortical structures were not studied because of their proximity which could alter the tractography performance.

Extraction of tract-specific metrics

DTI and NODDI-derived metrics (FA, MD, AD, RD, NDI, ODI) were extracted from each individual tract by calculating the weighted average value (metric $\bar{X}$) using the following equation:

$$\bar{X} = \frac{\sum(d_i \times X_i)}{\sum d_i}$$

where i denotes the tract voxels, d_i is the fiber density at voxel i of a tract, and X_i is value of the metric at voxel i (Hua et al., 2008). This weighted approach gave more weight to the central portion (with higher fiber density) compared to the tract periphery, rendered the measures independent on the number of streamlines assessed by the tractography algorithm, and limited the effect of potential artifacts related to tractography reconstruction.

Univariate tract-specific analyses

To investigate tract-specific relationships between the diffusion metrics and subject characteristics (prematurity, clinical factors, etc.), we performed three sets of univariate analyses on the tract diffusion metrics (see **Supplementary materials**: *Descriptive univariate analysis* section for the methods and results). This allowed us to identify parameters for the later multivariate analysis. In the univariate analyses, we did not observe interaction between hemisphere and the infant group for any of the six evaluated metrics justifying the *averaging* of the diffusion metrics over the *left and right tracts*. Additionally, evaluated clinical variables were not associated, or were only weakly associated, with the diffusion metrics in the PT group, which led us not to consider them as confounders. In contrast, we observed a strong association between the tract-specific diffusion metrics and (i) infant group (PT_{EV}, PT_{ML}, FT) or GA at birth; (ii) PMA at scan; and (iii) WM residuals (estimated as the residuals of the linear model considering the metric averaged over the whole WM mask as a function of GA at birth and PMA at scan). The tract-specific diffusion metrics were therefore adjusted for PMA at scan and WM residuals in all the subsequent analyses that aimed to study the effect of prematurity level or GA at birth. As a proxy of the maturational gap between PT and FT, we calculated the relative percentage difference in the metric values between each PT infant and its matched FT control, and averaged this over the PT_{EV} and PT_{ML} groups independently.

Multivariate tract-specific analyses on effects of prematurity

In order to characterize the potential difference at TEA between the microstructural profiles of PT infants compared to FT neonates for each tract, we used a previously proposed multiparametric approach based on the *Mahalanobis distance* (Kulikova et al., 2015). The goal was to evaluate the distance between each individual PT infant and the FT group as a

reference, by taking into account the inter-subject variability within the FT group and the collinearity between a set of diffusion metrics.

Firstly, we scaled each diffusion metric between [0; 1], considering all tracts and the mean WM in all the PT and FT infants. The tract scaled metrics were then corrected for GA at birth, PMA at scan and WM residuals, considering each of the three groups independently (PT_{EV}, PT_{ML}, and entire FT group) and keeping the respective group value means. Next, we divided the PT and FT *individual* tract metric values by their respective metric means from the FT group.

For the calculation of the Mahalanobis distance, it is beneficial to choose independent metrics that provide complementary information. With this in mind, we decided to subset the six metrics into three parallel analysis streams based on the nature of the metrics and models used to derive them. AD and RD, which are direct measures of the diffusivity within the tracts, were retained as *set 1*. More complex but commonly used DTI metrics: MD and FA, formed *set 2*. Finally, NODDI metrics (NDI and ODI) formed an independent *set 3* to dissociate them from the more widely established DTI metrics and test their relevance for microstructure in the context of SM network and prematurity.

For a given tract, the Mahalanobis distance (Dtract) for a given PT individual was then computed using the following equation:

$$Dtract\ (\vec{x}) = \sqrt{(\vec{x} - \vec{\mu})^T S^{-1} (\vec{x} - \vec{\mu})}$$

where $\vec{x}$ is a multivariate vector describing the PT individual tract-specific metrics, $\vec{\mu} = [1, \ldots, 1]$ is the mean vector for the corresponding FT group, and S is a covariation matrix for diffusion metrics in FT infants.

In the interpretation, the smaller the distance, the closer the individual preterm infant is to the distribution within the control FT cohort. Differences in distances across tracts can thus be interpreted as a differential, tract-specific effect of prematurity on maturation.

Regarding statistical analyses, we first evaluated whether the distances for each of the two PT subgroups were significantly different from 0 (meaning that the PT subgroups are different from the FT reference group) using one-sample Wilcoxon signed rank tests corrected for multiple comparisons (FDR) across all tracts and metric sets. We further evaluated the effect of tracts and PT subgroups on the Mahalanobis distances using global ANOVA modeling with these two factors. We additionally compared distances between the two PT subgroups based on unpaired *t*-tests with FDR correction for multiple comparisons. Both ANOVA and *t*-tests were performed after checking for normality of the Mahalanobis tract values using Shapiro–Wilk test corrected for multiple comparisons across sets.

To establish whether SM tracts were differentially affected by the prematurity level, we compared all possible pairs of tracts within each PT group, using paired *t*-tests corrected for multiple comparisons (FDR) across all studied metric sets and tracts.

We finally evaluated the relationship between this maturational distance related to prematurity and neurodevelopmental outcome. For each tract, we evaluated Pearson's correlations between the Mahalanobis distances in each metrics set and the 5 BSID-III scaled scores, considering infants with outcome data in each group separately (PT_{EV} $N = 24$; PT_{ML} $N = 20$) given the between-subgroup differences observed in distances but not BSID-III scores (see Results section). The reported results were corrected for multiple comparisons (FDR) across all tract and metric sets.

Statistical analyses were performed in R (version 4.0.5, 2021.03.31). Statistical tests throughout the analyses were considered with a 0.95 significance level.

Results

Cohort characteristics

A summary of the demographic and clinical characteristics for each group and detailed results of the group comparisons are presented in Table 1. Obstetric factors, multiple pregnancies, IUGR, and delivery by cesarean section were significantly more frequent in the PT group compared to FT (30.5 vs 1.5, 31 vs 2, and 68 vs 49%, respectively). As expected, PT infants differed significantly from FT group in weight, length, and head circumference at birth, as well as Apgar scores. Among the neonates admitted to NICU, only PT needed surfactant, ventilatory support and parenteral nutrition, with 7 (13%) infants needing mechanical ventilation >7 days and 4 (7.5%) parenteral nutrition >21 days.

Morbidities linked to prematurity were seen in 25 PT infants (56.8% of the 44 with available data), including chronic lung disease for 18 infants (15 needing oxygen at discharge), 16 infants had an abnormality identified on cUS during NICU period, 6 had NEC and 2 had ROP. Of note, weight, length, and head circumference at TEA were not available in the dHCP dataset for all infants.

As would be expected, some differences were observed in Radiology scores at TEA between PT and FT babies, with more PT infants having a neuroradiology score equal to 3.

Selected clinical descriptors for the 4 infant subgroups included in the next descriptive analyses are presented in Supplementary Table 1.

Neurodevelopmental outcome and characteristics at 18 months

Significant differences were observed in IMD scores reported at 18mCA ($n = 96$) (Supplementary Table 2), with

TABLE 1 Detailed clinical and sociodemographic information for the 59 pairs of infants.

	Preterm group (*N* = 59)			Full-term controls (*N* = 59)			
	NA	***N* (%)**	**Median (IQR) [Range]**	***NA***	***N* (%)**	**Median (IQR) [Range]**	***p***
Obstetric factors							
Multiple pregnancy, *twins*		18 (30.5)			1 (1.7)		****
IUGR, *yes*	*4*	17 (30.9)¤		*2*	1 (1.8)¤		****
Maternal antenatal steroids, *given*		48 (81.4)			/		
Maternal antenatal magnesium sulphate, *yes*	*3*	25 (44.6)¤			/		
Mode of delivery, *cesarean section*		40 (67.8)			29 (49.2)		**
Newborn characteristics at birth							
Gestational age (*weeks)*			31.7 (28.8; 34.1) [23.7; 36.0]			40.1 (39.4; 41.1) [37.4; 42.3]	****
GA grouping (by wGA)							
Extremely PT *(<28 w)*		10 (16.9)			0		
Very PT *(≥28 to<32 w)*		23 (39.0)			0		
Moderate to late PT *(≥32 to < 37 w)*		26 (44.1)			0		
Full-term birth *(≥37 w)*		0			59 (100)		
Sex, *male*		33 (55.9)			33 (55.9)		#
Birth weight (*kg*)			1.48 (1.10; 1.99) [0.54; 3.06]			3.47 (3.24; 3.74) [2.44; 4.14]	****
Birth length (*cm*)	*38*		44 (40; 47) [29; 53]	*11*		52 (50; 54) [46; 57]	****
Birth head circumference (*cm*)	*2*		29 (26; 31) [21.5; 35]	*1*		35 (34; 35.5) [31.5; 37]	****
Neonatal period factors							
Admitted in NICU, *yes*		51 (86.4)			2 (3.4)		****
Apgar score at first minute			7 (5; 9) [1; 10]			9 (8.5; 9) [1; 10]	****
Apgar score at fifth minute			9 (8; 9.5) [1; 10]			10 (10; 10) [6; 10]	***
Surfactant, *given*	*13*	22 (47.8)¤			/		
Mechanical ventilation > 7 days	*5*	7 (12.9)¤			0		***
Ventilatory support, *total days*	*5*		3.0 (1.0;19.5) [0.0;90.0]		/		
Oxygen needed, *total days*	*5*		1.0 (0.0;23.8) [0.0;99.0]		/		
Parenteral nutrition > 21 days	*5*	4 (7.4)¤			0		**
Parenteral nutrition, *total days*	*5*		5.0 (0.0;12.0) [0.0;29.0]		/		
Postnatal sepsis		14 (23.7)			4 (6.8)		*
Neonatal morbidities, *yes*	*15*	25 (56.8)¤			0		
CLD/O2 dependency at discharge	*5*	18 (33.3)/15 (27.7)¤			/		
Necrotizing enterocolitis	*5*	6 (11.2)¤			/		
Retinopathy of prematurity	*5*	2 (3.7)			/		
Any abnormal cUS	*16*	14 (32.5)¤			/		
MRI scan around TEA							
PMA (weeks) at MRI			41.3 (40.1; 42.1) [38.4; 44.9]			41.3 (40.2; 42.1) [38.3; 44.7]	#
Radiology score			2 (1; 3) [1; 3]			1 (1; 2) [1; 3]	*
1. Normal appearance for age		22 (37.3)			35 (59.3)		
2. Incidental findings with unlikely significance for clinical outcome or analysis		18 (30.5)			17 (28.8)		
3. Incidental findings with unlikely clinical significance but possible analysis significance		19 (32.2)			7 (11.9)		

Median IQR: interquartile range (25%; 75%); range: [minimum; maximum]. NA: data not available (number of subjects).

¤Percentage over the available data (see NA for missing data). Comparisons were performed with suitable tests (Wilcoxon rank sum test for ordinal and continuous variables; Fisher's exact test for binary factors; Pearson's Chi-squared test for non-binary nominal factors).

#No comparisons performed since these variables were used for pairing the full-term infants to preterm ones. cUS, cranial ultrasonography; CLD, chronic lung disease; FT, full-term birth; IUGR, intrauterine growth restriction; NICU, neonatal intensive care unit; PMA, post-menstrual age; PT, preterm birth; TEA, term equivalent age; wGA, weeks of gestational age. *p*-value ≤ 0.0001 [****], ≤0.001 [***], ≤0.01 [**], < 0.05 [*], <0.1 [.], ≥0.1 [ns].

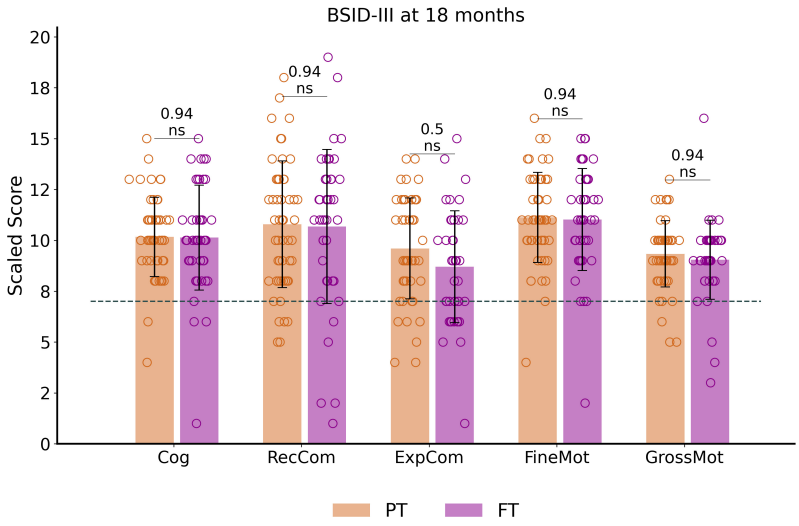

FIGURE 2
Outcome assessment at around 18 months of corrected age: BSID-III scaled scores distribution and comparisons between preterm and full-term infant groups. The dotted line corresponds to the pathological threshold, with scores <7 (<-1 SD) indicating a developmental delay. Of note, only one extreme PT (male, born at 27.6wGA) presented severe developmental delay (scores <-3SD) for cognitive and both communication scores (with fine motor score at −2SD and gross motor score on the norm values). Reported *p*-values come from *t*-tests corrected for multiple comparisons. See **Supplementary Figure 1** for infant subgroup analysis using one-way ANOVA. BSID-III, Bayley Scales of Infant and Toddler Development, Third edition. PT, preterm; FT, full-term. Cog, cognitive; RecCom, receptive communication; ExpCom, expressive communication; FineMot, fine motor; GrossMot, gross motor scaled scores; ns, non-significant.

PT families tending to live in more deprived areas than the FT ones (quintiles $\leq$ 3 for 64.3 vs 29.6%, respectively, *data not shown*).

Among the 97 infants with available BSID-III data, no significant differences between PT and FT controls were observed for the corrected age at assessment. Paired *t*-tests on scaled scores showed no significant differences between PT and FT groups after correcting the results for multiple comparisons (**Figure 2**). BSID-III scaled scores across PT_{EV}, PT_{ML} FT_{EVCt} and FT_{MLCt} subgroups (presented in **Supplementary Figure 1**) also showed no significant group effect.

Over the whole cohort, only a small number of infants showed scaled scores indicating a developmental delay (scores below 7 and corresponding to < -1SD), with no significant difference between PT and FT. These consisted of developmental delay in 30.9% of infants for expressive communication (N = 30, 19 PT), 14.4% for receptive communication (N = 14, 7 PT), 11.3% for gross motor (N = 11, 5 PT), 6.2% for fine motor (N = 6, 4 PT) and cognition (N = 6, 4 PT).

Sensorimotor tract reconstructions

Visual inspection of the automated reconstructions for all tracts was performed on some randomly selected infants which allowed us to evaluate the quality of reconstructions for all the 15 tracts of interest, in a similar way across PT and FT infants. Examples of individual tract reconstructions and diffusion metric maps are shown in **Figures 1C,D** for a representative FT infant.

Univariate tract-specific metrics

Tract-specific distributions of diffusion metrics across the 4 infant groups are presented in **Figure 3**. Visual assessment suggested important microstructural differences between groups. Results of the univariate analyses are presented in **Supplementary materials**: *Descriptive univariate analysis* section. Interestingly, we observed that AD, RD, MD (controlled for the effects of PMA at scan and WM microstructure) decreased with GA at birth in all tracts, while corrected FA, NDI and ODI increased.

The analysis of the relative percent difference in diffusion metrics between the PT and paired FT neonates allowed us to estimate a proxy of the maturational gap related to prematurity for each PT_{EV} and PT_{ML} group (**Supplementary Figure 2**). Visual inspection suggested a larger gap in the PT_{EV} subgroup than in PT_{ML}, highlighting the effect of prematurity degree on tract microstructural characteristics. However, the observed variability between the metrics rendered the interpretation of different maturational patterns across tracts difficult, justifying the need for a multivariate approach.

Mahalanobis distance of preterm subjects from the typical full-term profile

To explore the impact of prematurity on tract-specific microstructure, we computed multi-metric Mahalanobis distances of PT subgroups (PT_{EV} and PT_{ML} independently) to all FT infants as reference, using the 3 metric sets: *set 1* (AD and RD), *set 2* (MD and FA), and *set 3* (NDI and ODI) (**Figure 4**). For a given tract, computed Mahalanobis distance can be understood as a *maturational distance* for a given PT infant compared to the FT group.

For both PT subgroups (PT_{EV} and PT_{ML}), all sets and all tracts, distances were highly significantly different from 0 as assessed by Wilcoxon tests corrected for multiple comparisons (all $p < 0.001$), suggesting that SM network microstructure is affected by prematurity, even moderate/late. Considering all PT infants, ANOVA modeling on distances for each set confirmed the expected effects of group, tract, and the interaction between group and tract for all three sets (**Supplementary Table 3**). As expected, the distance increased with the prematurity levels, with unpaired *t*-tests per tract comparing the two PT subgroups revealing higher distances in PT_{EV} than in PT_{ML} (**Figure 4A**). In addition, the tracts were not affected in the same manner: distances were different between PT_{EV} and PT_{ML} for all tracts except for ParaC-Caud in both DTI sets (1 and 2), and for set 3: S1-Bstem, M1-Bstem, ParaC-Bstem and M1-Caud.

Tract-specific effects of prematurity

To further evaluate the differential effect of prematurity on specific tracts, we subsequently compared distances for each pair of tracts through paired *t*-tests in each PT subgroup independently (**Supplementary Figure 3**). Many more significant tract-by-tract differences were observed in the PT_{EV} than in the PT_{ML} group (69 vs 26/105 for *set 1*; 70 vs 22/105 for *set 2*; 61 vs 23/105 for *set 3*), but the trends were rather consistent between the two PT subgroups.

Focusing on the PT_{EV} *subgroup*, the significant differences between tracts assessed by the paired *t*-tests allowed us to propose an ordering of the tracts based on the relative effects of prematurity on microstructural characteristics (**Figure 4B**). For *sets 1 and 2* (DTI sets), the orderings were highly similar, with, somewhat schematically, the following tracts showing the lowest to highest distances: (1) M1-Bstem; (2) ParaC-Bstem, S1-Bstem, M1-Thal, ParaC-Thal, M1-Caud, ParaC-Caud; (3) M1-Lenti, ParaC-Lenti, S1-Thal, S1-Caud; (4) S1-Lenti, $S1_L$-$S1_R$, $M1_L$-$M1_R$; (5) S1–M1. For *set 3* (NODDI set), the ordering showed schematically, from the lowest to highest distances of

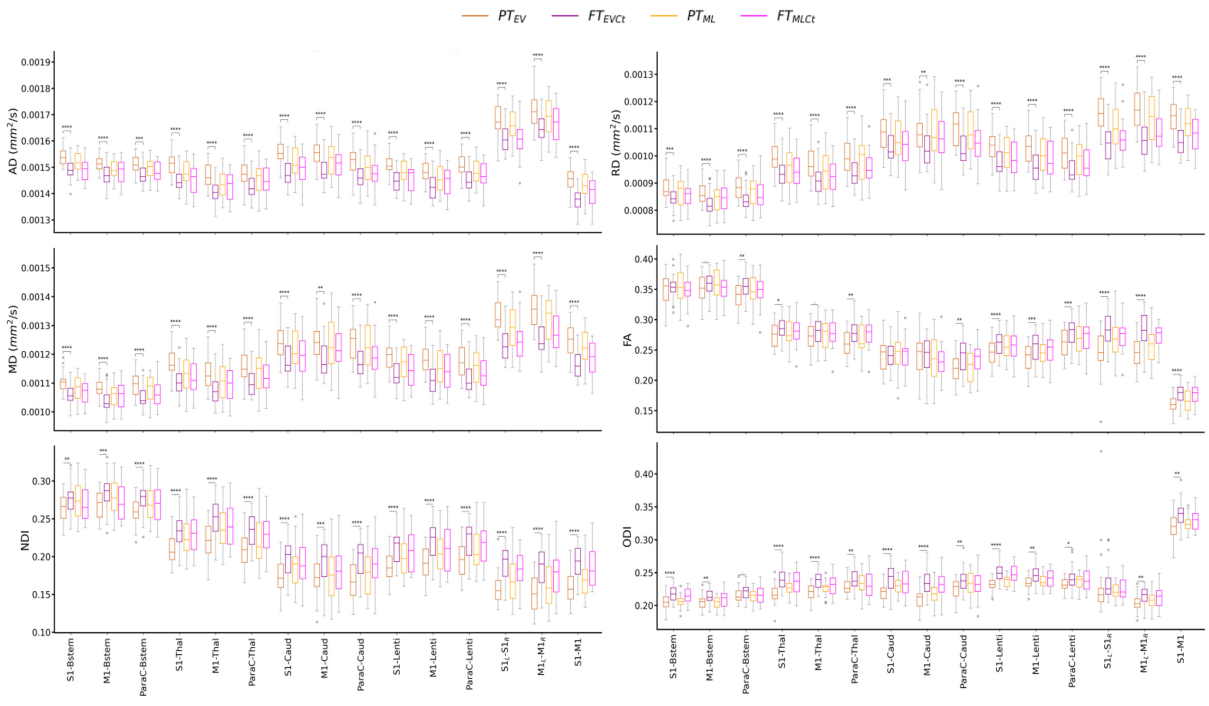

FIGURE 3
Diffusion metrics across tracts and cohort subgroups: extreme to very preterm group (PT_{EV}, dark orange) compared to paired full-term controls (FT_{EVCt}, dark purple), and moderate to late preterm group (PT_{ML}, light orange) compared to paired controls (FT_{MLCt}, light purple). Significances are results of the tract-specific paired *t*-tests between paired groups, corrected for multiple comparisons. Only the comparisons between PT_{EV} – FT_{EVCt} reached significance. Refer to **Figure 1** legend for abbreviations and to **Table 1** for *p*-value legend.

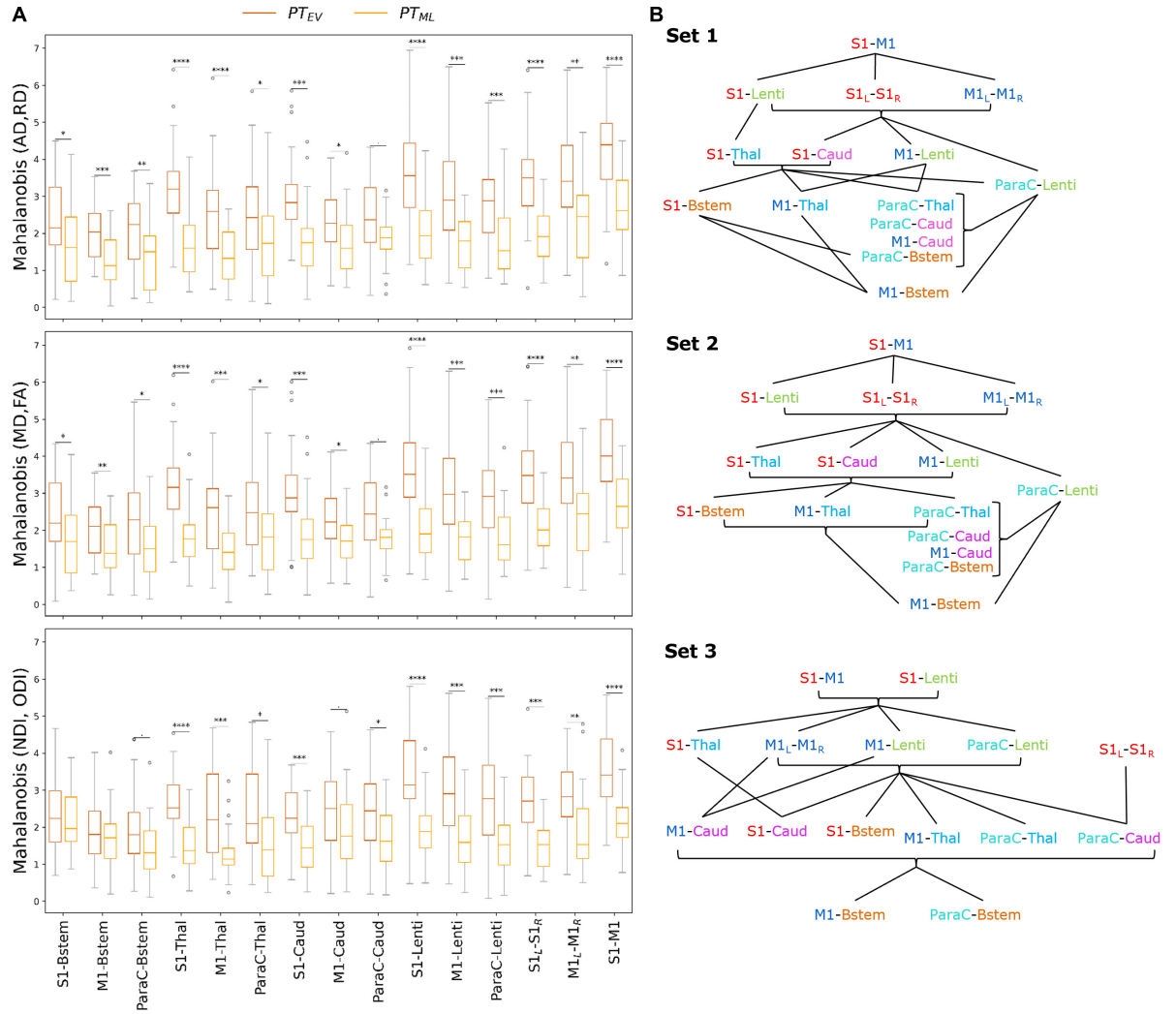

FIGURE 4
(A) Multi-metric Mahalanobis distance across tracts and PT subgroups (PT_{EV} and PT_{ML} with FT controls as reference) at TEA. The smaller the distance, the less the microstructural profile of the PT infant differs from the FT reference group. Note that the effect of prematurity is globally smaller for PT_{ML} than for PT_{EV} infants across the studied SM tracts. Significances are results of the comparison of Mahalanobis distances (PT_{EV} vs PT_{ML}) with unpaired *t*-tests (*p*-values corrected for multiple corrections) for each set and each tract. For visualization purposes, outliers (mean ± 3SD) were removed (6 points for PT_{EV}, 3 for PT_{ML} infants). **(B)** Order of the SM tracts in the PT_{EV} subgroup based on the Mahalanobis distance per metrics set (higher values on the top), highlighting the differential effect of prematurity on SM tracts microstructure. The lines represent the significant differences between tracts according to paired *t*-tests (corrected for multiple comparisons) over the PT_{EV} group (for visualization purposes, the statistical threshold was relaxed to $p < 0.1$). Metrics sets: 1 (AD, RD); 2 (MD, FA); 3 (NDI, ODI). Refer to **Figure 1** legend for ROIs color code and abbreviations.

tracts: (1) M1-Bstem, ParaC-Bstem; (2) S1-Bstem, M1-Thal, ParaC-Thal, M1-Caud, ParaC-Caud, S1-Caud; (3) S1-Thal, M1-Lenti, ParaC-Lenti, $S1_L$-$S1_R$, $M1_L$-$M1_R$; (4) S1-Lenti, S1–M1 (**Figure 4B**).

Despite a few differences in the ordering of a couple of tracts, the results were quite consistent across the three sets and revealed a differential impact of prematurity on the SM tracts microstructure. Overall, the tract ordering based on maturational distances highlighted a coherent *caudo-rostral and central-to-periphery pattern*, with: the cortico-*Brainstem* tracts presenting the lowest distances and thus the least impact of prematurity; the cortico-*Thalamic* and cortico-*Caudate* tracts showing "intermediate" distances; the cortico-*Lenticular* tracts appearing with the highest distances among the cortico-subcortical tracts; and the *cortico-cortical* tracts revealing the highest prematurity impact. Inter-hemispheric tracts ($S1_L$-$S1_R$ and $M1_L$-$M1_R$) showed lower distances than the intra-hemispheric tracts (S1–M1). *S1 tracts* generally had higher distances than the M1 and ParaC tracts, both presenting similar profiles.

This approach of tract ordering based on the maturational distance related to prematurity was not considered for the PT_{ML}

subgroup as tract pairwise comparisons were less systematically significant than in the PT_{EV} group and the ordering was more difficult to synthesize. For this subgroup, the distances of all tracts were more homogeneous (**Supplementary Figure 3**), which may be associated with a lesser effect of prematurity on the microstructural profiles of the SM tracts.

Tract-specific maturational distance associated with neurodevelopmental outcome

Finally, we assessed whether maturational distances related to prematurity at TEA might be related to outcome (BSID-III scaled scores) at 18mCA, considering each PT subgroup independently. Pearson correlations showed significant results only in PT_{EV} group (N = 24), for *Set 3* (*NODDI*) (**Supplementary Table 4**) and for specific tracts: *M1-Bstem and ParaC-Bstem* distances were both negatively correlated with *Cognitive* scaled score and *Fine motor* score, while *M1-Lenti, ParaC-Lenti* and *S1–M1* tracts were also negatively correlated with *Fine motor* score (the lower the maturational distance, the higher the score and thus the better the outcome) (**Figure 5**). Interestingly, these five tracts showed different levels of distances over the PT_{EV} group, with M1- and ParaC-Bstem having a distance closest to 0, whereas S1–M1 was the tract with the highest distance; and M1- and ParaC-Lenti presented a similar and intermediate distance.

Discussion

In this study, we considered an unprecedented set of primary SM cortico-cortical and cortico-subcortical tracts that are thought to underpin a wide range of early SM experiences. We observed significant differences in diffusion MRI derived metrics of WM microstructure between low-risk PT and FT infants at TEA. Multi-parametric assessment showed that the maturational gap differs with the prematurity level and across SM tracts, with alterations particularly affecting S1-related tracts and more rostral tracts. Importantly, these findings are of functional significance as correlations were also observed between specific measures of microstructural maturation within particular tracts and neurodevelopmental outcomes evaluated at 18mCA.

Exploring the developing sensorimotor network microstructure with diffusion magnetic resonance imaging

A robust automated approach to delineate primary sensorimotor tracts in neonates

After meeting the challenge of extracting reliable individual SM tracts by optimizing the settings of an automated tractography-based approach benefitting from the dHCP multi-shell dMRI data, we explored the WM *maturational differences* of *low-risk* preterm infants at TEA compared to full-term neonates. We then quantified the microstructure of each tract by extracting DTI and NODDI-derived diffusion metrics using a weighting approach which privileges the core of the tract and avoids potential bias linked to some inter-individual differences in tract volumes.

Relevance of diffusion MRI models to characterize white matter maturation

DTI and NODDI models present different trade-offs between complexity, biological plausibility, robustness, and run-time duration (Jelescu and Budde, 2017). Despite its widespread use in most studies of WM development (Dubois et al., 2014; Ouyang et al., 2019), DTI-derived metrics can be affected by several microstructural features and lack specificity to disentangle the complex properties of voxels containing crossing, kissing and fanning fibers (Zhang et al., 2012; Jeurissen et al., 2013). In contrast, NODDI allows a more sophisticated and biologically plausible multi-compartment model, relevant for developmental studies (Chang et al., 2015; Genc et al., 2017; Mah et al., 2017; Kimpton et al., 2021), but requires multi-shell data and increased processing time. Although potentially sub-optimal, we opted for default settings of diffusivities in the NODDI model, which were optimized for the adult WM but not for infants (Guerrero et al., 2019). In the absence of gold standards for infant-specific NODDI fitting to evaluate the metric maps, this was performed to maintain some consistency with previous studies (Guerrero et al., 2019; Fenchel et al., 2020).

Overall, the resulting metrics maps were consistent among PT and FT subjects, and metric differences across tracts were largely coherent between DTI and NODDI results in all infants. Once controlled for the effects of PMA at scan and global WM microstructure, we observed that AD, RD, MD decreased with GA at birth in all tracts, while FA, NDI and ODI increased. Globally, MD differences across tracts presented an opposite pattern to NDI (Kimpton et al., 2021), and differences in RD were highly similar to MD in all tracts, and opposite to FA in cortico-subcortical tracts, confirming that variations in MD and FA are likely largely driven by RD. Such diverse profiles across tracts might result from differences in both intrinsic microstructure (similar to adults) and in maturation (according to different myelination stages across tracts) (Dubois et al., 2014). During WM development, MD tends to decrease and NDI to increase with the growth of fibers and membranes, acting as barriers to the random water motion, while FA tends to increase, reflecting several factors including the presence of compact fiber tracts and increasing myelination (Beaulieu and Allen, 1994; Batalle et al., 2017; Kimpton et al., 2021). ODI describes

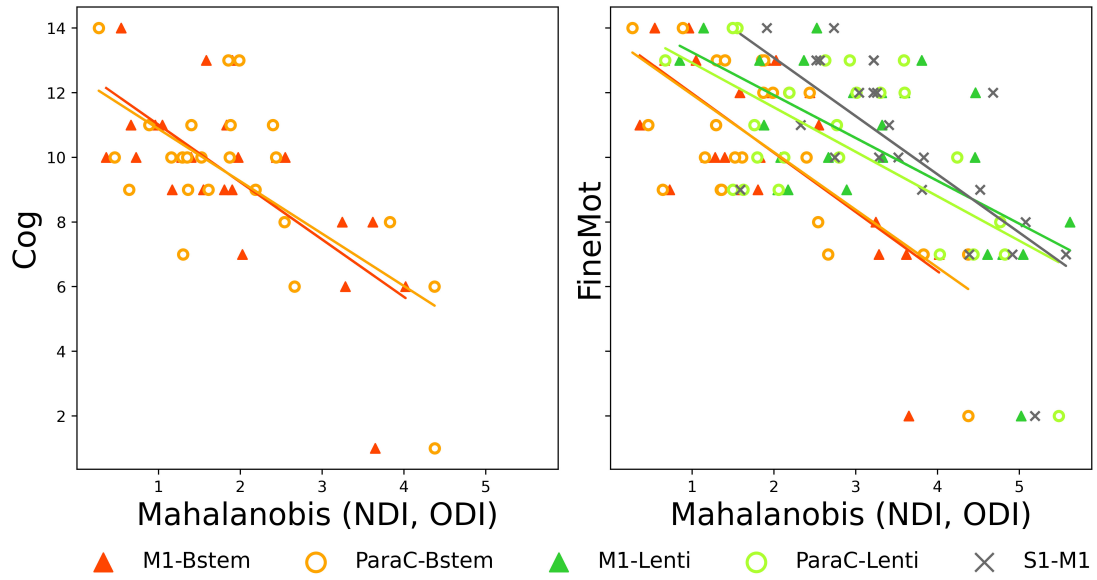

FIGURE 5
Significant correlations between Mahalanobis distances and neurodevelopmental scores at 18mCA, for NODDI set. Scatter plots of the significant Pearson correlations between tract-specific maturational distance related to prematurity at TEA in PT_{EV} group and BSID-III scores. Cog, cognitive; FineMot, fine motor scaled scores. Refer to **Figure 1** legend for abbreviations.

the orientational dispersion of fibers within a tract, which is highly variable across tracts and likely changes during the growth and maturation of crossing fibers (Raghavan et al., 2021). Interestingly, in a few tracts, we did not observe significant relationship between FA or ODI (corrected for PMA at scan and WM residuals) and GA at birth, suggesting that both metrics might be less sensitive to detect subtle variations of microstructure in the settings of this study. Further analyses (beyond the scope of this study) could be performed to evaluate the potential correlations between all these metrics, as performed in previous studies (Kunz et al., 2014).

Moreover, the results of the maturational distance analyses underlined a high coherence between DTI sets which seemed fairly intuitive and in line with previous studies (Li et al., 2022). The differences observed between the DTI and NODDI sets (with NODDI set presenting more compact and roughly lower Mahalanobis distances values across tracts, with subtle variations in the main order of distances) suggested that NODDI metrics provide complementary information, probably due to their differing sensitivity to neurites growth and maturation. Thus, in line with previous studies (Batalle et al., 2017; Kimpton et al., 2021), our results highlighted the complementarity of these models and confirmed the relevance of NODDI-derived metrics for the study of WM microstructure maturation in the context of prematurity.

Studying the effects of prematurity on sensorimotor network maturation at term-equivalent age

Hypotheses about the differential effect of prematurity across primary sensorimotor tracts

In contrast to the majority of previous studies, we focused on low-risk PT infants without overt brain abnormality at TEA, which is representative of the majority of children now born preterm in developed countries. Despite the presence of specific clinical risk factors in some of the PT infants (e.g., morbidities related to prematurity), the absence of a significant difference in the BSID-III outcome at 18 months of age between PT and FT infants corroborated that the included PT infants were at low-risk for neurodevelopment impairment.

In this study, we hypothesized that WM microstructure within SM tracts would show a significant maturational delay at TEA in PT infants compared to FT neonates, with distinct patterns as a function of GA at birth and across cortico-subcortical and cortico-cortical tracts. This was based on the assumption that early peripheral stimuli are essential for the emerging SM network maturation, and that preterm birth is associated with modified SM stimuli and experiences, notably related to numerous and various procedures in NICU (Mörelius et al., 2006; Gibbins et al., 2008), which might have a differential effect on somatosensory and motor systems (Duerden et al., 2018; Schneider et al., 2018; Jones et al., 2022). Of direct relevance, previous studies have reported either higher tactile

sensitivity in PT infants at TEA (André et al., 2020), tactile hyporeactivity, lower brain responses (Maitre et al., 2017) and/or undifferentiated integration of nociceptive versus non-nociceptive stimuli (Fabrizi et al., 2011), in association with WM abnormalities (Brummelte et al., 2012; Zwicker et al., 2013).

Approaching the effects of prematurity on WM microstructure with univariate analyses

Univariate dMRI approaches, based on individual derived metrics, are commonly applied to reveal WM developmental changes in the neonatal brain (Kunz et al., 2014; Ouyang et al., 2019). These analyses were thus used to evaluate the effects of several factors on the diffusion metrics measured in SM tracts.

Firstly, these were not related to the infants' sex in our cohort. Combined with previous studies which showed inconsistent results (Pannek et al., 2014; Barnett et al., 2018; Kimpton et al., 2021), this observation suggests that sex effects may vary according to the studied brain regions. Surprisingly, we also observed no effect of main perinatal clinical risk factors (including preterm morbidities), despite numerous studies describing associations of WM abnormalities with obstetric, neonatal and postnatal factors (Pogribna et al., 2013; Brouwer et al., 2017; Barnett et al., 2018; Parikh et al., 2021), and with exposure to cumulative risk factors (Barnett et al., 2018). These negative results might be partly due to the specific study of low-risk PT infants.

In line with previous literature, we observed that diffusion metrics –even measured at TEA– were dependent on PMA at MRI (de Bruïne et al., 2011; van Pul et al., 2012; Kimpton et al., 2021) and were influenced by prematurity (Kunz et al., 2014; Kelly et al., 2016a; Batalle et al., 2017; Thompson et al., 2019; Dibble et al., 2021; Kimpton et al., 2021), with PT_{EV} infants showing more "immature" microstructural profiles (higher AD, RD, MD, lower FA, NDI, ODI) than PT_{ML} and FT infants. Interestingly, when group analyses were performed at the tract level, PT_{ML} showed no difference with the FT paired group, suggesting that the specific SM tracts studied here might not contribute significantly to the well-described whole-brain WM diffusion abnormalities in moderate-late PT (Kelly et al., 2016a; Thompson et al., 2019).

Evaluating the maturational distances related to prematurity with a multivariate approach

We then aimed to evaluate the maturational gap between PT infants and their full-term peers, based on SM tracts microstructural characteristics at TEA. Although univariate dMRI approaches allow some inference about the effects of prematurity on SM tract microstructure, they cannot reflect the inter-related complexity of processes involved in early brain maturation (Kostović et al., 2019), and are limited by the difficulties interpreting findings related to single metrics which are sensitive to different underlying microstructural properties and maturational processes. Also, quantifying the maturational degree across regions requires comparison of an infant's data with a mature reference to account for "intrinsic" microstructural differences (Dubois et al., 2014). To overcome these limitations, we implemented an original multivariate approach already validated in neonatal and pediatric data (Kulikova et al., 2015; Dean et al., 2017; Li et al., 2022), that took advantage of the complementary information described by different DTI and NODDI metrics, to enable better characterization of SM tract maturation and the effects of prematurity as compared to typical development. Multivariate *Mahalanobis distance* was calculated in respect to a reference group (FT neonates) which provided typical values for the given tract. Importantly, this approach also allowed to take into consideration both the inherent variability of the diffusion metrics across tracts in the FT group and the correlations between these metrics. For each tract, the resulting maturational distance related to prematurity could be interpreted as a developmental gap between a PT infant at TEA and the FT control group.

Highlighting the tract-specific effects of prematurity on SM network

Focusing on the PT_{EV} group, the comparison of distances across tracts highlighted the *differential impact of prematurity* on the SM tracts at TEA. For all sets of diffusion metrics, the impact increased in a *caudo-rostral and central-to-peripheral manner* following the typical progression of WM growth and myelination during infancy (Yakovlev and Lecours, 1967; Dubois et al., 2014) and within the CST tract (Kimpton et al., 2021), suggesting that early maturing tracts are less impacted. Furthermore, while this spatial pattern is globally consistent with previous studies of preterm infants (Wu et al., 2017; Knight et al., 2018), our results raise several interesting points regarding the functional role of the different SM tracts and related GM structures during development.

Firstly, we observed a differential impact of prematurity among tracts related to different cortical seeds. *S1-subcortical* tracts were systematically more impacted than M1- and ParaC-subcortical tracts. This suggests that S1 tracts may have a *specific vulnerability* to the deleterious effects of prematurity, possibly due to the altered SM perceptions and experiences as a result of early exposure to the ex-utero environment. Alternatively, the observed differences may reflect compensatory faster and/or more efficient maturational "catch-up" mechanisms in the M1/ParaC-subcortical tracts during the first post-natal weeks after preterm birth.

The similar profiles seen in the *ParaC-subcortical* tracts and related *M1-subcortical* tracts are less straightforward to interpret as the paracentral lobule includes both motor and somatosensory regions. Given the somatotopic organization of S1 and M1, this could suggest that connections related to the lower limb representations are less impacted by prematurity,

which may be linked to the possible advanced maturation of these representations at early ages (Devisscher et al., 2021). A further possible explanation is that a greater number of motor fibers than sensory fibers were included in ParaC- tracts.

Secondly, the prematurity impact was also variable across sub-cortical related tracts. Of these, the *cortico-Brainstem* tracts appeared the least impacted. As these mainly correspond of CST fibers that myelinate early, notably at the level of the PLIC (Dubois et al., 2014; Kulikova et al., 2015; Kimpton et al., 2021), this is consistent with connections that have more advanced maturation at the time of birth being less vulnerable to prematurity (Wu et al., 2017). In agreement with the acknowledged vulnerability of thalamocortical connections following preterm birth (Ball et al., 2013a), the *cortico-Thalamic* tracts showed higher impact than cortico-Brainstem tracts, giving an "intermediate" profile compared to other studied tracts. The specific functional role of the thalamus, with essential input and output projections to the different SM regions, might help to modulate this vulnerability compared to other sub-cortical structures (Duerden et al., 2018; Schneider et al., 2018). Similarly, the *cortico-Caudate* tracts showed "intermediate" profile. This might result from an interplay between the high vulnerability of the caudate nuclei to prematurity (Nosarti et al., 2014; Back, 2015; Loh et al., 2017) and the adverse effects on the major efferent projections (McClendon et al., 2014) compared with more "preserved" afferent connections (from SM cortices). The *cortico-Lenticular* tracts systematically presented the maturational distance profile with the greatest impact of prematurity, suggesting their specific vulnerability. In addition to the known structural consequences of preterm birth on BG growth (Loh et al., 2017, 2020), different hypotheses can be proposed to explain this specific profile, especially knowing the anatomo-functional particularities of these tracts. As the dissected tracts include both (afferent) *cortico-putaminal* and (efferent) *pallido-cortical* fibers, the observed alteration may involve both the input (putamen) and output (GPi) structures of the BG, which have different functions in cortico-BG loops. We hypothesize that maturation of the *efferent* pallido-cortical fibers is specifically altered by prematurity, with functional effects on information reaching SM cortices, which might secondarily induce alterations of the descending cortico-striatal and cortico-pallidal fibers.

Finally, we observed the highest impact of prematurity in the *cortico-cortical* tracts, suggesting a particular vulnerability of these rostral structures, in line with the well-described caudo-rostral maturational pattern. *Inter*-hemispheric tracts presented lower impact than *intra*-hemispheric S1–M1 tracts, in line with the late and protracted maturation of such short-range connections (Kostović et al., 2019).

While interesting, the results should be interpreted cautiously given the limitations of diffusion MRI and tractography with relation to the image spatial resolution and the size of neonatal structures, and the presence of crossing fibers notably at the level of the corona radiata. However, the rare high-quality of dHCP neonatal data, the use of HARDI acquisition, the consistency of the tract's delineation and the multivariate approach allowed us to overcome, at least partially, these limitations. In the future, it would be interesting to further investigate whether the vulnerability of SM tracts to prematurity is stable over development or whether "catch-up" development is present for some tracts, either before or after TEA. This would require the longitudinal evaluation of maturational distances defined with similar settings.

Relating the early microstructure of sensorimotor tracts with neurodevelopmental outcome

The final aim of this study was to investigate the relationship between SM microstructural characteristics at TEA and neurodevelopmental outcome at 18mCA. In the specific low-risk preterm cohort studied, no substantial developmental delay or specific disability was expected, as confirmed by the results in terms of BSID-III scores.

Nevertheless we hypothesized that correlations would exist between diffusion metrics profiles and BSID-III scores based on previous studies showing that, even in the absence of overt brain lesions, neonatal microstructural WM measures are associated with neurodevelopmental outcome in toddlers and children (van Kooij et al., 2012; Duerden et al., 2015; Barnett et al., 2018; Girault et al., 2019; Kelly et al., 2020; Pannek et al., 2020; Parikh et al., 2021). In particular, reduced neonatal FA (especially in the PLIC) has been associated with delayed psychomotor development and motor disability at different ages (Rose et al., 2007; Skranes et al., 2007; De Bruïne et al., 2013; Groeschel et al., 2014; Kelly et al., 2016b), and neonatal NODDI metrics have been found to relate to later neurodevelopmental outcomes (Kelly et al., 2016b; Young et al., 2019).

Our results showed negative correlations in PT_{EV} infants between maturational distances and *Cognitive* and *Fine motor scaled scores* for a number of tracts in the *NODDI set* only. This suggested that the early microstructural information as modeled by NODDI is more sensitive than DTI based metrics such as FA for detecting subtle WM tract alterations related to later neurodevelopmental impairments in preterm infants (Batalle et al., 2017; Kimpton et al., 2021). Moreover, early SM tract microstructure was further correlated with *cognitive* outcomes, confirming essential developmental interactions between the SM system and higher-order functions, and the common clinical overlap of motor and cognitive impairments in the PT population.

Regarding the tracts concerned, we first observed that *fine motor* score was related to five tracts with different

maturational distance profiles: *M1-Brainstem and ParaC-Brainstem* which were the least impacted by prematurity; *M1-Lenti and ParaC-Lenti* with intermediate profile; and *S1–M1* with the greatest impact. This suggested that the degree of maturational gap at TEA by itself is not the only factor explaining motor outcomes.

In the light of our results showing the high vulnerability of *lenticular* tracts to prematurity, it is not surprising that microstructural alterations in the motor tracts connected to this key BG structure may underpin early SM impairments with further consequences on fine motor skill acquisition (Leisman et al., 2014). Likewise, as intra-hemispheric SM connections contribute to improve SM integration and functions, the correlation observed for *S1–M1* tract suggests that early impact of prematurity on these tracts may alter later neuromotor development.

Maturational distances for *M1-Brainstem and ParaC-Brainstem* tracts were also correlated with *cognitive* scores, suggesting that early microstructural alterations in these tracts might have global functional consequences, beyond motor skills. Nevertheless, further studies are needed to better understand the involvement in these developmental domains of the brainstem, a complex structure that plays an essential role as a relay for a large number of connections from the whole nervous system, in addition to the functions associated with its many GM sub-structures.

The observed relationships in PT_{EV} infants between SM tract microstructure at TEA and outcome at 18mCA are of particular interest in the context of prematurity, as even low-risk populations are at increased risk of –sometimes subtle– neuromotor impairments (e.g., developmental coordination disorder) (Edwards et al., 2011; Spittle and Orton, 2014; Zwicker, 2014; Groeschel et al., 2019). These disorders are generally not visible enough to be diagnosed until much later (often at school age) (Williams et al., 2010; de Jong et al., 2012; Van Hus et al., 2014), which underlines the need for early diagnostic biomarkers. Thus, the specific impact of prematurity on the five primary SM tracts previously mentioned should be further explored, in order to investigate their potential value as early markers of motor and/or other neurodevelopmental disorders such as developmental coordination disorder.

Nevertheless, whilst relating early brain markers and long-term outcome has important clinical relevance, previous studies have described that environmental factors (e.g., socio-familial) could explain the greatest part of interindividual variability in neurodevelopment later in childhood, with the influence of perinatal risk factors diminishing over time (Thompson et al., 1998; Miceli et al., 2000; Anderson and Doyle, 2008; Linsell et al., 2015). Thus, future studies should incorporate more accurate predictive models to intend to approach the complex relationship between early brain characteristics, environmental factors and outcome.

Conclusion

Using an unprecedented combination of diffusion MRI data and innovative analysis methods, our results confirmed that prematurity impacts early microstructural development of the primary SM network, even in low-risk preterm infants. We further found that these effects differ according to the level of prematurity and across the SM tracts, with the most rostral tracts as well as those involving S1 showing the greatest vulnerability to prematurity at TEA. Our study also showed the complementarity between DTI and NODDI models as well as the interest of using multiparametric approaches for assessing maturational processes and microstructural developmental differences. Longitudinal studies incorporating earlier MRI evaluation as well as behavioral follow-up through to later childhood would provide a better understanding of the impact of early-life disturbances in SM tracts microstructure on neurodevelopmental outcomes.

Data availability statement

Publicly available datasets were analyzed in this study. This data can be found here: http://www.developingconnectome.org.

Ethics statement

The studies involving human participants were reviewed and approved by UK NHS Research Ethics Committee (14/LO/1169, IRAS 138070). Written informed consent to participate in this study was provided by the participants' legal guardian/next of kin.

Author contributions

SN, AG, LH-P, TA, and JD: conceptualization. SN, AG, YL, and JD: methodology. SN, AG, TA, and JD: resources and investigation. SN and AG: data curation. SN, AG, and JD: validation and formal analysis, visualization, and writing – original draft. AG and YL: software. TA and JD: supervision. SN, AG, YL, LH-P, TA, and JD: writing – review and editing. All authors contributed to the article and approved the submitted version.

Funding

The developing Human Connectome Project was funded by the European Research Council under the European

Union Seventh Framework Programme (FP/2007–2013)/ERC Grant Agreement No. 319456. SN was supported by a postdoctoral fellowship from the Bettencourt Schueller Foundation (www.fondationbs.org). AG was supported by the CEA NUMERICS program, which has received funding from the European Union's Horizon 2020 Research and Innovation Program under the Marie Skłodowska-Curie grant agreement No. 800945. TA was supported by a MRC Clinician Scientist Fellowship (MR/P008712/1) and MRC Transition Support Award (MR/V036874/1). JD received support from the Fondation Médisite (under the aegis of the Fondation de France, grant FdF-18-00092867), the IdEx Université de Paris (ANR-18-IDEX-0001), the Fondation de France (grant FdF-20-00111908), and the French National Agency for Research (grant ANR-20-CE17-0014).

Acknowledgments

We thank Jean-François Mangin for the methodological support, Nicholas Harper for providing the individual clinical data, and the infants and their families for their participation in this study.

Conflict of interest

The authors declare that the research was conducted in the absence of any commercial or financial relationships that could be construed as a potential conflict of interest.

Publisher's note

Supplementary material

The Supplementary Material for this article can be found online at: https://www.frontiersin.org/articles/10.3389/fnins.2022.932386/full#supplementary-material

References

Adamson, C. L., Alexander, B., Ball, G., Beare, R., Cheong, J. L. Y., Spittle, A. J., et al. (2020). Parcellation of the neonatal cortex using Surface-based Melbourne Children's Regional Infant Brain atlases (M-CRIB-S). *Sci. Rep.* 10:4359. doi: 10.1038/s41598-020-61326-2

Anderson, P. J., and Doyle, L. W. (2008). Cognitive and educational deficits in children born extremely preterm. *Semin. Perinatol.* 32, 51–58. doi: 10.1053/j.semperi.2007.12.009

André, V., Durier, V., Beuchée, A., Roué, J.-M., Lemasson, A., Hausberger, M., et al. (2020). Higher tactile sensitivity in preterm infants at term-equivalent age: A pilot study. *PLoS One* 15:e0229270. doi: 10.1371/journal.pone.0229270

Back, S. A. (2015). Brain Injury in the Preterm Infant: New Horizons for Pathogenesis and Prevention. *Pediatr. Neurol.* 53, 185–192. doi: 10.1016/j.pediatrneurol.2015.04.006

Ball, G., Aljabar, P., Zebari, S., Tusor, N., Arichi, T., Merchant, N., et al. (2014). Rich-club organization of the newborn human brain. *Proc. Natl. Acad. Sci. U. S. A.* 111, 7456–7461. doi: 10.1073/pnas.1324118111

Ball, G., Srinivasan, L., Aljabar, P., Counsell, S. J., Durighel, G., Hajnal, J. V., et al. (2013b). Development of cortical microstructure in the preterm human brain. *Proc. Natl. Acad. Sci. U. S. A.* 110, 9541–9546. doi: 10.1073/pnas.1301652110

Ball, G., Boardman, J. P., Aljabar, P., Pandit, A., Arichi, T., Merchant, N., et al. (2013a). The influence of preterm birth on the developing thalamocortical connectome. *Cortex* 49, 1711–1721. doi: 10.1016/j.cortex.2012.07.006

Barnett, M. L., Tusor, N., Ball, G., Chew, A., Falconer, S., Aljabar, P., et al. (2018). Exploring the multiple-hit hypothesis of preterm white matter damage using diffusion MRI. *NeuroImage Clin.* 17, 596–606. doi: 10.1016/j.nicl.2017.11.017

Batalle, D., Edwards, A. D., and O'Muircheartaigh, J. (2018). Annual Research Review: Not just a small adult brain: Understanding later neurodevelopment through imaging the neonatal brain. *J. Child Psychol. Psychiatry* 59, 350–371. doi: 10.1111/jcpp.12838

Batalle, D., Hughes, E. J., Zhang, H., Tournier, J.-D., Tusor, N., Aljabar, P., et al. (2017). Early development of structural networks and the impact of prematurity on brain connectivity. *NeuroImage* 149, 379–392. doi: 10.1016/j.neuroimage.2017.01.065

Bayley, N. (2006). *Bayley Scales of Infant and Toddler Development*, 3rd Edn. San Antonio, TX: Harcourt Assessment.

Beaulieu, C., and Allen, P. S. (1994). Determinants of anisotropic water diffusion in nerves. *Magn. Reson. Med.* 31, 394–400. doi: 10.1002/mrm.1910310408

Behrens, T. E. J., Berg, H. J., Jbabdi, S., Rushworth, M. F. S., and Woolrich, M. W. (2007). Probabilistic diffusion tractography with multiple fibre orientations: What can we gain? *NeuroImage* 34, 144–155. doi: 10.1016/j.neuroimage.2006.09.018

Brouwer, M. J., Kersbergen, K. J., van Kooij, B. J. M., Benders, M. J. N. L., van Haastert, I. C., Koopman-Esseboom, C., et al. (2017). Preterm brain injury on term-equivalent age MRI in relation to perinatal factors and neurodevelopmental outcome at two years. *PLoS One* 12:e0177128. doi: 10.1371/journal.pone.0177128

Brummelte, S., Grunau, R. E., Chau, V., Poskitt, K. J., Brant, R., Vinall, J., et al. (2012). Procedural pain and brain development in premature newborns. *Ann. Neurol.* 71, 385–396. doi: 10.1002/ana.22267

Chang, Y. S., Owen, J. P., Pojman, N. J., Thieu, T., Bukshpun, P., Wakahiro, M. L. J., et al. (2015). White Matter Changes of Neurite Density and Fiber Orientation Dispersion during Human Brain Maturation. *PLoS One* 10:e0123656. doi: 10.1371/journal.pone.0123656

Christiaens, D., Cordero-Grande, L., Pietsch, M., Hutter, J., Price, A. N., Hughes, E. J., et al. (2021). Scattered slice SHARD reconstruction for motion correction in multi-shell diffusion MRI. *NeuroImage* 225:117437. doi: 10.1016/j.neuroimage.2020.117437

Cordero-Grande, L., Hughes, E. J., Hutter, J., Price, A. N., and Hajnal, J. V. (2018). Three-dimensional motion corrected sensitivity encoding reconstruction for multi-shot multi-slice MRI: Application to neonatal brain imaging. *Magn. Reson. Med.* 79, 1365–1376. doi: 10.1002/mrm.26796

De Bruïne, F. T., Van Wezel-Meijler, G., Leijser, L. M., Steggerda, S. J., Van Den Berg-Huysmans, A. A., Rijken, M., et al. (2013). Tractography of white-matter tracts in very preterm infants: A 2-year follow-up study. *Dev. Med. Child Neurol.* 55, 427–433. doi: 10.1111/dmcn.12099

de Bruïne, F. T., van Wezel-Meijler, G., Leijser, L. M., van den Berg-Huysmans, A. A., van Steenis, A., van Buchem, M. A., et al. (2011). Tractography of developing

white matter of the internal capsule and corpus callosum in very preterm infants. *Eur. Radiol.* 21, 538–547. doi: 10.1007/s00330-010-1945-x

de Jong, M., Verhoeven, M., and van Baar, A. L. (2012). School outcome, cognitive functioning, and behaviour problems in moderate and late preterm children and adults: A review. *Semin. Fetal. Neonatal Med.* 17, 163–169. doi: 10.1016/j.siny.2012.02.003

Dean, D. C., Lange, N., Travers, B. G., Prigge, M. B., Matsunami, N., Kellett, K. A., et al. (2017). Multivariate characterization of white matter heterogeneity in autism spectrum disorder. *NeuroImage Clin.* 14, 54–66. doi: 10.1016/j.nicl.2017.01.002

Devisscher, L., Chauvel, M., Rolland, C., Labra, N., Aubrain, K., Leroy, F., et al. (2021). "Disentangling the differential maturation of sensorimotor cortices in newborns compared to adults," in *Proceedings of the OHBM 2021 – Organization for human brain mapping, virtual meeting, France*.

Dewey, D., Thompson, D. K., Kelly, C. E., Spittle, A. J., Cheong, J. L. Y., Doyle, L. W., et al. (2019). Very preterm children at risk for developmental coordination disorder have brain alterations in motor areas. *Acta Paediatr.* 1992, 1649–1660. doi: 10.1111/apa.14786

Dibble, M., Ang, J. Z., Mariga, L., Molloy, E. J., and Bokde, A. L. W. (2021). Diffusion Tensor Imaging in Very Preterm, Moderate-Late Preterm and Term-Born Neonates: A Systematic Review. *J. Pediatr.* 232, 48–58.e3. doi: 10.1016/j.jpeds.2021.01.008

Dubois, J., Adibpour, P., Poupon, C., Hertz-Pannier, L., and Dehaene-Lambertz, G. (2016). MRI and M/EEG studies of the White Matter Development in Human Fetuses and Infants: Review and Opinion. *Brain Plast.* 2, 49–69. doi: 10.3233/BPL-160031

Dubois, J., Dehaene-Lambertz, G., Kulikova, S., Poupon, C., Hüppi, P. S., and Hertz-Pannier, L. (2014). The early development of brain white matter: A review of imaging studies in fetuses, newborns and infants. *Neuroscience* 276, 48–71. doi: 10.1016/j.neuroscience.2013.12.044

Duerden, E. G., Foong, J., Chau, V., Branson, H., Poskitt, K. J., Grunau, R. E., et al. (2015). Tract-Based Spatial Statistics in Preterm-Born Neonates Predicts Cognitive and Motor Outcomes at 18 Months. *AJNR Am. J. Neuroradiol.* 36, 1565–1571. doi: 10.3174/ajnr.A4312

Duerden, E. G., Grunau, R. E., Guo, T., Foong, J., Pearson, A., Au-Young, S., et al. (2018). Early Procedural Pain Is Associated with Regionally-Specific Alterations in Thalamic Development in Preterm Neonates. *J. Neurosci.* 38, 878–886. doi: 10.1523/JNEUROSCI.0867-17.2017

Edwards, A. D., Rueckert, D., Smith, S. M., Abo Seada, S., Alansary, A., Almalbis, J., et al. (2022). The Developing Human Connectome Project Neonatal Data Release. *Front. Neurosci.* 16:886772. doi: 10.3389/fnins.2022.886772

Edwards, J., Berube, M., Erlandson, K., Haug, S., Johnstone, H., Meagher, M., et al. (2011). Developmental coordination disorder in school-aged children born very preterm and/or at very low birth weight: A systematic review. *J. Dev. Behav. Pediatr.* 32, 678–687. doi: 10.1097/DBP.0b013e31822a396a

Evensen, K. A. I., Ustad, T., Tikanmäki, M., Haaramo, P., and Kajantie, E. (2020). Long-term motor outcomes of very preterm and/or very low birth weight individuals without cerebral palsy: A review of the current evidence. *Semin. Fetal. Neonatal Med.* 25:101116. doi: 10.1016/j.siny.2020.101116

Fabrizi, L., Slater, R., Worley, A., Meek, J., Boyd, S., Olhede, S., et al. (2011). A Shift in Sensory Processing that Enables the Developing Human Brain to Discriminate Touch from Pain. *Curr. Biol.* 21, 1552–1558. doi: 10.1016/j.cub.2011.08.010

Fenchel, D., Dimitrova, R., Seidlitz, J., Robinson, E. C., Batalle, D., Hutter, J., et al. (2020). Development of Microstructural and Morphological Cortical Profiles in the Neonatal Brain. *Cereb. Cortex* 30, 5767–5779. doi: 10.1093/cercor/bhaa150

Genc, S., Malpas, C. B., Holland, S. K., Beare, R., and Silk, T. J. (2017). Neurite density index is sensitive to age related differences in the developing brain. *NeuroImage* 148, 373–380. doi: 10.1016/j.neuroimage.2017.01.023

Gibbins, S., Stevens, B., Beyene, J., Chan, P. C., Bagg, M., and Asztalos, E. (2008). Pain behaviours in Extremely Low Gestational Age infants. *Early Hum. Dev.* 84, 451–458. doi: 10.1016/j.earlhumdev.2007.12.007

Gilmore, J. H., Knickmeyer, R. C., and Gao, W. (2018). Imaging structural and functional brain development in early childhood. *Nat. Rev. Neurosci.* 19, 123–137. doi: 10.1038/nrn.2018.1

Girault, J. B., Munsell, B. C., Puechmaille, D., Goldman, B. D., Prieto, J. C., Styner, M., et al. (2019). White matter connectomes at birth accurately predict cognitive abilities at age 2. *NeuroImage* 192, 145–155. doi: 10.1016/j.neuroimage.2019.02.060

Groeschel, S., Holmström, L., Northam, G., Tournier, J.-D., Baldeweg, T., Latal, B., et al. (2019). Motor Abilities in Adolescents Born Preterm Are Associated With Microstructure of the Corpus Callosum. *Front. Neurol.* 10:367. doi: 10.3389/fneur.2019.00367

Groeschel, S., Tournier, J.-D., Northam, G. B., Baldeweg, T., Wyatt, J., Vollmer, B., et al. (2014). Identification and interpretation of microstructural abnormalities in motor pathways in adolescents born preterm. *NeuroImage* 87, 209–219. doi: 10.1016/j.neuroimage.2013.10.034

Guerrero, J. M., Adluru, N., Bendlin, B. B., Goldsmith, H. H., Schaefer, S. M., Davidson, R. J., et al. (2019). Optimizing the intrinsic parallel diffusivity in NODDI: An extensive empirical evaluation. *PLoS One* 14:e0217118. doi: 10.1371/journal.pone.0217118

Hatsopoulos, N. G., and Suminski, A. J. (2011). Sensing with the Motor Cortex. *Neuron* 72, 477–487. doi: 10.1016/j.neuron.2011.10.020

Hernández, M., Guerrero, G. D., Cecilia, J. M., García, J. M., Inuggi, A., Jbabdi, S., et al. (2013). Accelerating fibre orientation estimation from diffusion weighted magnetic resonance imaging using GPUs. *PLoS One* 8:e61892. doi: 10.1371/journal.pone.0061892

Hernandez-Fernandez, M., Reguly, I., Jbabdi, S., Giles, M., Smith, S., and Sotiropoulos, S. N. (2019). Using GPUs to accelerate computational diffusion MRI: From microstructure estimation to tractography and connectomes. *NeuroImage* 188, 598–615. doi: 10.1016/j.neuroimage.2018.12.015

Hua, K., Zhang, J., Wakana, S., Jiang, H., Li, X., Reich, D. S., et al. (2008). Tract Probability Maps in Stereotaxic Spaces: Analyses of White Matter Anatomy and Tract-Specific Quantification. *NeuroImage* 39, 336–347. doi: 10.1016/j.neuroimage.2007.07.053

Hughes, E. J., Winchman, T., Padormo, F., Teixeira, R., Wurie, J., Sharma, M., et al. (2017). A dedicated neonatal brain imaging system. *Magn. Reson. Med.* 78, 794–804. doi: 10.1002/mrm.26462

Hutter, J., Tournier, J. D., Price, A. N., Cordero-Grande, L., Hughes, E. J., Malik, S., et al. (2018). Time-efficient and flexible design of optimized multishell HARDI diffusion. *Magn. Reson. Med.* 79, 1276–1292. doi: 10.1002/mrm.26765

Jelescu, I. O., and Budde, M. D. (2017). Design and validation of diffusion MRI models of white matter. *Front. Phys.* 28:61. doi: 10.3389/fphy.2017.00061

Jeurissen, B., Leemans, A., Tournier, J., Jones, D. K., and Sijbers, J. (2013). Investigating the prevalence of complex fiber configurations in white matter tissue with diffusion magnetic resonance imaging. *Hum. Brain Mapp.* 34, 2747–2766. doi: 10.1002/hbm.22099

Jones, L., Verriotis, M., Cooper, R. J., Laudiano-Dray, M. P., Rupawala, M., Meek, J., et al. (2022). Widespread nociceptive maps in the human neonatal somatosensory cortex. *Elife* 11:e71655. doi: 10.7554/eLife.71655

Kelly, C. E., Cheong, J. L. Y., Gabra Fam, L., Leemans, A., Seal, M. L., Doyle, L. W., et al. (2016a). Moderate and late preterm infants exhibit widespread brain white matter microstructure alterations at term-equivalent age relative to term-born controls. *Brain Imaging Behav.* 10, 41–49. doi: 10.1007/s11682-015-9361-0

Kelly, C. E., Thompson, D. K., Chen, J., Leemans, A., Adamson, C. L., Inder, T. E., et al. (2016b). Axon density and axon orientation dispersion in children born preterm. *Hum. Brain Mapp.* 37, 3080–3102. doi: 10.1002/hbm.23227

Kelly, C. E., Thompson, D. K., Genc, S., Chen, J., Yang, J. Y., Adamson, C., et al. (2020). Long-term development of white matter fibre density and morphology up to 13 years after preterm birth: A fixel-based analysis. *NeuroImage* 220, 117068. doi: 10.1016/j.neuroimage.2020.117068

Keunen, K., Counsell, S. J., and Benders, M. J. N. L. (2017). The emergence of functional architecture during early brain development. *NeuroImage* 160, 2–14. doi: 10.1016/j.neuroimage.2017.01.047

Keunen, K., Kersbergen, K. J., Groenendaal, F., Isgum, I., de Vries, L. S., and Benders, M. J. N. L. (2012). Brain tissue volumes in preterm infants: prematurity, perinatal risk factors and neurodevelopmental outcome: A systematic review. *J. Matern.-Fetal Neonatal Med.* 25, 89–100. doi: 10.3109/14767058.2012.664343

Kimpton, J. A., Batalle, D., Barnett, M. L., Hughes, E. J., Chew, A. T. M., Falconer, S., et al. (2021). Diffusion magnetic resonance imaging assessment of regional white matter maturation in preterm neonates. *Neuroradiology* 63, 573–583. doi: 10.1007/s00234-020-02584-9

Klein, A., and Tourville, J. (2012). 101 labeled brain images and a consistent human cortical labeling protocol. *Front. Neurosci.* 6:171. doi: 10.3389/fnins.2012.00171

Knight, M. J., Smith-Collins, A., Newell, S., Denbow, M., and Kauppinen, R. A. (2018). Cerebral White Matter Maturation Patterns in Preterm Infants: An MRI T2 Relaxation Anisotropy and Diffusion Tensor Imaging Study. *J. Neuroimaging* 28, 86–94. doi: 10.1111/jon.12486

Kostović, I., Sedmak, G., and Judaš, M. (2019). Neural histology and neurogenesis of the human fetal and infant brain. *NeuroImage* 188, 743–773. doi: 10.1016/j.neuroimage.2018.12.043

Kulikova, S., Hertz-Pannier, L., Dehaene-Lambertz, G., Buzmakov, A., Poupon, C., and Dubois, J. (2015). Multi-parametric evaluation of the white matter maturation. *Brain Struct. Funct.* 220, 3657–3672. doi: 10.1007/s00429-014-0881-y

Kunz, N., Zhang, H., Vasung, L., O'Brien, K. R., Assaf, Y., Lazeyras, F., et al. (2014). Assessing white matter microstructure of the newborn with multi-shell diffusion MRI and biophysical compartment models. *NeuroImage* 96, 288–299. doi: 10.1016/j.neuroimage.2014.03.057

Leisman, G., Braun-Benjamin, O., and Melillo, R. (2014). Cognitive-motor interactions of the basal ganglia in development. *Front. Syst. Neurosci.* 8:16. doi: 10.3389/fnsys.2014.00016

Li, X., Li, M., Wang, M., Wu, F., Liu, H., Sun, Q., et al. (2022). Mapping white matter maturational processes and degrees on neonates by diffusion kurtosis imaging with multiparametric analysis. *Hum. Brain Mapp.* 43, 799–815. doi: 10.1002/hbm.25689

Linsell, L., Malouf, R., Morris, J., Kurinczuk, J. J., and Marlow, N. (2015). Prognostic Factors for Poor Cognitive Development in Children Born Very Preterm or With Very Low Birth Weight: A Systematic Review. *JAMA Pediatr.* 169, 1162–1172. doi: 10.1001/jamapediatrics.2015.2175

Loh, W. Y., Anderson, P. J., Cheong, J. L. Y., Spittle, A. J., Chen, J., Lee, K. J., et al. (2017). Neonatal basal ganglia and thalamic volumes: Very preterm birth and 7-year neurodevelopmental outcomes. *Pediatr. Res.* 82, 970–978. doi: 10.1038/pr.2017.161

Loh, W. Y., Anderson, P. J., Cheong, J. L. Y., Spittle, A. J., Chen, J., Lee, K. J., et al. (2020). Longitudinal growth of the basal ganglia and thalamus in very preterm children. *Brain Imaging Behav.* 14, 998–1011. doi: 10.1007/s11682-019-00057-z

Machado-Rivas, F., Afacan, O., Khan, S., Marami, B., Velasco-Annis, C., Lidov, H., et al. (2021). Spatiotemporal changes in diffusivity and anisotropy in fetal brain tractography. *Hum. Brain Mapp.* 42, 5771–5784. doi: 10.1002/hbm.25653

Mah, A., Geeraert, B., and Lebel, C. (2017). Detailing neuroanatomical development in late childhood and early adolescence using NODDI. *PLoS One* 12:e0182340. doi: 10.1371/journal.pone.0182340

Maitre, N. L., Key, A. P., Chorna, O. D., Slaughter, J. C., Matusz, P. J., Wallace, M. T., et al. (2017). The Dual Nature of Early-Life Experience on Somatosensory Processing in the Human Infant Brain. *Curr. Biol.* 27, 1048–1054. doi: 10.1016/j.cub.2017.02.036

Makropoulos, A., Gousias, I. S., Ledig, C., Aljabar, P., Serag, A., Hajnal, J. V., et al. (2014). Automatic whole brain MRI segmentation of the developing neonatal brain. *IEEE Trans. Med. Imaging* 33, 1818–1831. doi: 10.1109/TMI.2014.2322280

Makropoulos, A., Robinson, E. C., Schuh, A., Wright, R., Fitzgibbon, S., Bozek, J., et al. (2018). The developing human connectome project: A minimal processing pipeline for neonatal cortical surface reconstruction. *NeuroImage* 173, 88–112. doi: 10.1016/j.neuroimage.2018.01.054

McClendon, E., Chen, K., Gong, X., Sharifnia, E., Hagen, M., Cai, V., et al. (2014). Prenatal cerebral ischemia triggers dysmaturation of caudate projection neurons. *Ann. Neurol.* 75, 508–524. doi: 10.1002/ana.24100

Miceli, P. J., Goeke-Morey, M. C., Whitman, T. L., Kolberg, K. S., Miller-Loncar, C., and White, R. D. (2000). Brief report: Birth status, medical complications, and social environment: Individual differences in development of preterm, very low birth weight infants. *J. Pediatr. Psychol.* 25, 353–358. doi: 10.1093/jpepsy/25.5.353

Mörelius, E., Hellström-Westas, L., Carlén, C., Norman, E., and Nelson, N. (2006). Is a nappy change stressful to neonates? *Early Hum. Dev.* 82, 669–676. doi: 10.1016/j.earlhumdev.2005.12.013

Nosarti, C., Nam, K. W., Walshe, M., Murray, R. M., Cuddy, M., Rifkin, L., et al. (2014). Preterm birth and structural brain alterations in early adulthood. *NeuroImage Clin.* 6, 180–191. doi: 10.1016/j.nicl.2014.08.005

Odd, D. E., Lingam, R., Emond, A., and Whitelaw, A. (2013). Movement outcomes of infants born moderate and late preterm. *Acta Paediatr.* 1992, 876–882. doi: 10.1111/apa.12320

Ouyang, M., Dubois, J., Yu, Q., Mukherjee, P., and Huang, H. (2019). Delineation of early brain development from fetuses to infants with diffusion MRI and beyond. *NeuroImage* 185, 836–850. doi: 10.1016/j.neuroimage.2018.04.017

Padilla, N., Alexandrou, G., Blennow, M., Lagercrantz, H., and Ådén, U. (2015). Brain Growth Gains and Losses in Extremely Preterm Infants at Term. *Cereb. Cortex* 1991, 1897–1905. doi: 10.1093/cercor/bht431

Pannek, K., George, J. M., Boyd, R. N., Colditz, P. B., Rose, S. E., and Fripp, J. (2020). Brain microstructure and morphology of very preterm-born infants at term equivalent age: Associations with motor and cognitive outcomes at 1 and 2 years. *NeuroImage* 221:117163. doi: 10.1016/j.neuroimage.2020.117163

Pannek, K., Scheck, S. M., Colditz, P. B., Boyd, R. N., and Rose, S. E. (2014). Magnetic resonance diffusion tractography of the preterm infant brain: A systematic review. *Dev. Med. Child Neurol.* 56, 113–124. doi: 10.1111/dmcn.12250

Parikh, M. N., Chen, M., Braimah, A., Kline, J., McNally, K., Logan, J. W., et al. (2021). Diffusion MRI Microstructural Abnormalities at Term-Equivalent Age Are Associated with Neurodevelopmental Outcomes at 3 Years of Age in Very Preterm Infants. *Am. J. Neuroradiol.* 42, 1535–1542. doi: 10.3174/ajnr.A7135

Pecheva, D., Kelly, C., Kimpton, J., Bonthrone, A., Batalle, D., Zhang, H., et al. (2018). Recent advances in diffusion neuroimaging: Applications in the developing preterm brain. *F1000Research* 7, F1000FacultyRev–1326. doi: 10.12688/f1000research.15073.1

Pines, A. R., Cieslak, M., Larsen, B., Baum, G. L., Cook, P. A., Adebimpe, A., et al. (2020). Leveraging multi-shell diffusion for studies of brain development in youth and young adulthood. *Dev. Cogn. Neurosci.* 43:100788. doi: 10.1016/j.dcn.2020.100788

Pogribna, U., Yu, X., Burson, K., Zhou, Y., Lasky, R. E., Narayana, P. A., et al. (2013). Perinatal Clinical Antecedents of White Matter Microstructural Abnormalities on Diffusion Tensor Imaging in Extremely Preterm Infants. *PLoS One* 8:e72974. doi: 10.1371/journal.pone.0072974

Raghavan, S., Reid, R. I., Przybelski, S. A., Lesnick, T. G., Graff-Radford, J., Schwarz, C. G., et al. (2021). Diffusion models reveal white matter microstructural changes with ageing, pathology and cognition. *Brain Commun.* 3:fcab106. doi: 10.1093/braincomms/fcab106

Rose, J., Mirmiran, M., Butler, E. E., Lin, C. Y., Barnes, P. D., Kermoian, R., et al. (2007). Neonatal microstructural development of the internal capsule on diffusion tensor imaging correlates with severity of gait and motor deficits. *Dev. Med. Child Neurol.* 49, 745–750. doi: 10.1111/j.1469-8749.2007.00745.x

Schneider, J., Duerden, E. G., Guo, T., Ng, K., Hagmann, P., Bickle Graz, M., et al. (2018). Procedural pain and oral glucose in preterm neonates: Brain development and sex-specific effects. *Pain* 159, 515–525. doi: 10.1097/j.pain.0000000000001123

Skranes, J., Vangberg, T. R., Kulseng, S., Indredavik, M. S., Evensen, K. A., Martinussen, M., et al. (2007). Clinical findings and white matter abnormalities seen on diffusion tensor imaging in adolescents with very low birth weight. *Brain J. Neurol.* 130, 654–666. doi: 10.1093/brain/awm001

Spittle, A. J., and Orton, J. (2014). Cerebral palsy and developmental coordination disorder in children born preterm. *Semin. Fetal Neonatal Med.* 19, 84–89. doi: 10.1016/j.siny.2013.11.005

Suzuki, K. (2007). Neuropathology of developmental abnormalities. *Brain Dev.* 29, 129–141. doi: 10.1016/j.braindev.2006.08.006

Thompson, D. K., Inder, T. E., Faggian, N., Johnston, L., Warfield, S. K., Anderson, P. J., et al. (2011). Characterization of the corpus callosum in very preterm and full-term infants utilizing MRI. *NeuroImage* 55, 479–490. doi: 10.1016/j.neuroimage.2010.12.025

Thompson, D. K., Kelly, C. E., Chen, J., Beare, R., Alexander, B., Seal, M. L., et al. (2019). Characterisation of brain volume and microstructure at term-equivalent age in infants born across the gestational age spectrum. *NeuroImage Clin.* 21:101630. doi: 10.1016/j.nicl.2018.101630

Thompson, D. K., Loh, W. Y., Connelly, A., Cheong, J. L. Y., Spittle, A. J., Chen, J., et al. (2020). Basal ganglia and thalamic tract connectivity in very preterm and full-term children; associations with 7-year neurodevelopment. *Pediatr. Res.* 87, 48–56. doi: 10.1038/s41390-019-0546-x

Thompson, R. J. Jr., Catlett, A. T., Oehler, J. M., Gustafson, K. E., Goldstein, R. F., and Prochaska, J. J. (1998). Home Environment and Developmental Outcome of African American and White Infants With Very Low Birthweight. *Child. Health Care* 27, 1–14. doi: 10.1207/s15326888chc2701_1

Tomasino, B., and Gremese, M. (2016). The Cognitive Side of M1. *Front. Hum. Neurosci.* 10:298. doi: 10.3389/fnhum.2016.00298

van den Heuvel, M. P., Kersbergen, K. J., de Reus, M. A., Keunen, K., Kahn, R. S., Groenendaal, F., et al. (2015). The Neonatal Connectome During Preterm Brain Development. *Cereb. Cortex* 1991, 3000–3013. doi: 10.1093/cercor/bhu095

Van Hus, J. W., Potharst, E. S., Jeukens-Visser, M., Kok, J. H., and Van Wassenaer-Leemhuis, A. G. (2014). Motor impairment in very preterm-born children: Links with other developmental deficits at 5 years of age. *Dev. Med. Child Neurol.* 56, 587–594. doi: 10.1111/dmcn.12295

van Kooij, B. J. M., de Vries, L. S., Ball, G., van Haastert, I. C., Benders, M. J. N. L., Groenendaal, F., et al. (2012). Neonatal tract-based spatial statistics findings and outcome in preterm infants. *AJNR Am. J. Neuroradiol.* 33, 188–194. doi: 10.3174/ajnr.A2723

van Pul, C., van Kooij, B. J. M., de Vries, L. S., Benders, M. J. N. L., Vilanova, A., and Groenendaal, F. (2012). Quantitative fiber tracking in the corpus callosum and internal capsule reveals microstructural abnormalities in preterm infants at term-equivalent age. *AJNR Am. J. Neuroradiol.* 33, 678–684. doi: 10.3174/ajnr.A2859

Volpe, J. J. (2021). Primary neuronal dysmaturation in preterm brain: Important and likely modifiable. *J. Neonatal Perinat. Med.* 14, 1–6. doi: 10.3233/NPM-200606

Williams, J., Lee, K. J., and Anderson, P. J. (2010). Prevalence of motor-skill impairment in preterm children who do not develop cerebral palsy: A systematic review. *Dev. Med. Child Neurol.* 52, 232–237. doi: 10.1111/j.1469-8749.2009.03544.x

Wu, D., Chang, L., Akazawa, K., Oishi, K., Skranes, J., Ernst, T., et al. (2017). Mapping the Critical Gestational Age at Birth that Alters Brain Development in Preterm-born Infants using Multi-Modal MRI. *NeuroImage* 149, 33–43. doi: 10.1016/j.neuroimage.2017.01.046

Yakovlev, P. I., and Lecours, A. R. (1967). "The Myelogenetic Cycles of Regional Maturation of the Brain," in *Regional Development of the Brain in early Life ScienceOpen*, ed. A. Minkowski (Oxford: Blackwell), 3–69. doi: 10.1007/BF00192215

Young, J. M., Vandewouw, M. M., Mossad, S. I., Morgan, B. R., Lee, W., Smith, M. L., et al. (2019). White matter microstructural differences identified using multi-shell diffusion imaging in six-year-old children born very preterm. *NeuroImage Clin.* 23:101855. doi: 10.1016/j.nicl.2019.101855

Zhang, H., Schneider, T., Wheeler-Kingshott, C. A., and Alexander, D. C. (2012). NODDI: Practical *in vivo* neurite orientation dispersion and density imaging of the human brain. *NeuroImage* 61, 1000–1016. doi: 10.1016/j.neuroimage.2012.03.072

Zhao, T., Mishra, V., Jeon, T., Ouyang, M., Peng, Q., Chalak, L., et al. (2019). Structural network maturation of the preterm human brain. *NeuroImage* 185, 699–710. doi: 10.1016/j.neuroimage.2018.06.047

Zwicker, J. G. (2014). Motor impairment in very preterm infants: Implications for clinical practice and research. *Dev. Med. Child Neurol.* 56, 514–515. doi: 10.1111/dmcn.12454

Zwicker, J. G., Grunau, R. E., Adams, E., Chau, V., Brant, R., Poskitt, K. J., et al. (2013). Score for neonatal acute physiology-II and neonatal pain predict corticospinal tract development in premature newborns. *Pediatr. Neurol.* 48, 123–129.e1. doi: 10.1016/j.pediatrneurol.2012.10.016

Frontiers in Neuroscience

Provides a holistic understanding of brain function from genes to behavior

Part of the most cited neuroscience journal series which explores the brain - from the new eras of causation and anatomical neurosciences to neuroeconomics and neuroenergetics.

Discover the latest Research Topics

See more →

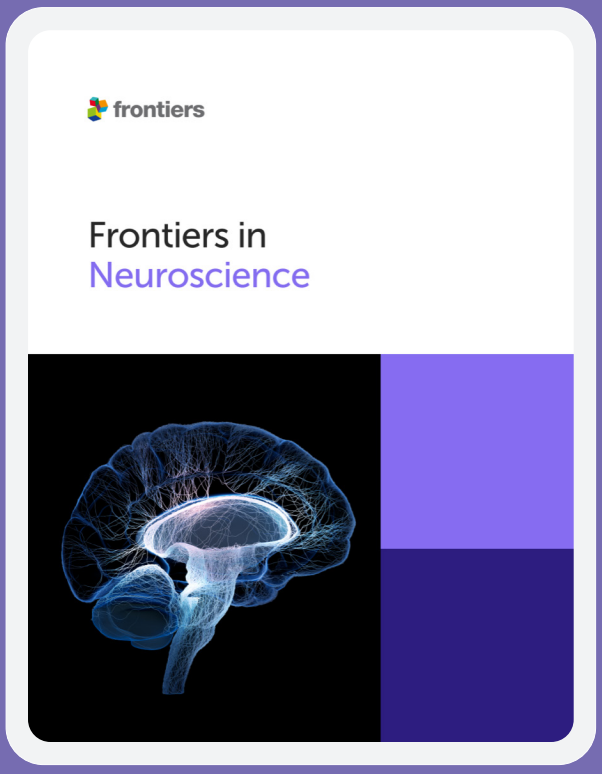

Frontiers

Avenue du Tribunal-Fédéral 34
1005 Lausanne, Switzerland
frontiersin.org

Contact us

+41 (0)21 510 17 00
frontiersin.org/about/contact